Aristotle University of Thessaloniki
School of Geology
Department of Physical & Environmental Geography

Angelos Mousouliotis
M.Sc. Petroleum Engineering

Simulation of the development of the pre-deltaic depositional strata of the Nile River in the Herodotus Basin and comparison with seismic stratigraphic data within the Exclusive Economic Zone of Cyprus

Doctoral Dissertation

Thessaloniki 2021

Angelos Mousouliotis

Simulation of the development of the pre-deltaic depositional strata of the Nile River in the Herodotus Basin and comparison with seismic stratigraphic data within the Exclusive Economic Zone of Cyprus

Doctoral Dissertation

Submitted to School of Geology
Department of Physical & Environmental Geography
Oral examination date: 18/10/2021

Examination Committee
Professor K. Albanakis, Supervisor
Professor A. Georgakopoulos, member of Advisory Committee
Professor G. Papatheodorou, member of Advisory Committee
Professor C. Papazachos, Aristotle University of Thessaloniki
Professor F. Tsikalas, University of Oslo & Chief Exploration Vår Energi AS, Norway
Dr. Dimitrios Sakellariou, Reasearch Director of Structural/Marine Geology and Marine Geoarchaelogy at the Institute of Oceanography of HCMR
Dr. Benjamin Medvedev, Adjunct Lecturer, Hebrew University (HUJI) and Intra University Institute for Marine Sciences (IUI) and Consultant geophysicist at Schlumberger

Simulation of the development of the pre-deltaic depositional strata of the Nile River in the Herodotus Basin and comparison with seismic stratigraphic data within the Exclusive Economic Zone of Cyprus

ISBN

"Approval of this doctoral thesis by the School of Geology of Aristotle University of Thessaloniki does not imply endorsement of the author's opinions" (L. 5343/1932, article 202, par. 2)

Acknowledgments

The present doctoral thesis was prepared in the School of Geology, Department of Physical & Environmental Geography, and with its completion, I would like to acknowledge those who have made a significant contribution and support me to finalize this effort during the four years that have lasted.

I would like to acknowledge:

Konstantinos Albanakis, Professor at the School of Geology, AUTh, for the confidence he has shown me in supporting the assignment of this subject as well as for his constant and tireless supervision.

Andreas Georgakopoulos, Professor at the School of Geology, AUTh and member of the Advisory Committee, for the excellent cooperation, continuing interest, and pursuing the evolution of the doctoral dissertation, and for all the understanding and moral support. I would also like to express my sincere thanks for providing all the infrastructure (hardware and software) that have contributed decisively to the preparation of the doctoral thesis, as well as for the financial support for presenting the outcomes of this research at international conferences.

George Papatheodorou, Professor at the School of Geology, University of Patras and member of the Advisory Committee, for his notes and corrections in the manuscript of the dissertation.

Cypriot Ministry of Energy, Commerce, and Industry for granting full support for this study, financial support, and data concession.

Petroleum Geo-Services is deeply acknowledged for providing the seismic data set.

Schlumberger is acknowledged for kindly providing the Petrel software used for seismic interpretation.

Konstantinos Vouvalidis, Associate Professor at the School of Geology, AUTh, for the extremely helpful discussions and exchange of opinions and ideas.

Dr. Benjamin Medvedev geophysicist at Schlumberger, for his critical help in the operation of Petrel software. In addition, I would like to thank him for the lessons on velocity modeling.

Dr. Efthymios Tripsanas, sedimentologist, for his guidance on how channel lobe complexes are analyzed. In addition, I would like to thank him for the provided relevant literature.

Triantafyllos Chatziantoniou, special teaching fellow at the School of Physics, AUTh, for his technical support.

Sofia Doani, Ph.D. student at the School of Geology, AUTh, for her assistance in the creation of figures, maps, and drawings.

Stergios Christodoulou, English philologist and friend, for his crucial assistance in text editing in the English language.

Dr. Maria Voutsa, my wife and friend, for the valuable help, without which the present work could not be completed, as for her patience and moral support.

Finally, I would like to deeply acknowledge my family for their moral and meaningful support throughout my endeavor.

Abstract

The doctoral dissertation analyzes the main deformation mechanisms of the 2-3 km thick Messinian Salinity Crisis sequence by using 2310 kilometers of high quality multichannel seismic-reflection profiles located at the west part of the Cypriot Exclusive Economic Zone. The study area is separated into five salt-tectonic structural provinces and the different triggered and deformation mechanisms are described. The overall seismic image of the Messinian Salinity Crisis sequence refers to allochthonous salt derived from a different direction because of the various triggered mechanism acting in the study area. The main deformation mechanism into Herodotus Basin is attributed to the Messinian salt gliding northward from the Nile Delta area. The only area that partially suffers from thin skin salt tectonics is located at the West Eratosthenes sub-Basin; the seismic image of the Messinian sequence in this area refers to autochthonous salt deposits. Discrimination of the classic intra-salt reflections is not possible in the deep Herodotus Basin. However, at the base of the Messinian salt located into the deep Herodotus Basin medium to high amplitude discontinuous reflections are observed.

The interpretation of the various Messinian sequence deformation patterns and the separation of the Messinian Salinity Crisis sequence into dinstict stratigraphic subdivisions, allows the seismic interpretation medium to high amplitude high frequency reflection located at the base of the Messinian Salinity Crisis sequence. The doctoral dissertation is focused on the architectural characteristics of the offshore extension of a late Messinian deep-sea fan system through the analysis of 2310 kilometers of high quality multichannel seismic-reflection profiles. A 2-3 km thick Messinian Salinity Crisis sequence occurs on top of a clastic system, indicating that even during the maximum sea-level drop, this part of the Herodotus Basin was still a marine setting. The top of the clastic system is characterized by a sharp surface on which several shear surfaces within the overlying Messinian salt terminate. This is attributed to the northward gliding of the Messinian mobile salt layer from the Nile cone to the deep Herodotus Basin. Mapping the base of the clastic system, demonstrates that the bathymetric relief on which the clastic system evolved was complex, forming valley-like structures in the southern half of the study area. The sediment source of this clastic system is interpreted to have originated from the Nile River through gravity flows during the early stages of the Messinian Salinity Crisis that resulted in thick deposits at the deepest parts of the Herodotus basin. Medium to high amplitude discontinuous reflections with multiple sudden terminations representing local (channel-like) to broader-scale erosional surfaces characterize the late Messinian clastic system. Such a seismic character, in combination with its confined nature, indicates the development of a submarine channel complex set. On the other hand, towards the north, the convex top surface of the clastic system and the discontinuous internal reflections, exhibit on multiple occasions, bidirectional downlap geometries that point to the basinward evolution of the channel complex set into a lobe complex set at the most unconfined parts of the basin. This clastic system is time equivalent to the fluvio-deltaic deposits of the Abu Madi Formation of the Nile Delta region.

The doctoral thesis ttempts to simulate the main processes that had shaped the deep-sea fan located at the base of the Messinian sequence by using Stratigraphic Forward Model (SFM) (Geological Process Model, GPM) as a tool. 1D backstripping was performed in order to obtain the pre-Messinian relef and simulate the late Messinian clastic deposition by using unsteady (turbiditic) flow. The main input parameters used for the simulation were the sediment sources, the diffusion coefficient, the transport coefficient, erodibility, and various

flow velocities. Sensitivity experiments were performed in a small surface in order to understand the importance of each parameter, prior to the simulation of the late Messinian clastic accumulations. The input parameters, the results, and the limitations of the model are well analyzed and discussed.

Table of Contents

A.1 Introduction

A.1.1 General setting

A review of the geological evolution of the Eastern Mediterranean is performed to describe the main geomorphological features of the study area and the present tectonic regime. In the geological setting, extensive reviews of the Messinian Salinity Crisis and the various deposition scenarios of the Messinian sequence are performed to understand the environments and the conditions under which these thick salt sequences have been deposited. In addition, a review of the evolution of the northeast African drainage networks and climatic conditions prevailing during Late Messinian is presented focusing on the evolution of the Late Messinian River Nile.

The present study utilizes seismic interpretation of high-quality 2D seismic data granted from PGS after the agreement of the Ministry of Energy of the Republic of Cyprus. The seismic interpretation and the separation of the seismic strata into different stratigraphic units used as a tool to unravel the salt-tectonic regime of the area are always compiled with the available international literature. The Messinian salt internal seismic stratigraphy was described to interpret the various salt deformation mechanisms and understand the differences of the sedimentological processes prevailing during the Late Messinian era between the deep Herodotus Basin and West Eratosthenes sub-Basin.

After the discrimination of the Messinian sequence into different stratigraphic layers, the differences of the internal seismic stratigraphy with the deep Herodotus Basin are noted and described. The study concentrates on the medium to high amplitude reflections located at the base of the Messinian sequence into the Herodotus Basin. In the seismic data set, the medium to high amplitude reflections has been interpreted as

channel complex sets. An attempt is made to map and quantify the medium to high amplitude reflections at the base of the Messinian sequence using the 2D seismic data, taking into consideration the deformation of the Messinian sequence from the Nile cone towards the deep Herodotus Basin in combination with the Late Messinian geomorphology. The results of the seismic interpretation suggest that during the early stages of the Messinian Salinity Crisis, clastic sediments originating from the Nile were deposited at the deepest area of the Herodotus Basin shaping a deep-sea fan. In addition, the implications of the presence of clastic accumulations so far from the source area to a possible salt deposition scenario are widely discussed.

Finally, numerical simulations were conducted to reproduce the physical conditions under which the interpreted deep-sea fan was shaped. During the numerical simulations parameters as sediment input, diffusion coefficient, transport coefficient and unsteady flow velocities were used. The results of the simulations are discussed and compared with the 2D interpreted seismic lines.

A.1.2 Scope of the study

The region of the Eastern Mediterranean has been characterized as a gas-bearing province especially after the discovery of giant gas fields (Leviathan, Tamar, Aphrodite, Zohr, Calypso, and Glaucus) in the last fifteen years. With finds in offshore Egypt, Cyprus, and the Levant Basin the area is now considered a highly prospective petroleum province, with intense drilling activity expected in the coming years. Due to intense exploration activities, a substantial database of seismic data was created by geoservices and oil companies, to unravel many geological challenges that emerged from the complex geodynamic history of the area. For the fulfillment of the present study, seismic data gathered from MC2D-CYP 2006 (https://www.pgs.com/data-

library/europe/mediterranean/cyprus-2006/) and MC2D-CYP 2008 (https://www.pgs.com/data-library/europe/mediterranean/cyprus-2008/) surveys were provided by PGS with the agreement of the Ministry of Energy of the Republic of Cyprus. The data covers the western part of the Eratosthenes Continental Block (ECB) towards the Herodotus Basin, offshore Cyprus.

The scope of the study is to provide a comprehensive explanation of sedimentation in the Herodotus Basin during Late Messinian based on the interpretation of the 2D seismic data. This study aims to highlight the individual modules that constitute a deep-sea fan system and help in a better understanding of the sedimentological parameters that formed the pro-deltaic deposits of the river Nile during Late Messinian, based on pioneering concepts and analogs used in similar environments of deposition around the globe. In addition, the present work contributes to the knowledge concerning the evolution of sedimentary accumulations in a deep-sea environment located in a frontier basin. In the context of the thesis, an attempt is made to simulate the sedimentary accumulations located in the Herodotus basin by using stratigraphic forward modeling. This innovative methodology aims to explore the parameters that affect deep-sea processes. Finally, a comparison between the results of the simulation and the interpreted seismic data occur based on the overall geometry of the sedimentary system.

The study contributes to the discussion on the development of the source-to-sink system of the Messinian River Nile and on the evolution of the evaporitic sequence based on new results derived by seismic data. The main objective of the present work is the evaluation of the sedimentary accumulations located at the base of the Messinian sequence as potential hydrocarbons reservoirs, and support this evaluation by using stratigraphic forward modeling. Finally, the main objective of the dissertation is to add

value to the seismic interpretation of the late Messinian clastic sequences by using stratigraphic forward modeling.

A.1.3 Structure of the study

The doctoral dissertation is separated into five main sections (A, B, C, D, and E). Section A includes the introduction and the literature review (chapters 1 and 2) concerning the geological evolution of the study area. Section B includes the data description and methodology used for seismic interpretation and it is entirely consisting of chapter 3. Section C includes chapters 4 and 5 and focuses on seismic interpretation. Section D is concentrated on the numerical simulation and numerical modeling of the interpreted Messinian clastic sequences and includes chapters6 and 7. Finally, section E presents the main outcomes of the doctoral dissertation.

The following structure was adopted for the most effective presentation of the study:

A.1.3.1 Section A

In the first chapter, the general setting, the purpose of the doctoral thesis, and the structure of the study are listed.

In the second chapter, the geological setting of the study area and its geological evolution are presented. Particularly in this chapter scenarios for the Messinian Salinity Crisis (MSC) and Messinian salt deposition, the climate of North-West Africa, the evolution of the drainage systems of North Africa, and the natural seepage of hydrocarbons observed from offshore Nile Delta towards the Herodotus Basin are described. All the data presented in this chapter result from the study of the relevant international literature. The development of the sediment source area, in terms of

drainage networks, erosion, denudation, and sediment routing systems as vital to the sedimentary basin system are reviewed because the Herodotus Basin must be treated as a multi-component system that requires a multi-faceted approach which will advance our understanding of its infilling development.

A.1.3.2 Section B

In the third chapter, a detailed description of the methodology and the data used for the accomplishment of the doctoral dissertation is listed.

A.1.3.3 Section C

In the fourth chapter, an introduction to the seismic interpretation of the main salt-deformation mechanisms of the Messinian Salinity Crisis sequence is performed. The interpretation of the main seismic reflectors and the main seismic phases are analyzed and evaluated to separate the sedimentary strata into seismic stratigraphic units and seismic surfaces (both in time and depth). The internal seismic stratigraphy of the Messinian sequence (unit 2) is analyzed and compared with results from other seismic interpretations around the Eastern Mediterranean. The differences in the internal seismic stratigraphy used to distinguish variations of the clastic sediment accumulation and salt deformation. Based on the geomorphology and the internal stratigraphy of the Messinian sequence, the study area is divided into five salt-tectonic structural provinces. The salt-tectonic structural provinces are described, and the main salt-deformation mechanisms are discussed.

In the fifth chapter, after the division of the study area into five salt-tectonic structural provinces, the thesis is focused on the presence of medium to high amplitude reflectors at the base of the Messinian sequence in the deep Herodotus Basin. An introduction about the evolution of submarine channels and the possible consequences

of the MSC sea-level draw-down in the erosion and deposition of clastic sediments is performed. The Late Messinian paleo bathymetry is analyzed and the medium to high amplitude reflectors interpreted as a channel lobe complex. The discussion of the seismic interpretation is concentrated on the Late Messinian sedimentary accumulations located west of the West Eratosthenes High (WEH) and a comparison between the Late Messinian channel lobe complex and a Plio-Quaternary channel complex is presented. The channel lobe complex deposits are correlated with the onshore Late Messinian deposits of the Abu Madi Formation leading to the creation of a conceptual model about the evolution of the clastic accumulations during the Late Messinian. Finally, the implications of the presence of the late Messinian clastic deposits at the base of the Messinian sequence in the salt deposition scenarios are discussed.

A.1.3.4 Section D

In the sixth chapter, an introduction to the complex nature and the main natural processes that shape a deep-sea fan is performed to understand the main natural variables that have to be modeled by a simulator. Using empirical equations based on synchronous analogs from around the globe the water and sediment supply of the Late Messinian River Nile are computed to investigate the magnitude of the clastic sediments transported by the riverine system considering the sediment volumes transported as available to produce an active turbidite system. An introduction about the evolution and the various types of mathematic numerical models is performed to select a suitable mathematic model for the simulations of this thesis and an extensive description of the selected model GPM (Geological Process Model) is made. Finally, the input data of the mathematical model are specified and the results of the simulation from different sensitivity experiments are listed.

In the seventh chapter, a comparison between the seismic profiles and simulation results is attempted, to verify the precision and correctness of the model. In addition, general results, restrictions, and future work are listed.

A.1.3.5 Section E

In the eighth chapter, the conclusions and a synopsis of the doctoral dissertation are presented.

A.2 Geological setting

A.2.1 Geological evolution of Eastern Mediterranean

The Eastern Mediterranean basin is a relic of the Mesozoic Neotethys Ocean (e.g., Garfunkel 2004; Van Hinsbergen et al., 2019) (Fig. 1). The present-day geological setting was shaped from plate tectonics among the African, Arabian, and Eurasian plates since the Permo-Triassic. Two major periods of the tectonic evolution of the Neotethys Ocean are identified, a period of rifting from the Triassic to the mid-Jurassic and seafloor spreading from the Upper Jurassic to the Lower Cretaceous (Gardosh et al., 2010; Schattner and Ben-Avraham, 2007; Walley 1998) (Fig. 1).

The second period resulted in the creation of transform faults generally NNW-SSE oriented (Montadert et al., 2014). During the first period, a ribbon of continental crust was cut off from Arabia resulting in the creation of the Eratosthenes Continental Block (ECB) (Robertson 1998; Van Hinsbergen et al., 2019) (Fig. 1). At the end of the rifting, a carbonate platform developed on the ECB (Papadimitriou et al., 2018) isolated from any clastic input or salt precipitation. On the contrary, east and west of the ECB two basins were formed, the Levantine and the Herodotus (Fig. 1). In the Upper Cretaceous until the Eocene the whole Tethyan region underwent a period of North-South compression triggering the continental collision between African and Eurasia plates. The results of this compression phase were the progressive isolation of the Mediterranean Sea, the subduction of Neotethyan oceanic crust along the Cyprus and Hellenic arcs which formed the accretionary prism located south of the island of Crete (Fig. 1) known as the Mediterranean Ridge (Jackson and McKenzie, 1988; Mascle et al., 2000; Robertson and Dixon, 1984; Robertson and Mountrakis, 2006), and the placement of the Troodos ophiolites that created the island of Cyprus (Robertson and Dixon, 1984). In the Upper Eocene-Early Oligocene, a major tectonic event occurs, namely the

separation of Arabia from Africa through the opening of the Suez rift (Garfunkel 1988). This event had enormous implications in the structural and sedimentary setting of the region, as amounts of clastic sediments started to enter the Eastern Mediterranean basin. During the Oligocene-Miocene an NW-SE strike-slip faulting west of ECB took place and it remains active until today (Montadert et al., 2014).

Because of the Messinian Salinity Cricis, a huge volume of clastic sediments entered the basinal areas of the Eastern Mediterranean due to the erosion of the margins, along with an important contribution from the river Nile. The river Nile alone is estimated to have transported in the region west of ECB 70,000 cubic kilometers of sediments in less than three million years (Said 1981). The deposition of these clastic materials took place in front of low stand deltas.

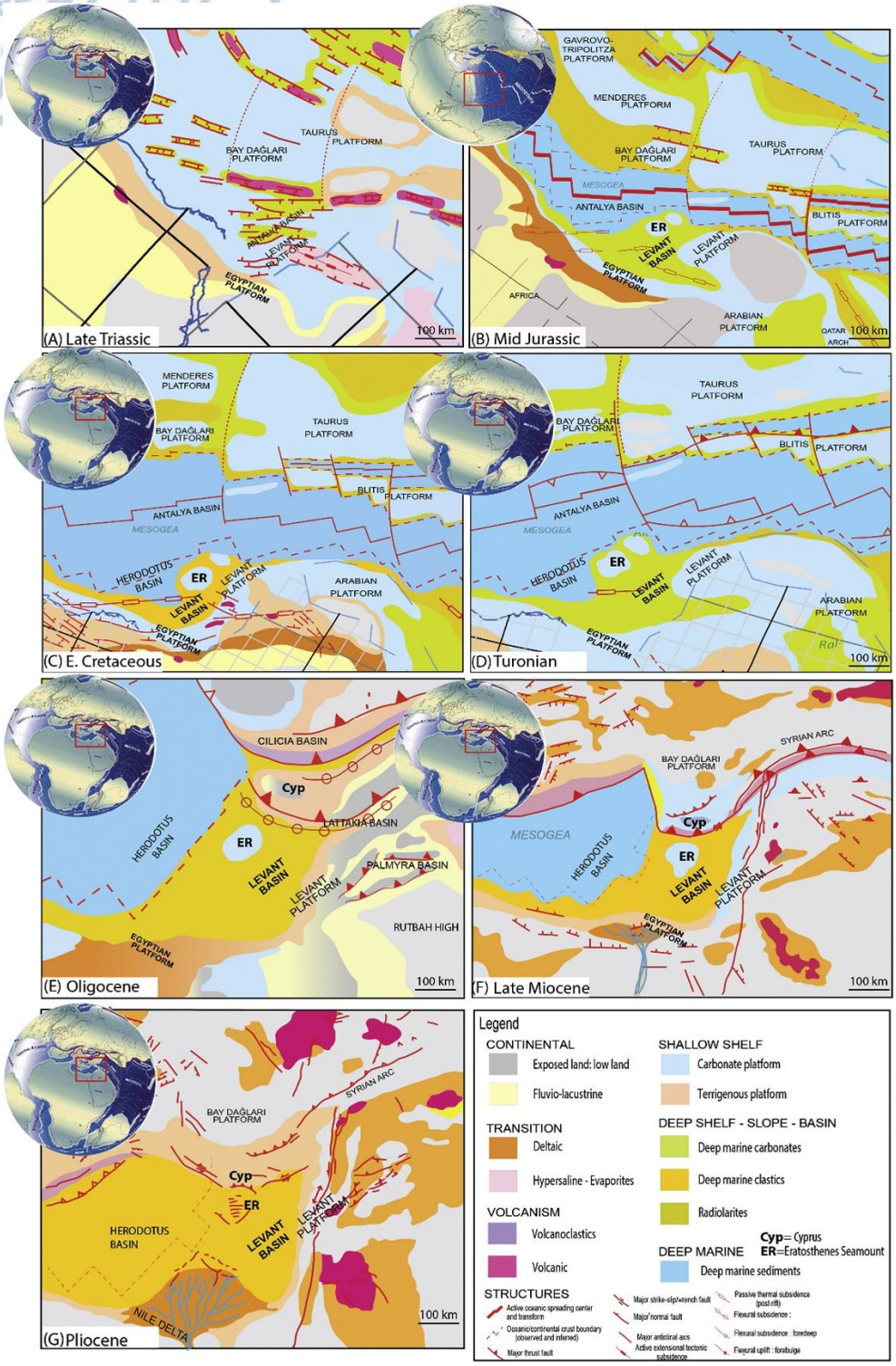

Figure 1: Paleogeographic reconstructions showing the different depositional environments and the main geodynamic events that have shaped the Eastern Mediterranean region since the Late Triassic (Papadimitriou et al., 2018)

A.2.1.1 The Levantine Basin (LB)

The Levantine Basin (LB) is a NE-trending depression (~1.5 km deep) located east and southeast offshore the island of Cyprus (Fig. 2). It has a basement probably composed of thinned continental crust shaped via lithospheric stretching (Granot 2016; Hawie et al., 2013; Montadert et al., 2014) and contains a thick infill of Mesozoic–Cenozoic sediments (>12 km) (Ben-Avraham et al. 2002; Netzeband et al. 2006) including the up to 2 km thick MSC sequence.

A.2.1.2 Eratosthenes Continental Block (ECB)

The Eratosthenes Continental Block (ECB) is an isolated ~150 km wide SSW-NNE oriented continental fragment located south offshore the island of Cyprus (Fig. 2), forms the easternmost limit of the Herodotus Basin, and represents the natural boundary between the Nile Deep-Sea Fan, the Herodotus Basin, and the Levantine Basin. The north boundary of the ECB is delineated by the Cyprus Arc (Fig. 2), a tectonic structure that represents the ECB ongoing continental collision with the island of Cyprus (Robertson 1998; Symeou et al., 2018). The type of the ECB underlying basement remains unknown. However, recent studies (Gardosh et al., 2010; Granot 2016) support a thinned continental crust ~25 km thick. Magnetic anomalies in the proximity of the ECB are associated with pre-Cretaceous or Lower Cretaceous syn-rift related magmatic activity (intrusions or extrusions) (Montdert et al., 2014; Robertson 1998). It is now widely accepted that since the end of the rifting, a carbonate platform developed on the ECB until the Late Miocene (Papadimitriou et al., 2018), isolated from any clastic input or salt precipitation.

A.2.1.3 West Eratosthenes sub-Basin and High (WEsB and WEH)

The steep slope of the ECB is bounded to the west by a distinct topographic depression well delineated in the bathymetry map (Fig. 2). This 50 km wide, SSW-NNE oriented asymmetrical topographic depression, is known as the West Eratosthenes sub-Basin (WEsB) (Montadert et al., 2014). The WEsB was created during the Miocene simultaneously to the formation of its SSW-NNE oriented west boundary which is represented by an anticline structure named the West Eratosthenes High (WEH) (Fig. 2) (Montadert et al., 2014) that separates it from the thick Herodotus Basin in the west. The WEH is probably the true western boundary of the ECB with the deep Herodotus Basin (Montadert et al., 2014) representing the Continental-Oceanic Boundary (COB), an assertion supported by Granot et al., 2016. The WEsB is bounded to the south by the ECB westward extension, a segment that constitutes the natural prolongation of the carbonate platform to the west (Fig.2).

A.2.1.4 The Herodotus Basin (HB)

The Herodotus Basin (HB) is a 3 km deep, northeast-trending depression that constitutes a relic of the Early Mesozoic Neotethys Ocean (Fig. 2) (Garfunkel 2004; Lamotte et al., 2011), is bounded to the north by the Mediterranean Ridge, to the northeast by the western portion of the Cyprus Arc and the south by the Nile Delta (Allen et al., 2016). The HB has a basement of oceanic crust and a thick sedimentary cover with an estimated thickness between 12 and 15 km (Granot 2016; Montadert et al., 2014). More specifically, it contains a ~7 km thick Mesozoic–Cenozoic succession (Garfunkel 1998; Voogd and Truffert 1992), overlain by a 2-3 km layer of Messinian evaporites, topped by 1-4 km of Plio-Quaternary Nile derived clastic accumulations (Aal et al., 2000; Garfunkel 1998; Loncke et al., 2006; Macgregor 2012).

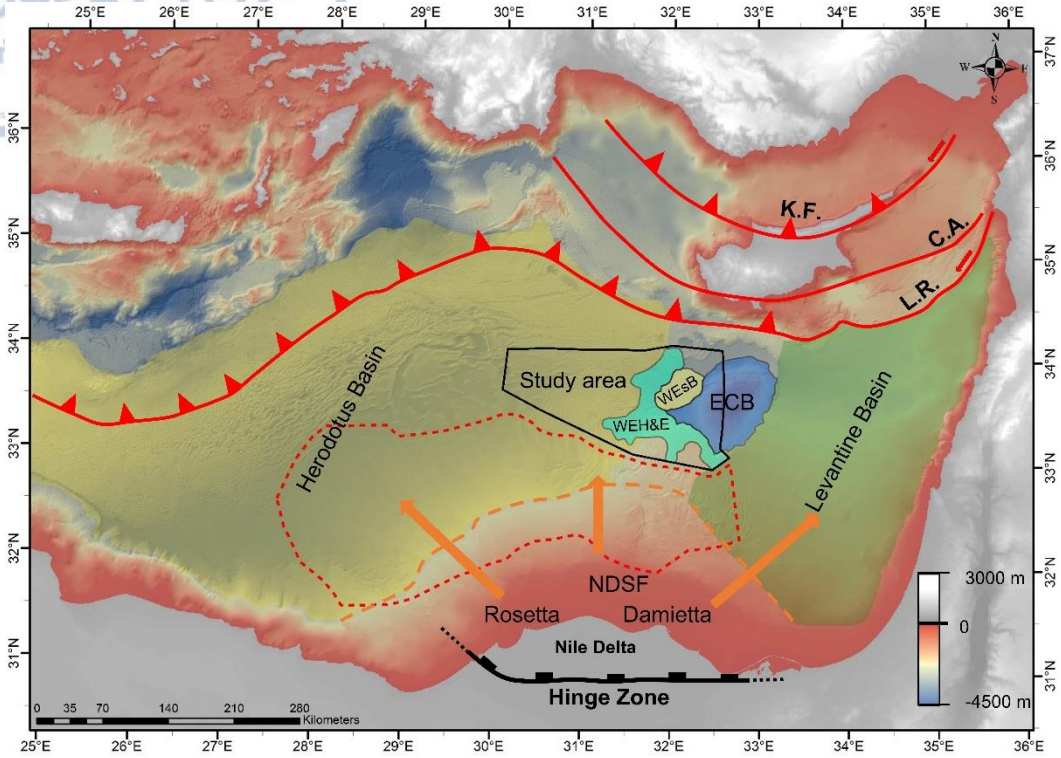

***Figure 2**: The topographic map illustrates the main structural features of the Eastern Mediterranean: Herodotus and Levantine Basins (Montadert et al., 2014) separated by Eratosthenes Continental Block (ECB) (Robertson 1998), West Eratosthenes sub-Basin (WEsB) (Montadert et al., 2014), West Eratosthenes High & Extension (WEH&E) (Montadert et al., 2014) NDSF = Nile Deep-Sea Fan (Loncke et al., 2006), L.R. = Latakia Ridge (Hall et al., 2005), C.A. = Cyprus Arc (Robertson and Dixon 1984), K.F. = Kyrenia Fault (Robertson and Kinnaird 2016). The study area is located west of ECB into Herodotus Basin. The orange arrows indicate the synchronous sediment supply of River Nile. Rosetta and Damietta constitute the present main branches of the Nile Delta. The Red dashed line represents the outline of Figure 7.*

A.2.2 Scenarios for the Messinian sequence deposition

It is generally accepted that petroleum systems are closely linked to basins that had passed through an evaporitic phase (Warren 2006). Tangible examples are the petroleum systems of South East America, West Africa (Rabinowitz and LaBrecque 1979), Gulf of Mexico (Salvador 1987), North Sea (Brunstrom and Walmsley 1969), and Middle East (Murris 1981). The classic evaporitic model requires in most cases a basin resulting from continental rifting under specific climatic conditions that determine a negative water budget; a living example is the Red Sea (Girdler and Styles 1974). For the Mediterranean Sea, this scenario is not applicable. The Mediterranean Sea is a basin with a negative water budget that follows its natural course toward shrinking and extinction as the African plate moves north.

The Mediterranean Sea owes its existence to a narrow strait that links it to the Atlantic Ocean, the Gibraltar Straits. Approximately 5.97 Ma ago (Manzi et al. 2013) one of the most remarkable events of the Earth's history happened, the Gibraltar Straits that give life to the basin were limited in a way that converted the Mediterranean Sea to a semi-closed evaporitic basin; this event was named Messinian Salinity Crisis (MSC) (Hsü et al., 1973, 1977).

After the discovery of the Messinian Evaporite from the Glomar Challenger drilling campaign in 1970 (Hsü et al., 1973, 1977), a debate between researchers about the origin and the timing of the deposition has been shaped. As far as the depositional conditions are concerned, three basic scenarios were shaped: shallow basin-shallow water (Nesteroff 1973), deep basin-deep water (Ryan and Cita 1978), and deep basin-shallow water (Hsü et al., 1973). Concerning the time of deposition two basic scenarios dominate: a synchronous deposition of the Lower Evaporites (LE) at peripheral basins with the massive halite at deep basins (Fig.3) (Krijgsman et al., 1999; Meilijson et al., 2018), and a diachronous deposition (Fig.3) (Clauzon et al., 1996; Manzi et al., 2018). The deposition of evaporites begun 5.97 Ma ago (Manzi et al., 2013) and terminated 5.33 Ma ago with the sudden reopening of Gibraltar's straits (Garcia-Castellanos et al., 2009).

However, the huge volume (10^6 km^3) of evaporites deposited (Meijer and Krijgsman 2005) with an estimated mass of 6.44 to 7.88×10^{18}kg (Rohling et al., 2008) could not result from the amount of the Mediterranean Sea's water. The next goal was the decoding of the Messinian Salinity Crisis through the comprehension of physical processes (i.e. evaporation rates, sources of water influx, sea-level variations). The main way to justify the huge deposits of evaporites is the influx of sea water from the Atlantic Ocean while the water of the Mediterranean could not be ejected back. This has fostered the development of many models aiming to address the evaporitic mass budget under a quantitative assessment (Blanc 2006; Krijgsman and Meijer 2008; Meijer and Krijgsman 2005; Meijer 2006).

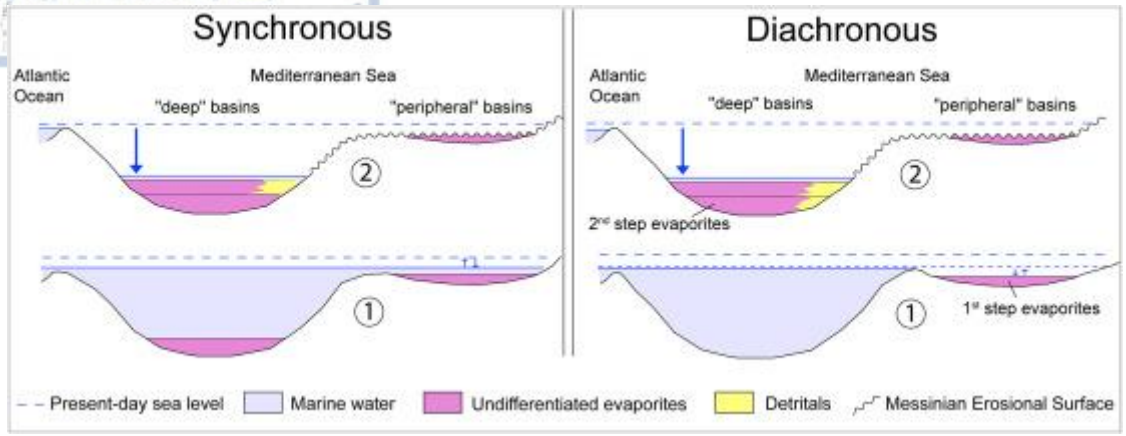

Figure 3: *The synchronous and diachronous scenarios for the deposition of the Messinian evaporites in the Mediterranean Sea (Bache et al., 2015). In the synchronous scenario phase 1 corresponds to a series of limited sea-level fall and rise leading to evaporite deposition in both the central and peripheral basins. Phase 2 is characterized by a large sea-level drop, evaporite deposition in the central basins, and subaerial erosion of the margins. In the diachronous scenarios, evaporites were only deposited in the peripheral basins during phase 1 and in the central basins during phase 2.*

A.2.3 The deposition of the Messinian sequence

A.2.3.1Anhydrites at peripheral basins and anoxia at the deep basins (5.97-5.6 Ma)

Many researchers support that inflow from the Atlantic Ocean to the Mediterranean Sea was limited and lasted only from 5.97 to 5.6-5.59 Ma (Bache et al., 2015; Gargani and Rigollet 2007; Krijgsman and Meijer 2008; Rohling et al., 2008). They link this period to the deposition of the Lower Evaporites (massive selenitic gypsum) (Fig. 4, Step 1). The term Primary Lower Gypsum (PLG) was recently introduced by Manzi et al., (2016) and Roveri et al., (2016) to describe the deposition of anhydrite in the shallower regions of the Mediterranean (peripheral basins). The deposition of anhydrite would not be possible in the deep basins due to the existence of strong anoxic conditions, as the chemical formula of anhydrite ($CaSO_4 2H_2O$) requires oxygen (Krijgsman and Meijer 2008). Therefore, the deposition of anhydrite at the peripheral basins, and deposition of high organic matter

(euxinic shale) (Roveri et al., 2014a) in the deep basins of the Mediterranean, may have occurred simultaneously (Manzi et al., 2018; Roveri et al., 2016).

The evaporitic process in West Mediterranean begins with the deposition of 17 cycles of anhydrite alternating with marls at the peripheral basins (Rohling et al., 2008). By the start of the MSC, the Mediterranean Sea had already begun to stratify because of the different densities (Simon and Meijer 2017). The stratification of the water is not an unusual phenomenon, as it had previously been observed in the Dead Sea until 1980, before an incident of waters overturning (Gertman and Hecht 2002). Stratified waters exist in the Mediterranean Sea even today in well protected from sea currents deep basins (Camerlenghi and Cita 1987; Camerlenghi 1990; De Lange et al 1990a, 1990b). In these basins brine water exists, emerging from Messinian salt dissolution. These brine pools do not have a significant size, but they create strong anoxic conditions that lead to the deposition of rich organic mud (De Lange et al 1990a, 1990b). These conditions can be an analogue to the conditions that were dominant 5.97 Ma ago. Furthermore, the presence of MgCl solution, derived from bischofite ($MgCl_2 \cdot 6H_2O$) deposits, which consists of the end product of the evaporation process, points to a Mediterranean very close to absolute desiccation (Cita 2006; Ryan 2009).

A.2.3.2 Massive halite deposition in deep setting coeval with desiccation and subaerial erosion of the margins (5.6-5.55 Ma)

At 5.6-5.59 Ma the inflow from the Atlantic was reduced, all the known pre-MSC gateways through southern Spain and northern Morocco were closed, leaving the “Gibraltar Corridor” at its Messinian configuration as the sole candidate for seawater in the Mediterranean (Krijgsman et al., 2018), triggering the massive halite precipitation or Resedimented Lower Gypsum (RLG) lasted from 5.6-5.59 to 5.5-5.2 Ma (Krijgsman and Meijer 2008; Manzi et al., 2018) (Fig. 4, Step 2). The massive halite precipitation occurred

quickly in parallel to a moderate drop of the sea level. The first geomorphological systems forced to adjust to this new base level were the rivers. In the geographical locations where river deltas existed, deep canyons were formed (Blanc 2006; Clauzon et al., 1996; Gargani and Rigollet 2007; Krijgsman and Meijer 2008; Loget et al., 2005, 2006; Rohling et al., 2008; Ryan 2008, 2009; Urgeles et al., 2011). All major rivers of the area (the Nile, Rhone, and the Ebro) transported vast amounts of clastic sediments in the deep basins of the Mediterranean, deposited in a hypersaline environment probably coeval with the massive halite precipitation (Gorini et al., 2015; Montadert et al., 2014).

A.2.3.3 Lago Mare deposition (5.55-5.33 Ma)

The transportation of clastic sediments from the drainage systems and the continental margins coeval with the massive halite precipitation filled the deepest part of the basins. This event, in combination with an extreme sea-level drop, created a “shallow basin” system. Inside those “shallow basins”, a very different sequence of sediments was deposited, which is widely known as Lago Mare (Hsü et al., 1973) (Fig. 4, Step 3). This sequence (interchange of dolomite, gypsum, anhydrite, etc.) shows saline and not a hypersaline environment and is easily identifiable in seismic surveys because of its high amplitude reflections. The decreasing salt concentration can be attributed to the fact that most of the NaCl had already been precipitated, while fresh or brackish water entered the system, floating as brackish “pools or plumes” and eventually diluting, decreasing the concentration of the brines. The source of this fresh or brackish water was either the North African river network or the Sea of Paratethys (Hsü et al., 1973; Rouchy and Caruso 2006; Ryan2009). These evaporites were named Upper Evaporites (*Lago Mare*) and their composition is well known from ODP borehole data.

A.2.3.4 End of the MSC (5.33 Ma)

The end of the MSC meets the "opening" of Gibraltar straits at 5.33 Ma that caused the Zanclean reflooding(Fig. 4, Step 4). Normal marine conditions were restored by the deposition of marine sediments above the evaporitic deposits (Blanc 2006; Ryan 2008). The Messinian reflooding filled the deep marine and continental canyons with early Pliocene sediments (Loget et al., 2005). The primary causes of this reopening have concerned the scientific community. For instance, Blanc (2006) and Loget et al. (2005) claim that a drainage system flowing to the east eroded the straits and lead to the straits' collapse. Other studies claim that a tectonic reason or the erosion of a porous formation may be the cause of the straits' reopening (Ryan 2008).

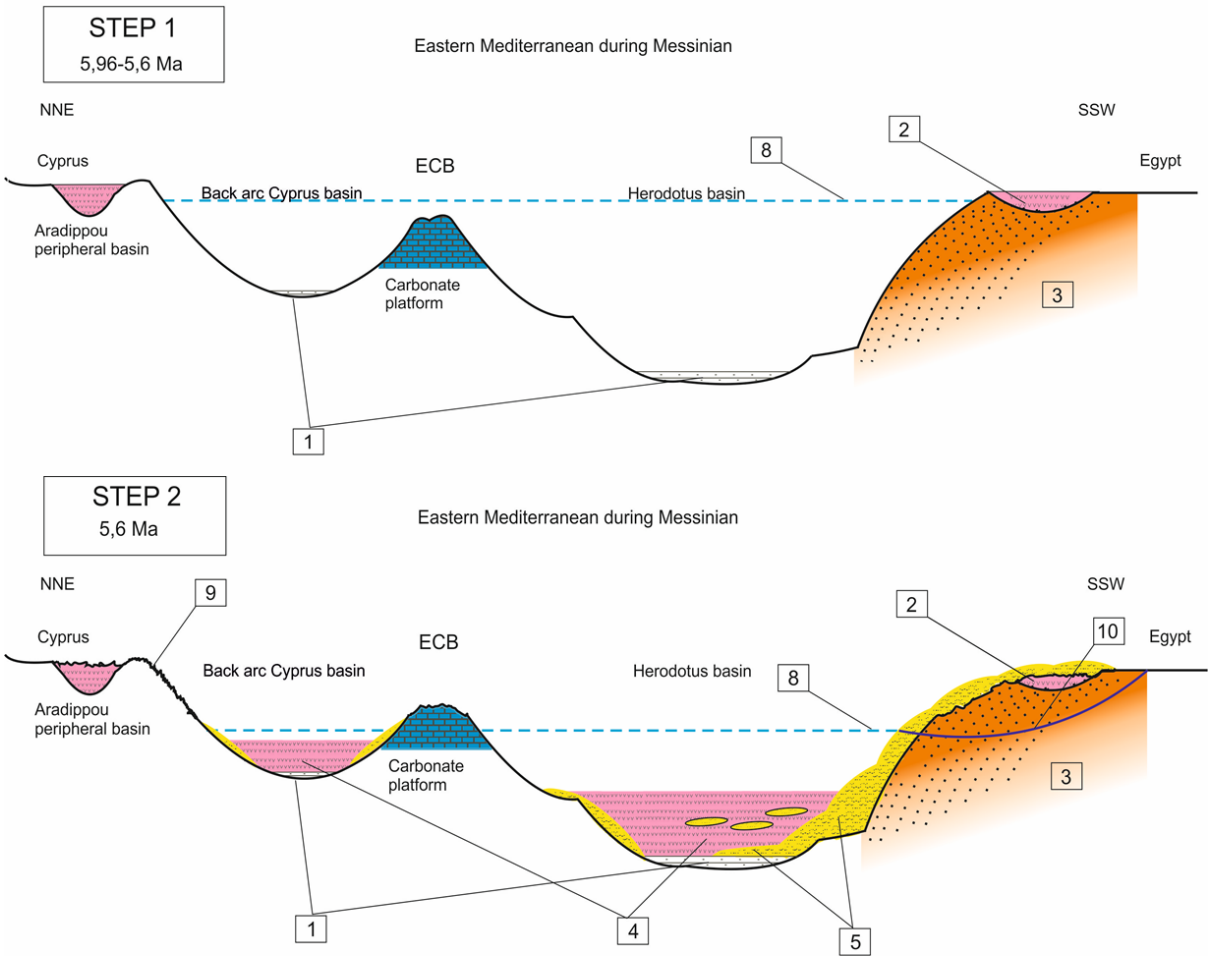

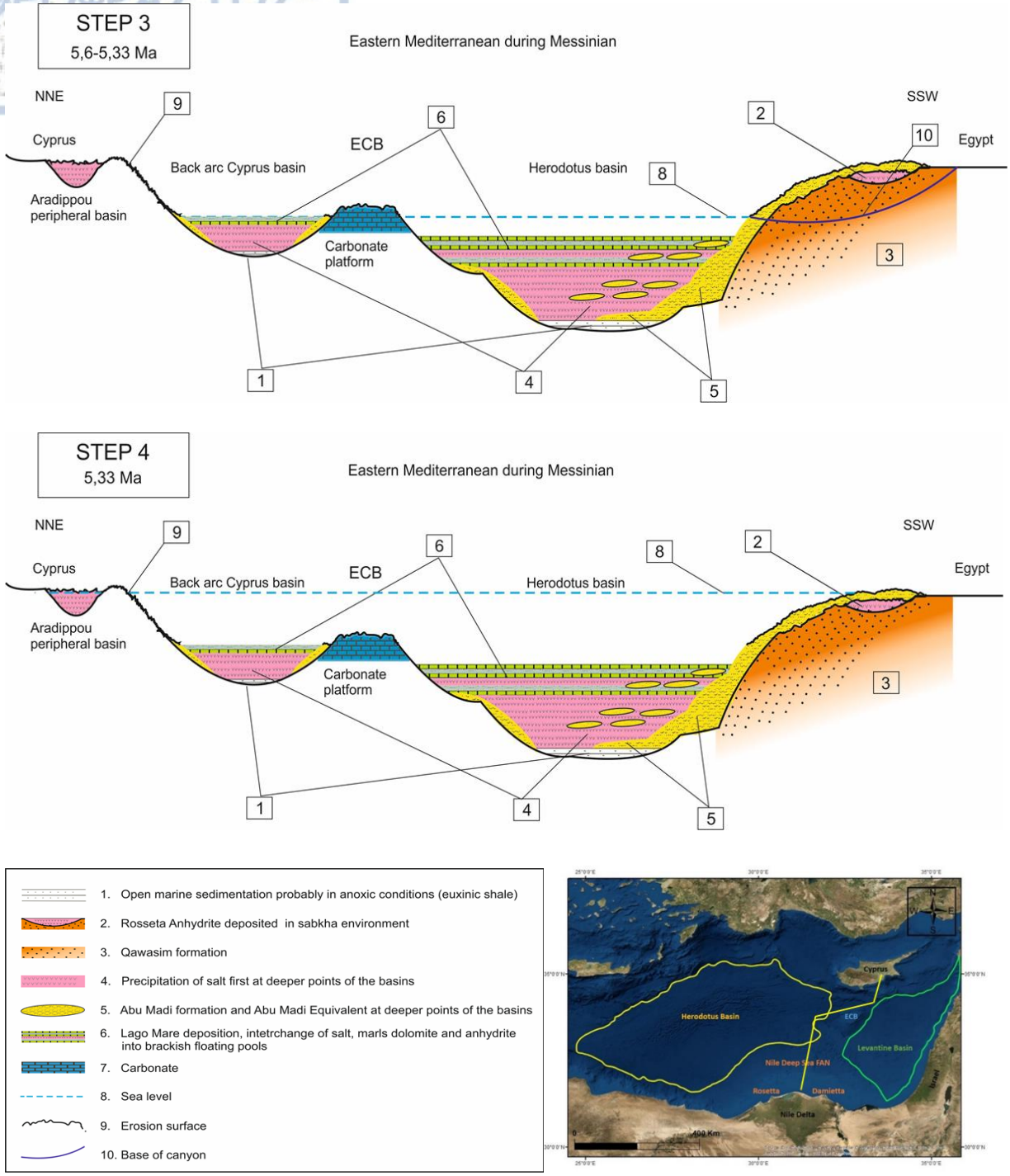

Figure 4: *Conceptual Model of salt deposition during MSC in the cross-section A-A΄ (Eastern Mediterranean Sea). Step 1, deposition of anhydrite in peripheral basins. Step 2, deposition of Messinian clastic accumulations and precipitation of massive halite. Step 3, Lago Mare in brackish floating pools. Step 4, Zanclean reflooding which led to the restoration of normal marine conditions.*

A.2.4 Climate in North-West Africa during Messinian

The climate of the Mediterranean during the Messinian was not very different from today (Fig 5). All geological evidence shows a subarid climate (Gladstone et al., 2007). On the contrary, the climate of North Africa did not resemble at all the modern superarid climate. The factors that played a pivotal role in the shaping of the climate during the Messinian were: the northward shift of the jet stream along with the Intertropical Convergence Zone (Gladstone et al., 2007), the uplift of the Himalayans, which also played a decisive role in the creation and function of the Monsoonal system (Colin et al.,2014; Griffin 2002), the geographical position of North Africa closer to the Equator (Abdelkarrem et al., 2012) and the moisture from the desiccated Mediterranean (Said 1993). During that period, enormous amounts of moisture were transferred in North Africa from the desiccated Mediterranean resulting in the creation of a very well-organized drainage system which today lies buried under the dunes of the Sahara Desert. Climate models (Gladstone et al., 2007) suggest a subtropical climate and support the estimates derived from geological data indicating significant precipitations (1200-1500 mm/year according to Issawi and Osman 2008) above the regions of North Africa (Fig 5). This humid period was called Zeit WetFace and seems to have ended with the restoration of normal marine conditions in the Mediterranean with rainy seasons becoming more periodic.

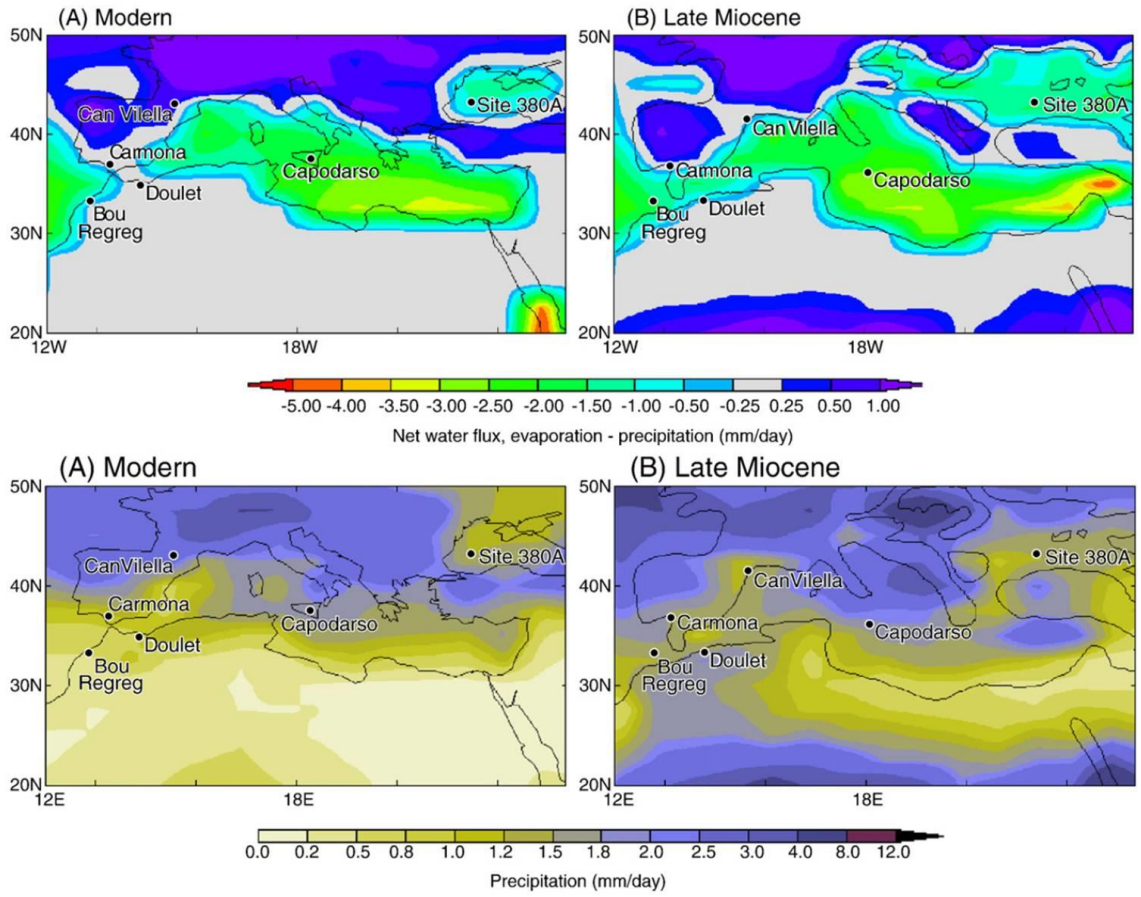

Figure 5: *Modern evaporation and precipitation and Messinian evaporation and precipitation. A basic observation is that climatic conditions above the Mediterranean during the Messinian did not differ from today, but the distribution of rainfall in North Africa was different (Gladstone et al., 2007).*

A.2.5 Evolution of drainage systems in North Africa

The Nile had already formed in the Upper Eocene-Early Oligocene when the rifting face of Suez started. Northern Egypt tilted northward and an influx of great clastic quantities began in the Herodotus and Levantine basins (Montadert et al., 2014). Some researchers claim that the MSC is the cause of the formation of the Nile (R.Said, 1981, 1993). Issawi and McCauley (1992) indicated that during the Cenozoic, Egypt was drained from three different drainage systems which competed for dominance over the region (Fig.6). This antagonism took place in the Upper Eocene parallel to the regression of the Tethys Ocean and the various tectonic movements. Eocene Nile, due to its advantageous gradient, captured the south-flowing Qena system and created the first river system that flowed to the north (Goudie

2005). One other opinion from Italian researchers with the use of RADAR images suggests that it is possible that the Nile flowed in the Gulf of PaleoSirt (Carmignani et al., 2009). A different hypothesis supports the existence of another drainage system that was created in the Late Eocene. This system originated from the Red Sea Hills and followed a westward course in the mouth of the modern Niger River (Burke and Wells 1989). It was named trans-Africans drainage system (TADS) and reached its highest point, in the Early Miocene. However, it was destroyed by the Late Miocene volcanic activity and the MSC (Burke and Wells 1989) and led to the creation of the "Eonile" as described by Said (1981).

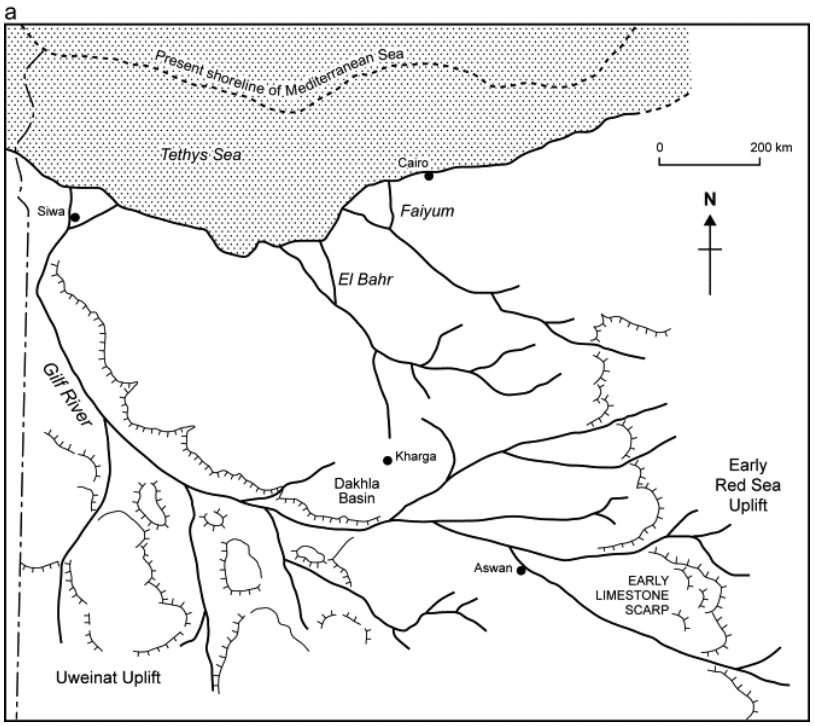

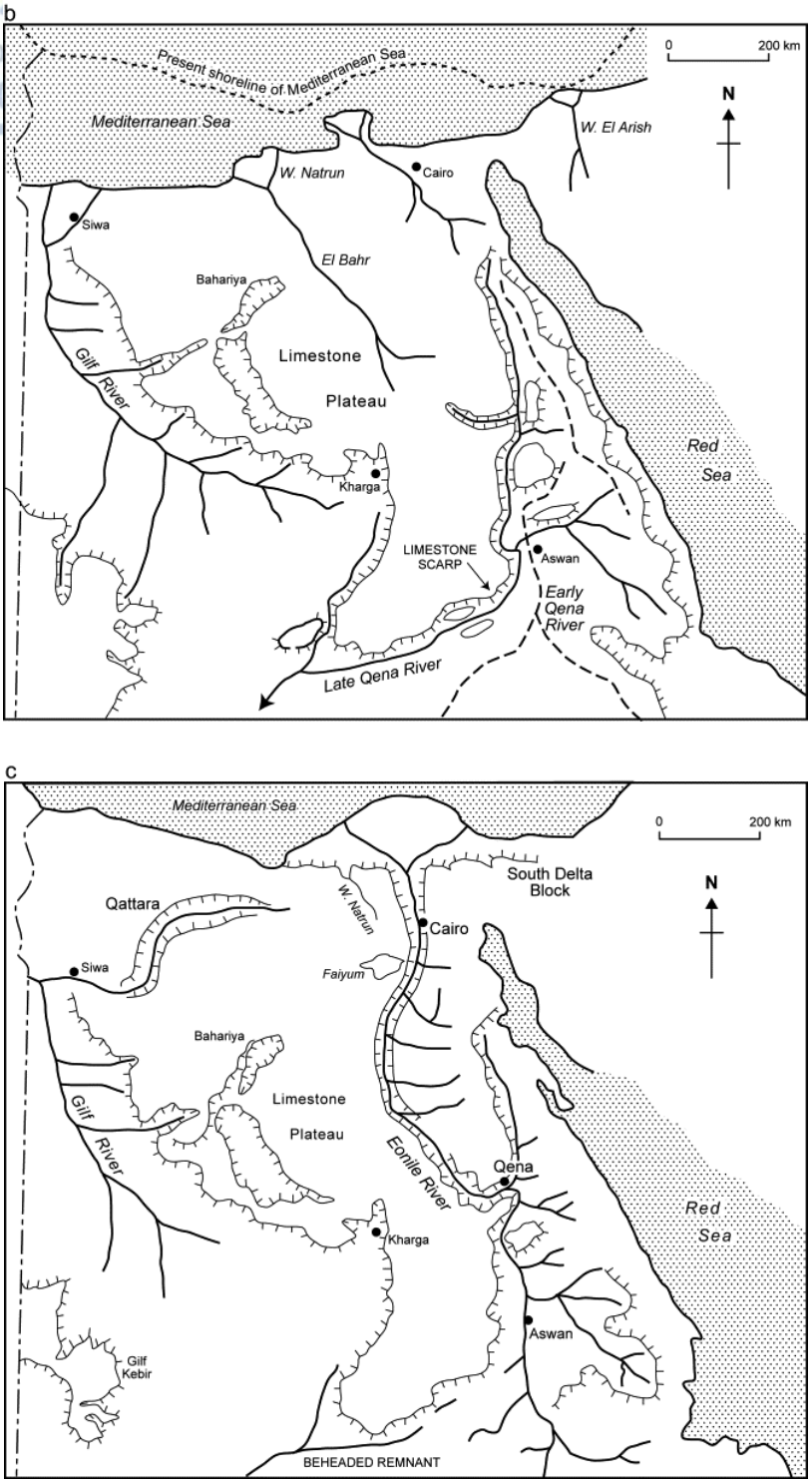

Figure 6: *(a) Sketch showing Gilf system (System I) at approximate end of Oligocene Epoch (Chattian Age, =24 Ma) (Goudie 2005). (b) Sketch showing Qena system (System II) in approximately middle Miocene time (Langian Age, about 16 Ma) (Goudie 2005). (c) Sketch showing Nile system (System III), which resulted from a major drop in sea-level of Mediterranean in Messinian time (about 6 Ma) (Goudie 2005).*

A.2.5.1 Evolution of River Nile during Messinian

As mentioned in paragraph 2.3.2, the first geomorphological systems forced to adjust to the new basic level were the rivers. The Nile formed in the Upper Eocene-Early Oligocene in parallel with the rifting of Suez. Northern Egypt tilted northward and a great influx of clastic quantities began in the Herodotus and Levantine basins (Montadert et al., 2014). Until the Tortonian, a substantial delta complex had already been formed as described by R. Said (1981, 1993), which suffered great erosion from the Messinian moderate change of the base level (Barber, 1981). The Messinian Erosion Surfaces (MES) are apparent from seismic data in a depth of 2-3km (Loncke et al., 2006) (Fig. 7).

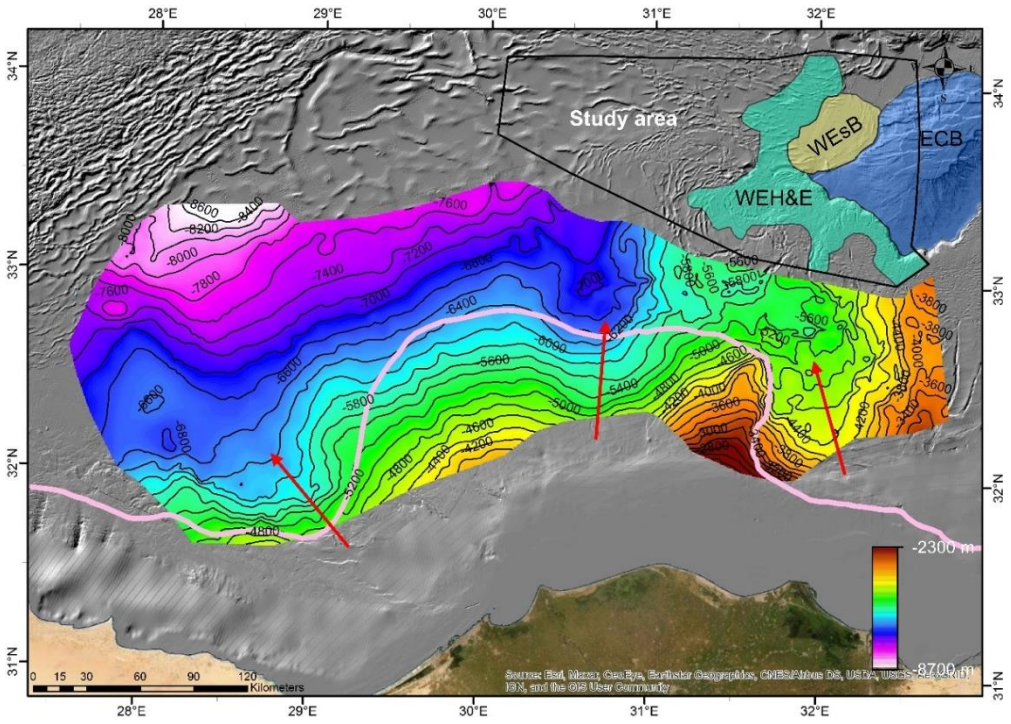

Figure 7: *The map illustrates the Base of the MSC sequence surface in meters (datum plane sea level, modified after Loncke et al., 2006) offshore Egypt. Red arrows indicate the possible pathways of turbidity flows during the MSC. The Margin erosion surfaces (MES) are delineated by the pink continuous line. The black continuous line represents the outline of the data used in the present study shown in figures10 and 11. Eratosthenes Continental Block, West Eratosthenes sub-Basin, and West Eratosthenes High & Extension are also presented. (Contour interval 200m).*

Based on borehole, seismic, and gravity data, Said (1981, 1993) and Embabi (2017) suggest that during the MSC the Nile created an enormous canyon. This canyon today is located at a

depth of 170 m at Aswan, 800 m at Assiut, 2500 m north of Cairo, and more than 4000 m below sea level in the northern reaches of the delta. This drainage system transferred enormous quantities of sand-prone sediments, mainly from the red sea rift shoulders and the outcropping Nubia sandstone (Macgrecor 2011, 2012) from Southern Egypt and Sudan, chiefly during the wetter periods (Macgrecor 2011, 2012). The largest contributor of sediments was the Red Sea Hills, where the average erosion was of the order of 1200-1500 m (total denudation) (Macgregor 2012). The Oligocene-Miocene isopach map shows two distinct lobes extending out into the Herodotus and Levantine basins, separated by thin deposits of sediments corresponding to the Rosetta-Eratosthenes High (Fig. 8).

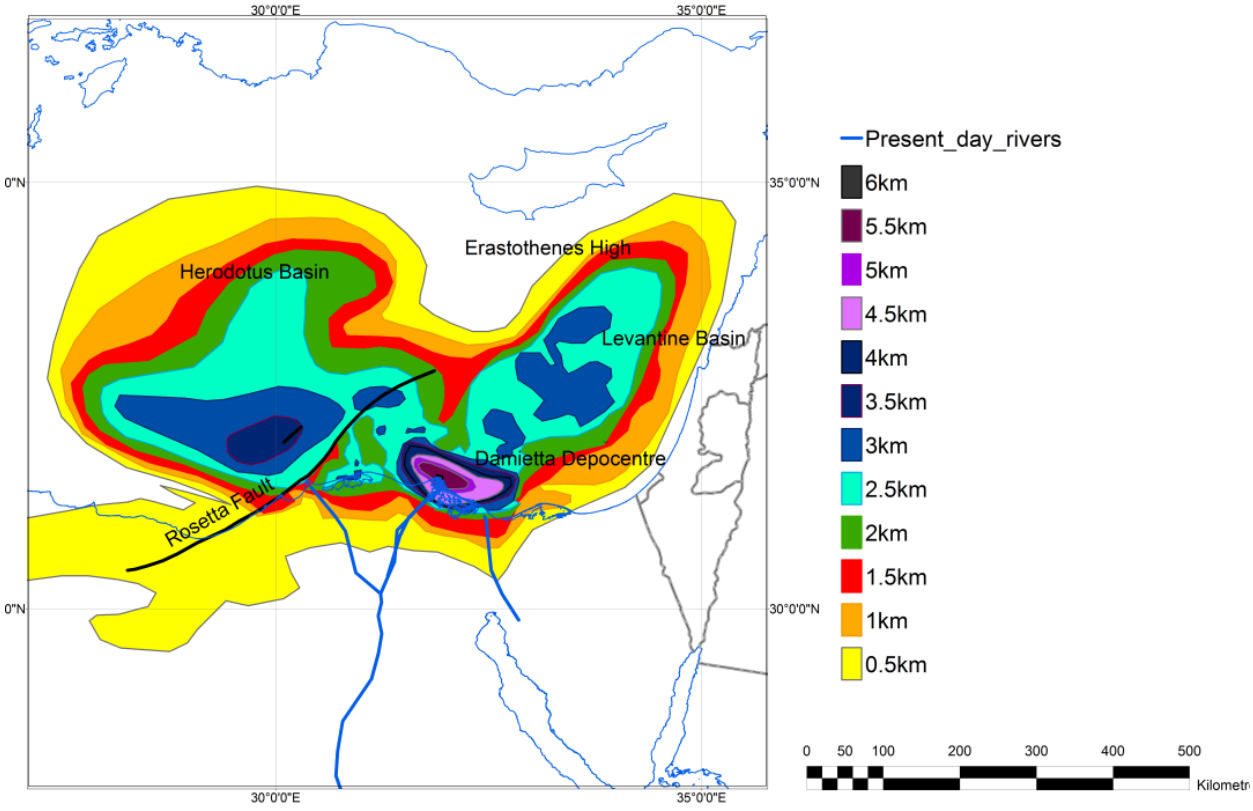

Figure 8: *Isopach map of Oligocene-Miocene sediments of the Nile cone (Macgrecor 2011) in Levantine and Herodotus basins. It is easy to recognize the two lobes that represent the distant sand sheets of the Nile.*

These two lobes show the probable areas where the sand was deposited, similar to those reported in the discoveries of Tamar, Leviathan, and Aphrodite in the Levantine basin

(Macgrecor 2011, 2012). Sedimentation rate changes and seismic phase indicators also suggest thick prodelta sediments over the Oligocene-Miocene section. In this section, the deposition of clastic material may have periodically switched between the Herodotus and Levantine basins during the Oligocene-Miocene but the Late Messinian deposits that represent the lowstand delta lie west of the Eratosthenes Continental Block (Fig. 9). Distal turbidite reservoirs can extend several kilometers beyond the Egyptian waters, correspondingly to the Niger sediment system, where turbidite sands extend hundreds of kilometers from the shelf edge and appear to have a very similar sediment supply pattern to the Nile. This is a good analogue for predicting deep-sea reservoirs (Macgregor 2011, 2012).

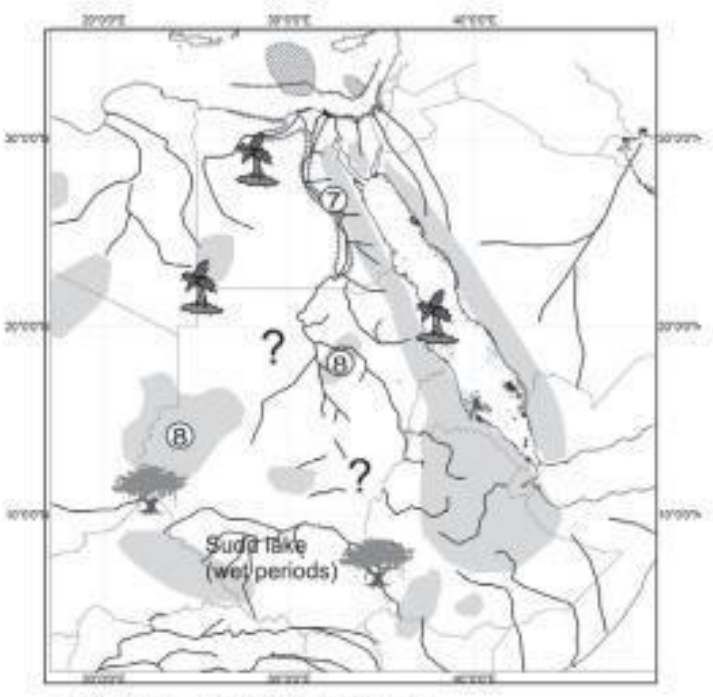

Figure 9: *Map of the Messinian clastic deposits (Macgrecor 2012) that were deposited West of the Eratosthenes Continental Block during the Late Messinian era.*

A.2.5.2 Messinian deposits in Nile Delta

The deposits of the canyon at the North Delta and offshore of the North Delta constitute the Qawasim and Abu Mandi formations (Farouk et al., 2014). The Rosetta Anhydrite

formation shows an intermitted appearance between them (Abd-Allah et al., 2012; Farouk et al., 2014). Within these formations, proven hydrocarbon reserves are found (Ottes et al., 2008), mainly gas of thermogenic and microbial origin (Vandre et al., 2007). Gas producing wells prove that the Abu Madi fluvial channels are good sand reservoirs with important charging potential (Mahmoud et al., 2017; Piggot and Abdel-Fattah 2014). The thickness of those reservoir targets seems to increase to the North and extends offshore in the Egyptian NEMED block (Abd-Allah et al., 2012; Ottes et al., 2008; Sarhan 2015). Piggot and Abdel (2014) mention that while the Qawasim formation responds to the global sea-level changes, the Abu Madi formation does not. They also claim that Abu Madi is the one that erodes the deposits of the Qawasim formation and represents the Messinian deposition in incised valley fluvial channels (Teama et al., 2017). Besides, sediments from the Abu Madi formation is considered to fill the topographic relief of the Messinian unconformity (Sarhan 2015).

A.2.6 Natural seepage of hydrocarbons and the main reservoir plays in the area

Numerous different instances of fluid migration inside the sedimentary accumulations also exist, stemming from the pre-Messinian section (Bertoni et al., 2017). Characteristic formations such as gas chimneys, that represent hydrocarbon pathways, often occur in the seismic data. This natural process of seepage usually ends with the creation of mud volcanoes and pockmarks at the seabed, these geomorphs are found with great frequency in the Nile deep-sea fan area (Bayon et al., 2009; Dapre et al., 2007, 2008, 2010; Gontharef et al 2007; Loncke et al 2004; Moss et al., 2012).

The main reservoir plays in the area, according to several studies (Dolson et al., 2005; Montadert et al., 2010, 2014; Peck 2008; Peck and Horscroft 2005), are:

- The pre-Messinian clastics, where a horst-graben scheme exists and stops at the base of the Messinian.

- The Messinian low-stand delta, comprised from Messinian sands of equivalent age to the Abu Madi formation deposited as a complex deltaic in shallow hypersaline setting, or as turbiditic currents in front of major fluviatile canyons.
- Upper Cretaceous marine carbonates developed in fringing reef formations around the ECB high are also expected, especially after Zohr, Calypso, and Glaucus discoveries that confirm the carbonate play hypothesis.

This study is trying to contribute to the discussion on the development of the source to sink system of the Late Messinian River Nile and on the evolution of the evaporitic sequence based on new results derived by 2D seismic data.

B.3 Methodology

B.3.1 Data and methods

The seismic data were provided by PGS, with the agreement of the Ministry of Energy of the Republic of Cyprus. The data covers the western part of the Eratosthenes Continental Block to the Herodotus Basin, offshore Cyprus (Fig. 3). About 18000 km of regional 2D (two-way-time and depth) seismic reflection profiles, shot with the dual sensor GeoStreamer® technology, were gathered from the MC2D-CYP2006 and MC2D-CYP2008 surveys (acquired in 2006 and 2008). The dataset has European polarity (a downward increase in acoustic impedance corresponds to a negative amplitude and blue color) and vertical-horizontal resolution 4 ms and 12.5 m respectively. Both surveys used one streamer 8100 m long and with a 9.216 seconds recording length. High-quality 2D two-way travel time (TWTT) and depth seismic reflection profiles were used in the present study. The TWTT-depth conversion was performed by PGS and PETREL 2019 software was used for the seismic interpretation that was based on the seismic stratigraphy concepts proposed in recent studies (Gorini et al., 2015; Güneş et al., 2018; Gvirtzman et al., 2017; Feng et al., 2016). The seismic stratigraphy concepts separate the MSC sequence into several distinct stratigraphic units based on amplitude and frequency alternations.

Changes of the MSC sequence thickness and salt-deformation styles allow the subdivision of the study area into five salt-tectonic structural provinces (Fig.10): P1, which occurs in the WEsB and is characterized by moderate deformed salt with ~1500m average thickness; P2, which occurs northwest of the ECB and is distinguished by intermediate size segments of highly deformed salt; P3, which occurs south-southwest of the ECB and is characterized by thick, severely deformed salt; P4, which occurs west of the WEH and the ECB westward extension and is discriminated by thick salt diapirs flanked by sediment

wedges; and P5, which occurs in the HB and is characterized by thick, highly folded salt. High-quality 2D industrial seismic data are used to describe and interpret the five salt-tectonic structural provinces.

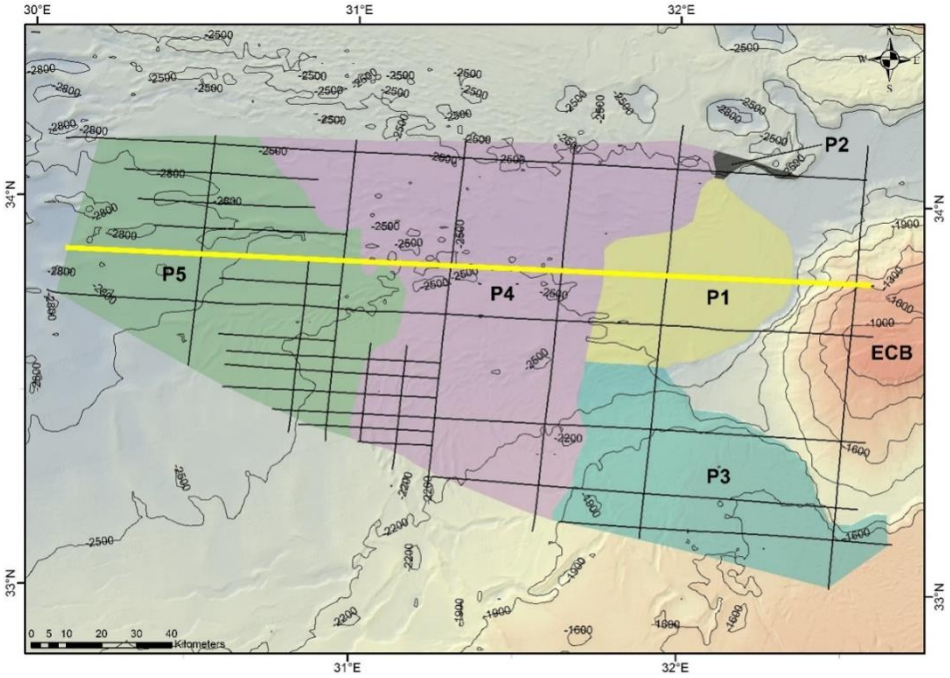

Figure 10: *Present-day bathymetry map of Eastern Mediterranean showing the seismic lines used in this study (ownership of PGS). The map illustrates the five salt-tectonic structural provinces (P1, P2, P3, P4, P5) presented in this study. The yellow section is shown in figure 12. Contour interval 300 m.*

The interpretation of MSC clastic accumulations was based on the division of Di Celma et al. (2011), where a Channel Complex Set (abbreviated to CCS) is defined as a series of stacked channel complexes fed by the same canyon, while a channel complex is defined as a series of stacked elementary channels that are traced in the seismic dataset as channel-forms. Subsequent incisions of elementary channels result in the deposition of a new channel complex, which is a first-order control on fan architecture.

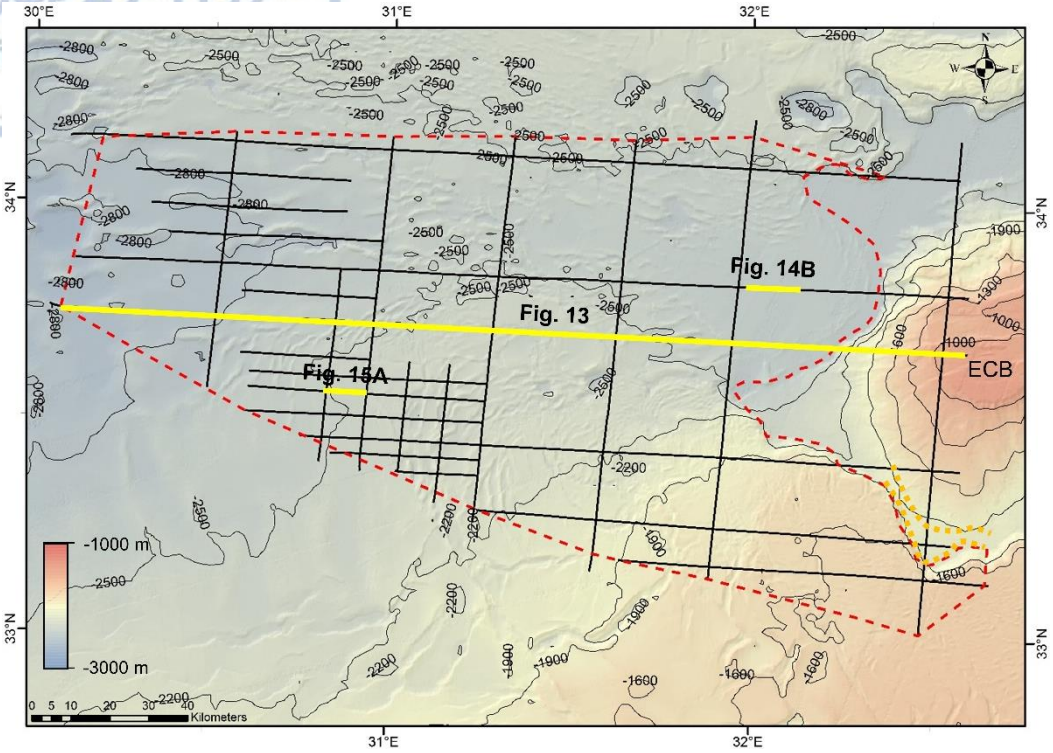

Figure 11: *Present-day bathymetry map of Eastern Mediterranean showing the seismic lines used in this study (ownership of PGS). Yellow sections are presented in chapters 3.3.2,3.3.3, Red dashed line represents the outlines of figures17, 18, and 31. Orange dotted lines represent the bathymetric scar located southwest of ECB. Contour interval 300 m.*

B.3.2 Seismic stratigraphy

Two main surfaces define the top (TS/TES Top Surface and Top Erosion Surface) and bottom (BS/BES Bottom Surface and Bottom Erosion Surface) of the MSC sequence (Lofi et al., 2018). At the continental margins, these surfaces merge to form the Margin Erosion Surface (MES). Where no erosion is observed at the top of the MSC sequence in the study area, its top is labeled as TS. The seismic reflector at the base of the MSC sequence can be traced and correlated across the Herodotus basin. This thesis mainly focuses on the salt deformation patterns observed in the study area and on the internal seismic stratigraphy of the clastic accumulations located at the BS/BES of the MSC sequence (Fig. 12, 13).

Seismic stratigraphic Units: Based on the acoustic character, stratigraphic position, and location of the TS and BS/BES, four distinct seismic units are identified in the study area

(Figs. 12, 13): Unit 1: Messinian–Plio Quaternary clastic sequence, Unit 2: MSC sequence, Unit 3: The Pre-MSC clastic accumulations of West Eratosthenes sub-Basin (WEsB) and Herodotus Basin, and Unit 4: the carbonate accumulations of ECB.

- Unit 1 is characterized by a clastic sediment package that consists of high amplitude, high-frequency reflections with relatively good lateral continuity, and it is topped by the seabed reflector (Figs. 12, 13). The base of Unit 1 is marked by a strong and distinctive reflector, identified in the Herodotus Basin as TS.

- Unit 2 is characterized by strong and continuous reflections at the top and base and a transparent section in the middle (Figs. 12, 13). Based on their stratigraphic position, the upper and lower bounding surfaces of Unit 2 are correlated with TS and BS/BES. In the seismic reflection profiles, TS corresponds to the top of the MSC sequence and is imaged as a bright, laterally continuous, acoustically strong marker with a negative (hard) amplitude. The BS/BES delineates the base of Unit 2 and separates the MSC sequence from the Tortonian and older accumulations. In seismic reflection profiles, BS/BES is imaged as a variably strong, moderately continuous marker with positive (soft) amplitude.

- Unit 3 is represented by a package of parallel, sub-parallel, continuous low amplitude reflections. Unit 3 is bounded at the top by the BS/BES reflector and represents the pre-MSC and older accumulations in the WEsB and Herodotus Basin (Figs. 12, 13).

- Unit 4 is characterized by the low to high amplitude reflectors of the ECB carbonate accumulations (Figs. 12, 13).

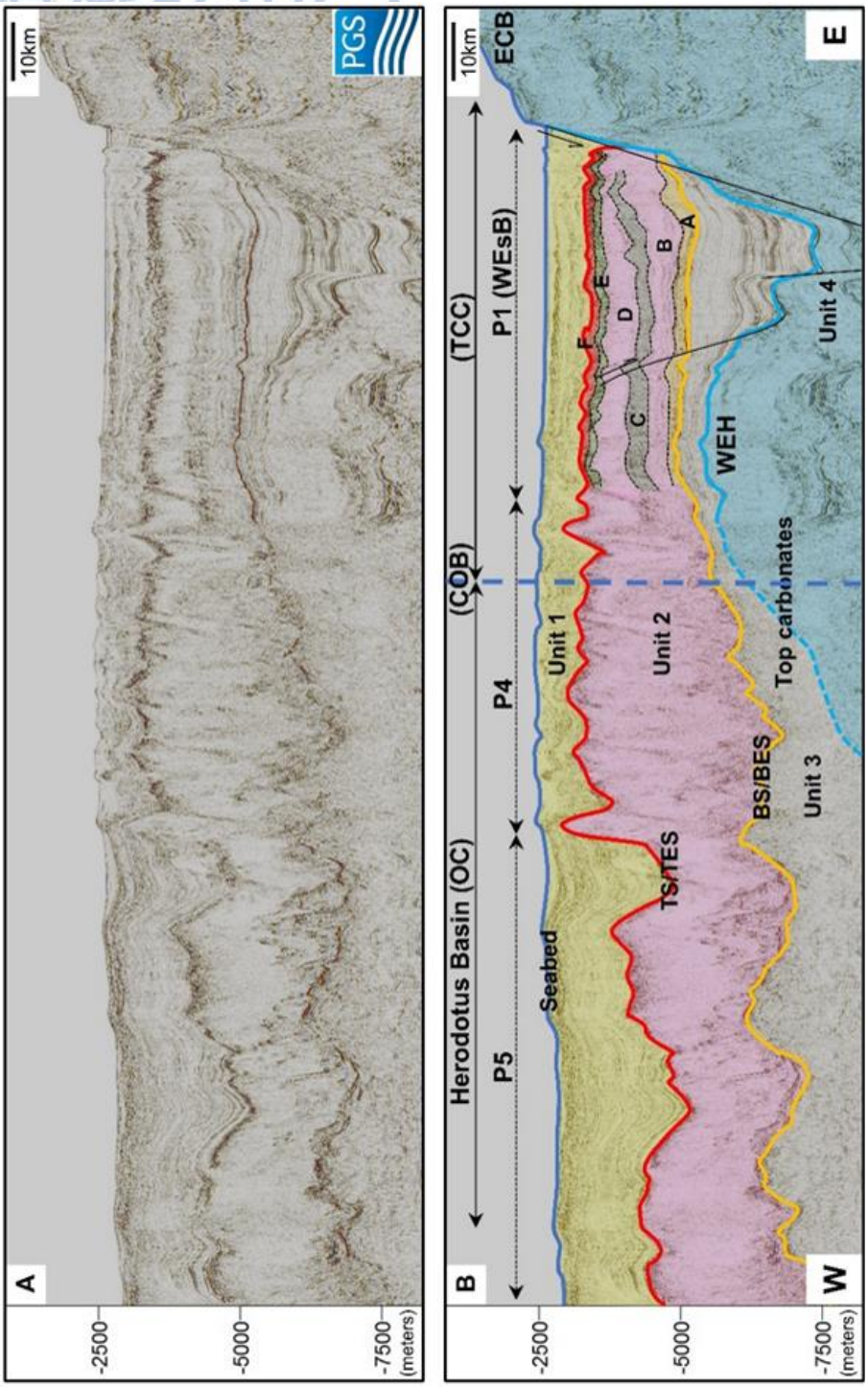

Figure 12: *West-East uninterpreted (A) and interpreted (B) depth seismic cross-section across the Eratosthenes Continental Block (ECB), West Eratosthenes sub-Basin (WEsB, P1), the West Eratosthenes High (WEH), and the Herodotus Basin (P4 & P5), depicting four main seismic stratigraphic units (Units 1-4) and their bounding surfaces i.e., Seabed, Top Surface/Top Erosional Surface (TS/TES), Bottom Surface/Bottom Erosional Surface (BS/BES), and Top carbonates (for location see Fig. 10). The six seismic stratigraphic subdivisions (A, B, C, D, E, F) of the MSC sequence in WEsB are also shown. Note the elevation difference between the West Eratosthenes High and the deep Herodotus Basin across the TS/TES and BS/BES reflectors and the significant thickness increase of the Plio-Quaternary clastic sediments (Unit 1) towards the Herodotus Basin. The basement of Herodotus Basin consists of Oceanic Crust (OC) and the basements of ECB, WEsB, and WEH consist of Thinned Continental Crust (TCC). Blue dashed line illustrates the Continental Oceanic Boundary (COB) (Granot, 2016). Vertical exaggeration of the cross-section is 10:1.*

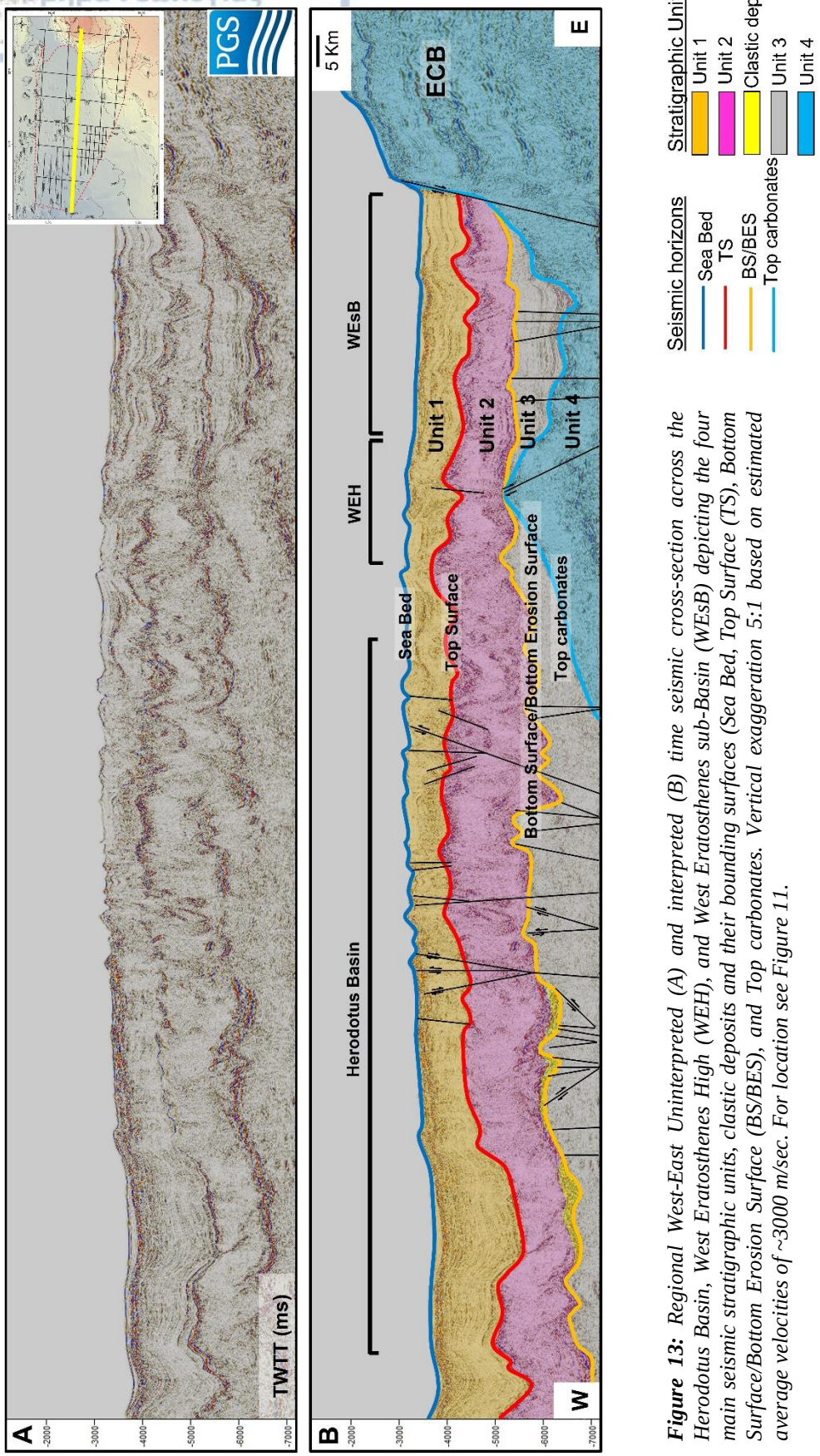

Figure 13: *Regional West-East Uninterpreted (A) and interpreted (B) time seismic cross-section across the Herodotus Basin, West Eratosthenes High (WEH), and West Eratosthenes sub-Basin (WEsB) depicting the four main seismic stratigraphic units, clastic deposits and their bounding surfaces (Sea Bed, Top Surface (TS), Bottom Surface/Bottom Erosion Surface (BS/BES), and Top carbonates. Vertical exaggeration 5:1 based on estimated average velocities of ~3000 m/sec. For location see Figure 11.*

Unit 2 corresponds to the MSC sequence, consisting of six distinct seismic stratigraphic subdivisions termed A, B, C, D, E, and Lago Mare (Fig. 14C). Based on the seismic reflections, two areas of different stratigraphic structures and salt tectonics of the MSC sequence are distinguished. In the first area, situated at the WEsB (Fig. 12), the structure of the MSC sequence indicates an environment of deposition comparable to the Levantine basin with a similar stratigraphic structure as described in detail by Gorini et al. (2015) (Fig. 14A).

- Layer (A), is located at the base of the MSC sequence and consists of parallel high amplitude, low-frequency reflections, probably because of high clastic content.
- Layer (B), is characterized by transparent, limited, and weak reflections, probably because of high salt content and the presence of clastic material.
- Above the weak reflections, layer C is characterized by high amplitude high-frequency reflections, possibly due to the presence of continuous sequences of alternating thin layers of halite with thin layers of silt and clay (Feng et al., 2016). The conditions that prevailed during the deposition of layer C allowed small-size particles (silt and clay) to settle in the center of the MSC sequence as interfingering layers.
- Layer D is similar to layer B, primarily composed of transparent seismic facies. It most likely consists entirely of halite.
- Layer E is comprised of high-frequency chaotic reflections. High-frequency reflections probably represent a change in the depositional environment (possibly hydrological changes, a gradual change from hypersaline to brackish conditions). The changes in the depositional environment of this sequence could be attributed to a decreasing salt concentration in the Messinian brines once most of the NaCl had already been precipitated, while fresh or brackish water entered the depositional environment. The

source of this fresh or brackish water was either the North African river network or the Sea of Paratethys (Hsü et al., 1973).

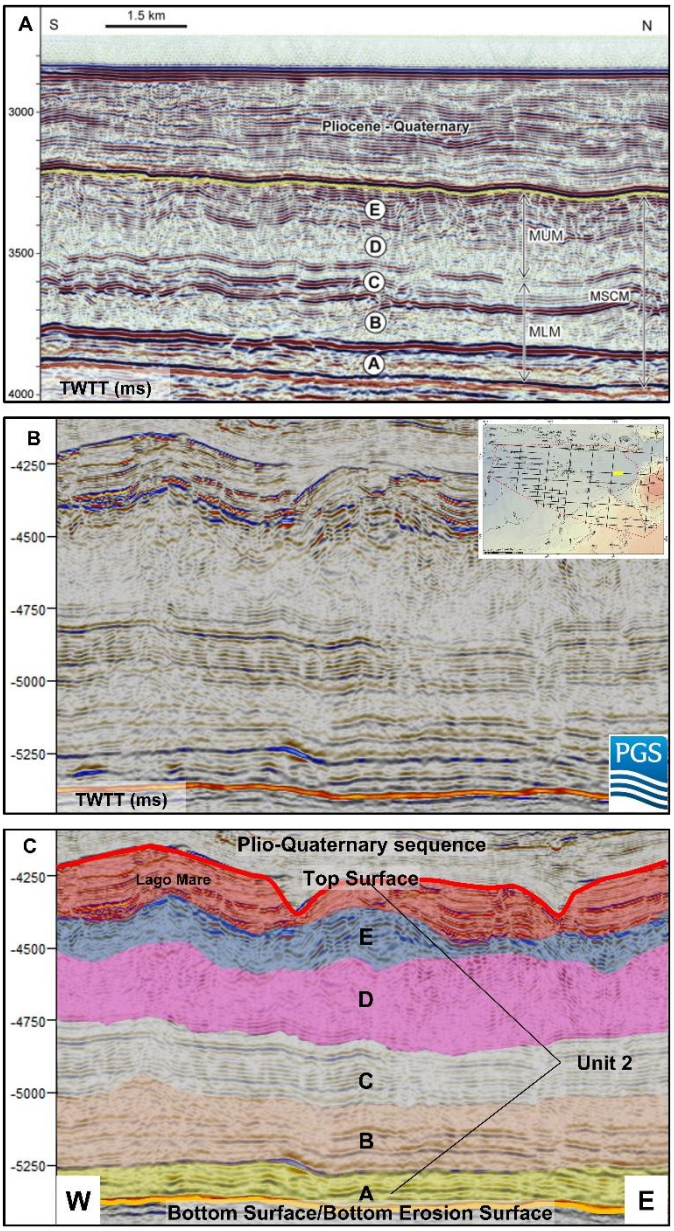

Figure 14: *Architectural style of the MSC sequence. A) Time seismic section depicting the five stratigraphic subdivisions (A, B, C, D, E) introduced by Gorini et al., (2015) located at the NW Levantine basin. Uninterpreted (B) and interpreted (C) time seismic cross-section across the WEsB depicting the five stratigraphic subdivisions and Lago Mare. A similar stratigraphic structure with the NW Levantine basin is distinguished, in the West Eratosthenes sub-Basin. This seismic image suggests that the area does not suffer any deformation due to salt tectonics. Vertical exaggeration 3.5:1 based on estimated average velocities of ~2800 m/sec. For location see Figure 11.*

- A characteristic section of parallel to sub-parallel high-amplitude high-frequency reflections occur above layer E. These reflections represent abrupt lithological changes (bedding/layering of dolomite, gypsum, anhydrite, etc.) of the Lago Mare deposits (Hsü et al., 1973; Popescu et al., 2015; Marzocchi et al., 2016) (Fig. 14C); the lithologic changes indicate inception of a brackish environment of deposition. This sequence is limited only to the WEsB and is absent in the deep Herodotus basin.

Based on the seismic dataset, a limited clastic input occurred in the area of WEsB (average time thickness of layer A 125 ms ~350 m). The discrimination of the MSC stratigraphic subdivisions in this area is only possible because intense salt tectonics are not observed.

The seismic character of the MSC sequence in the Herodotus basin (Fig. 15B) is usually chaotic with internal shear surfaces that terminate on a gliding surface, stringer zones discernible in areas with high clastic content, and internal imbrications. The MSC sequence in Herodotus Basin is comprised of three stratigraphic sections (Fig. 15B):

- The first is a section with medium to high amplitude, high-frequency reflections located at the base of the MSC sequence.
- The second is a section with chaotic medium to high amplitude, low to high-frequency reflections that probably relate to subdivisions A, B, and C of the WEsB region.
- The third section is transparent and equivalent to the mobile salt layer (subdivision D of the WEsB).

This chaotic seismic image of the MSC sequence (Fig. 15B) in the Herodotus Basin is interpreted to be partially caused by the northward salt gliding.

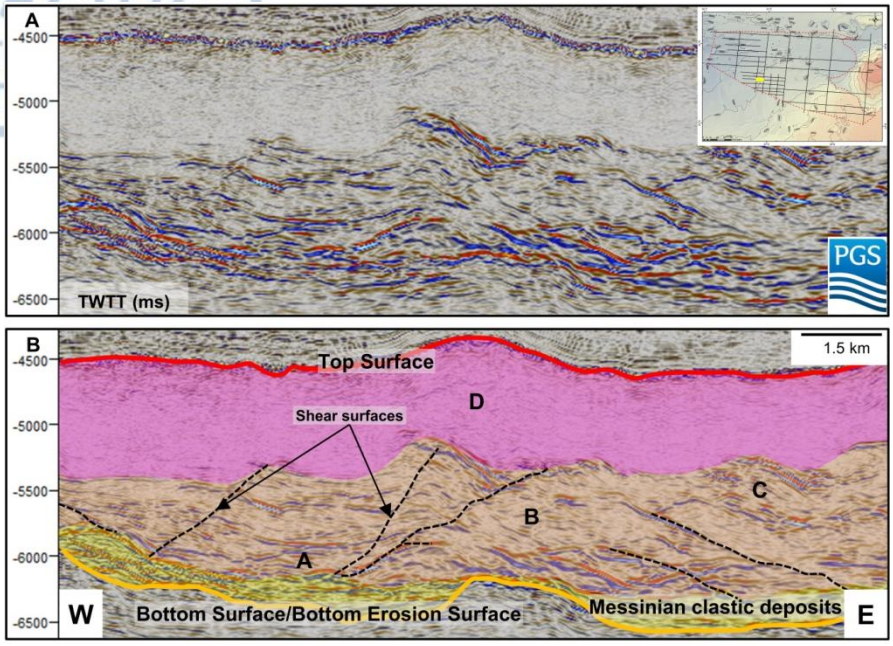

Figure 15: *Architectural style of the MSC sequence in the Herodotus Basin. Uninterpreted (A) and interpreted (B) time seismic cross-section from the Herodotus basin indicating the differences in the stratigraphic structure of the MSC sequence. The discrimination of the five stratigraphic sections observed in West Eratosthenes sub-basin is not possible in the Herodotus basin where three stratigraphic subdivisions were observed. Vertical exaggeration 2:1 based on estimated average velocities of ~2800 m/sec. For location see Figure 11.*

B.3.3 Geomorphology of the main seismic surfaces

B.3.3.1 Seabed seismic surface

Seabed surface: The interpretation of seismic data shows a bathymetric scar on the seafloor at the southwest side of the ECB and an elevated seafloor between Herodotus and West Eratosthenes sub-Basin. Based on the seismic interpretation, the bathymetric step represents the pinch out of the Messinian sequence (Fig. 16). On the west side of the ECB, a flat topography is observed, which represents a small basin referred to as the West Eratosthenes sub-Basin (WEsB).

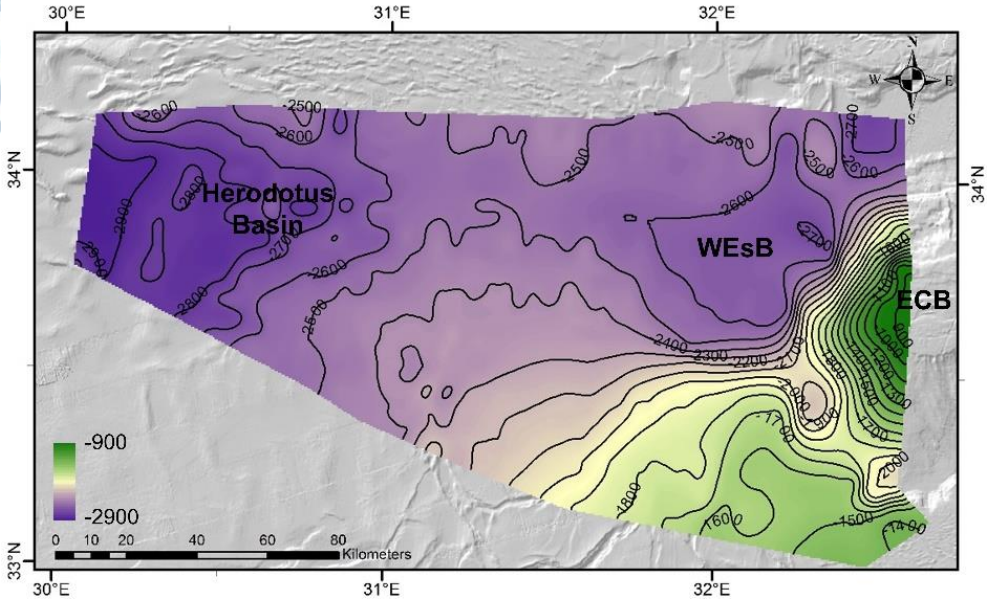

Figure 16: *Map depicting the seabed seismic surface. The seafloor of the study area in meters (m), ECB, WEsB, and Herodotus basin are distinguished (contour interval 100 m). Data used to produce this map are shown in figure 10.*

B.3.3.2 Top Messinian sequence seismic surface (TS/TES)

Top Messinian sequence surface (TS/TES): The high amplitude, high-frequency reflections of Unit 1 are based on a bright, laterally continuous, acoustically strong marker with a negative (hard) amplitude interpreted as the (TS/TES). The TS/TES is located at a depth of -2000 m south-west of the ECB deepening towards the Herodotus Basin where intense alternations of the surface elevation are observed with a maximum depth of -5200 m. In the WEsB, the TS/TES is generally flat with some tiny fluctuations of the surface morphology detected only at the south and east margins of the mini basin (Fig.17).

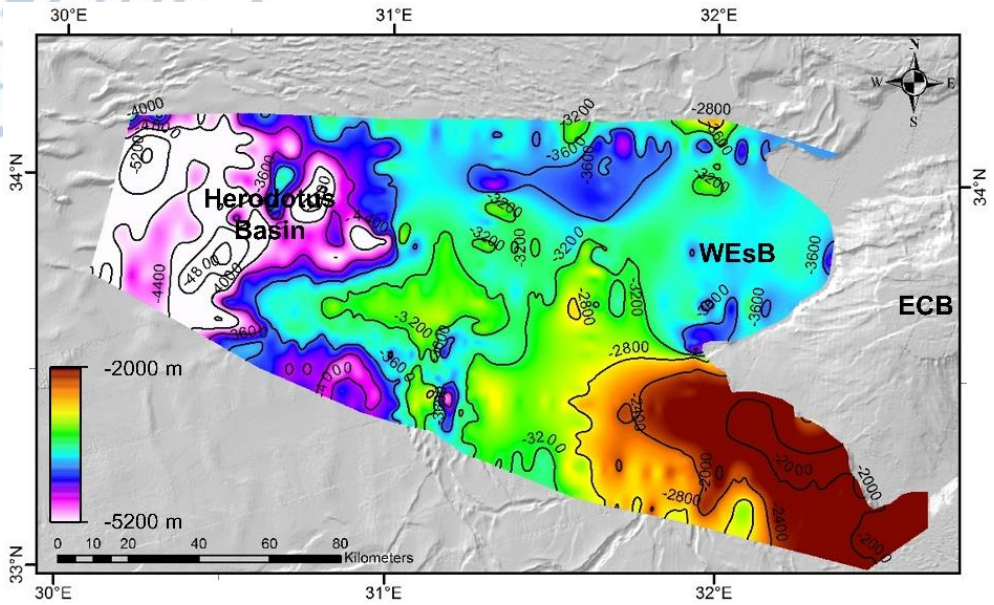

Figure 17: *Map depicting the top Messinian sequence seismic surface (TS/TES). The TS/TES surface of the study area in meters (m), ECB, WEsB, and Herodotus basin are distinguished. The pinch out at the southwest flanks of the ECB, the flat topography at WEsB, and the intense surface alternations towards the Herodotus basin are also observed. For location see Figure 11 (contour interval 400 m). Data used to produce this map are shown in figure 10.*

B.3.3.3 Base Messinian sequence seismic surface (BS/BES)

Base Messinian sequence surface (BS/BES): Above the pre-Messinian clastic deposits of Unit 3, a strong reflector was detected which in some areas is in direct contact with the carbonate deposits of Unit 4. This reflector represents the base of the Messinian sequence (BS/BES) (Fig. 18). The base Messinian surface (Fig. 18) has a maximum elevation (in meters) at the southwest of the ECB and a minimum elevation towards the deep Herodotus Basin. In the area of the WEsB, flat topography of the base Messinian surface is observed. West of the WEsB, the morphology of the base Messinian surface displays intense alternations. However, on the southwest side of the study area, a complex morphology of the base Messinian surface is discerned.

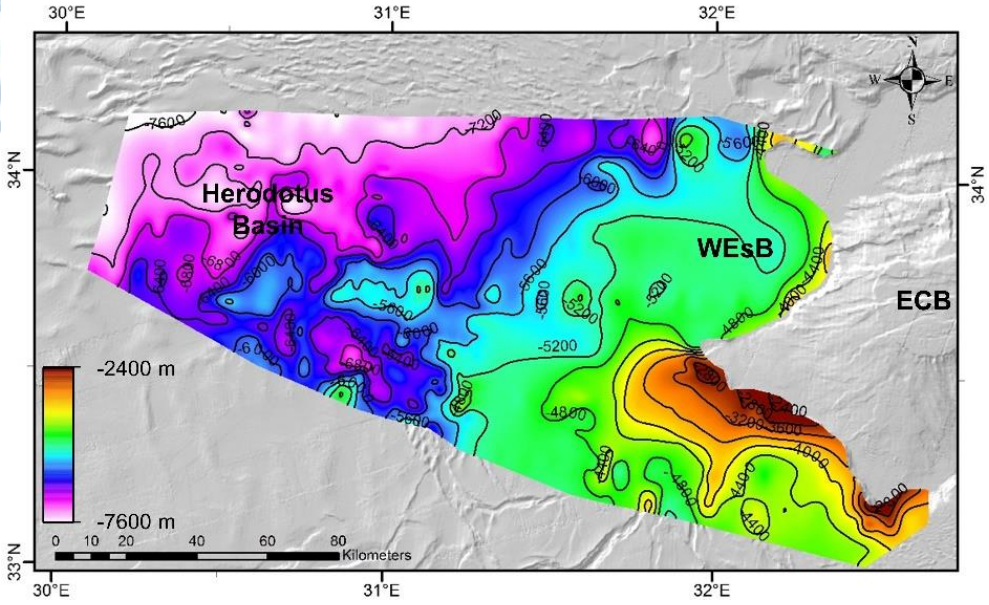

Figure 18: *Map depicting the base Messiniansequence seismic surface (BS/BES). The BS/BESsurface of the study area in meters (m), ECB, WEsB, and Herodotus Basin are distinguished. The pinch out at the southwest flanks of the ECB, the flat topography at WEsB, and the intense surface alternations towards the Herodotus Basin are also observed. For location see Figure 11 (contour interval 400 m). Data used to produce this map are shown in figure 10.*

B.3.3.4 Top carbonates seismic surface

Top carbonate surface: The top carbonate surface in meters was mapped based on the seismic dataset. The top carbonate surface (Fig. 19) does not represent a unique age and is used only for geomorphological description. In this map, a westward extension of the ECB is observed. West of the ECB a depression is revealed. This depression represents the basement of the WEsB. West of the topographic depression an elevated area is well defined. This area is addressed as the West Eratosthenes High (WEH). The carbonates are dipping west towards the Herodotus Basin and the top carbonates seismic reflector cannot be followed with confidence.

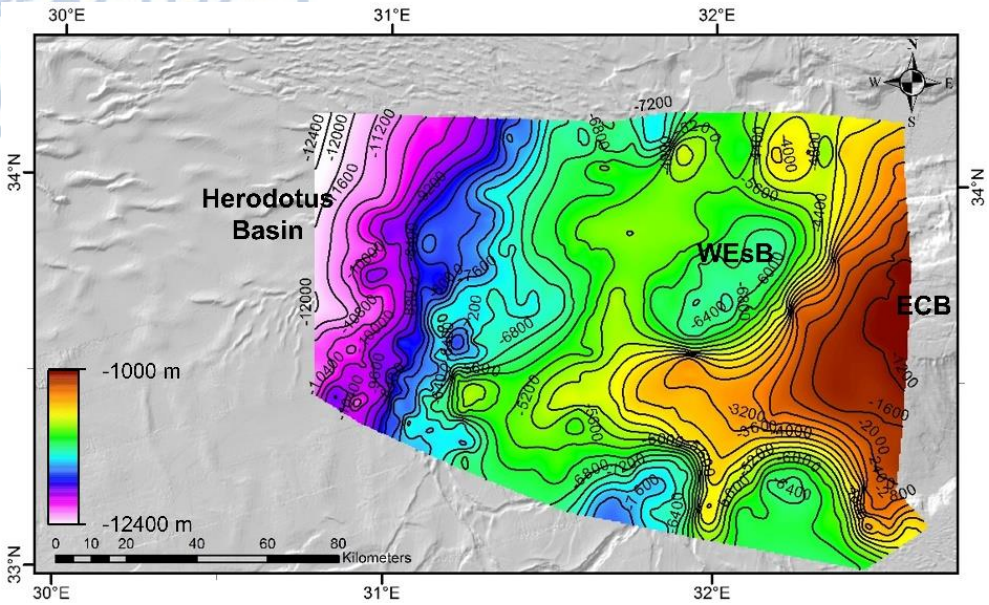

Figure 19: *Map depicting the top carbonate seismic surface. The top carbonate surface of the study area in meters (m), ECB, WEsB, and Herodotus basin are distinguished. The basement of the WEsB, the WEH, and the ECB extension towards the west are also observed (contour interval 400 m). Data used to produce this map are shown in figure 10.*

C.4 Deformation of the MSC sequence from the ECB towards the Herodotus Basin

C.4.1 Introduction

Decoding the triggering and driving mechanisms of salt-related deformation is key in understanding evolutionary patterns of salt-bearing basins. Salt flow and overburden deformation are commonly attributed to regional crust tectonics (e.g., Hudec and Jackson 2007) and gravity processes referred to as gravity spreading and gravity gliding (Allen et al., 2016). Gravity spreading is associated with differential loading by seaward-thinning sediment wedges sourced from onshore (Hudec and Jackson, 2007; Hudec et al., 2009) (Fig. 20). The asymmetric and irregular distribution of sediments causes a pressure profile that forces the salt to flow basinward (Vendeville, 2005). On the other hand, gravity gliding is commonly associated with the pressure gradient built by the basinward tilting of the salt and its overburden (Fig. 20). Salt flows basinward from topographic highs to topographic lows until an equilibrium profile is achieved (Brun and Fort, 2011; Hudec and Jackson, 2007; Jackson et al., 1994; Rowan et al., 2004, 2012; Schultz-Ela, 2001). However, salt flow and overburden deformation are result, in most cases, from the combination of gravity spreading and gliding mechanisms (e.g., Allen et al., 2016; Brun and Fort, 2011). Both mechanisms generally result in the formation of an extensional domain landward, which passes into a compressional domain basinward (e.g., Fort et al., 2004; Gaullier and Vendeville, 2005; Letouzey et al., 1995; Schultz-Ela, 2001; Tari et al., 2002; Vendeville, 2005).

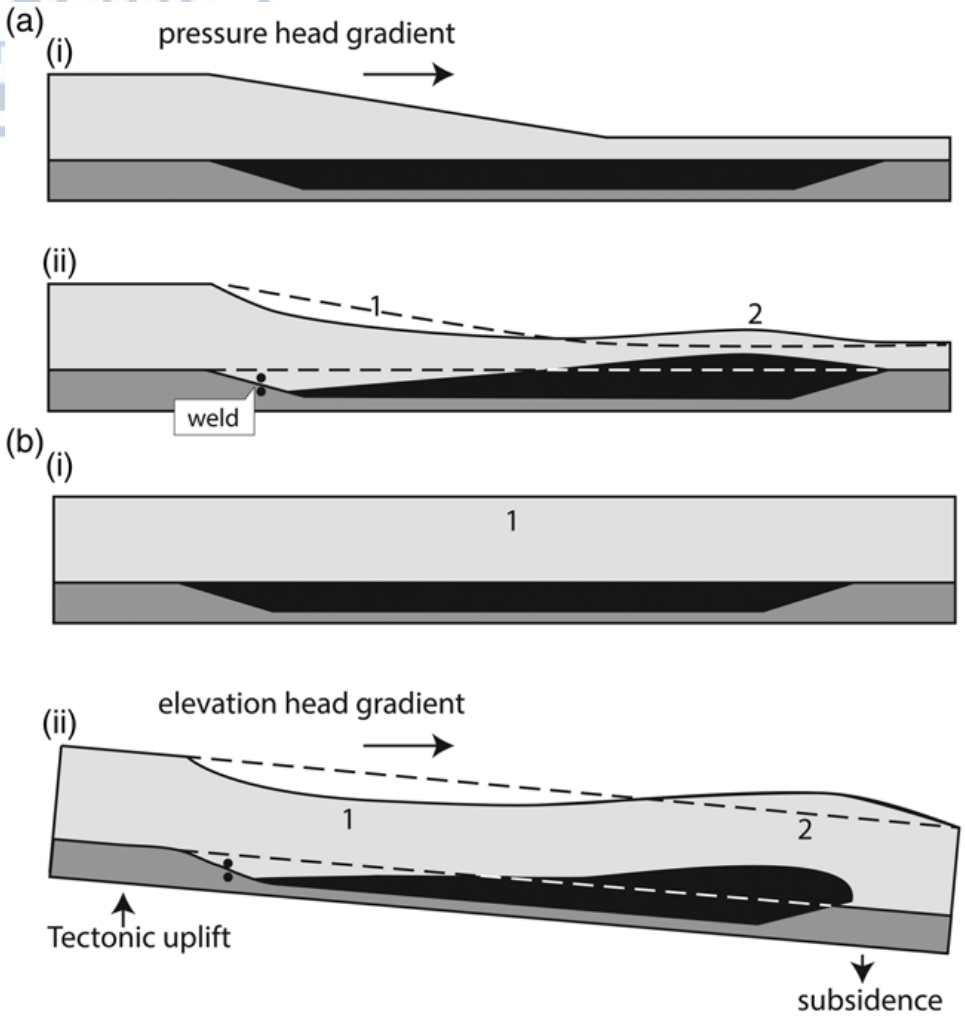

Figure 20: *Comparison of the two main triggers for initiating and driving prolonged salt flow (Allen et al., 2016). (a) A laterally varying overburden thickness above a horizontal, tabular salt layer: (i) initial stage, assuming instantaneous overburden deposition: that is, the loading of a salt layer (black) by a sediment wedge (light grey) creates a pressure head gradient from left to right; (ii) salt flows along the pressure head gradient, leading to expulsion and eventual welding, coupled with the collapse of the proximal overburden (1), and the inflation of the distal salt and overburden (2), resulting in updip extension and downdip compression-related structures. (b) Salt flow and deformation assuming a uniform overburden thickness above a tilted, tabular salt layer: (i) initial stage: before base-salt tilting, and with a tabular overburden, salt remains stable owing to the lack of any pressure head gradient; (ii) tilting creates an elevation head gradient from left to right and salt will flow along this gradient. Note the similarity between the resultant salt body geometries and the structural styles despite the different triggers (Allen et al., 2016).*

Over the last years, there has been an increasing interest in understanding salt-tectonic deformation associated with the Messinian (i.e., Late Miocene) evaporite sequence, which was deposited during the Messinian Salinity Crisis (MSC) throughout the Mediterranean (Hsu et al., 1973, 1977). This is because the MSC sequence is relatively young and is characterized by thin overburden, therefore it is well imaged in seismic reflection data.

Studies based on 2D and 3D seismic datasets have been focused on understanding salt-related deformation in sub-basins offshore Eastern Mediterranean and in particular, in the Levantine Basin (Bertoni and Cartwright, 2006; Cartwright et al., 2012; Elfassi et al., 2019; Feng et al., 2017; Gvirtzman et al., 2013; 2015; Netzeband et al., 2006b; Reiche et al., 2014), in the Nile Deep-Sea Fan (NDSF) (Gaullier and Vendeville, 2005; Gaullier et al., 2000; Loncke et al., 2006; Mascle et al., 2006; Vendeville, 2005; Zucker et al., 2019), and in the Herodotus Basin (Allen et al., 2016; Zucker et al., 2019). These studies have shown that the relative contribution of gravity spreading and gliding mechanisms varies significantly both in time and in space.

More specifically, seismic reflection data revealed that the main mechanism of salt-deformation in the eastern margin of the Levantine Basin is that of gravity gliding caused by basinward tilting of the salt and its overburden due to regional inland uplift and basin subsidence (Elfassi et al., 2019; Gvirtzman et al., 2013; Reiche et al., 2014). However, there is significant controversy and disagreement related to the timing of salt deformation. Gvirtzman et al. (2013) suggested two phases of salt deformation; a syn-depositional deformation during the Messinian and a second deformation phase during the Plio-Pleistocene. This interpretation is challenged in the study conducted by Allen et al. (2016), which supports a single Plio-Pleistocene deformation phase of the Levantine margin. Moreover, according to Reiche et al. (2014), the Messinian evaporite deformation in the northern Levantine Basin is related to a sub-salt Miocene extensional fault system, which has caused the formation of intra-salt fault-propagation folds. On the contrary, gravity spreading is the dominant mechanism of salt-deformation in the southern Levantine Basin due to the differential loading emerging from the Nile-derived clastic sediments (Reiche et al., 2014; Zucker et al., 2019). Furthermore, in the Nile Deep-Sea Fan, salt deformation is attributed to both gravity and spreading mechanisms (Allen et al., 2016; Gaullier and Vendeville, 2005;

Loncke et al., 2006; Zucker et al., 2019). Gravity spreading is dominant near the Plio-Quaternary Nile cone while gliding is dominant towards the Herodotus Basin (Allen et al., 2016; Zucker et al., 2019).

In this chapter, high-quality 2D seismic reflection profiles are used in order to better understand salt-related deformation at the eastern part of the Herodotus Basin and the broader area of the Eratosthenes Continental Block (ECB) that separates the Herodotus Basin from the Levantine Basin (Fig. 1). The ECB is interpreted as an irregular-shaped carbonate platform (Papadimitriou et al., 2018) delineated by a prominent bathymetric step adjacent to its northern, eastern, and southern flanks. The formation of this bathymetric step is attributed to the pinch out of the Late Messinian evaporites (Reiche et al., 2016; Gaullier et al., 2000 Loncke et al., 2006), however, the absence of a similar topographic figure at the western side of the ECB has not yet been investigated. This study aims to explore the key controls on salt tectonic deformation from the ECB towards the deep Herodotus Basin, where this topographic feature is lacking. In particular, the following questions are sought to be answered: Which are the main triggers and driving mechanisms that are responsible for the observed salt deformation in the study area? Which is the relative contribution of each mechanism to the observed deformation styles? How does the morphology of the Eratosthenes Continental Block (ECB) affect the different deformation styles?

C.4.2 Salt tectonics and structure

C.4.2.1 West Eratosthenes sub-Basin (P1)

In the WEsB (see Figure 10), the structure of the MSC sequence indicates an area that partially suffered from salt tectonics. In the southern WEsB, the TS/TES presents variations that are very well imprinted in the isopach map of Figure 21A and the seismic section of

Figure 21C. The salt-deformation is limited to the southern WEsB and is characterized by salt-core anticlines flanked by Plio-Quaternary clastic sediment wedges (Fig. 21C). Collapse grabens are observed above the salt-core anticlines (Fig. 21C). In the eastern WEsB, the MSC sequence is slightly deformed by the fault that outlines the western flanks of the ECB. The BS/BES and TS/TES reflectors in the central WEsB are relatively flat without any intense alternations (Figures 12, 17, and 18). The MSC sequence in the central and northern WEsB is represented by highly reflective seismic packages (Figs. 12, 14C, and 21C) which are very similar to those that have been reported in the LB (see Gorini et al., 2015 fig. 2b; Feng et al., 2016 fig. 7b and Reiche et al., 2014). The MSC sequence in the WEsB is separated into distinct seismic stratigraphic subdivisions based on the nomenclature proposed by Gorini et al. (2015). The seismic stratigraphic subdivisions from the BS/BES to the TS/TES are: (A), which occurs at the base of the MSC sequence and is represented by parallel high amplitude, low-frequency reflections; (B), which occurs above A and is represented by transparent, limited, and weak reflections; (C), which occurs at the center of the MSC sequence and is characterized by high amplitude high-frequency reflections; (D), which occurs above C and is represented by a very characteristic transparent unit; (E), which occurs above D and is consisted of high-frequency chaotic reflections, and (F), which occurs at the top of E and is characterized by parallel to sub-parallel high-amplitude high-frequency reflections. Subdivision F probably represents sharp lithological alternations (bedding/layering of dolomite, gypsum, anhydrite, etc.) of the Lago Mare sequence that was deposited during the last stage of the MSC (Hsu et al., 1973). This unit is missing in the Levantine Basin most likely because during the final stage of the MSC the easternmost Mediterranean Sea was essentially desiccated (Netzeband et al., 2006b; Bertoni and Cartwright, 2007). This sequence is limited only to the WEsB and is absent in the deep Herodotus Basin. The separation of the

MSC sequence in distinct stratigraphic subdivisions is applicable in the WEsB because intense salt tectonics are absent.

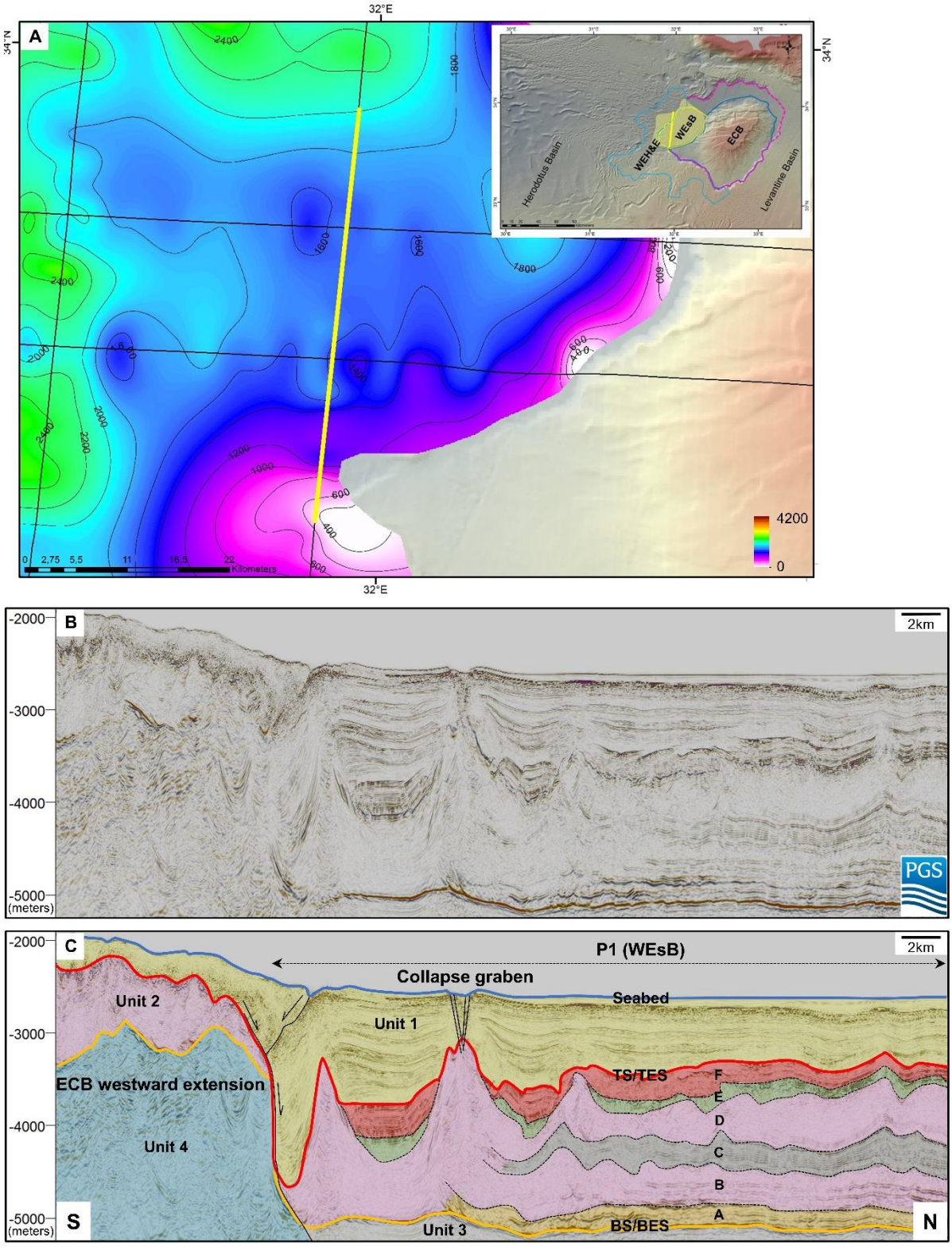

Figure 21: *(A) Isopach map of the MSC sequence (contour interval is 200 m) in the WEsB (P1). Note that thickness variations are observed only in the southern part of the WEsB. Yellow line depicts the cross section shown in (B) and (C). S-N uninterpreted (B) and interpreted (C) depth seismic cross-section across the WEsB*

illustrating the four main seismic stratigraphic units and their bounding surfaces i.e., Seabed, Top Surface/Top Erosional Surface (TS/TES) and Bottom Surface/Bottom Erosional Surface (BS/BES). Deformation of the MSC sequence is characterized by salt core anticlines topped by collapse grabens. The six seismic stratigraphic subdivisions (A, B, C, D, E, F) of the MSC sequence are also shown. The WEsB is bounded to the south by a north-dipping normal fault. Vertical exaggeration of the cross-section is 5:1.

C.4.2.2 North-west of the Eratosthenes Continental Block (P2)

In the area located north-west of the ECB (see Figure 10), the MSC sequence is characterized by severely deformed transparent to chaotic reflections. The MSC sequence presents irregular distribution characterized by thickness variations, ranging from few meters to several kilometers (Fig. 5). The transparent to chaotic reflections observed in P2 illustrate crept structureless salt segments delimited by reverse faults, dipping west and east that lead to a characteristic uplift of the seafloor (Fig. 22C). In this province, the BS/BES is bottomed by the low to high amplitude reflections of the ECB carbonate accumulations of Unit 4 because Unit 3 is absent, and the TS/TES is topped by the thin Plio-Quaternary clastic accumulations of Unit 1. In some portions of the seismic section shown in figure 22C, salt deposits of Unit 2 are completely absent, and the Plio-Quaternary clastic accumulations of Unit 1 are deposited directly on top of the carbonate accumulations of Unit 4. Unit 4 presents strong relief variations referring to a horsts-graben scheme (Fig. 22C).

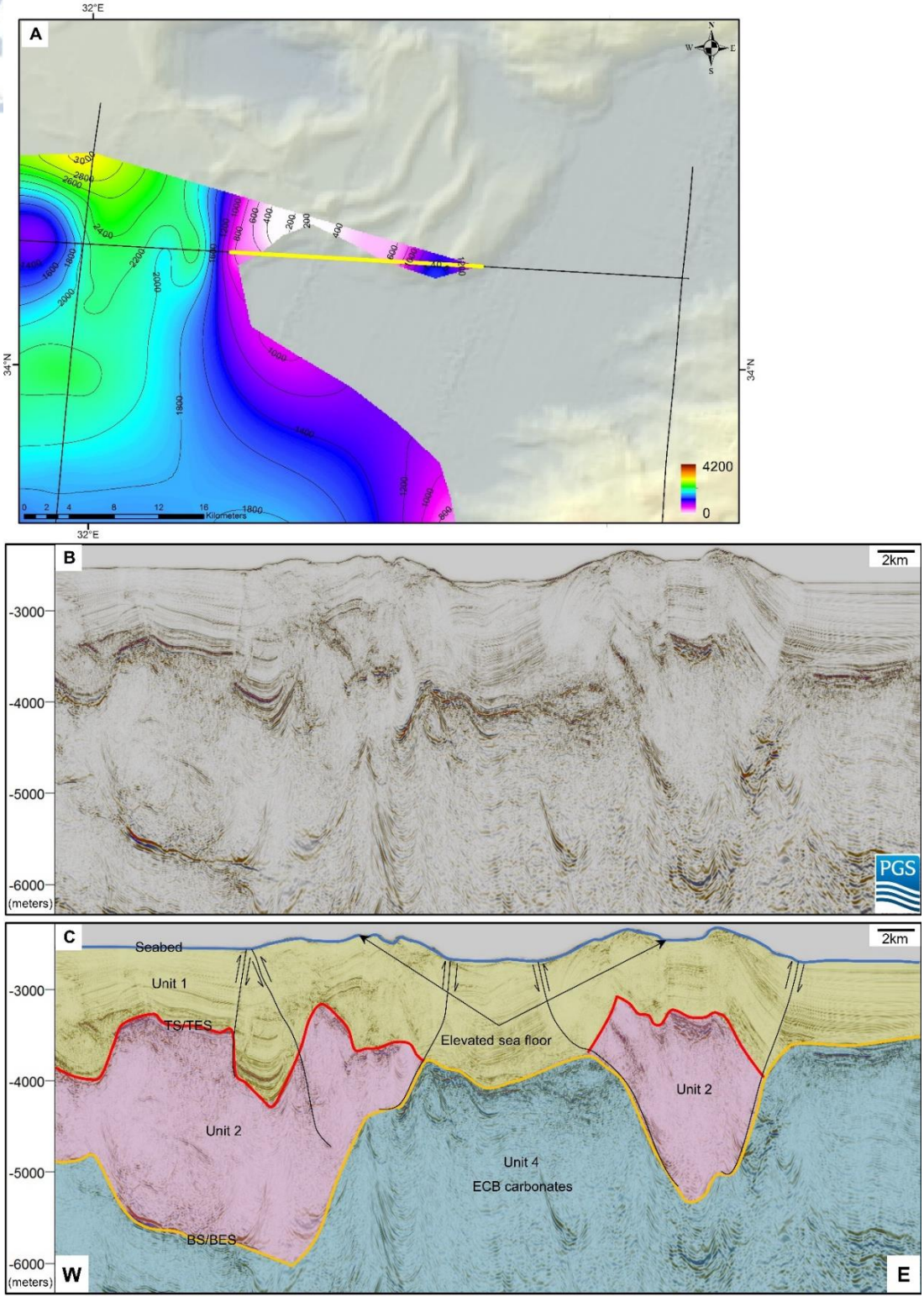

Figure 22: *(A) depicts the isopach map of the MSC sequence (contour interval 200 m) in the area north-west of the ECB (P2). Highly deformed salt which presents intense thickness variations characterize this salt-tectonic province. Yellow line depicts the cross-section shown in (B) and (C). W-E uninterpreted (B) and interpreted (C) depth seismic cross-section across the area north-west of the ECB illustrating the main seismic stratigraphic units and their bounding surfaces, i.e., Seabed, Top Surface/Top Erosional Surface (TS/TES) and Bottom Surface/Bottom Erosional Surface (BS/BES). Unit 3 is absent and the MSC sequence is bottomed by the carbonates of Unit 4. The top surface of Unit 4 presents strong relief variations. The MSC sequence is characterized by crept structureless salt segments bounded by reverse faults leading to elevated seafloor. Vertical exaggeration of the cross-section is 5:1.*

C.4.2.3 Area S & SW of the ECB (P3)

In the area located south and south-west of the ECB (see Figure 10), the MSC sequence shows significant thickness variability (Fig. 23A). In areas where the MSC succession is relatively thick (i.e., > 2200 m), BS/BES surface is bottomed by the pre-Messinian clastic accumulations of Unit 3 (Figs. 23B, C & 24A, B). Conversely, in areas where the MSC sequence is thin (i.e., < 1800 m), BS/BES surface is bottomed by the carbonate accumulations of Unit 4 (Figs. 24A, B). In a zone located south of the ECB (Figs. 23B, C), a dense network of south-dipping reverse faults is observed in the TS/TES reflector and the stratigraphic subdivision C of the MSC sequence. In this area, the MSC sequence overthrusts the ECB leading to the formation of a prominent bathymetric step on the seafloor (Fig. 23C). The bathymetric step is 20-25 km wide, ranging between -1700 m at the crest of the step to -2300 m at its bottom (Fig. 23D). It is separated by the relatively elevated seafloor towards the south and southwest and represents the pinch out of the MSC sequence. In the area south-west of the ECB, both south and north dipping reverse faults are observed (Fig. 24B) that lead to thickened salt deposits at the southern flanks of the ECB westward extension. The TS/TES and BS/BES reflectors can be traced approximately at a depth of -2200 and -3600 m at the top of the ECB westward extension and are deepening at a depth of -2800 and -5000 m to the south of P3 (Fig. 24B).

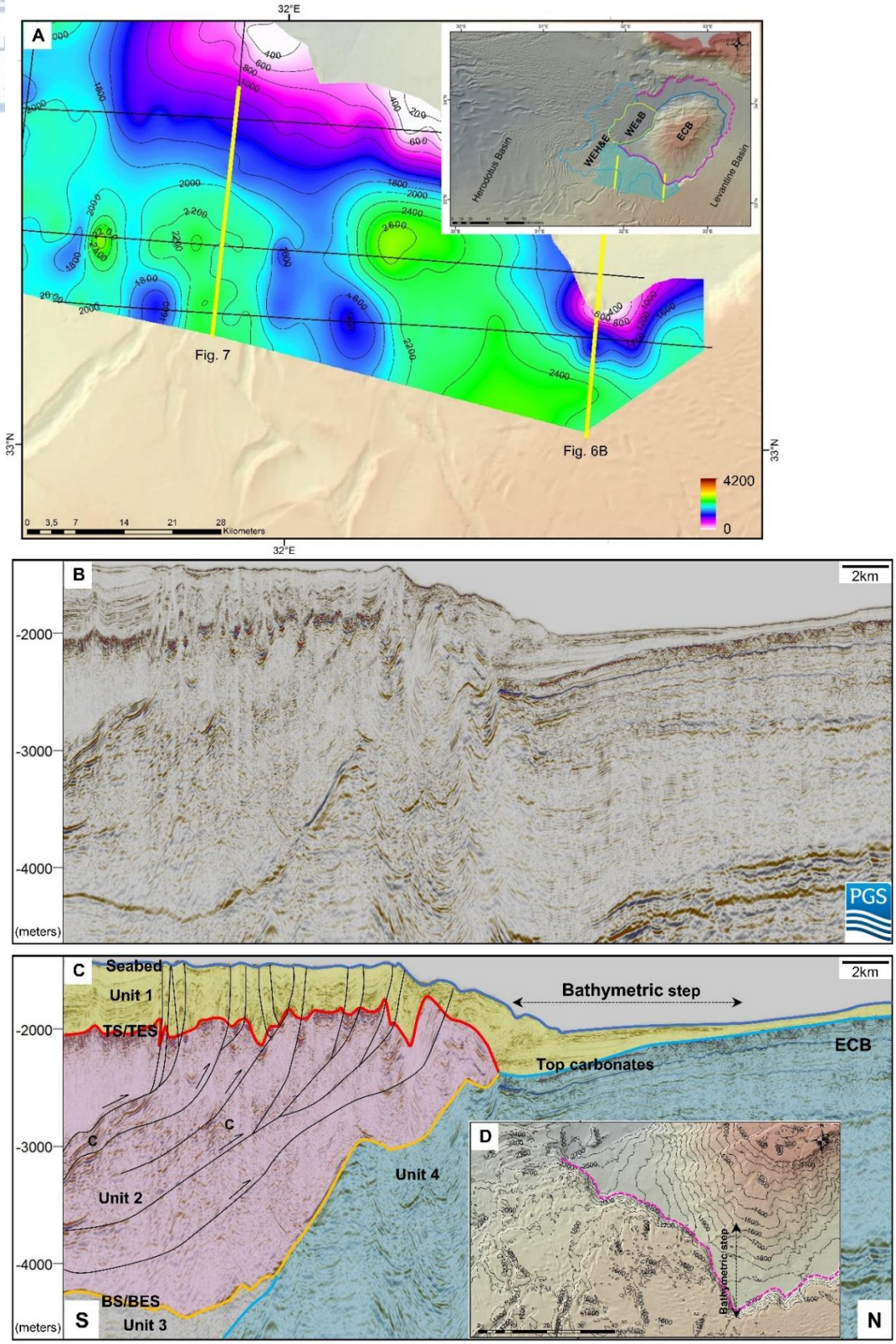

Figure 23: *(A) Isopach map of the MSC sequence (contour interval 200 m) in the area south and south-west of the ECB (P3). Yellow lines depict the cross-section shown in Figs. 23A,B and 24A,B. S-N uninterpreted (B) and interpreted (C) depth seismic cross-section across the area south of the ECB illustrating the four main seismic stratigraphic units and their bounding surfaces i.e., Seabed, Top Surface/Top Erosional Surface (TS/TES), Bottom Surface/Bottom Erosional Surface (BS/BES), and Top carbonates. The MSC sequence is characterized by severely deformed and thickened salt deposits which overthrust the southern flanks of the ECB. (D) bathymetric step at the seafloor. Vertical exaggeration of the cross-section is 5:1.*

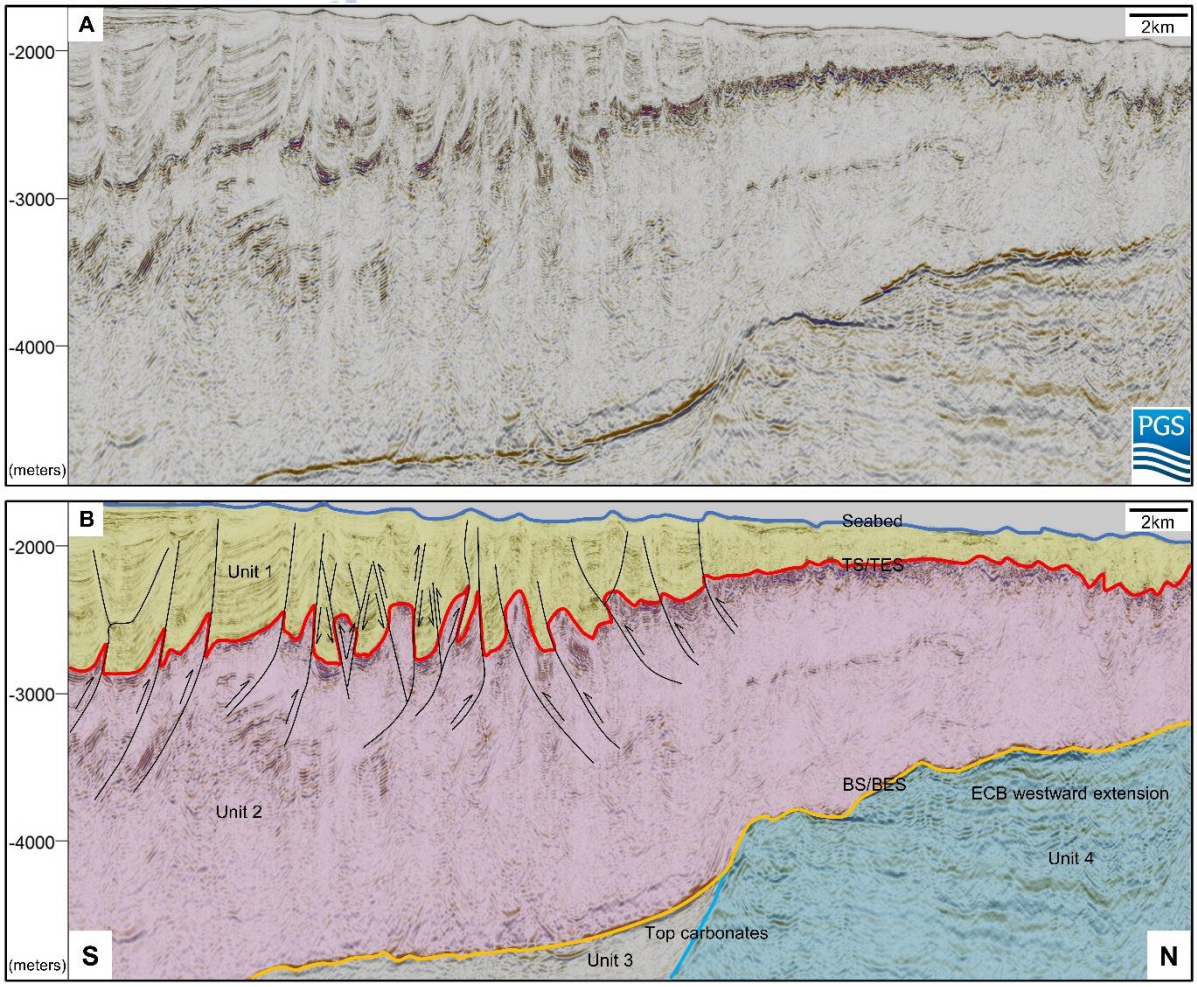

Figure 24: *S-N uninterpreted (A) and interpreted (B) depth seismic cross-section across the area south-west of the ECB (P3) illustrating the four main seismic stratigraphic units and their bounding surfaces i.e., Seabed, Top Surface/Top Erosional Surface (TS/TES), Bottom Surface/Bottom Erosional Surface (BS/BES), and Top carbonates (for location see Figure 23A). The MSC sequence is severely deformed by south and north dipping reverse faults that lead to thickened salt deposits at the southern flanks of the ECB westward extension. The elevation differences between the BS/BES reflector and the south-north dipping reverse faults can be discerned. Vertical exaggeration of the cross-section is 5:1.*

C.4.2.4 The easternmost part of the Herodotus Basin (P4)

The seismic dataset shows that the area located west of the WEH and the ECB westward extension into the Herodotus Basin has been deformed by compressional salt tectonics (Figs. 25, 26, and 27). Significant thickness variations of the MSC sequence are observed that show an overall thickness decrease to the west towards the deep Herodotus Basin (Fig. 25A). Moreover, this province is characterized by an elevated seafloor (~200 m) compared to the

WEsB and the deep Herodotus Basin (Fig. 25B). The seismic character of the MSC sequence in P4 is chaotic with internal shear surfaces (see Fig. 26) and therefore prohibits its division into further seismic stratigraphic sections.

At the southern part of P4, the thickness of salt deposits varies from 1200 m to 3400 m (Fig. 25A); these thickness variations reveal large salt diapirs flanked by Plio-Quaternary clastic sediment wedges (Fig. 26B). These salt diapirs are characterized by large east and west-dipping shear surfaces with opposite offsets (Fig. 26B). The BS/BES reflector can be traced at a depth of approximately -4500 m at the top of the ECB westward extension, dipping sharply towards the west at a depth of more than -6000 m. The MSC sequence is considerably thick (~3 km) at the central part of P4 (Fig. 25A). In this area, the MSC sequence is severely deformed, especially at the western flanks of the WEH (see Fig. 3B). The TS/TES and BS/BES reflectors can be traced approximately at a depth of -3000 and -5000 m at the top of the WEH (Fig. 12B) and a depth of -5000 and -7000 m towards the deep Herodotus Basin.

The northern part of P4 shows a compressional domain characterized by considerably thick (~3 km) (Fig. 27), highly deformed salt deposits with internal shear surfaces, and small diapirs (Fig. 27). Moreover, at the northeast boundary of P4, a dense thrust zone is observed (Fig. 27A). This compressional domain is characterized by dense kink zones towards the north and northwest (Figs. 27B, C, D). Furthermore, in this compressional domain, numerous incidents of fluid migration are observed inside the sedimentary accumulations stemming from the pre-Messinian section (Figs. 27C, D). Characteristic formations such as gas chimneys that represent hydrocarbon pathways are shown by anomalies due to velocity pushdowns (Figs. 27C, D). This seepage process leads to the formation of mud volcanoes and pockmarks that are commonly observed at the seafloor.

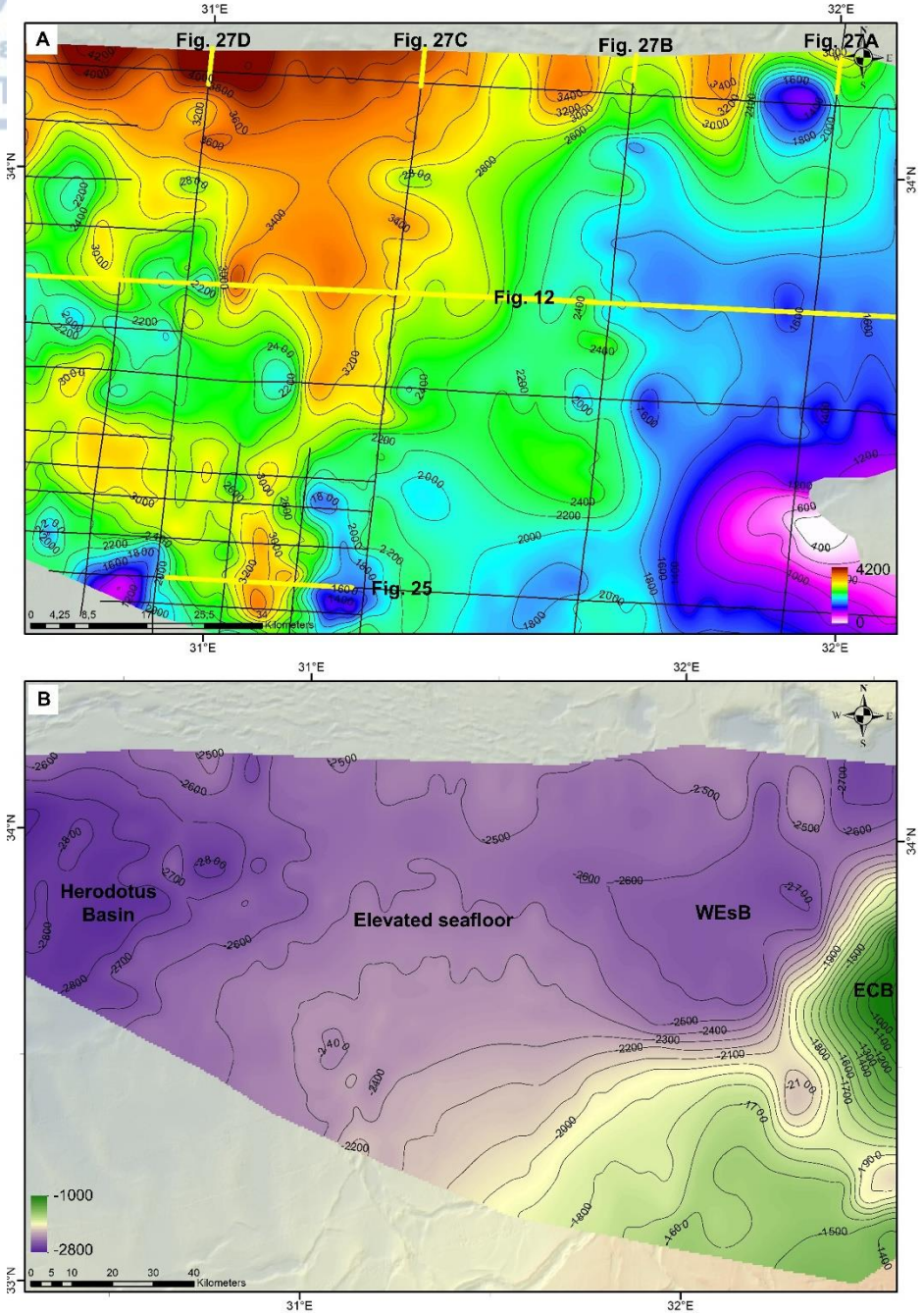

Figure 25: *(A) Isopach map of the MSC sequence (contour interval 200 m) in the area west of the WEH (P4). Note the thickness variations that characterize this salt-tectonic province. Yellow lines (A) depict the cross sections shown in figures 26 and 27. The location of the cross-section illustrated in Fig. 12 is also shown. (B) Seafloor morphology of the area west of the WEH that shows the elevated seafloor of the salt-tectonic province P4 (contour interval 100 m).*

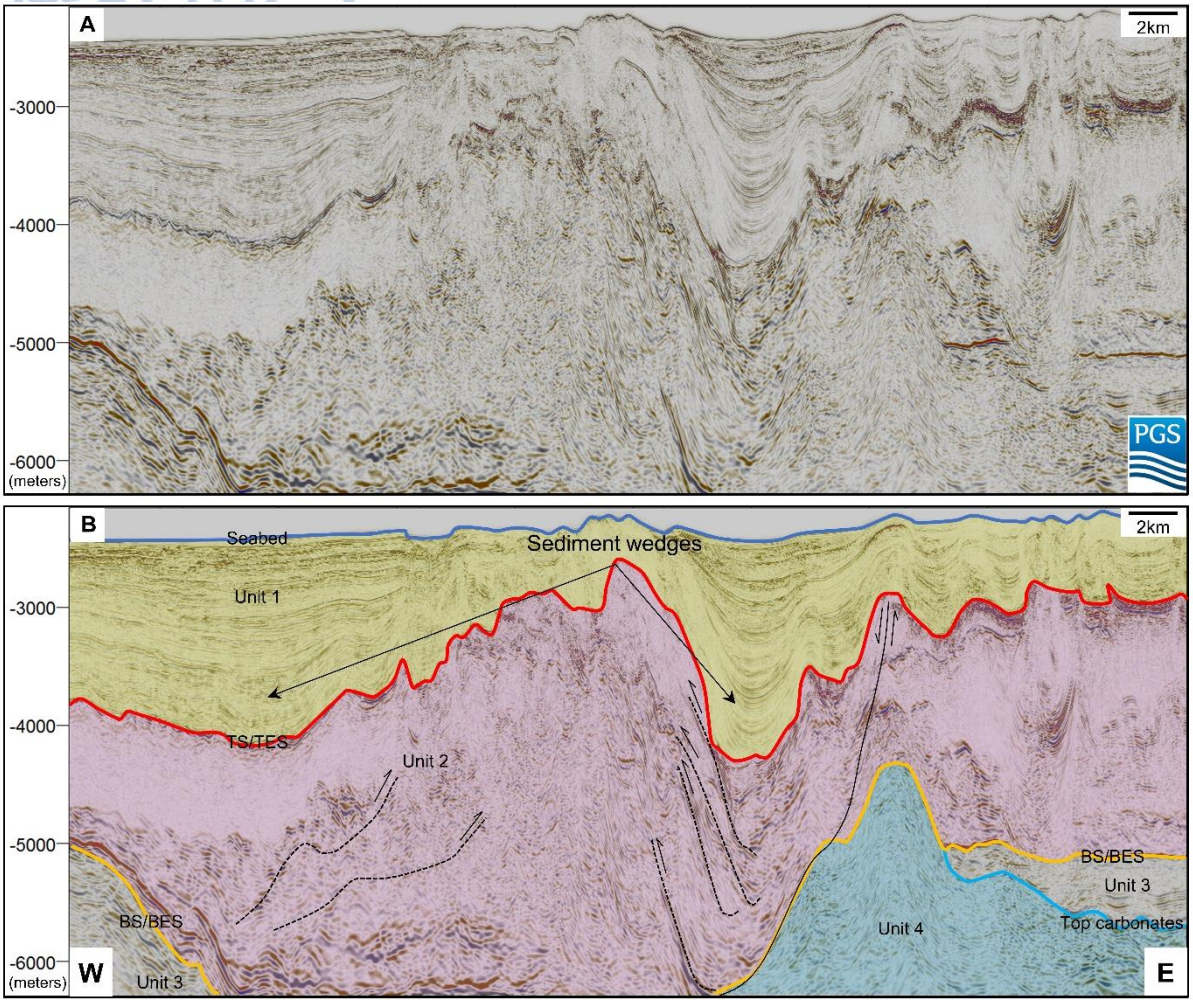

Figure 26: *W-E uninterpreted (A) and interpreted (B) depth seismic cross-section across the area west of the ECB westward extension illustrating the four main seismic stratigraphic units and their bounding surfaces, i.e., Seabed, Top Surface/Top Erosional Surface (TS/TES), Bottom Surface/Bottom Erosional Surface (BS/BES), and Top carbonates (for location see Figure 25A). The MSC sequence is characterized by west-east compressionally thickened salt with internal shear surfaces shown with black dashed lines. Note the elevation profile differences of the BS/BES reflector, the significant thickness increase of the Plio-Quaternary clastic sediments (Unit 1) towards the west, and the normal fault that delineates the western boundary of the ECB westward extension. Vertical exaggeration of the cross-section is 5:1.*

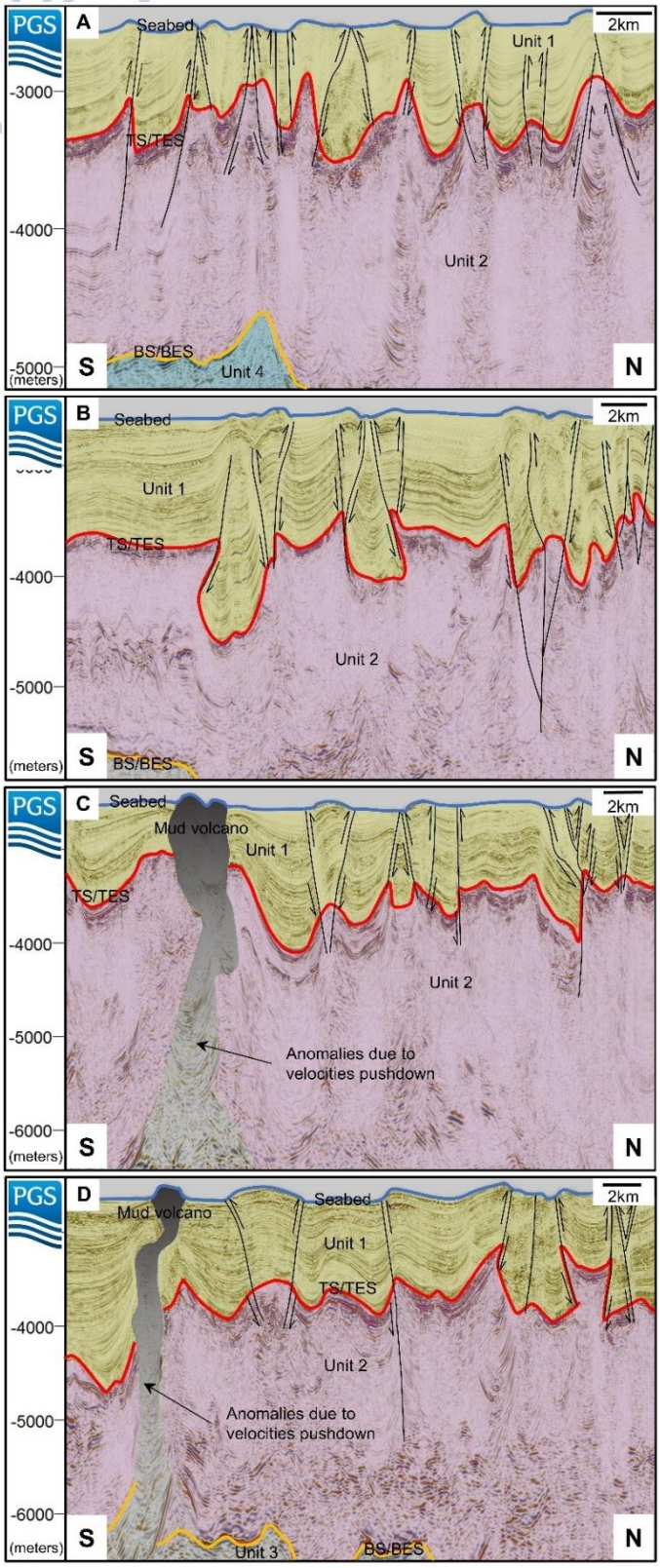

Figure 27: *South-North interpreted depth seismic cross-sections across the north domain of P4 illustrating the seismic stratigraphic units and their bounding surfaces (for location see Figure 25A). The MSC sequence is characterized by thick highly deformed salt with internal shear surfaces. This domain is characterized by dense kink and thrust zones. Many instances of fluid migration are observed in the seismic data set creating structures as mud volcanoes at the seafloor. Vertical exaggeration 5:1.*

C.4.2.5 The deep Herodotus Basin (P5)

The seismic reflection data show a highly folded MSC sequence within the deep Herodotus Basin (Fig. 28). The fold axes are predominantly East-West oriented (Fig. 28). The fold wavelength is locally variable, but it generally decreases northwards from ~22 km to ~7 km and the fold amplitude decreases, whereas the folding frequency increases towards the north (Fig. 28). The MSC sequence depicts chaotic internal seismic stratigraphy with a thickness of ~2 km at the southern part of the area, which increases to approximately 3 km towards the northern part (Fig. 28). The deep Herodotus Basin constitutes an active depocenter for the clastic sediments derived from the north African passive margin and the River Nile since the end of the MSC. Figure 29B illustrates an isopach map of the Plio-Quaternary clastic deposits. By comparing the thickness of the Plio-Quaternary overburden to the thickness of the MSC sequence (Fig. 29A), a broadly inverse relationship is observed (areas of relatively thin salt correspond to areas of thick overburden and vice versa).

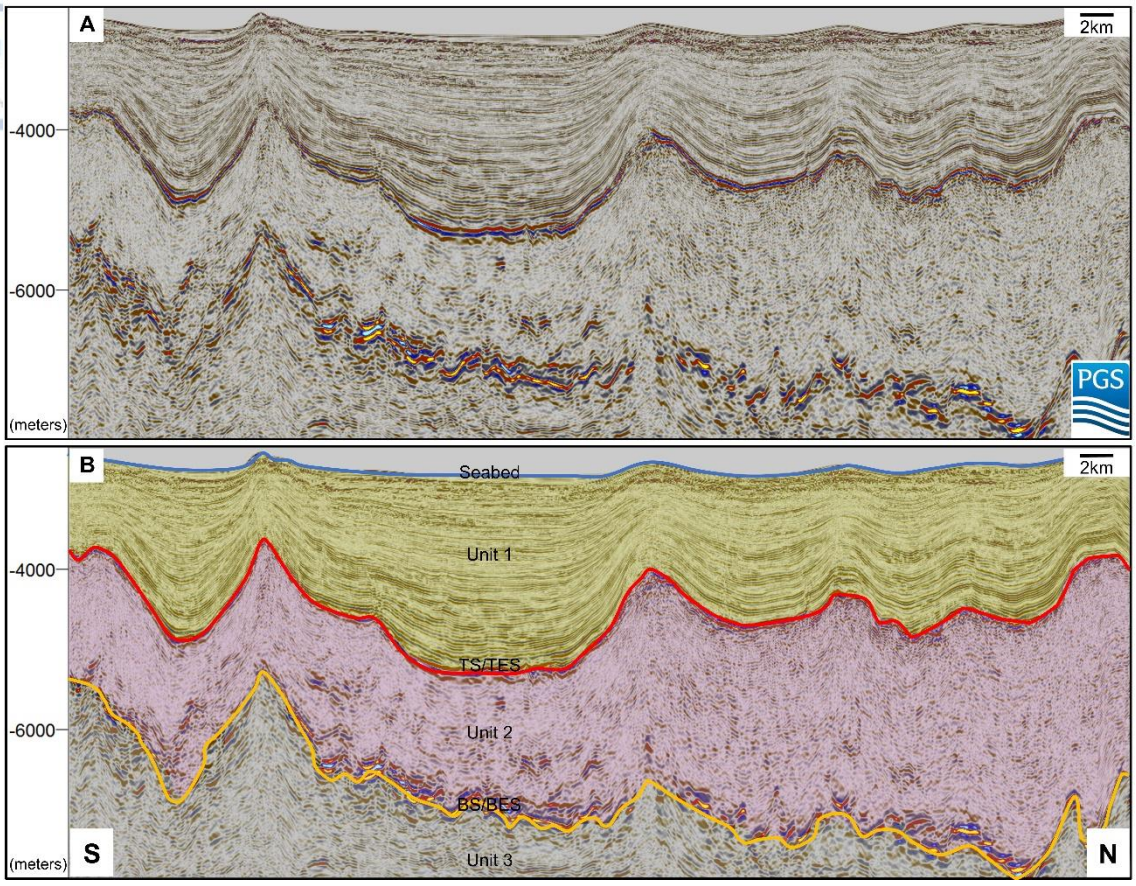

Figure 28: *S-N uninterpreted* ***(A)*** *and interpreted* ***(B)*** *depth seismic cross-section across the deep Herodotus Basin (P5) illustrating the main seismic stratigraphic units and their bounding surfaces, i.e., Seabed, Top Surface/Top Erosional Surface (TS/TES) and Bottom Surface/Bottom Erosional Surface (BS/BES) (for location see Figure 29A). The MSC sequence in P5 is folded with decreasing fold amplitude and increasing fold frequency towards the north. Note the thickening of the MSC sequence towards the north and the thick Plio-Quaternary clastic sediments. Vertical exaggeration of the cross-section is 5:1.*

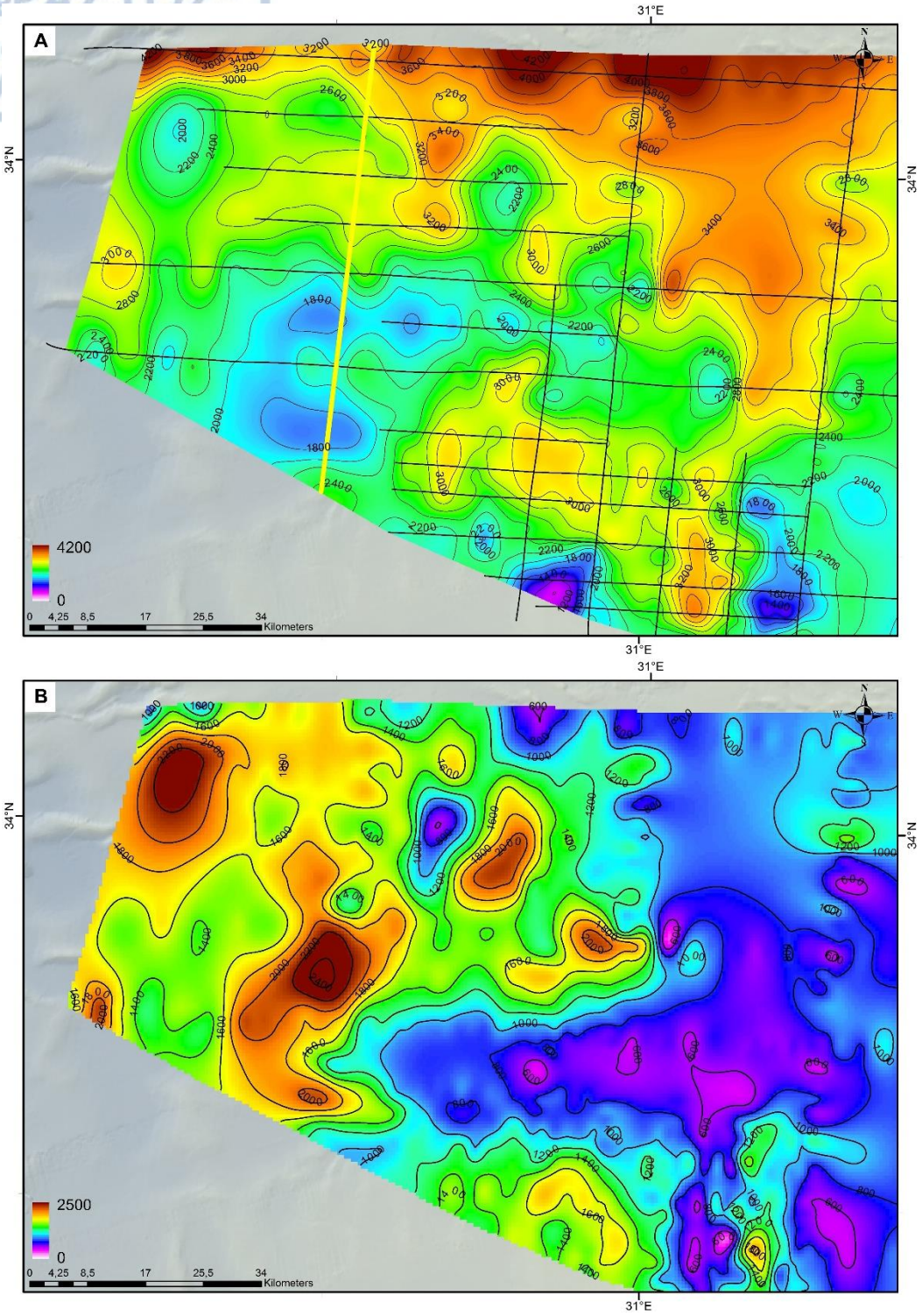

Figure 29: *(A) depicts the isopach map of the MSC sequence (contour interval 200 m) at the deep Herodotus Basin (P5), where intense thickness alternations are observed. The yellow line in (A) illustrates the location of Figure 28. (B) depicts the isopach map of the Plio-Quaternary clastic sediments (contour interval 200 m) at the deep Herodotus Basin (P5), where intense thickness alternations are observed. An inverse thickness relationship between the two isopach maps can clearly be distinguished.*

C.4.3 Discussion about salt deformation

This chapter aims to understand salt-related deformation patterns at the eastern part of the Herodotus Basin and to unravel the main mechanisms that trigger salt flow and overburden deformation at the south, south-west, north-west, and western area of the Eratosthenes Continental Block (ECB) that constitutes the natural boundary between the Herodotus and the Levantine Basins (see Figure 2). The available dataset reveals significant variations in the thickness of the MSC sequence and the Plio-Quaternary clastic sediments that allows assessing the relative contribution of the key controls on salt-related deformation (i.e., regional tectonics, gravity spreading, and gravity gliding) at five distinct salt-tectonic structural provinces (i.e., P1 - P5). Figure 30 summarizes the main mechanisms of salt-related deformation in the study area.

C.4.3.1 Structural Province - P1

Salt-tectonic structural province (P1) that covers the West Eratosthenes sub-Basin (WEsB) is deformed only at its southern and eastern parts (Figs. 12 and 21). In this area, normal faults bound the northern margins of the ECB westward extension and the western margins of the ECB (Figs. 12B, 21C, and 30) creating the available accommodation space for the Plio-Quaternary clastic sediments to be stored. These early rift related normal faults represent the boundaries of the Neotethys ocean and were reactivated during the Pliocene and Quaternary (Gao et al., 2020). Therefore, the Plio-Quaternary clastic sediments are thicker at the southern and eastern parts of the WEsB in the proximity of the normal faults and thinner to the rest of the WEsB area (Figs. 12 and 21C). The greater thickness of the Plio-Quaternary sediments lead the Messinian salt to flow towards the north and west, away from the normal faults (Figs. 12B, 21C, and 30). The observed deformation is limited only to the fault's proximal areas, whereas the larger part of the WEsB remains generally undeformed. The salt layer in the WEsB is autochthonous and can be divided into distinct stratigraphic

subdivisions (i.e., stratigraphic subdivisions A, B, C, D, E, and F) (Figs. 12B and 21C). However, stratigraphic subdivision F is detected only to the WEsB and is absent in the deep Herodotus Basin (Figs. 12B and 21C). Overall, the seismic reflection profiles suggest that regional crust tectonics followed by differential sediment loading is the controlling mechanism of the observed salt-related deformation in this salt-tectonic structural province.

C.4.3.2 Structural Province - P2

Salt-tectonic structural province (P2) is located north-west of the ECB and is characterized by crept structureless salt segments bounded by reverse faults that result in seafloor uplift (Fig. 22C). In this province, Unit 3 is absent and the MSC sequence is bottomed by the low to high amplitude reflections of the ECB carbonate accumulations (i.e., Unit 4). The absence of Unit 3 indicate that this province was a shallow carbonate platform (Papadimitriou et al., 2018) throughout the deposition of the Mesozoic - Cenozoic sedimentary succession into the deep Herodotus basin. The horsts-graben scheme observed on top of Unit 4 (Fig. 22C) with deep depressions filled by MSC evaporites and structural highs free of MSC deposits is attributed to the migration of the subduction front of the South Neotethys ocean southward to the south of the Cyprus arc during Early Miocene and to the intensive Messinian compressional deformation caused by the collision between the island of Cyprus and the ECB (Gao et al., 2020). The observed salt-related deformation is associated with the active compressional tectonics that take place further north, in the area located south of the Cyprus island. Grabens created during the intense Miocene compressional tectonic events, accommodate the observed diapirism of the MSC sequence. The reverse faults illustrated in the seismic section of figure 5, is the result of the thin skin salt tectonics as a consequence of the compression caused by the ongoing continental collision between the ECB and the island of Cyprus. This implies that P2 represents the westernmost boundary of a

salt deformation belt located south of the island of Cyprus (Fig. 30). This agrees with the recent study of Reiche et al., (2016), where they state that the MSC sequence "escapes" from the Cyprus subduction zone because of salt shortening and overthrusts the northern slopes of the ECB. This process generates a bathymetric step at the present-day seafloor north of the ECB (see Fig. 30).

C.4.3.3 Structural Province - P3

The seismic dataset from the salt-tectonic structural province (P3), which is located south and south-west of the ECB (Fig. 10), shows that the salt flowing from the Nile Delta towards the southern slopes of the ECB gets severely deformed and overthrusts the ECB leading to the formation of a bathymetric step at the seafloor (Figs. 23C and 30). Because of this process, the seismic image of the MSC sequence south of the ECB and the ECB westward extension is chaotic, referred to as an allochthonous salt (Figs. 23 and 24). South of the ECB westward extension compression-related structures such as reverse faults with opposite offsets are observed (Fig. 24B). The formation of the south-dipping reverse faults is attributed to the salt that flows northwards away from the Nile Delta region due to a combination of gravity processes, i.e., spreading and gliding (Allen et al., 2016). On the other hand, the north-dipping reverse faults (Fig. 24B) are attributed to the salt derived from the top of the ECB westward extension in response to the significant elevation difference across the TS/TES surface (i.e., ~ 600 – 1400 m; Fig. 24B). The overall seismic image in this area points to that gravity gliding is the main mechanism for the observed salt-related deformation. The south gliding salt originated from the top of the ECB westward extension meets the salt derived from the Nile Delta region resulting in the compressional thickening of the MSC sequence. Furthermore, significant thickness variations of the MSC sequence are observed in this salt-tectonic structural province (Fig. 23A). These variations are attributed to

the in-situ deposition of salt onto the pre-existing (i.e., Messinian) topography. At topographic highs of the ECB, salt deposits are relatively thin (~ 1400 - 1600 m), compared to the deep basins where salt deposits have a greater thickness (~ 2400 - 2600 m). Also, the compressionally thickened salt at the southern flanks of the ECB and ECB westward extension contributes to the increased thickness of the MSC sequence.

C.4.3.4 Structural Province - P4

West of the ECB westward extension, the southern part of the salt-tectonic structural province P4 is characterized by thick and large salt diapirs flanked by Plio-Quaternary clastic sediment wedges (Fig. 26B). Also, large east and west dipping shear surfaces occur due to compression (Fig. 26B). This salt-related deformation is considered the result of the deep Earth dynamic processes (Leroux et al., 2015; Rabineau et al., 2014) and the regional crust tectonic regime (e.g., Hudec and Jackson, 2007). The eastern margin of the P4 salt tectonic structural province, is delimited by the continental oceanic boundary (COB) (Fig 12B) which describes the limit between the thinned continental crust of the WEH and the oceanic crust underlying the deep Herodotus Basin. Vertical and high subsidence rates are expected in the deep Herodotus Basin similarly to areas located in the Western Mediterranean (Leroux et al., 2015; Rabineau et al., 2014). The vertical and high subsidence rates can justify the elevation gradient built between the WEH and the deep Herodotus Basin. The Plio-Quaternary clastic sediments that are accommodated along the west-dipping normal fault at the westernmost flanks of the ECB westward extension (Figs. 26B and 30) are squeezing the MSC sequence towards the west. Salt-related deformation at the southern part of P4 is further controlled by the processes that trigger salt flow from the adjacent salt-tectonic structural province P5 (i.e., the deep Herodotus Basin) towards the west flanks of the ECB westward extension and WEH. Moreover, the central part of the P4 is characterized by considerably thickened and

severely deformed salt that shows a chaotic internal seismic stratigraphy (Fig. 12). The intense salt-deformation is mainly observed at the western flanks of the WEH. This seismic image is considered as the result of gravity spreading that prevails at the deep Herodotus Basin (P5) combined with the significant elevation difference of the TS/TES reflector between the deep Herodotus Basin and the WEH (~2 km), which acts as a backstop for the salt to flow further east towards the ECB western flanks (Fig. 12). The Messinian salt is forced to be compressed at the western flanks of WEH and almost double its thickness compared to the salt deposits located at the WEsB and the deep Herodotus Basin (Fig. 12). However, the compressionally thickened salt leads to the slightly elevated seafloor (~200 m) (Fig. 25B) observed throughout P4 compared to P1 and P5 salt tectonic structural provinces. Furthermore, at the northern part of P4, the MSC sequence is characterized by an east-west wide thick compressional domain that depicts thrust and kink zones (Fig. 27). This thick compressional domain is attributed to the gravity processes that prevail in this salt-tectonic structural province, squeezing the Messinian salt to move further north. Therefore, gravity gliding towards the west, regional salt tectonics and salt deformation occurring in the adjacent salt-tectonic structural province P5, because of gravity spreading, are the main mechanisms that shape the observed salt deformation.

C.4.3.5 Structural Province - P5

The elevation gradient between the western Nile Delta area and the deep Herodotus Basin is responsible for the gliding of the entire MSC-overburden sequence downslope (Zucker et al., 2020). This intense elevation gradient is probably linked to deep Earth dynamic processes, which in turn is affecting critically the surface geological processes. Based on the results of recent research in the Western Mediterranean (Leroux et al., 2015; Rabineau et al., 2014) dissimilar amount of total subsidence depends on the varying nature of

the underlying crust. Because of the different nature of the crust, seaward tilting is excepted on the platform and the slope of the African passive margin (continental crust) and purely vertical subsidence in the deep Herodotus Basin (oceanic crust) (Fig.12). The motion of the MSC sequence and its overburden (because of gravity gliding induced by the elevation gradient due to the varying nature of the underlying crust) from the Nile Delta area towards the deep Herodotus Basin creates compression. This compression produces the observed West-East oriented folds in the deep Herodotus Basin. The synclines created between the fold crests filled later with Plio-Quaternary Nile derived deposits. The observed inverse thickness relationship of the MSC sequence with the Plio-Quaternary overburden (Fig. 29) implies that gravity spreading predominates in the deep Herodotus Basin that has been receiving Plio-Quaternary clastic sediments since the end of the MSC and constitutes an active depocenter for the Nile derived clastic sediments even today. The significant increase of the Plio-Quaternary overburden thickness at the deep Herodotus Basin (Fig. 29B) squeezes the MSC sequence towards the ECB westward extension and WEH (Fig. 30). Therefore, the observed deformation in the P5 salt tectonic structural province is attributed primarily to gravity gliding occurring from Nile Delta area towards the deep Herodotus Basin and secondarily to gravity spreading induced by the differential loading of the Plio-Quaternary clastic sediments above the MSC sequence.

C.4.3.6 The chronicle of salt deformation

The area located north of the ECB (P2) is under compressive regime since the Miocene subduction up to the present because of the ongoing continental collision initiated during the Messinian between the ECB and the island of Cyprus (Gao et al., 2020). Therefore, it is proposed that the Messinian evaporites in this area underwent syn-depositional deformation.

In the Western Mediterranean Sea very high, nearly vertical subsidence rates (up to 960 m/Ma) have been computed in areas underly by oceanic crust (Leroux et al., 2015; Rabineau et al., 2014). Similar high vertical subsidence rates are expected in the deep Herodotus Basin. High vertical subsidence rates create a pressure gradient built by the basinward tilting. Immediately after its deposition, the MSC sequence starts to glide northward because of the elevation gradient created by the great difference in subsidence rates between the Nile Delta area and the deep Herodotus Basin. After the deformation, due to gravity gliding, a second phase of deformation is induced by the differential loading of the Plio-Quaternary. Time was needed for the Plio-Quaternary deposits to reach and be deposited in the deep Herodotus Basin, because the Pliocene River Nile had to first fill its Late Messinian canyon with clastic material before building its present Delta. Furthermore, a multi-phase deformation model can justify the structureless seismic stratigraphic structure imaged in the seismic dataset.

In salt tectonic structural province P4 the elevation gradient build by the differential subsidence, because of the difference of the underlying crust nature, in combination with the regional crust tectonics, forced the Messinian salt to glide towards the west. The regional tectonics observed in this salt tectonic structural province is correlated to the north extension of the Rosetta fault which shows sinistral transtension during the Messinian and the Holocene interrupted by Plio-Pleistocene normal slip at the south-eastern margin of the Herodotus Basin (El-Fattah et al., 2021). The MSC deformation probably occurred simultaneously or immediately after the gravity spreading in P5 salt tectonic structural province, but it was less intense, forcing the MSC sequence to be compressed in the western flanks of the WEH.

The most recent and less intensive deformation is observed in the P1 salt tectonic structural province. This deformation is attributed to the Plio-Quaternary reactivity of the Neotethys boundary fault (Gao et al., 2020). The separation of the MSC sequence into

distinct stratigraphic subdivisions is indicative of the weak and relatively recent salt deformation observed in this salt tectonic structural province.

C.4.3.7 The semi-circular bathymetric step around the Eratosthenes Continental Block (ECB)

Seafloor In this section, the role of the ECB carbonate accumulation morphology (Unit 4) to the observed salt-related deformation is discussed. A bathymetric step with a semi-circular shape characterizes the present seafloor morphology around the ECB. However, the seafloor at the western boundary of the ECB lacks a similar morphology (Fig. 30). It is widely accepted that this remarkable semi-circular bathymetric step owes its existence exclusively to compressive-related salt shortening. In particular, the northern flank of the ECB is overthrusted by the MSC sequence that is trying to “escape” from the Cyprus collision zone due to shortening along the plate boundary. Because of this process, MSC deposits were progressively pushed towards the ECB (Reiche et al., 2016). On the other hand, the eastern flank of the ECB is overthrusted by salt derived from the Levantine Basin due to the differential sediment loading at the marginal areas and the westward tilt along the base of the salt (Allen et al., 2016; Gaullier et al., 2000; Reiche et al., 2014). Finally, the southern flank of the ECB is overthrusted by salt derived from the Nile Delta area due to a combination of gravity processes, i.e., gravity spreading and gravity gliding (Gaullier et al., 2000; Loncke et al., 2006; Mascle et al., 2001; 2006). In all cases, the Plio-Quaternary clastic sediments onlapping the ECB acted as a backstop to salt flow, and the semi-circular bathymetric step was essentially formed by relative uplift of the surrounding seafloor. The present dataset clearly shows the formation of this bathymetric step south-west of the ECB (i.e., P3; Figure 23C) where the Plio-Quaternary clastic sediments onlapping the ECB act as a backstop and prevent the salt flow further north.

However, a bathymetric step is clearly absent on the western side of the ECB (Fig. 30). Salt derived from the Nile Delta area meets the topographic buttresses of the ECB and the ECB westward extension and gets severely deformed because of compressional thickening (Figs. 23 and 24). The ECB westward extension prevented the salt from a northward glide and protected the WEsB from thin skin salt-tectonics, while it redirects the salt derived from the Nile Delta area to west towards the Herodotus Basin following the pre-Messinian topography (Fig. 30). Nevertheless, because of gravity spreading that prevails at the deep Herodotus Basin, salt is being pushed towards the western flanks of the WEH. The significant elevation difference (~2 km) along the TS/TES reflector between the deep Herodotus Basin and the WEH acts as a backstop to the MSC sequence moving further east towards the ECB western flanks (Fig. 12). Thus, Messinian salt is forced to move north while doubling its thickness because of compressional thickening. Once is no longer influenced by the gravity spreading occurring at the deep Herodotus Basin and moves further north away from the WEH, the MSC sequence “spreads out” creating an east-west wide compressional domain represented by dense thrust and kink zones (Fig. 27). In summary, the ECB carbonate accumulation (Unit 4) morphology protect the WEsB from thin-skin salt tectonics while it redirects the salt to flow along the western flanks of the WEH towards the deep Herodotus Basin. This process explains the absence of a bathymetric step on the west side of the ECB (Fig. 30).

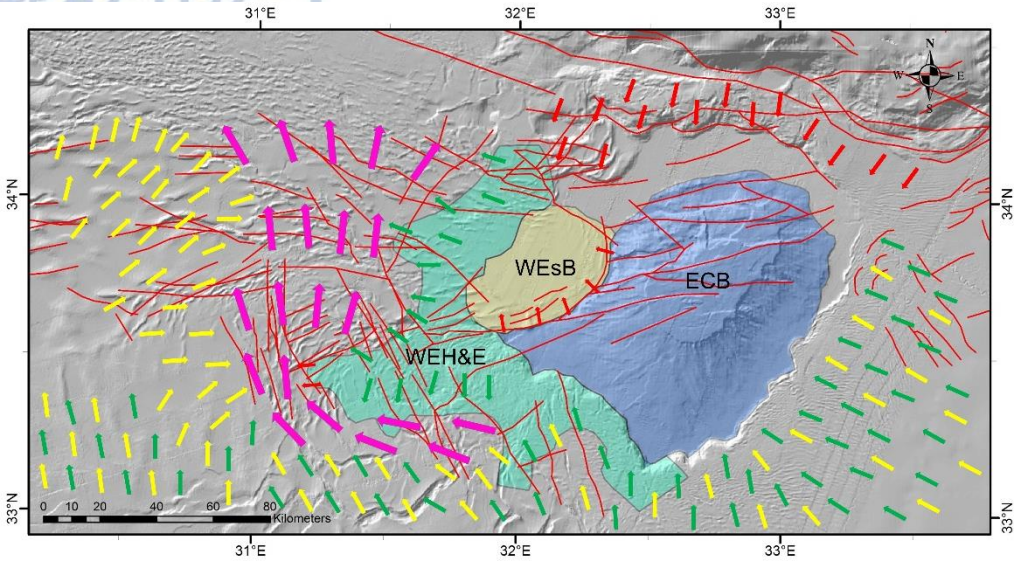

Figure 30: *Hillshade map of the seafloor at the eastern part of the Herodotus Basin showing the main trigger and driving mechanisms of salt flow and overburden deformation. Salt-related deformation due to gravity gliding is shown with green arrows, gravity spreading is shown with yellow arrows and regional tectonics is shown with red arrows. Pink arrows indicate thick deformed salt emerged by a combination of different deformation mechanisms. Gravity spreading is dominant in the deep Herodotus Basin while gravity gliding is dominant around the West Eratosthenes High and the ECB westward extension. Red lines depict the main faults after Montadert et al. (2014). Pink dashed line illustrates the bathymetric step at the seafloor that formed due to the pinch out of the Messinian evaporites. ECB: Eratosthenes Continental Block, WEsB: West Eratosthenes sub-Basin, WEH: West Eratosthenes High.*

.

C.5 Pre-salt clastic systems in the Herodotus Basin

C.5.1 Introduction (deep-sea processes)

Submarine channels act as conduits for sediment transported from continental margins into the deep sea (e.g. Deptuck et al., 2003) and are the central subject of many recent scientific studies (e.g. Catterall et al., 2010; Deptuck et al., 2003; Ducassou et al., 2009; Posamentier and Kolla 2003). Channels and their splay lobes comprise repositories of coarse-grained sediments that are generated through repeated episodes of confining and sorting mechanisms and thus could host economically important hydrocarbon reservoirs. Documentation of the depositional environment and the essential architectural elements of submarine channels provide valuable information on sudden changes in deep-sea processes, which might be directly related to sudden climatic changes, eustatic sea-level changes, changes in sediment source, and sediment supply, and tectonic events. For example, forced regression systems trigger erosional processes that result in the incision and progradation of submarine channels (e.g. Shanmugam 2016).

The Gibraltar Straits were limited in a way that converted the Mediterranean Sea into a semi-closed evaporitic basin 5.97 Ma ago (Manzi et al. 2013). The consequences of the MSC sea-level drop along the margins of the Mediterranean basin have been described in several recent scientific papers that are mainly based on seismic reflection data. For example, seismic surveys in the Eastern Mediterranean focus on the Levantine Basin offshore Israel, Lebanon, Cyprus, Egypt and in the offshore area between Cyprus and Turkey (Aal et al., 2000; Bertoni and Cartwright 2007; Gorini et al., 2015; Güneş et al., 2018; Gvirtzman et al., 2017; Hawie et al., 2013; Jagger et al., 2018; Loncke et al., 2006; Madof et al., 2019; Montadert et al., 2014). In the West Mediterranean, seismic surveys target the Gulf of Lyon, specifically the deposits of the rivers Rhone and Ebro (Bache et al., 2015; Cameselle et al., 2014; Lofi et al., 2005;

Urgeles et al., 2011). Through the study of these seismic surveys, researchers have attempted to understand the pattern of Messinian clastic deposition under the MSC sequence (Bertoni and Cartwright 2007; Lofi et al., 2005). In the deposits of the river Rhone, seismic survey results imply that significant erosion and sedimentation occurred immediately after the main Messinian sea-level drop (Bache et al., 2015) and suggest that large submarine gravity flows occurred before any significant accumulation of salt in the basin, creating fan-shaped Late Messinian deposits in the downstream part of the main Messinian valleys (Lofi et al., 2005). Moreover, studies at the Late Messinian deposits of the river Ebro, show that characteristic features of Late Messinian subaerial incision exist in the Ebro margin (Urgeles et al., 2011) and deltaic sediments of the Messinian Paleo-Ebro River deposited during the Tortonian and initial Late Messinian sea-level drop (Cameselle et al., 2014). In the eastern and western Mediterranean Sea, seismic surveys support the deposition of clastic sediments during the initial falling stage systems tract of MSC included mass transport deposits and forced regressive clinoforms (Bertoni and Cartwright 2007; Gorini et al., 2015). Additionally, the surveys suggest that this stage is characterized by a marked shift in the depocenter towards the deep basins (Gorini et al., 2015).

The MSC regression caused massive erosion of the continental margins of the Mediterranean, producing clastic sediments before, during, and after salt deposition (Aal et al., 2000; Bertoni and Cartwright 2007; Loncke et al., 2006; Madof et al., 2019; Radeff et al., 2017). The Late Messinian Nile canyons are filled with highly reflective clastic sediments referred to as the Abu-Madi Formation (Aal et al., 2000; Madof et al., 2019). This formation was probably deposited during the Messinian and it consists of thick sand bodies interbedded with shale in the onshore and offshore Nile Delta area (Leila et al., 2019; Leila and Moscariello 2019). These clastic sediments were deposited in a complex fluvial-deltaic/subaqueous setting (Loncke et al., 2006).

This chapter focuses on the seismic interpretation of high-quality 2D industrial, multichannel seismic-reflection data, covering the eastern part of the Herodotus Basin. Although it is widely known that the MSC resulted in the massive deposition of thick evaporitic sequences, little is known about the impact of the sea-level drop on the sedimentary processes in the submarine areas. The identification of a submarine clastic system directly underneath the Messinian salt provides a rare opportunity for determining the dominant sedimentary processes during the late Messinian within the Herodotus Basin. Assessment of the paleo-morphology on which the deep-sea fan system developed, in combination with the determination of its architectural characteristics, are the tools for investigating the origin and depositional evolution of the late Messinian submarine clastic system. A comparison between the architectural characteristics of the late Messinian deep-sea fan and the younger Quaternary deep-sea fans is also attempted to achieve a more thorough understading of the nature and the flow behavior of the gravity flows. Finally, this chapter contributes to the discussion about the development of the source-to-sink system of the Nile River during Messinian. This integration is achieved through the correlation of the late Messinian deep-sea fan system with the existing knowledge about the Messinian River Nile drainage system, combined with the detailed scientific works on MSC clastic sequences at the onshore and offshore areas of the Nile Delta (Abdel-Fattah and Slatt 2013; Abdel-Fattah 2014; Leila and Moscariello 2019; Pigott and Abdel-Fattah 2014).

C.5.2 Late Messinian paleo-bathymetric characteristics and seismic facies

Based on the seismic interpretation (Fig. 18), the BS/BES has a maximum elevation over the westward extension of the ECB (Fig. 31) and a minimum elevation towards the Herodotus basin. In the area of the WEsB, flat topography of the BS/BES is observed (Fig. 31). West of the ECB westward extension, the surface of the BS/BES displays intense

topography, fluctuating between 5 and 6.5 km. This topography was created by basement tectonics (Fig. 31) and resulted in topographic lows. Two prominent topographic lows are noted at the east and west side of the study area. The first topographic low (Fig. 31) is located to the east side of the study area and is characterized by a topography that was divided into smaller individual basins. The second topographic low (Fig. 31) is located at the west side of the study area and is characterized by smoother topography down-stepping towards the Herodotus basin. Corridors 1A and 2A represent the most confined parts (5 – 15 km wide) of the topographic lows, whereas corridors 1B and 2B are indicative of the wider (15 – 30 km wide) basin wards parts of the lows that eventually end to the north at the late Messinian basin floor.

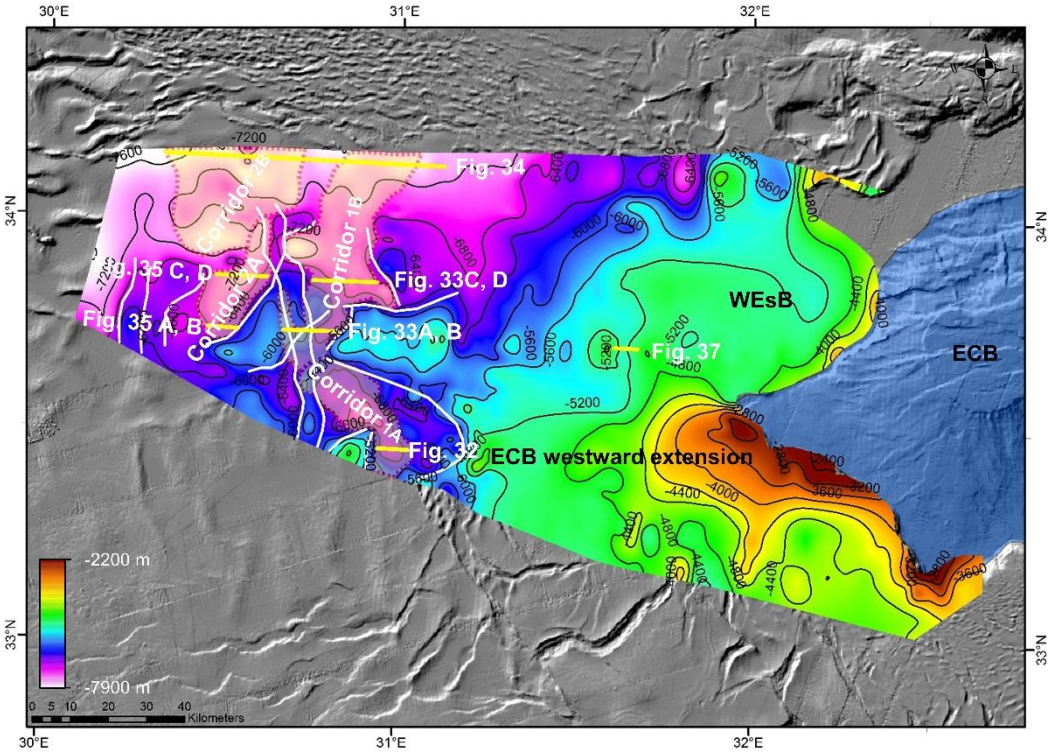

Figure 31: *Map of the Bottom Surface/Bottom Erosion Surface in meters (Fig. 18) illustrates the West Eratosthenes sub-basin where flat topography is observed, the Eratosthenes Continental Block westward extension, and the topographic lows located east and west of the study area. The east topographic low is subdivided into corridors 1A and 1B delineated by the red dashed lines. The west topographic low is subdivided into corridors 2A and 2B delineated by the red dashed lines. Figure 31 also illustrates the main faults (white lines) that define the topographic lows. Yellow lines represent time seismic cross-sections presented in chapters 5.2.1 and 5.2.2. Contour interval 400 m.*

Mid to high amplitude, high-frequency seismic reflections, moderately deformed by post-depositional tectonics (Fig.31) characterize the infill of both topographic lows just beneath the MSC evaporitic sequence (Figs. 32, 33, 34, and 35). The base of the mid to high amplitude, high-frequency seismic reflections in the confined (5 – 15 km wide) corridors 1A and 2A is erosional, truncating into the underlying seismic packages that comprise parallel to sub-parallel, low frequency, discontinuous to continuous, low amplitude reflections (Unit 3) (Figs. 32, 33A-B, and 35). The top surface of the mid to high amplitude, high-frequency seismic reflections is mapped as the first continuous high amplitude reflection beneath the chaotic low to high amplitude low-frequency reflections of the intra-salt deposits of the MSC sequence. The chaotic low to high amplitude low-frequency reflections of the intra-salt deposits can be traced lengthwise above the mid to high-amplitude, high-frequency, seismic reflections. Discontinuous to incoherent, mid to high-amplitude reflections characterize the seismic packages in its confined segments (Figs. 32, 33A-B, and 35). Large-scale erosional surfaces are also identified by the sudden termination of seismic reflections within the mid to high amplitude, high-frequency seismic packages, and they are interpreted to represent discrete phases of sediment bypass and deposition. Onlapping of internal seismic reflections on these erosional surfaces is common. Small-scale (20 – 100 ms and 200 – 700 m wide) v- to u-shaped erosional surfaces are also observed. Such seismic facies are identical to channel fairway facies described by Eldrett et al. (2015) from the Paleocene deep-sea fan formations in the Central North Sea.

On the other hand, the base of the mid to high amplitude, high frequency reflectionsis conformably sitting on the underlying formations in the unconfined (> 35 km wide) corridors 1B and 2B. Continuous to discontinuous, mid to high-amplitude reflections, exhibiting a bidirectional (east and west) downlap relationship with the base of the mid to high amplitude, high frequency packages and comprise the main seismic facies in this unconfined part (Figs.

33C-D and 34). Onlap between the internal reflections is also observed and is used as a criterion for the discrimination of the mid to high amplitude, high frequency reflections into several depositional packages. The top of the mid to high amplitude, high frequency reflections is convex, forming lobe-like morphology. Such seismic facies are characteristic of submarine lobe complexes (e.g.Eldrett et al., 2015).

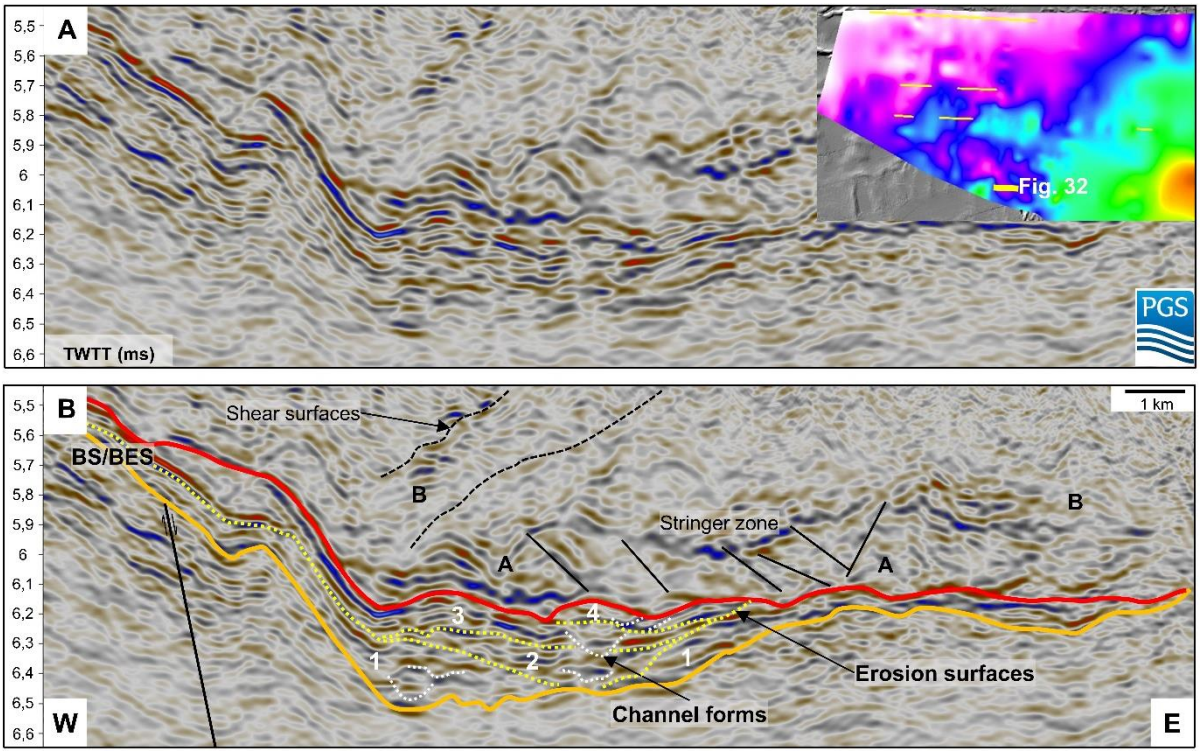

Figure 32: *Architectural style of the clastic deposits. Uninterpreted (A) and interpreted (B) time seismic cross-section across the corridor 1A indicating the seismic facies, erosional fairway (orange line), internal erosion surfaces (dotted yellow lines), top surface (red line), channel forms, and intra-salt deposits with internal shear surfaces and stringer zones. The erosional fairway truncates the underlying package of sub-parallel, continuous low amplitude reflections. Vertical exaggeration 3.5:1 based on estimated average interval velocities of ~2800 m/sec. For location see Figure 31.*

C.5.2.1 Depositional characterization of the late Messinian clastic systems

Two-channel fairways, the eastern (corridor 1A) and western (corridor 2A) are identified (Fig. 36), which feed two coalescing lobe complex systems on the deep unconfined Herodotus basin floor (Figs. 33C-D and 34). The maximum thickness of the eastern channel fairway is 300 ms (TWTT). Four units of seismic facies, separated by discrete erosional

surfaces and exhibiting large lateral offset with limited aggradation, comprise this fairway (Figs. 32 and 33A-B). The large lateral offset of these facies, combined with the absence of any well-developed overbank deposits, suggests the presence of winged channels, which are characteristic of sand-rich deep-sea fans (Hubbard et al., 2014). The thickness of the clastic systems decreases to less than 100m at the distal northern lobe complex (Figs. 34 and 36).

At the proximal area of corridor 1B, the channel fairways are separated into two branches (Fig. 33B). The seismic facies in the eastern branch are consistent with those of a channel complex, and thus, they are interpreted to represent deposits of the main channel fairway. Two internal erosional surfaces within the main fairway divide the channel complex system into three seismic facies units, which can be correlated to the seismic facies units observed in the upstream profile of corridor 1A in Figure 32. The western branch consists of lenticular, medium to high amplitude discontinuous reflections, which are more consistent with those of a proximal lobe system. The western branch is interpreted as splay lobe deposits, resulting from westward spill-over of gravity flows from the main fairway.

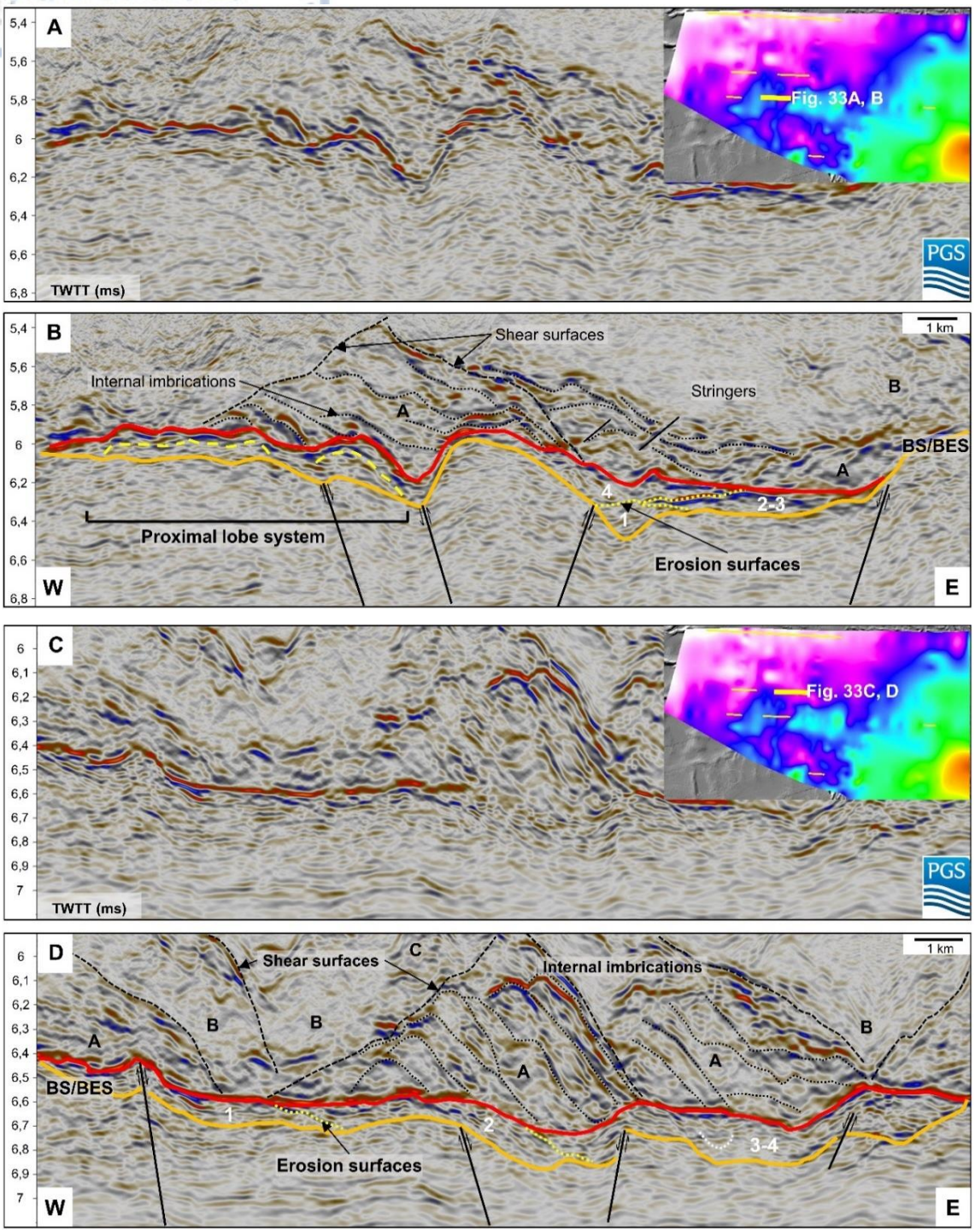

Figure 33: *Architectural style of the east clastic system located in corridor 1B. Uninterpreted (A) and interpreted (B) time seismic cross-section across the proximal area of corridor 1B. The proximal lobe system is distinguished by the lenticular geometries. Uninterpreted (C) and interpreted (D) time seismic cross-section across corridor 1B. The spread out of the clastic system is distinguished. Both images indicate the seismic facies, erosional fairway (orange line), internal erosion surfaces (dotted yellow lines), the top surface (red line), channel forms, and intra-salt deposits (with internal shear surfaces, internal imbrications, and stringer zones). Vertical exaggeration 3.5:1 based on estimated average interval velocities of ~2800 m/sec. For location see Figure 31.*

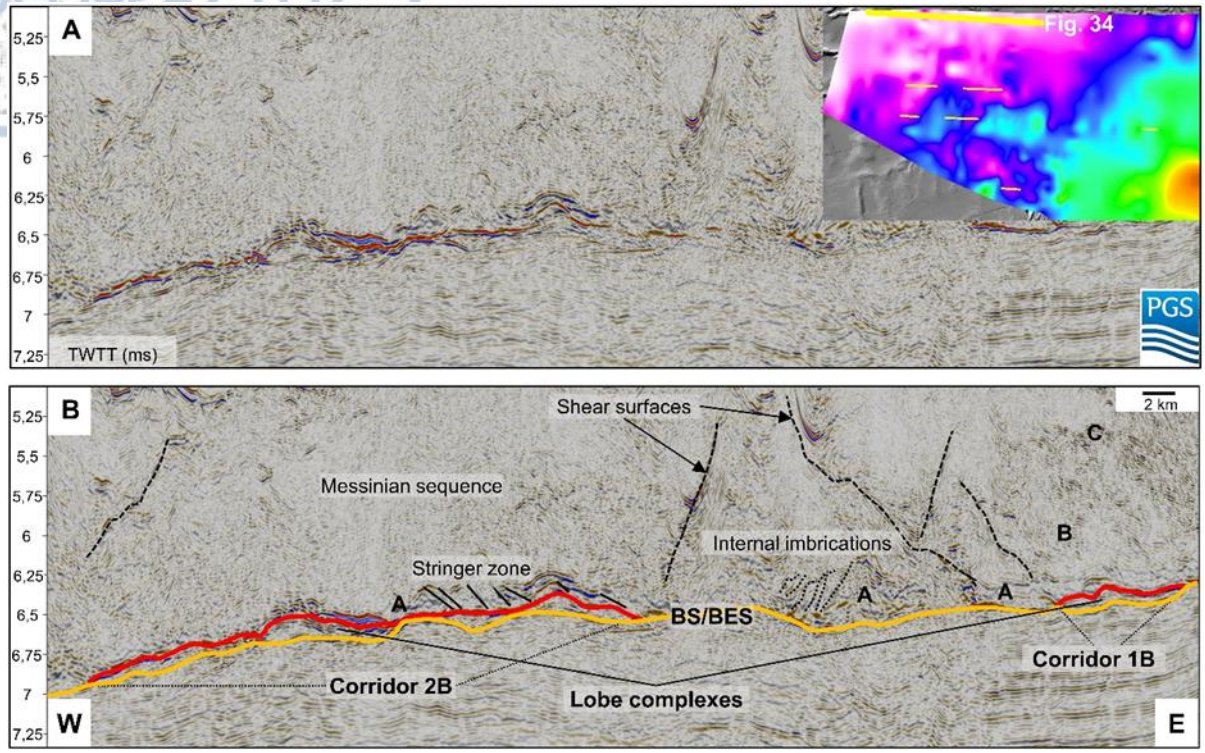

Figure34: *Architectural style of the lobe complexes located in corridors 1B and 2B. Uninterpreted (A) and interpreted (B) time seismic cross-section across the lobe complexes in the deep Herodotus basin indicating the base (orange line) and the top surface (red line) of the lobe complexes and the MSC sequence intra-salt deposits (with internal shear surfaces, internal imbrications, and stringer zones). The lobe complexes are characterized by semi-lenticular high to medium amplitude reflections located at the base of the MSC sequence. Vertical exaggeration 7:1 based on estimated average interval velocities of ~2800 m/sec. For location see Figure 31.*

Similarly, the western channel fairway (corridor 2A) consists of three seismic facies units of large lateral offset and limited aggradation (Fig. 35). The base of the seismic facies is erosional, deeply cutting into the underlying strata and each other. In the unconfined corridors 1B and 2B at the basin floor, there is a distinct spread out of the clastic system, which consists of successive lobate seismic-facies units, characteristic of a lobe complex system. The thickness of the lobe complex system ranges from 100 to 200 ms TWTT. Overall, the width of the late Messinian deep-sea fan increases from about 11 km in the confined channel fairways to the south to more than 30 km at the northern lobe complex system (Fig. 36).

The location of the lobe complexes at the northern boundaries of the study area, being fed by channel fairways to the south (Fig 36), indicate a southern sediment source, adjacent to the location of the present-day Nile River Delta.

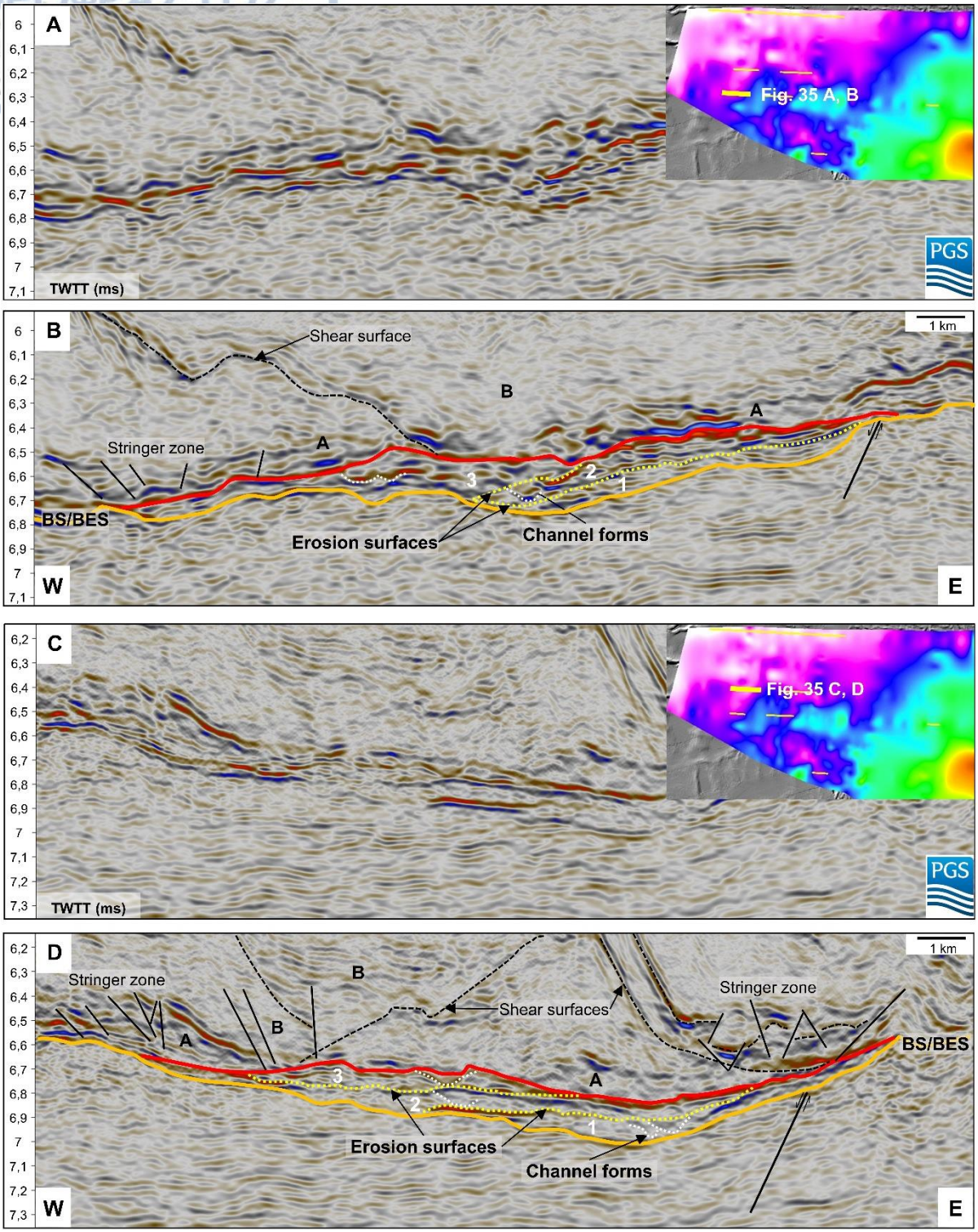

Figure 35: *Architectural style of the West clastic system located in corridor 2A. Uninterpreted (A, C) and interpreted (B, D) time seismic cross-sections across the area of corridor 2A indicating the seismic facies, erosional fairway (orange line), internal erosion surfaces (dotted yellow lines), top surface (red line), channel forms and intra-salt deposits (with internal shear surfaces and stringer zones). The confined erosional fairway with slightly concave-up cross-sectional geometry and limited aggradational architecture is distinguished. Vertical exaggeration 3.5:1 based on estimated average interval velocities of ~2800 m/sec. For location see Figure 31.*

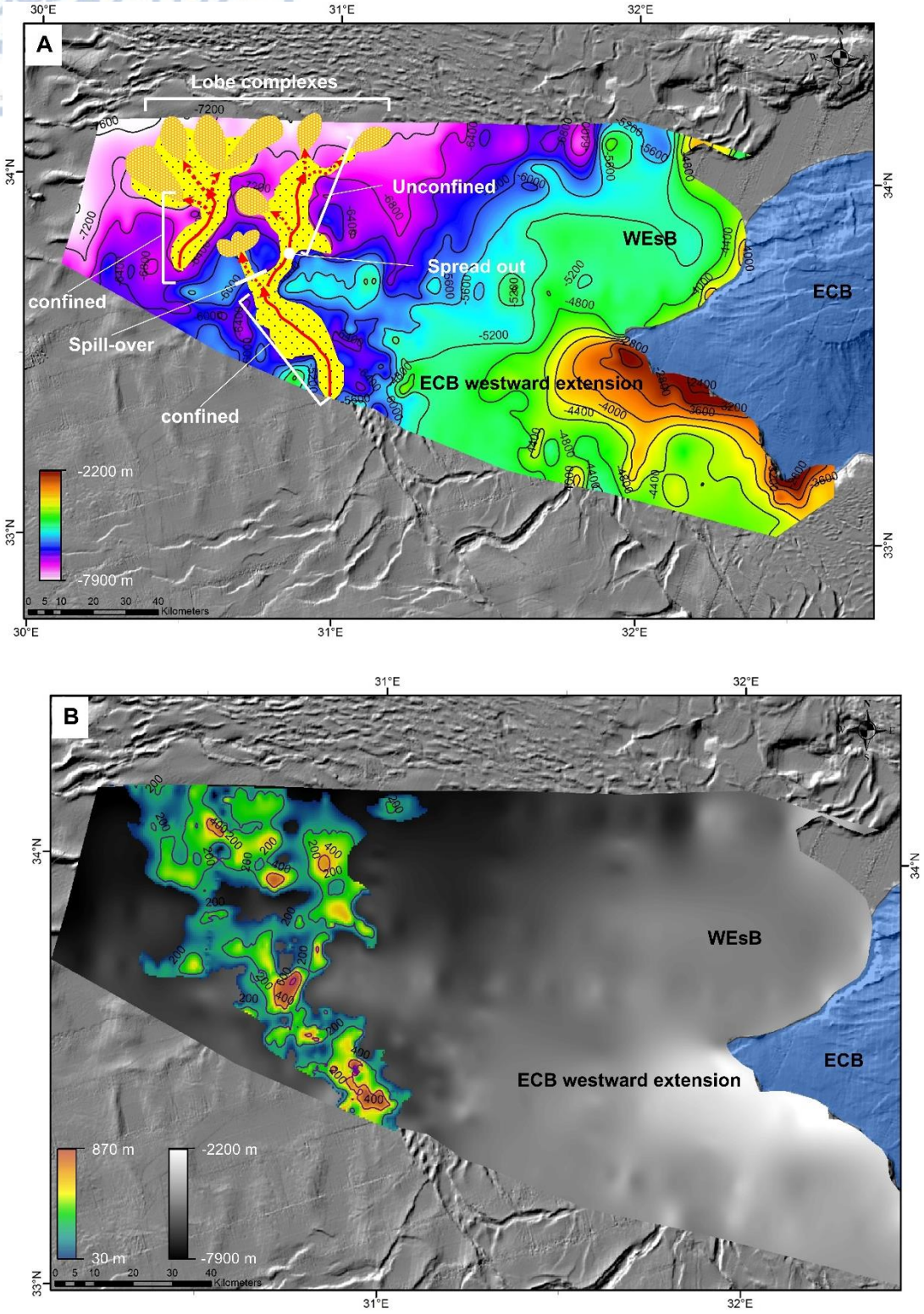

Figure 36: *A) Map of the Bottom Surface/Bottom Erosion Surface (in meters) depicts the general distribution of the clastic systems. Contour interval 400 m B) Bottom Surface/Bottom Erosion surface (in meters) in gray scale and isopach map (in meters) in the color scale of the clastic systems described in this study. The maximum thicknesses of the clastic systems are observed in the proximal area of corridor 1A and at the lobe complex located in corridor 2B.*

C.5.2.2 Plio-Quaternary channel complex sets

An example of a characteristic Plio-Quaternary channel complex set (CCS) is shown in Figure 37. The CCS consists of channel complexes (CCs), comprised of well-defined channel forms and overbank deposits (inner and outer levees). Channel forms within the CCs and the CCs exhibit an aggradational architecture with limited lateral migration. The entire CCS has a thickness of 300 ms TWTT. The surfaces separating the CCs are only erosional at their central parts (around the thalweg of the channels) and conformable under the outer levees.

Medium to high-amplitude high-frequency reflections are believed to correspond to coarse-grained sediments deposited along the channel axis. These reflections are interpreted following the suggestions of Deptuck et al. (2003) into three types: 1) discontinuous and chaotic reflections (D-C); 2) continuous and parallel reflections (C-P); 3) channel forms reflections (CF).

1. Basal D-C reflections overlay the erosional fairway of the Plio-Quaternary CCS and probably represent coarse-grained lithologies deposited by turbidity currents that bypass the clastic system. Such deposits originate from the vertical aggradation of sinuous channels.
2. C-P reflections suggest a sinuous plan-form geometry and represent channel-floor deposits consisting of stacked continuous horizons without lateral offsets. This morphology implies limited lateral migration during aggradation. C-P reflections are generally included within CF reflections.
3. CF reflections are interpreted as partially filled second-order incisions situated within U or V-shaped erosional surfaces that truncate underlying reflections. The characteristic U and V shapes are the result of intense contrast between the deposits that have eroded from

turbidity currents at the base and sidewalls of the channel and the younger deposits that have filled the channel.

Five internal erosional surfaces have been identified in the seismic cross-section, creating six-channel complexes with well-delineated aggradational morphology. The lowest channel complex is located immediately above the basal erosional fairway and comprised of D-C reflections, each ~25 ms thick. The five overlying channel complexes have an individual average thickness of about ~50 ms and consist of combinations of CF and C-P reflections. The identification of inner and outer levees (overbank deposits) is possible, represented by parallel to sub-parallel seismic facies of low to medium amplitude.

Submarine channels with similar architectural characteristics have also been observed in the late Quaternary stratigraphic interval offshore Nile River Delta (Ducassou et al., 2009; Catterall et al., 2010; Migeon et al., 2010). Such characteristics are typical of mud-rich deep-sea fans, the flows of which contain sufficient amounts of fines that allow for the construction of channel levees (Deptuck et al., 2003; 2007; Kolla et al., 2007; Posamentier et al., 2007).

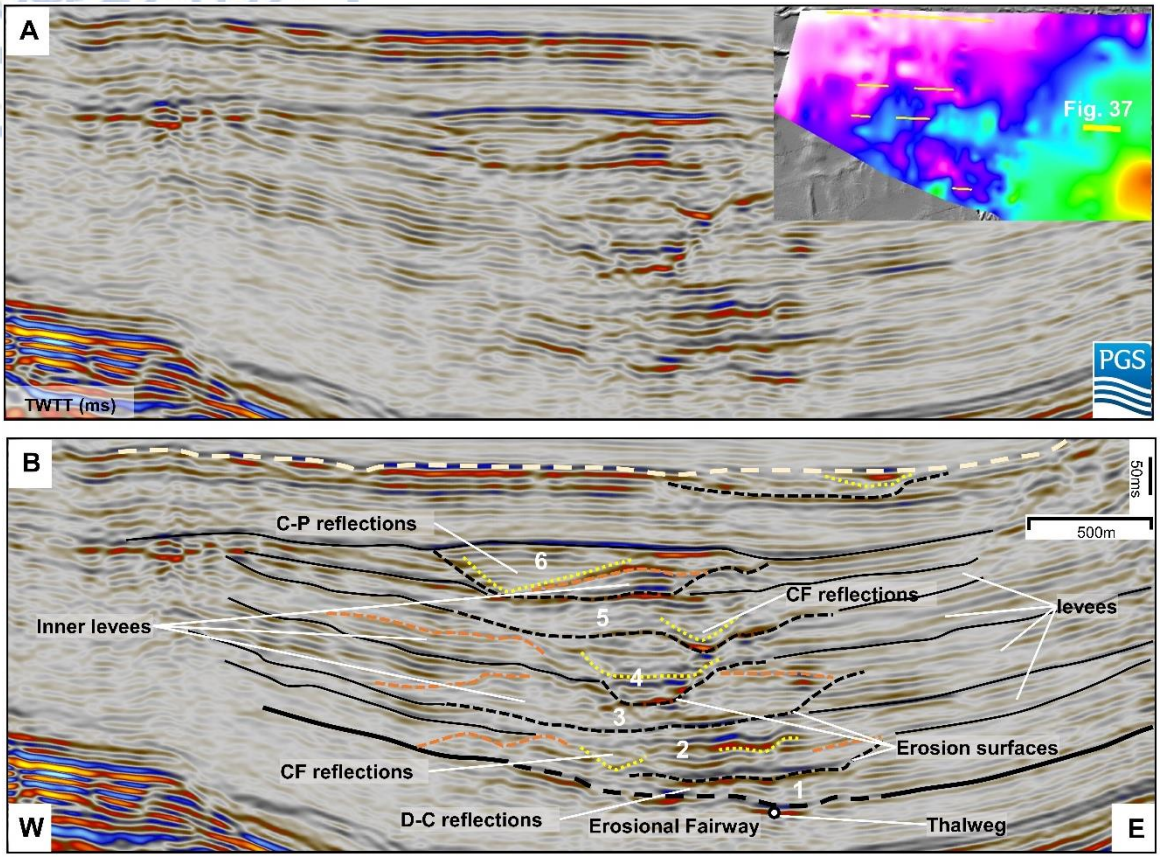

Figure 37: *Architectural style of Plio-Quaternary channel complex set. Uninterpreted (A) and interpreted (B) time seismic cross-section indicating the seismic facies, erosional fairway, top surface, inner and outer levees, and channel forms reflections. Plio-Quaternary CCS is characterized by its limited lateral size, strong vertical aggradation, and clear boundaries of inner and outer levees. Vertical exaggeration 3:1 based on estimated average interval velocities of ~2000 m/sec. For location see Figure 31.*

C.5.3 Discussion of seismic interpretation

C.5.3.1 Late Messinian clastic systems: sediment source and potential origin

The mid to high amplitude, high-frequency seismic reflections are interpreted as late Messinian clastic deposits due to their seismic stratigraphic emplacement. The exclusive development of these clastic accumulations within the eastern and western topographic lows suggests that they have acted as pathways for sediments to the deeper parts of the Herodotus Basin. A marine environment of deposition is presumed as the identified late Messinian clastic deposits are topped by the MSC evaporitic sequence. Seismic facies distribution of the late Messinian clastic systems (Fig. 36) clearly shows that the sediment source was located in

the south, through the two identified channel fairways. The Abu Madi Formation consists of sand-dominated fluvio-deltaic deposits, which developed at the mouth of a terrestrial, late MSC canyon system (Leila et al., 2019; Leila and Moscariello 2019). The location of the identified clastic systems immediately to the north of the age-equivalent Abu Madi Formation indicates that it represents its offshore extension (Fig. 38). More specifically, the observed clastic systems are considered as time equivalent to the Abu Madi Formations lower and middle units. The lower unit is represented by multiple erosional surfaces formed by bypassing fluvial discharges and landslides created by the instability of the canyon walls (Leila and Moscariello 2019) (Figs 38 and 39a, B). The middle unit consists of fluvial systems that have contributed to the formation of thick fluvio-deltaic deposits. The lower part of this unit is attributed to increased hydrodynamic energy events with increased sediment supply by MSC regression. The upper part of this unit is dominated by estuarine facies indicative of a more transgressive sedimentary setting (Leila and Moscariello 2019). Therefore, gravity flows either from hyperpycnal flows or sediment instabilities on the lowstand delta edge would have been generated from both lower and middle Abu Madi formation units. The sand-rich nature of the understudy clastic systems, based on the large lateral offset and limited aggradation of its channel complexes (Figs. 32, 33, 34, and 35), supports the linkage between the two clastic systems.

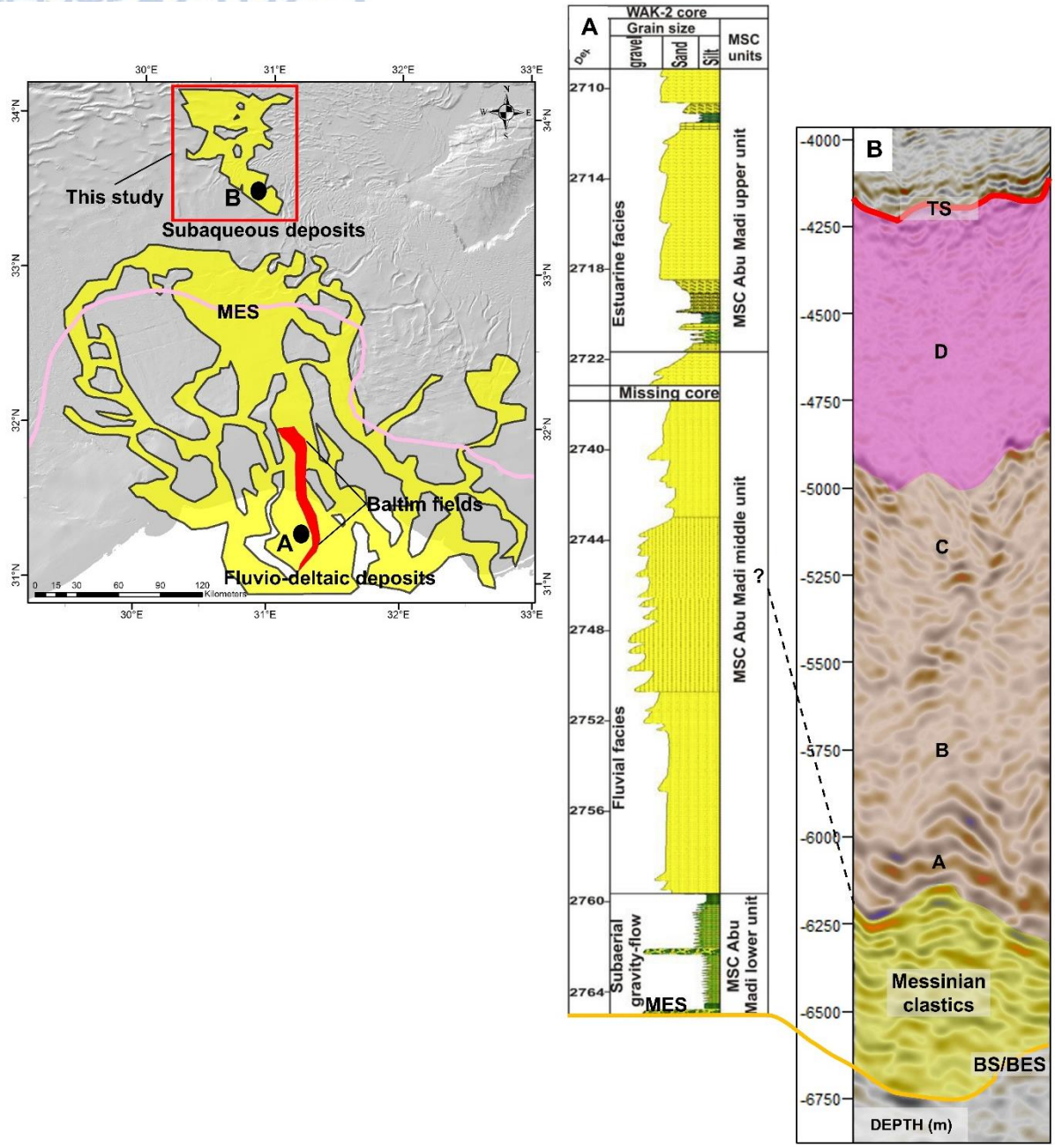

Figure 38: *The map illustrates the distribution of the Abu Madi Formation based on the results of the present study (Modified after Aal et al., 2000; Loncke et al., 2006; Madof et al., 2019). The pink line represents the boundary of the Margin Erosion Surface (MES) described by Loncke et al. (2006). A) Stratigraphic column in meters represents Abu Madi Formation sedimentary facies of the onshore Nile Delta area published in Leila and Moscariello (2019). B) Seismic illustration of age-equivalent deep-water sediments in the Herodotus Basin and correlation with the Abu Madi Formation sedimentary facies.*

On the other hand, Plio-Quaternary submarine channel complexes of the Nile River are of much smaller dimensions, aggradational and meandering (compare Fig. 37 with Figs. 32 and 35) with well-developed levees (Catterall et al., 2010; Ducassou et al., 2009; Migeon et al., 2010), which are typical features of mud-rich deep-sea fans (Reading, 2009). There are

several explanations for the discrepancy between the sand-rich late Messinian clastic systems and mud-rich Plio-Quaternary deep-sea fans. The most dominant are: 1) the enormous drawdown of the sea-level during the MSC and its impact on the drainage areas and erosional processes, 2) the different climatic conditions prevailing in the Nile drainage area during the MSC, and 3) the sediment source/provenance.

Base level change due to the enormous sea-level drop during the MSC (>1000 m) (Barber 1981; Gargani and Rigollet 2007; Urgeles et al., 2011) led to the formation of Nile canyons onshore (Said 1981). Rivers eroded into their riverbeds to attain an equilibrium profile as base-level drops. The result of the MSC forced regression was to enhance erosion from the Nile River that led to the development of an extensive low-stand delta (Abu Madi Formation). River discharges with high suspended load concentration likely have resulted in numerous hyperpycnal flows (Mulder et al., 2003), which explain the occurrence of the more extensive (higher energy), sand-rich late Messinian clastic systems identified in this study. In addition, sediment instability processes at the delta edge would have triggered multiple sediment failures, which through flow transformation processes would have evolved into sand-rich gravity flows (Tripsanas et al., 2008).

As it was indicated in chapter 2.4, the climate of the Eastern Mediterranean during the Messinian was not very different from today; all geological evidence show a sub-arid climate (Gladstone et al., 2007). The climate of North Africa, however, did not resemble the modern super-arid climate. Climate models (Gladstone et al., 2007) suggest a subtropical climate and support the estimates derived from geological data indicating a significant amount of precipitation (1200-1500 mm/year according to Issawi and Osman 2008) in the area of North Africa during Messinian. These climatic conditions in North Africa increased the strength of hydrodynamic energy events that controlled canyon incision within the Late Messinian Nile. Such riverine hydrodynamic conditions probably have resulted (through hyperpycnal flows

and slope instabilities at the delta edge) in the formation of massive, high-energy gravity flows that contributed to the formation of the late Messinian clastic systems.

As stated in chapter 2.5 the main sediment sources of the Late Messinian River Nile were the Red Sea rift shoulders and the outcrops of the Nubia sandstone located in Southern Egypt and Sudan (Macgregor 2012). According to Macgregor (2012), the Red Sea rift shoulders had the largest contribution of sand-prone clastic sediments originate mainly from the erosion of granitic material. The average erosion of the Red Sea rift shoulders was of the order of 1200-1500m (total denudation) (Macgregor 2012). During the initial stage of the MSC, the river Nile erodes the already well-sorted pre-Messinian clastic formations located at the Messinian Delta (Barber 1981; Pigott and Abdel 2014). The MSC sea-level drawdown adds a new sediment source because the Late Messinian River Nile had to rework and transfer additional clastic sediment volumes from the proto-delta area to the Late Messinian lowstand delta. Therefore, well-sorted sediments added in an already sand-prone riverine system during the incision process, resulting in massive sand discharge towards the deep Herodotus basin.

C.5.3.2 Conceptual sedimentological model of late Messinian deep-sea fan

The pre-MSC Qawasim Formation (Fig. 39a, A) constitutes parallel oblique seismic facies interpreted as a northward prograding deltaic system (Leila et al., 2019; Leila and Moscariello 2019). This formation is separated into five sedimentary facies (from bottom to top): prodelta, distal sand bars, subaqueous distributary channel, distributary mouthbar, and subaerial distributary channels (Leila and Moscariello 2019). In general, deposits in this formation coarsen upwards. The Abu Madi Formation represents the MSC deposits of the Nile canyon at the onshore and offshore areas of the Delta (Aal et al., 2000; Leila et al., 2019; Leila and Moscariello 2019; Farouk et al., 2014), described in detail by Leila and Moscariello

(2019) using 2D-3D seismic, log, well, and core data. The Abu Madi Formation is subdivided into three units (lower, middle, and upper) and five sedimentary facies associations (from bottom to top): subaerial gravity-flow, fluvial channel-fill, tidally influenced fluvial channel, tidal sand bars, and tidal flat (Leila and Moscariello 2019). Pigott and Abdel (2014) suggest that while the Qawasim Formation responds to the global sea-level changes, the Abu Madi Formation does not. The regression on the Qawasim Formation is demonstrated by the presence of fluvial terraces comprised of lateral accretionary units; these formed in response to the slow decline of the global sea level and shale channel fill during the global sea-level rise (Pigott and Abdel 2014). On the contrary, the regression channels of the Abu Madi Formation are represented by incised valley fluvial channels in response to MSC sea-level fall, as the Mediterranean became restricted, and finally covered by a rapid transgression because of the Zanclean reflooding (Pigott and Abdel 2014). Researchers also suggest that Abu Madi is the one that erodes the deposits of the Qawasim Formation and represents the Messinian deposition in incised valley fluvial channels (Leila and Moscariello 2019; Pigott and Abdel 2014; Teama et al., 2017).

The results of the 2D seismic line interpretation of the present study, integrated with published seismic, well and core analysis data from the onshore and offshore area of the Nile Delta (Abdel-Fattah and Slatt 2013; Abdel-Fattah 2014; Leila and Moscariello 2019; Pigott and Abdel-Fattah 2014) led to the construction of a conceptual model for the study area (Fig. 39).

The model begins from the last highstand during the deposition of the Qawasim Formation in a meandering fluvial environment (Leila and Moscariello 2019) and before the onset of the Messinian event (Fig. 39a, A). During the first stage of sea-level fall and before any salt precipitation occurs in the deep Herodotus basin, the Nile begins to incise its flood plain eroding the well-sorted pre-MSC Qawasim Formation (Leila and Moscariello 2019)

(Fig. 39a, B). Concurrent with the erosion of the Qawasim Formation, the MSC Nile transported sand-prone sediments from the Nubia sandstone outcrops and the Red Sea rift shoulders (Macgregor 2012). As sea-level gradually fell, erosion continued inside the MSC Nile canyon, and a new low-stand Delta formed on a steeper seafloor. The deposits of the low-stand Delta are represented by the fluvial deposits of the Abu Madi Formation of the Baltim fields (Abdel-Fattah and Slatt 2013; Abdel-Fattah 2014) (Fig. 38), located today in the offshore area of the Nile Delta (Figs. 38 and 39a, B). In front of the main fluvial channels of the low-stand Delta, sediment flows were generated from the collapse of the unstable newly created sand-rich slopes and the episodes of increased hydrodynamic energy events due to the subtropical (wetter) climate (Fig. 39a, B). The late Messinian clastic system identified in this study is age equivalent to the Abu Madi Formation and is interpreted to be deposited as a deep-sea fan system in front of a major fluviatile canyon. During the continuation of the MSC sea-level low-stand, the Nile River reached an equilibrium profile, ceased to incise, and the Messinian canyon filled with sand-prone clastic sediments (Leila and Moscariello 2019) (Fig. 39b, C). In the deep Herodotus basin, the massive halite precipitation took place coeval with clastic deposition. The conceptual model concludes with the restoration of normal marine conditions (Zanclean reflooding) and the deposition of Plio-Quaternary clastic sediments above the MSC sequence (Fig. 39b, D). Plio-Quaternary northward salt gliding from the offshore Nile Delta area to the deep Herodotus basin is delineated in Figure 39b, D. The conceptual model implies that the medium to high amplitude reflections interpreted as clastic systems were deposited during the onset of the MSC restriction and are correlated with the sand reservoirs of the Abu Madi Formation, both onshore and offshore of the Nile Delta area (Figs. 39a, B and 39b, C).

A long-distance conceptual correlation of age-equivalent units developed in very different sedimentary environments is allowed (between the Abu Madi Formation and the late

Messinian clastic systems) based on 1) the seismic interpretation of the high-quality 2D seismic data, 2) the overall depositional and geometric characteristics of the late Messinian mid to high amplitude, high-frequency reflections, 3) the to date scientific knowledge about the Messinian forced regression, 4) the Messinian River Nile sediment source, sediment supply, and sediment distribution and 5)the climatic conditions prevailing during the Messinian at northeast Africa. An updated map of the Abu Madi Formation distribution (which also represents the MSC Margin Erosion Surface and Bottom Erosion Surface) is provided in Figure 38. Unfortunately, the long-distance conceptual correlation shown schematically in Figure 38 is achieved without the benefits of well data. Future exploration wells in the area will lead to reconsideration and revaluation of the present conceptual model.

C.5.3.3 Hydrocarbon potential

Gas-producing wells indicate that Abu Madi fluvial channels are good sand reservoirs with an essential charging potential (Mahmoud et al., 2017; Pigott and Abdel-Fattah 2014). The thickness of these reservoir targets increases to the North and extends offshore towards the Egyptian NEMED block (Sarhan 2015). Distal turbidite reservoirs can spread several kilometers beyond Egyptian waters, correspondingly to the Niger turbidite system, which exhibits a very similar sediment supply pattern to the Nile (Macgregor 2012). The late Messinian clastic systems probably represent age-equivalent sands to the fluvio-deltaic deposits of the Abu Madi Formation located offshore and onshore of the Nile Delta region. Late Messinian sands deposited as turbiditic currents several kilometers beyond the major fluviatile Late Messinian Nile canyons may have similar petrophysical and reservoir properties.

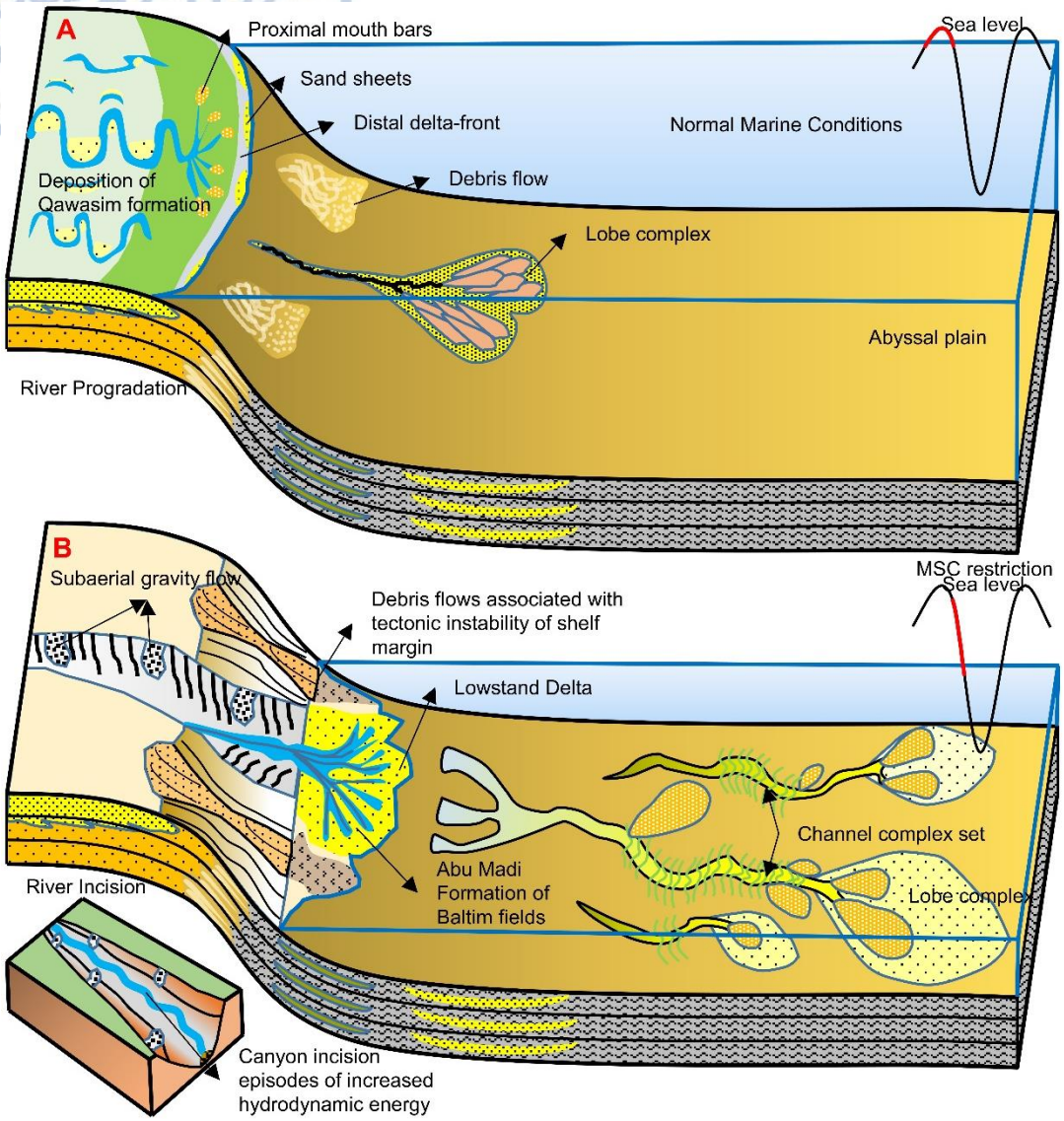

Figure 39a: *Conceptual model of the study area. A) Highstand deposits of the Qawasim Formation in meandering fluvial environment during river progradation B) MSC onset, drop off the base level, canyon incision, and deposition of Abu Madi formation in a fluvial environment. Abu Madi Formation of the Baltim fields is today located at the offshore area of the Nile Delta and is represented by fluvial sands. This period corresponds to the deposition of the Messinian clastic systems, taking place in front of the main fluvial channels of the low-stand Delta. In the Messinian canyon, erosion prevails.*

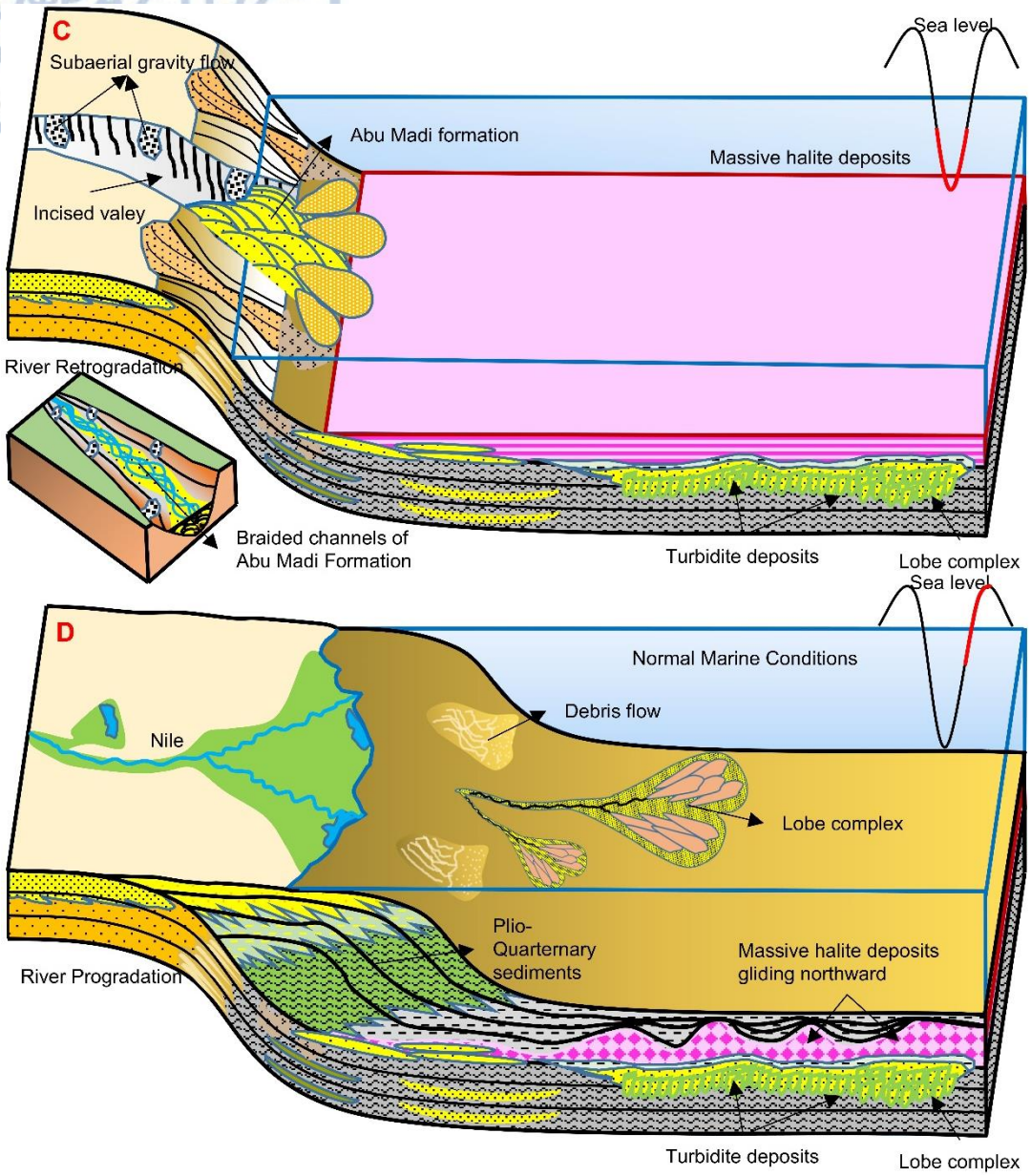

Figure 39b: *C) Lowstand during the Messinian, massive halite precipitation, intra-salt clastic deposition, and river retrogradation. Deposition of Abu Madi formation in braided fluvial channels inside the Messinian canyon, located today in the onshore area of the Nile Delta. D) Rising sea level, river progradation, and deposition of Plio-Quaternary clastic sediments over the MSC sequence. Northward gliding of the MSC sequence observed over the Messinian clastic systems.*

C.5.4 Implication of clastic sediment presence for a possible Messinian Salinity Crisis scenario

The MSC is still a highly debated geological event that happened under very complex physicochemical conditions. The timing and depositional environment of the Messinian evaporite is disputed among researchers. A classic example of an ongoing disagreement relating to the time of deposition is the work of Manzi et al., (2018) that supports the diachronous deposition scenario of evaporites in deep and peripheral basins when at the same time Meilijson et al. (2018) supports the synchronous deposition scenario. Research by both teams used borehole and core data available from the same region (the Levantine Basin), and yet their results strongly disagree. Many scenarios have been proposed to explain the MSC sea-level drawdown, fluctuating in a range between 200 m (Roveri et al., 2014b) and 2500 m (Gargani and Rigollet 2007). Most researchers agree with a deep-basin, deep-water scenario with the disagreements being limited to the variations of the sea level. The depth migrated seismic lines reveal a thick Messinian clastic section deposited in the deepest parts of the Herodotus basin before massive halite precipitation. A certain amount of time for the transportation and deposition of these clastic accumulations was needed. If a synchronous deposition scenario is applied, the deposition of the Late Messinian clastic sediments would have not been possible, unless the clastic accumulations appear sandwiched between salt layers analogous to the WEsB A-B-C stratigraphic subdivisions. Therefore, a diachronous scenario is adopted in this study to justify the presence of clastic accumulations at the base of the MSC sequence.

In this research, a hybrid scenario is proposed based on the 2D seismic data set. This scenario begins with the deposition of anhydrite only at peripheral basins, parallel with the deposition of high organic material at the deeper areas of the basin. The first stage (step 1, Fig. 4) has a duration of 370 thousand years (5.97-5.6 Ma) and is well documented (Roveri et

al., 2014a) at the peripheral basins (PLG deposition) by 87Sr/86Sr data. At the deeper areas of the basin, new data derived from industrial boreholes indicate that the first stage is represented from a foraminifer barren interval (FBI) (Manzi et al., 2018). This FBI is found only in the deepest areas of the Levantine Basin and its thickness is significantly reduced as it approaches the Israeli margin until it disappears. In the first stage, only a very limited drop of sea level was observed. A new alternative interpretation concerning the erosion of the Messinian margins during MSC has been proposed by Roveri et al. (2014b) following a series of isotopic stratigraphy research articles related to MSC (Roveri et al., 2014a). This scenario supports a subaqueous erosion of the Messinian margins proposing an additional important mechanism that leads to the creation of the Messinian canyons. This mechanism is named Dense Shelf Water Cascading (DSWC) and is applicable in case of moderate sea-level fall. This hypothesis justifies many geological forms; however, it could not be considered as the only process responsible for the development of the Late Messinian erosion. The first stage probably represents the interval where the mechanism of (DSWC) (Roveri et al., 2014b) “builds” the Messinian brines (that cause anoxia) at the deeper areas of the basin. The characteristic Messinian Erosion Surfaces (MES) and canyons’ formation across the Mediterranean margins may be a result of the DSWC mechanism.

The second stage (step 2, Fig. 4) lasted for fifty thousand years (5.6-5.55 Ma) and is closely linked to massive halite precipitation due to the limited connection with the Atlantic Ocean (Krijgsman and Meijer 2008; Manzi et al., 2018; Rohling et al., 2008). At the beginning of the second stage, the DSWC mechanism weakens as the brine at the deepest areas reaches saturation. Massive halite precipitation begins at a deep setting in parallel with a moderate sea level draw down as described by Roveri et al., (2016). An enormous sea-level drawdown (about 1.3 km-1.8 km) explains the incision of the great Late Messinian Nile canyon described by Said (1981) and Top Erosion Surfaces (TES) observed in seismic

surveys of the Messinian succession. Are these surfaces (TES) representatives of the sea-level change? The answer is far from easy. A possible explanation could be that during the Late Messinian the Mediterranean was different regarding geomorphology. Therefore, two questions arise. If the Levantine basin was shaped by lithospheric stretching as supported by Granot (2016), what was the actual basin's depth during Messinian? In the same reasoning if the obduction of the ECB under the Eurasian plate is an ongoing process from Upper Cretaceous-Oligocene (Symeou et al., 2018) what was the exact "altitude" of the ECB during Messinian? The answer is that these two areas were probably located at more elevated positions 6 Ma ago, a fact that justifies the subaerial erosion without requiring an extreme drop in sea level in the order of 2.5 km (Gargani and Rigollet 2007).

The third stage (step 3, Fig. 4) lasted for 200 thousand years (5.55-5.33Ma) (Roveri et al.,2014a, 2016; Manzi et al., 2016) and is characterized by a reduction of salinity and prevalence of brackish conditions that led to the Lago Mare deposition. After the second stage, the basin transformed into a "shallow basin" because of:

- the erosion of the Messinian margins from subaqueous (DSWC) and subaerial conditions during stages, 1 and 2, respectively
- the great clastic input derived from the Late Messinian Rivers was coeval with salt precipitation
- the significant sea-level drop due to high evaporation rates.

The water depth of the basin at this stage did not exceed 1.2 km, which agrees with Christeleitet al. (2015) and the Messinian deep record described by Lugli et al. (2015) from DSDP and ODP data. Lago Mare deposits are absent from the North-East area of the Cyprus subduction zone and the Levantine basin as during the final stage of the MSC the easternmost Mediterranean Sea was essentially desiccated (Reiche et al., 2015). This scenario follows the top erosional surfaces found at the west slopes of the ECB. Pre-Messinian topography and

Late Messinian sea-level change controlled the Lago Mare distribution. These series of sediments are completely absent in areas affected by erosion during the maximum sea-level drop at the final stage of MSC and are also missing in front of the Nile river probably because of large freshwater influx. Finally, they are absent from the deeper parts of the basin and are restricted to a zone peripherally of the residual basin. This can be attributed to the dilution of the Messinianbrines during stage 3 occured at a certain shallow depth.

The Messinian clastics were deposited strictly West of the West ECB High in the Herodotus basin (Macgregor 2012) at the base of the Messinian salt because the Levantine basin was a topographic high, which was almost or completely desiccated during MSC. This idea agrees with the Messinian relief depicted in the base salt map of Loncke et al. (2006) (Fig. 7) and the numerous canyons reported by Aal et al. (2000). The irregular shape of the ECB explains the five different salt-tectonic structural provinces. Moreover, it protected the West Eratosthenes sub-basin from thin skin salt tectonics and prevented the deposition of any clastic input, while it forced all the clastic input derived by the Late Messinian River Nile to deposit further west into the Herodotus basin. These deposits may represent the sediment supply of the Late Messinian Canyon (Fig. 39a) (“Eo-Nile” of Said).

D.6 Forward modeling of the Late Messinian clastic deposits

D.6.1 Introduction

The study of deep-sea fans and pre-deltaic deposits constitute a multi-dimensional issue because the deep-sea fan environments are complex and particularly sensitive to natural procedures/processes. The formation and evolution of deep-sea fans are of significant scientific interest, as sedimentary accumulations formed in deep-sea conditions, usually accommodate possible hydrocarbon reserves. This is the main reason why there are many research papers in the international literature investigating the individual conditions of formation and evolution of the pre-deltaic deposits. Scientific studies vary and are mainly supported by core and seismic data (Deptuk et al., 2003; 2007; Ducassou et al., 2009; Galloway 1998; Shamugan 2000, 2016; Posamentier and Kolla 2003).

Deep-sea fans are depositional sedimentary systems affected by many interrelated processes and are considered the most complex depositional environments. The main factors that affect the formation and the evolution of deep-sea fans are the quantity and quality of clastic sediments transported by the fluvial systems which are inextricably linked to the geology of the source area, the geomorphology of the basin where clastic sediments are deposited, the tectonic regime, the climate, and the isostatic and eustatic changes (Deptuk et al., 2003; 2007; Ducassou et al., 2009; Galloway 1998; Shamugan 2000, 2016; Posamentier and Kolla 2003). The complex nature of deep-sea fans can be analyzed and simulated by mathematic models to understand their formation and evolution. The simulation with mathematic models (2D or 3D) can predict the sedimentary sequences deposited in a deep-sea environment. However, mathematic models are considerably simplified in comparison with the natural processes and can simulate only the basic factors that shape the natural systems to achieve a simulation with reasonable results.

In this chapter, the mathematical model Geological Process Model (GPM, Schlumberger) is used to investigate the evolution of the pre-salt deep-sea fan described in the previous section. The simulations are based on the present scientific knowledge about the study area. The main goal is to reproduce a similar geometry with the channel complexes that have been interpreted in the seismic data and identify the main processes that govern the evolution of sediment accumulation in deep-sea environments.

D.6.2 Water and sediment supply of the Late Messinian River Nile

However, before any mathematic simulation is performed, empirical equations are used to investigate the magnitude of the sediment load transported by the Messinian River Nile towards the southeast shores of the Eastern Mediterranean. Thus, is estimated if there is enough available sediment to flow towards the deep Herodotus Basin. As aforementioned in chapter 2.5.1, the Late Messinian River Nile transferred enormous quantities of sand prone sediments primarily from the Red Sea Hills where the total denudation (1200-1500 m) has been computed by Macgregor (2012). As stated in chapter 2.4 subtropical climate was prevailing in North East Africa during the Late Messinian. Climate, erosion, and transportation are important factors to compute the suspended sediment load (Qs) of the understudy ancient river using analogs from synchronous examples.

Considering the available scientific knowledge that concerns the Late Messinian River Nile, the annual river water discharge can be estimated using the drainage area of the ancient riverine system. The drainage area of the Late Messinian Nile is computed by Macgregor (2012) at 2123737 km^2. Using the equation suggested by Syvitski and Milliman (2007) the annual water discharge of a river can be computed based on the drainage area.

$$Q \text{ (river water supply)} = 0.075\ A^{0.8}$$

The water discharge of the Messinian River Nile is calculated at 8644 m^3/s. To calculate the annual river water supply, (Q_{yr}) must be multiplied by 60 seconds 60 minutes 24 hours, and 365 days. Thus, the annual water discharge of the Late Messinian River Nile was 272.6 km^3/yr. Suspended sediment load according to Syvitski and Milliman (2007) is a function of:

$$Q_s \text{ (suspended sediment load)} = \omega\ B\ Q_{yr}^{0.31}\ A^{0.5}\ R\ T$$

Where:

- *ω (constant) = 0.0006 for values MT/yr*
- *B=1 (No human impact)*
- *Q= 272.6 Km^3/yr (annual water supply)*
- *Drainage Basin of Miocene Nile, A = 2123737 km^2 according to Macgrecor 2012*
- *R= maximum relief of the drainage basin in Km*
- *T= average temperature in Celsius*

Due to the uncertainty regarding the maximum relief and the average temperature a range of values was used (Fig. 40).

Average temperature of the drainage basin, °C

Possible maximum basin Relief, Km	23	24	25	26	27	28
2.5	287,5	300	312,5	325	337,5	350
2.6	299	312	325	338	351	364
2.7	310,5	324	337,5	351	364,5	378
2.8	322	336	350	364	378	392
2.9	333,5	348	362,5	377	391,5	406
3	345	360	375	390	405	420

Figure 40: *Calculations of suspended sediment-load (Q_s in MT/yr)transported into Nile Delta area for a range of maximum basin reliefs and basin average temperatures values.*

The bed load transported into the Delta area is also calculated. According to Syvitski and Kettner (2011), bedload ranges from less than 1 to 20% of the total sediment load for locations near river mouths and the bedload global average is 6.6% of the total sediment load. The Late Messinian River Nile is expected to have a bedload above the global average because it was situated close to a steep mountain gradient (Red sea Hills). Combining equations 1 and 2 the Bedload of a river can be computed.

- Total = Bedload + Suspended (1)
- Bedload = 0,066 Total (2)

- Bedload = 0,066 (Bedload + Suspended)
- Bedload = 0,066Bedload + 0,066Suspended
- 1 – 0,066Bedload = 0,066Suspended
- 0,934Bedload = 0,066Suspended
- Bedload = 0,066/0,934suspended = 7,06% Suspended
- if 20% then Bedload = 25% Suspended

The total sediment load (Q_t) of the Late Messinian River Nile was calculated considering a value of global average bedload 6.6% and an extreme case of 20% of the total sediment load (Fig. 41 and 42).

Average temperature of the drainage basin, °C

Possible maximum basin Relief, Km	23	24	25	26	27	28
2,5	20,2975	21,18	22,0625	22,945	23,8275	24,71
2,6	21,1094	22,0272	22,945	23,8628	24,7806	25,6984
2,7	21,9213	22,8744	23,8275	24,7806	25,7337	26,6868
2,8	22,7332	23,7216	24,71	25,6984	26,6868	27,6752
2,9	23,5451	24,5688	25,5925	26,6162	27,6399	28,6636
3	24,357	25,416	26,475	27,534	28,593	29,652

Average temperature of the drainage basin, °C

Possible maximum basin Relief, Km	23	24	25	26	27	28
2,5	307,7975	321,18	334,5625	347,945	361,3275	374,71
2,6	320,1094	334,0272	347,945	361,8628	375,7806	389,6984
2,7	332,4213	346,8744	361,3275	375,7806	390,2337	404,6868
2,8	344,7332	359,7216	374,71	389,6984	404,6868	419,6752
2,9	357,0451	372,5688	388,0925	403,6162	419,1399	434,6636
3	369,357	385,416	401,475	417,534	433,593	449,652

Figure 41: *Bedload 6,6% of total sediment load is presented in the first table and Q_{total} in MT/yr is presented in the second table for a range of maximum basin relief and basin average temperature values.*

Average temperature of the drainage basin, °C

Possible maximum basin Relief, Km	25	26	27	28	29	30
2,5	71,875	75	78,125	81,25	84,375	87,5
2,6	74,75	78	81,25	84,5	87,75	91
2,7	77,625	81	84,375	87,75	91,125	94,5
2,8	80,5	84	87,5	91	94,5	98
2,9	83,375	87	90,625	94,25	97,875	101,5
3	86,25	90	93,75	97,5	101,25	105

Average temperature of the drainage basin, °C

Possible maximum basin Relief, Km	25	26	27	28	29	30
2,5	359,375	375	390,625	406,25	421,875	437,5
2,6	373,75	390	406,25	422,5	438,75	455
2,7	388,125	405	421,875	438,75	455,625	472,5
2,8	402,5	420	437,5	455	472,5	490
2,9	416,875	435	453,125	471,25	489,375	507,5
3	431,25	450	468,75	487,5	506,25	525

Figure 42: *Bedload 20% of total sediment load is presented in the first table and Q_{total} in MT/yr is presented in the second table for a range of maximum basin relief and basin average temperature values.*

Based on the results of the empirical equations, it is safe to conclude that during the Late Messinian, the River Nile transport vast quantities of clastic materials towards the basins of the Eastern Mediterranean. This fact in combination with the Late Messinian sea-level drawdown must have resulted in the creation of an active turbidite system.

D.6.3 Sedimentary Forward Models (SFM's)

D.6.3.1 Types of sedimentary forward models

The detailed analysis of a dynamic system such as a deep-sea fan with simulation methods requires the right choice of a suitable stratigraphic forward model. The mathematic models can be separated into two basic categories, the geometric models, and process-based models (Koltermann and Gorelick 1996).

The geometric models are mainly used for the simulation of stratigraphic sequences for large periods (10^2 - 10^6yr) without the ability to simulate additive physical processes. This weakness to simulate physical processes makes them unsuitable for simulation in different geographic positions. The geometric models cannot forecast a range of basic physical parameters such as the grain size of the simulated clastic sequences. Controversially, process-based models can simulate a variety of natural processes simultaneously. As a result, process-based models can contribute to the research concerning the depositional evolution of clastic sequences (Morehead et al., 2001)

Another important difference between the mathematic models is their discrimination in deterministic and stochastic. In the deterministic mathematic models, the input and output data have fixed values while in the stochastic mathematic models the variables can have the form of probability. The mathematical models are also separated based on the time steps that can reproduce in static models where a sedimentary system is presented in a single time and dynamic where the evolution of a clastic system can be observed through time. Finally, another distinction in types of mathematic models is directionality: forward or inverse. Forward models start at some point in time and simulate the subsequent development using defined boundary conditions, whereas inverse models reconstruct the sedimentary evolution backward based on a given state (Overeem et al., 2005).

From the aforementioned categories of the mathematic models, to obtain the best results for the simulation of the pre-salt clastic deposits described in chapter 5 Geologic Process Model (GPM, Schlumberger) was selected which is a dynamic process-based, deterministic (where the input parameters can be stochastic) forward model working as a plugin for the software Petrel (Schlumberger). GPM is a simple, yet realistic, large-scale, and long-term sedimentation model used to estimate paleographic conditions. It is also useful for testing several input parameter combinations with the objective of best-fitting present seismic, well logs, and outcrop data (Tetzlaff et al., 2014).

D.6.3.2 Description of GPM

Stratigraphic forward modeling is based on simulating dynamic sedimentary processes involving sediment transport, erosion, and deposition. To reproduce a realistic three-dimensional model suitable to predict sediment distribution, the simulation process considers variable paleogeographic conditions (e.g. sea-level changes, amount and type of sediment source input, and tectonic events) (Tetzlaff et al., 2014).

Because the model is deterministic (but not the input parameters, which can be stochastic), the geological system state is obtained by propagating sampled initial parameters or conditions forward (forward model). In general, the model combines five parameters as main input (1) sediment components and their properties, (2) basin geomorphology, (3) sources, sinks, and boundary conditions, (4) sea-level curve and, (5) modeling time interval (Schlumberger, 2019).

Boundary conditions such as sediment transport, erosion, and deposition need to be set before the start of the stratigraphic simulation process. These physical processes can be modeled by three methods (1) diffusion, (2) steady flow, and (3) unsteady flow. Diffusion is the simplest physical process, and it assumes that the sediments move downslope based on

the slope gradient, topographic highs will be eroded, and the sediments produced will be deposited in the basins (Schlumberger, 2019). Diffusion assumes that the finer sediments (silt and clay) will be deposited farther and the coarser sediments (gravel and sand)closer to the source (Tetzlaff et al., 2014). Diffusion is used to model secondary transport mechanisms (small-scale) and is usually combined with free surface flow methods (e.g., steady flow, unsteady flow) (Tetzlaff and Schafmeister, 2007). The small-scale functionality of diffusion is a disadvantage because it does not consider that collapsing slopes can contribute to the reworking of sediments and mixed sediment grain size. However, features such as channels and canyons will have a sharp and unrealistic shape without diffusion (Tetzlaff and Schafmeister, 2007).

GPM simulates free-surface flow, for steady flow (river flow) and unsteady flow (turbidity currents and river floods) (Tetzlaff et al., 2014). The model assumes that the horizontal component of the vertical velocity profile does not vary anywhere. In consequence, the model just considers the vertically averaged horizontal velocity vectors (Tetzlaff and Schafmeister, 2007). The main disadvantage is that GPM does not simulate changes in the flow direction (e.g. helical flowing turbidite turns (Corney et al., 2006; Imran et al., 2008)) and simulate only changes of the flow velocity magnitude with depth (Tetzlaff and Schafmeister, 2007; Tetzlaff et al., 2014). However, this simplified representation of free-surface flow makes it possible to simulate geologic time scale models (Tetzlaff and Schafmeister, 2007). The flow acceleration of the GPM is governed by (1) the gravity and the elevation of the water surface, (2) the viscosity of the fluid, (3) the friction of the fluid against the bottom, and (4) the acceleration due to external forces, such as wave action (Tetzlaff and Schafmeister, 2007).

In general, both steady and unsteady flow will erode, transport, and deposit sediments primarily considering the grain sizes, the velocity of the flow, and depth (Tetzlaff et al.,

2014). Steady flow is used when the flow velocity and depth are undisturbed through time. A flow can be considered as steady if after several hours it continues undisturbed (e.g., a river). While unsteady flow is used to simulate unstable flow velocity and depth through time (e.g., a turbiditic flow). A flow can be considered unsteady when it runs over a determined amount of time and when the flow velocity and depth vary in a short lapse of time (Tetzlaff et al., 2014).

To forward-modeling turbidites, the process-based model elements required by the software are linked and changed in agreement with a pre-established time interval that displays sequence boundaries depending on the number of cycles set. The most important GPM elements that will be discussed later in detail are eustatic sea-level changes (user-defined), diffusion coefficient, erodibility and transport coefficient (user-defined - represent the magnitude of the erosion and how easily the sediment can be transported), sediment lithology, grain size, and flow velocity (user-defined size of the water source). Since the main goal is to understand the factors controlling turbidites, the GPM processes considered here are diffusion and unsteady flow.

D.6.4 Simulation of the pre-salt deep-sea fan

The main goal is to configure the parameters that control the sedimentation model. To achieve this, many simulations are run to find out the best parameter combination GPM needs to simulate turbidites deposition at deep-sea conditions. In general, these parameters are tested by setting ideal initial conditions forward in time and applying different ranges of the main input parameters (i.e., sediment components and their properties, sources, sinks and boundary conditions, flow velocities for unsteady flow, and modeling time interval).

Considering the existing knowledge from deep-water depositional environments in the Niger Delta (Deptuck et al., 2003), the Gulf of Mexico (Posamentier, 2003), and the Nile

Delta (Ducassou et al., 2009), this simulation aims to investigate the influence of the sediments grain size deposited by turbiditic flows on the geometry and stratigraphy of the deep-sea fan in the pre-Messinian topography, to increase the confidence of data interpretation in frontier basins, thus de-risking future oil and gas exploration activities in Eastern Mediterranean.

Sinuosity and direction of channels in deep-water settings change. Channel sinuosity changes are considered critical for reservoir prediction because a decrease in sinuosity increases the channel incision, decreasing possible levee development and vice-versa (Deptuck et al., 2003). An increase in channel incision is associated with major sediment erosion or non-deposition and lack of lateral channel migration (Deptuck et al., 2003). Lateral channel migration produces lateral amalgamation of individual channels that could result in a reservoir with high initial porosity and permeability. In general, channel geometries are important because they provide detailed information about sand deposition.

The existing knowledge about the channel flow path behavior helps to visualize the expected result after the simulation and what would be considered as a realistic and coherent model for turbidite deposition. Since GPM is a basin-scale forward stratigraphic model, it simulates regional geological processes that provide the big image of sediment distribution and channel migration (Tetzlaff et al., 2014). However, it is not possible to simulate a reservoir-scale model where detail geometrical relationships (e.g., onlap, downlap, toplap, etc.) can be recognized. Therefore, the main objective of the simulation is to recognize the changes in the geometry of deposition and specify how the pre-existing geomorphology, flow, and sediment parameters (i.e., size, grain properties, grain fractions, flow velocity) influence the sediment distribution.

D.6.4.1 Model setup

As mentioned in section 6.3.2, the model requires an initial surface that represents the basin paleo-geomorphology. The basin-floor surface that serves as an initial surface for the simulations was created after the backstripping of the Late Messinian relief of the study area (see the next chapter (D.6.4.2) for details). The area is sourced from the Late Messinian River Nile and the unsteady flow processes are defined as “source positions” in the south and south-east of the study area (see chapter D.6.4.6for details).

The time cycle of the simulation was set at 370 thousand years (ky) to represent the first phase of the Messinian Salinity Crisis (5.97-5.6 Ma). The display interval of the models is 10 thousand years (ky)such that the models have 37 timesteps and a large turbiditic event interval is set every 11 years based on the 11-yr Schwabe cycle. The surface dimension is approximately 100 x 50 km with a 20972 total number of 2D cells and the grid cells resolution is 500 x 500 m.

Before performing the simulations, it is important to understand the turbidites deposition. For this, it is necessary to fine-tune the model parameters by systematically changing them. The purpose is to produce results that are similar to the seismic interpretation described in the previous chapter (chapter 5).

For the initial model, the only fixed parameters that define the initial setup of the model are the initial basin geometry and the time interval. The most critical parameters are diffusion coefficient, erodibility, transport coefficient, sediment setting (lithology, grain size, contribution), and flow velocity. The remaining parameters, such as porosity, density, amount of tectonic subsidence among others, do not affect the scenarios simulated here but they affect more complex scenarios that are beyond the scope of this dissertation.

D.6.4.2 Backstripping

According to Allen and Allen 2013 (chapter 9.4 and page 336), to gain insights into subsidence rate and tectonic driving force on a 1D stratigraphic column, several modifications or 'corrections' to the stratigraphic column are needed. In this section, these modifications are performed to obtain a more realistic surface (paleo morphology) to use during the simulation experiments.

The total subsidence of the basement underlying a sedimentary basin is made of three parts at any time (t): the sediment deposited y(t), the water depth Wd(t), and the change in global sea level $\Delta_{SL}(t)$. An isostatic balance between a lithospheric column through the sedimentary basin can be performed, and a column in which the sediment load has been removed and has been replaced with water (Fig. 43) to obtain the tectonic or backstripped subsidence *Y*(*t*). The isostatic balance down to a depth of compensation in the ductile asthenosphere is:

$$\rho_w g W_d(t) + \rho_b g y(t) + \rho_c g y_c + \rho_m g_{\alpha 1} = \rho_w Y(t) + \rho_c g y_c + \rho_m g_{\alpha 1} \ldots\ldots (1)$$

Where y_c is the crustal thickness, α_1 and α_2 are the mantle lithosphere thicknesses before and after removal of the sediment load, and ρ_w, ρ_b, ρ_c, and ρ_m are the densities of water, bulk sediment, crust, and mantle respectively. Global sea-level change $\Delta_{SL}(t)$ changes the datum at the top of the lithospheric column.

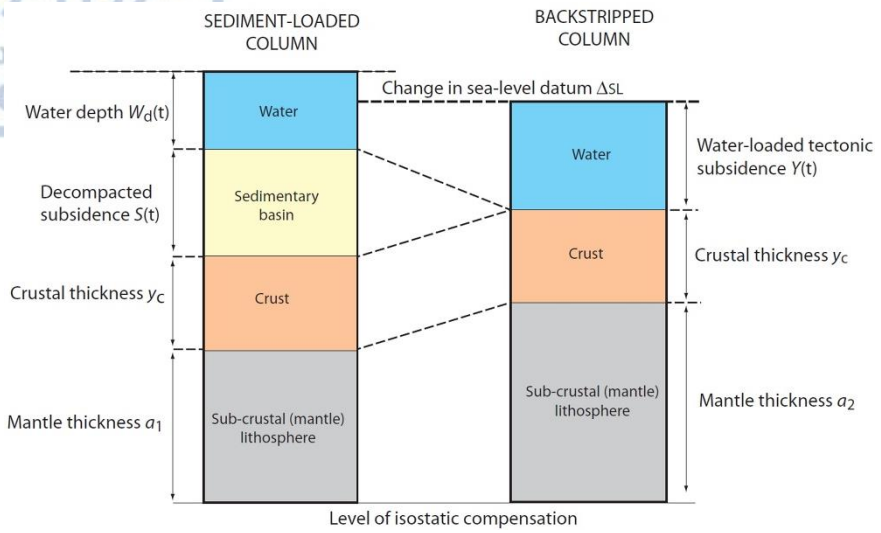

Figure 43: *Isostatic balance to illustrate backstripping of sediment load. From Allen and Allen (pp. 336).*

Equating the thicknesses in the two columns, and removing y_c since crustal thickness does not change, and g, since it occurs in each term the equation, is:

$$Wd(t) - \Delta_{SL}(t) + y(t) + \alpha_1 = Y(t) + \alpha_2 \ldots\ldots (2)$$

Combining the two equations (1) and (2) the general solution for tectonic subsidence can be obtained:

$$Y(t) = W_d(t) + y(t)\left(\frac{\rho m - \rho b}{\rho m - \rho w}\right) - \frac{\rho m}{\rho m - \rho w}\Delta_{SL}(t)$$

If the global sea level $\Delta_{SL}(t)$considered as negligible or zero, the general solution for tectonic subsidence is:

$$Y(t) = W_d(t) + y(t)\left(\frac{\rho m - \rho b}{\rho m - \rho w}\right)$$

The water depth $W_d(t)$ is known by the present-day bathymetry map of the Eastern Mediterranean. The sediments deposited y(t) are represented by the isopach map of the sediments from the seabed reflector to the depth of the BS-BES reflector. The density of the mantle in the Eastern Mediterranean is ~3.3 g/cm^3 (Casten and Snopek, 2006; Makris et al., 2013), the density of sediments is set at ~2.7 g/cm^3, and the density of seawater is 1.027 g/cm^3. By performing computations between surfaces into the Petrel software the isostatic corrected (backstripped) surface can be obtained (Fig. 44).

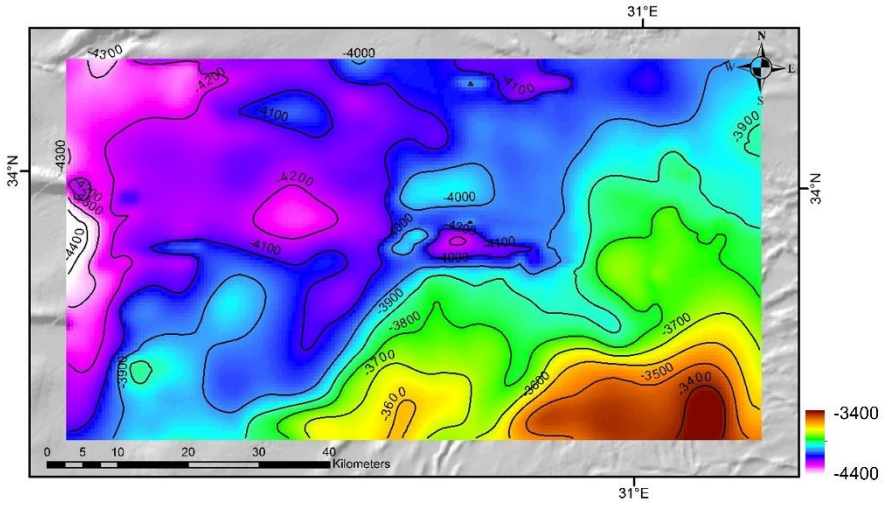

Figure 44: *Map of the isostatic corrected surface (backstripped surface). This map was used as the initial basin geomorphology.*

D.6.4.3 Eustasy

For the simulation experiments, the sea-level curve is not included as an input because a sea-level curve is not strictly required by GPM. If a sea-level curve is not provided, sea-level assumed to be at elevation zero (Schlumberger, 2019). The sea-level curve is very important and affects drastically the deep-water sediment distribution patterns, but the present simulation sources are set already at deep-sea conditions. In addition, the sea level fluctuation during the onset of the Messinian Salinity Crisis is still a subject under study by the scientific community.

D.6.4.4 Sediment input

Four different lithologies are modeled: coarse sand, fine sand, silt, and clay. GPM models each lithology and assigns to them a distinctive color depending on the composition (Schlumberger, 2019). The color is a single color if the lithology is not mixed, e.g. coarse sand (red), fine sand (green), silt (blue), and clay (black), but if the sediments comprise mixed lithologies they are represented as additive color mixtures (Schlumberger, 2019). To test the sediment distribution, the sediment's grain properties (size, density, and fraction) are set. This is because turbidity currents are the most important mechanism for transport coarse-grained sediments towards deep-sea environments by fluid turbulence (Deptuck et al., 2003). During sea-level fall periods, different sediment sizes will reach deep-water environments. The following parameters (Fig.45) were tested and adjusted until the results show the grain property distribution and diameter that best fit an environment rich in sand-size fractions.

Lithology	Grain properties		
	Diameter (mm)	Density (g/cm^3)	Fraction ranges
Coarse sand	1	2.7	0.35-0.4
Fine sand	0.1	2.65	0.35-0.4
Silt	0.01	2.6	0.15-0.2
Clay	0.001	2.55	0.05-0.1

Figure 45: *Sediment types, grain properties, and fraction range used in the simulation process.*

Therefore, the sediment contribution was assumed to be mostly sand and in minor proportions silt and clay. The sediment fractions were varied to show the preferential distribution of the sediments.

D.6.4.5 Diffusion coefficient, erodibility, and transport coefficient

The model requires a diffusion coefficient and a diffusion curve that is used to simulate the amount of erosion. The strength of the erosion is controlled by the diffusion coefficient (m^2/a). The diffusion curve acts as a unitless multiplier (Schlumberger, 2019); this curve shows a slow and progressive increase at relatively shallow water and above sea level, where the sediments are more exposed to wave action and aerial erosion, whereas the diffusion values decrease below sea level. In addition, GPM considers that the diffusion coefficient is not equal everywhere and each sediment diffuses at a different rate. In general, GPM diffusion is depth, sediment type, and grain size-dependent (Tetzlaff and Schafmeister, 2007). Since the initial surface is located in a deep-sea environment where the diffusion is insignificant, the diffusion values were kept below 0.05 m^2/a.

Erodibility controls how easily erosion will occur and how much materials through time will be removed and deposited in the basins (Schlumberger, 2019). The transport coefficient on the other hand enables a simulation of how efficiently the sediments can be transported. The GPM manual state that transport coefficient act as a multiplier for the transportability specified in the settings for each sediment type with values usually ranges between 0.01 to 1. GPM manual also states that low values produce smoother models and high values can result in noisy models (Schlumberger, 2019). During the sensitivity experiments, high values resulted in smoother models and lower values resulted in noisy models. These two coefficients are environment-dependent (Schlumberger, 2019).

Erodibility values are kept between 80 and 95 % because for these values, the pre-existing geomorphology is not dramatically eroded. Several values were tested for the transport coefficient and values between 0.1 and 0.2 were chosen since they make the transportability reasonable when combined with the flow velocities for unsteady flow.

D.6.4.6 Flow velocity, sources, and source position map

Flow velocity is very sensitive and is linked to the diffusion and unsteady flow geological processes. It is considered the main mechanism for transporting sediments in GPM (Tetzlaff and Schafmeister, 2007), and it is used to compute the transport capacity which is dependent on the flow depth and velocity (Schlumberger, 2019). This parameter combines mainly two inputs: a water supply curve which is in meters per second (m/s) per unit of time (thousands or millions of years), and a source position map (Fig. 46). The water supply curve controls water velocity through time (Schlumberger, 2019). Additionally, the water supply curve is combined with the fluid element depth that controls the number of particles added in the flow and a delta time element that is the internal computational time step that allows the particles in the flow to settle down (Schlumberger, 2019). By decreasing the element depth, the number of particles is increased which makes the process results smoother. Based on the GPM manual the optimum number is a few hundred fluid elements (Schlumberger, 2019). The number of fluid elements can be checked in the message log where is displayed after each simulation. The source position map controls the water and sediment flow rates (Schlumberger, 2019). The source is cell size dependent and very sensitive to changes in the model surface, trial and error are needed to find the best parameters fit for each flow velocity (Schlumberger, 2019). For that reason, the unsteady flow process without diffusion was tested several times to calibrate the flow velocity in combination with the various parameters (i.e., fluid element depth, duration time, display time, delta time element, and transport coefficient). Besides, the unsteady flow process without sediment movement was tested several times until a suitable flow velocity was achieved (reach the borders of the model). The locations of the source's positions (Fig. 46) were selected based on the seismic interpretation in chapter 5 to represent sediment distribution that emerged from the Messinian River Nile (i.e., source points located at the southern edges of the simulated area).

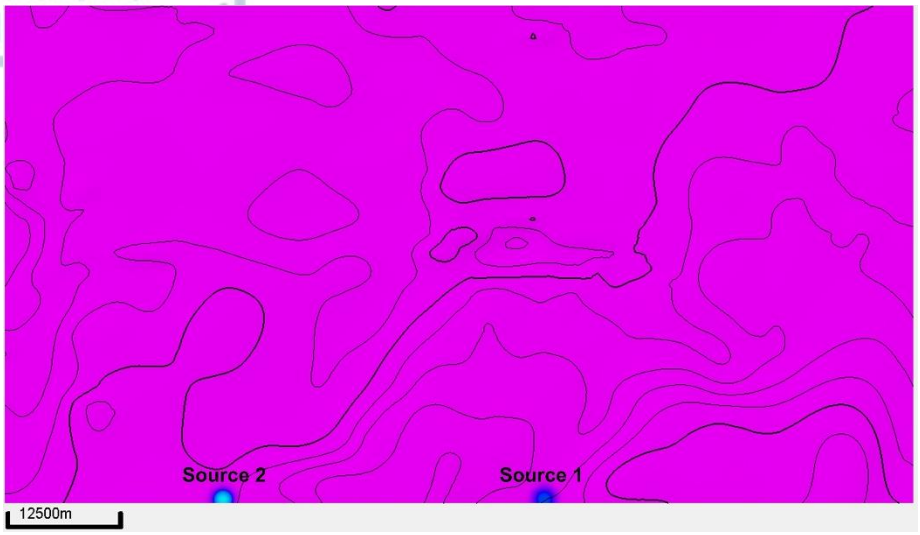

Figure 46: Map showed in Figure 44 used as source position map during the simulation process.

As already mentioned, the flow velocity is the most sensitive parameter. Searching for an appropriate flow velocity parameter range involves several calibrations. The source depends on the position, size (the number of cells), the grid resolution, and the water supply curve (which controls water velocity through time), multiple simulations were performed to decide the best size of the source that gives an appropriate amount of water and water velocity.GPM manual considers that the water and sediment flow inputs depend on the number of cells that correspond to a source, the area of those cells, and the water and sediment rates in the stratigraphic curves that control the water and sediment flow with time. (i.e., source with 20 cells, each cell size 100 x 100 m with water rate 0.1m/s, the total water rate for this source is 20 x 10.000 x 0.1 = 20000 m^3/s).

The source positions (Fig. 46) were fixed at the confined parts of corridors 1A and 2A at the south edge of the simulated area. The sources cover approximately 6-8 cells of 500 x 500 m, with values ranging between 5-20 m/s for the water supply curve for different experiments. The velocities used in the water supply curve were based on recent measurements of turbiditic velocities from the Monterey canyon (Heerema et al., 2020) and

historically recorded turbiditic events (e.g., Grand Banks, Newfoundland event). The results of the simulation based on these values show that the modeled flow reached the boundaries of the simulated area.

As previously mentioned, the water supply curve depends on a delta time element that is the internal computational time step helping the particles in the flow to settle down (Schlumberger, 2019). Because the computational time step controls how much time takes for the flow to travel across each cell, reducing this parameter makes the flow more stable. Although the value for this parameter is found by dividing the flow velocity by the cell length (e.g. it takes 36 s for the flow to travel across the cell for a flow velocity of 50 km/h and a 500 m cells length). The GPM manual considers (for flow velocity 50 km/h and a 500 m cells length) that an appropriate value is not 36 s but 10 s (Schlumberger, 2019). During the sensitivity experiments process, was found out that the computational time is usually smaller than the value calculated with this relationship. Finally, to be sure that the selected delta time element was appropriate for the different experiments, the message log was checked after every simulation for possible errors (e.g., sediments jump over cells, delta time element must be decreased).

D.6.5 Simulation results

As already mentioned, one turbiditic event every 11 years was simulated based on the 11-yr Schwabe cycle. The 11 years' time span is indicative as many turbiditic events occur every year (Heerema et al., 2020). The simulation was set every 11 years to save computation time and to simulate only the large turbiditic episodes. The simulation results represent two basic scenarios with flow velocities at 5and 20 meters per second (18 and 72 km/hour).

D.6.5.1 Experiments with 5 m/s

The first experiments without sediment movement were performed to investigate if the unsteady flow parameters set (described in chapter D.6.4) are creating a flow that reaches the boundaries of the model (Fig. 47). Once the unsteady flow is checked, experiments are performed including the clastic sediments (Fig. 48). As stated in chapter D.6.4.4 the results color is a single color if the lithology is not mixed, e.g., coarse sand (red), fine sand (green), silt (blue), and clay (black), and color mixtures if the sediments comprise mixed lithologies (Fig. 48). Sediments fractions (sand coarse, sand fine, silt, and clay) are presented in Figure 49 as property maps. Coarse sand is mainly deposited in the confined parts of the simulated surface while fine sand is deposited immediately after the spread out of the sediments towards the unconfined parts of the simulated surface (Fig. 49). Silt and clay are mainly deposited at the most remote and unconfined parts of the simulated surface (Fig.49). Finally, an isopach map of the deposited sediments is presented in Figure 50.

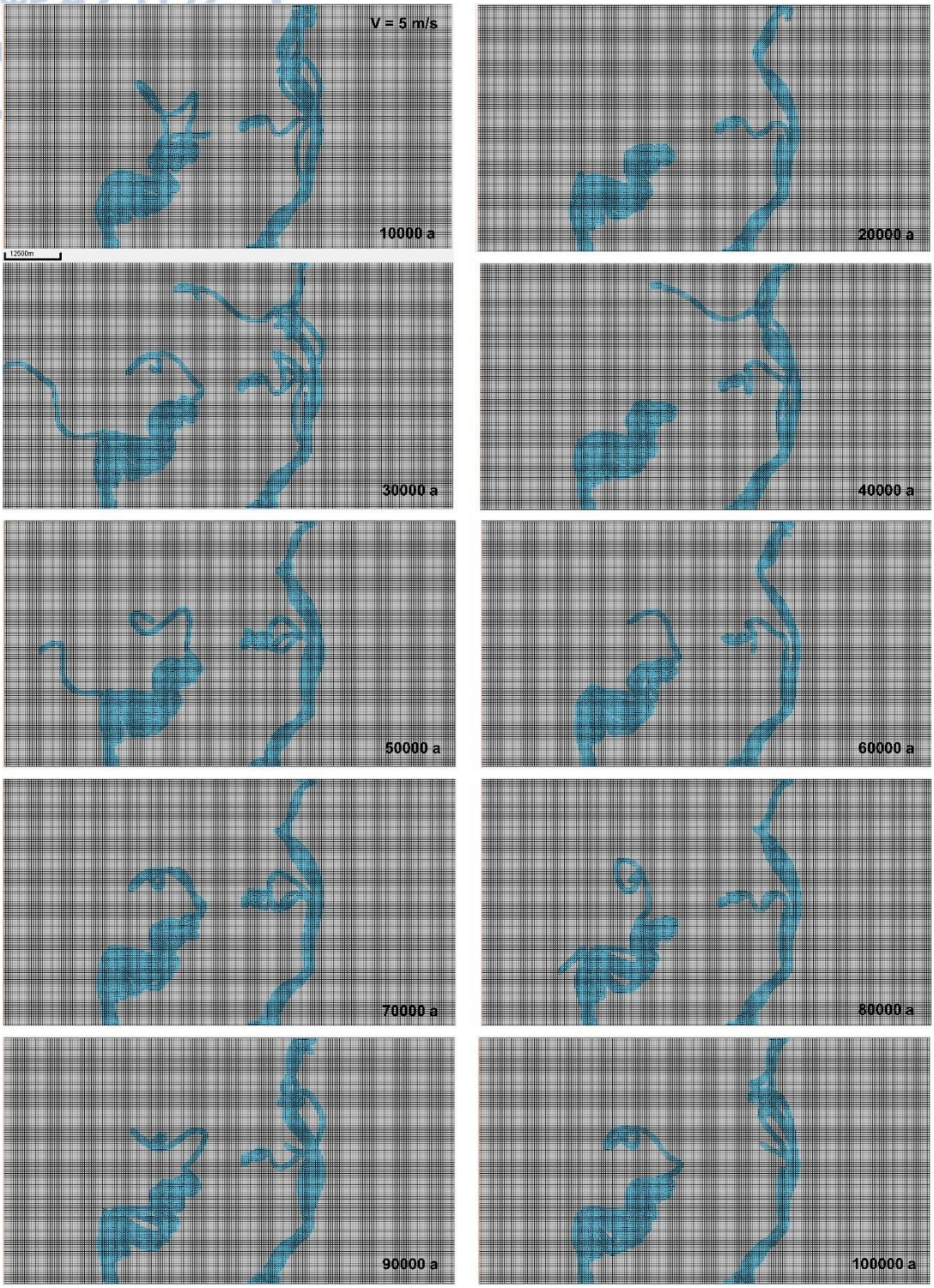

Figure 47: *Simulation results using as initial basin geomorphology the map introduced in Figure 44. Flow velocity of 5 m/s simulated without sediment movement from zero to 100 thousand years.*

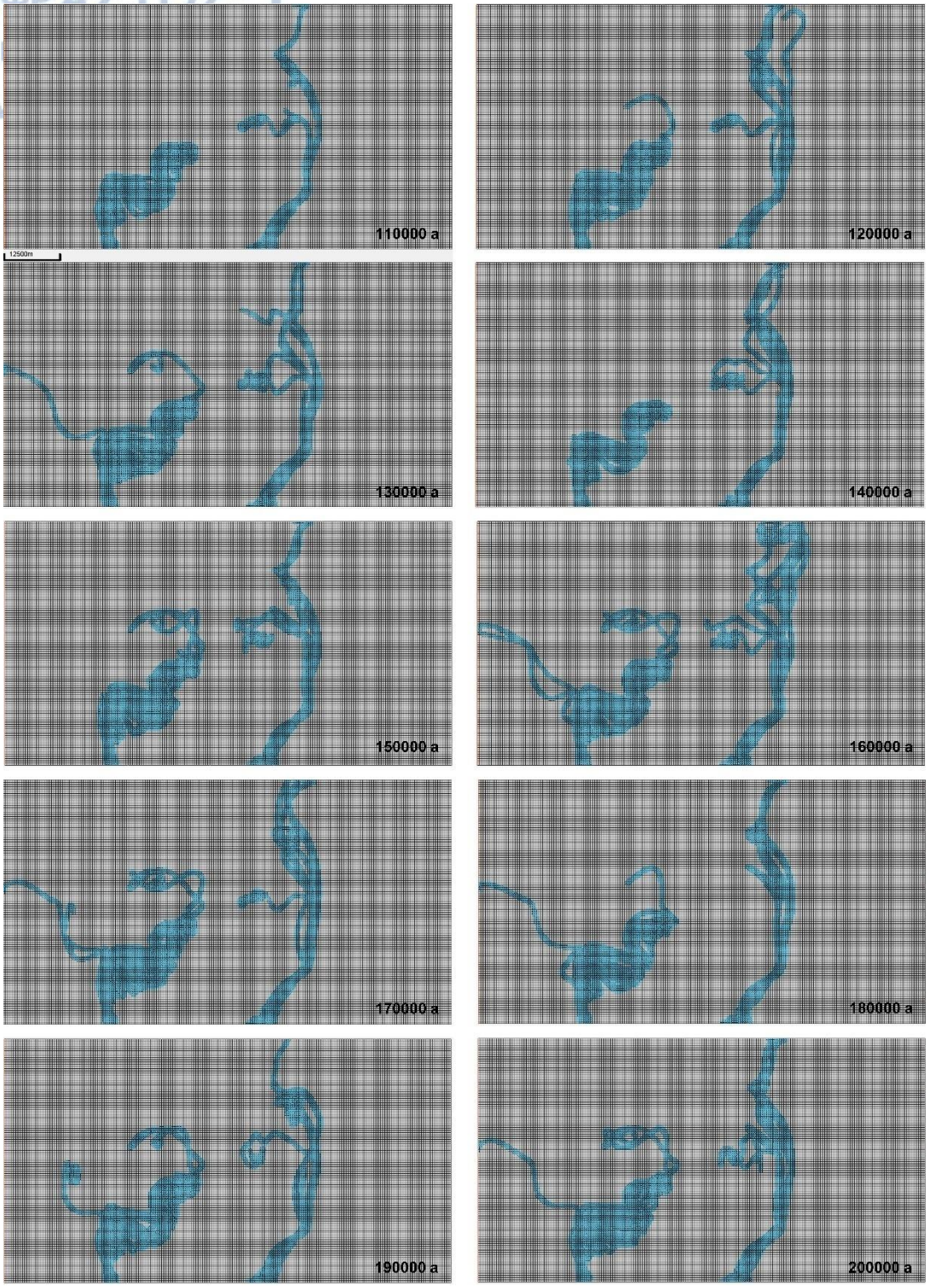

Figure 47 (continued): *Simulation results using as initial basin geomorphology the map introduced in Figure 44. Flow velocity of 5 m/s simulated without sediment movement from 100 to 200 thousand years.*

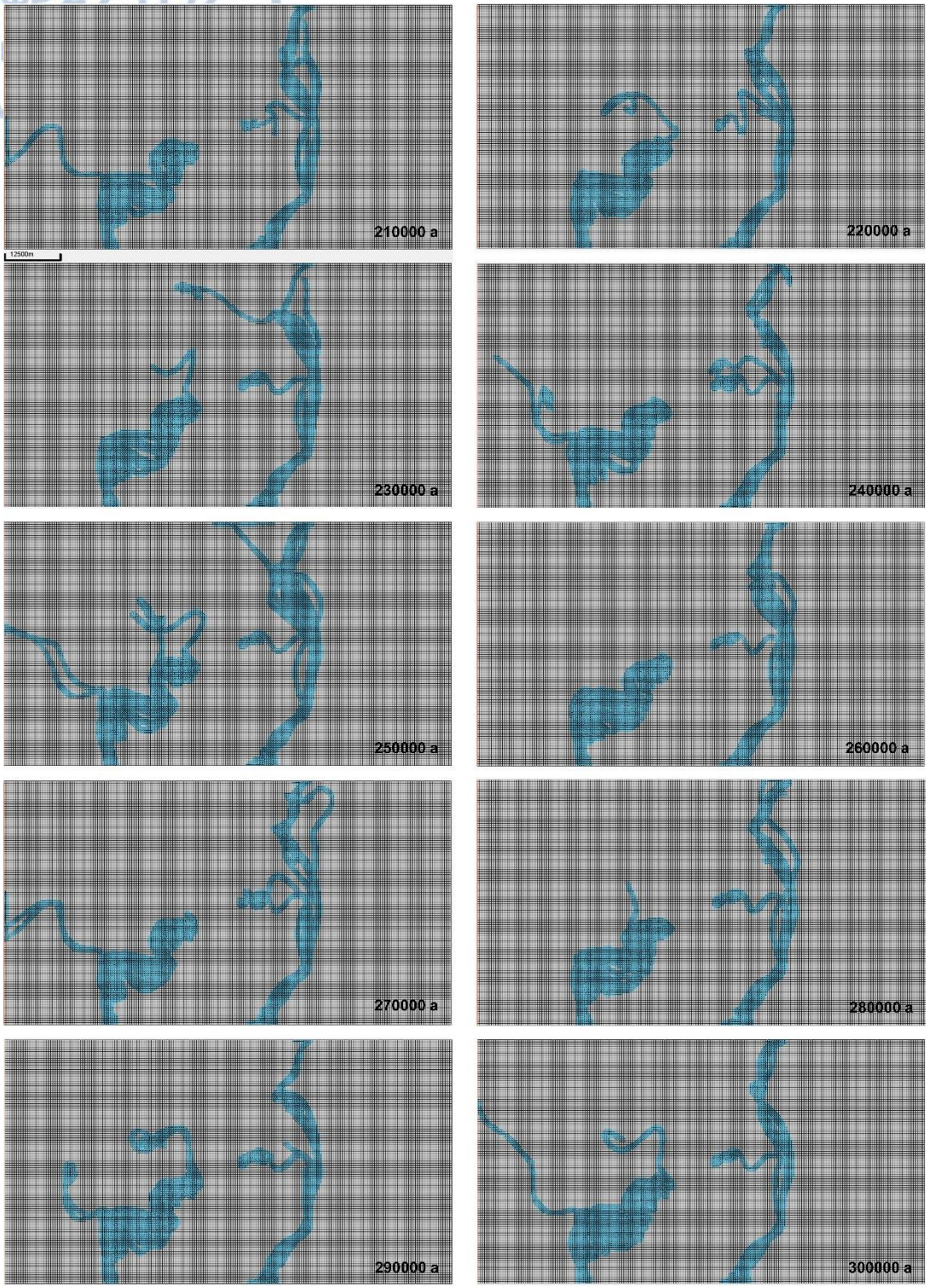

Figure 47 (continued): *Simulation results using as initial basin geomorphology the map introduced in Figure 44. Flow velocity of 5 m/s simulated without sediments movement from 200 to 300 thousand years.*

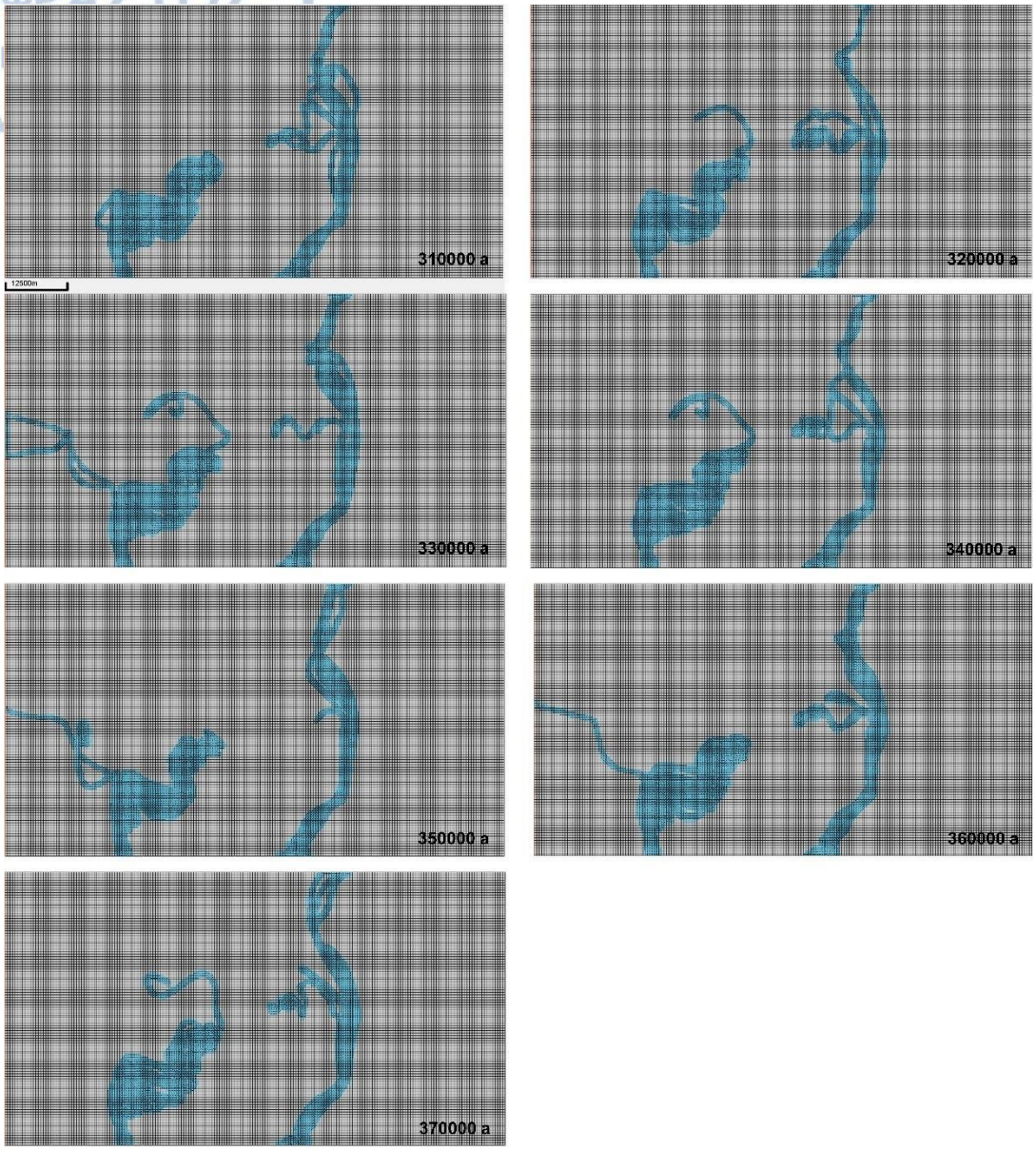

Figure 47 (continued): *Simulation results using as initial basin geomorphology the map introduced in Figure 44. Flow velocity of 5 m/s simulated without sediments movement from 300 to 370 thousand years.*

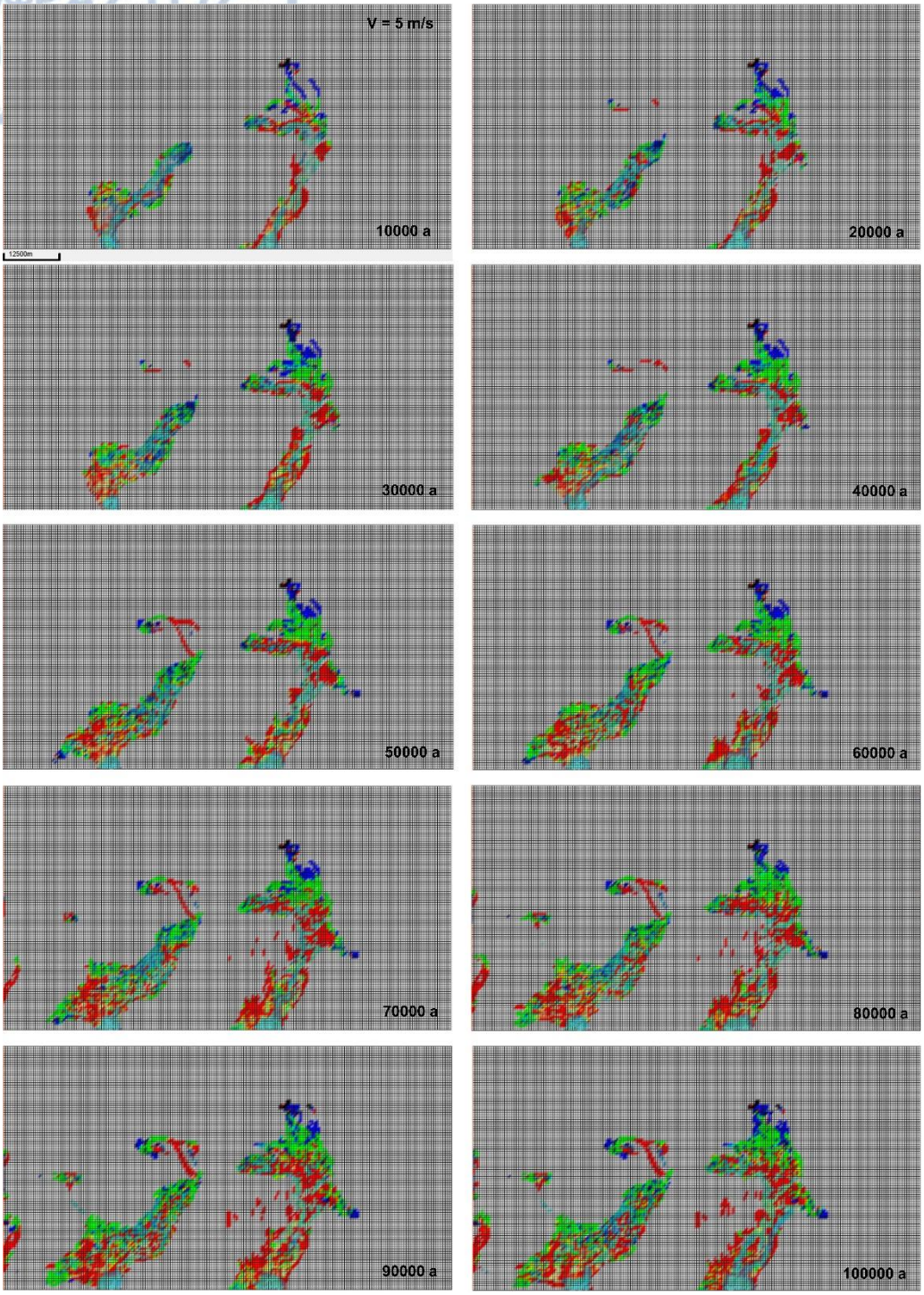

Figure 48: *Simulation results using as initial basin geomorphology the map introduced in Figure 44. Flow velocity of 5 m/s simulated including sediments movement from zero to 100 thousand years. The results color is a single color if the lithology is not mixed, e.g., coarse sand (red), fine sand (green), silt (blue), and clay (black), and color mixtures if the sediments comprise mixed lithologies.*

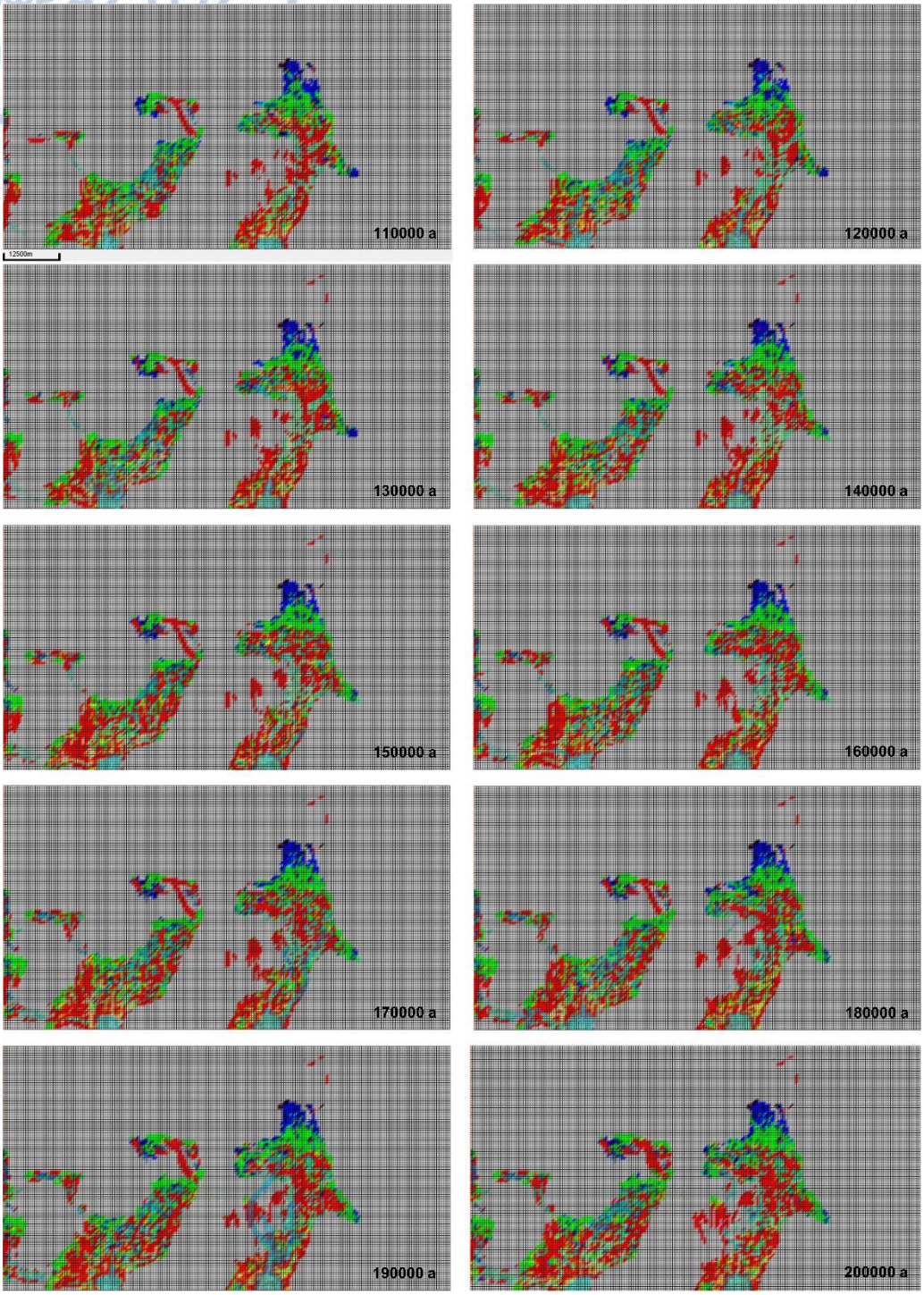

Figure 48 (continued): *Simulation results using as initial basin geomorphology the map introduced in Figure 44. Flow velocity of 5 m/s simulated including sediments movement from 100 to 200 thousand years. The results color is a single color if the lithology is not mixed, e.g., coarse sand (red), fine sand (green), silt (blue), and clay (black), and color mixtures if the sediments comprise mixed lithologies.*

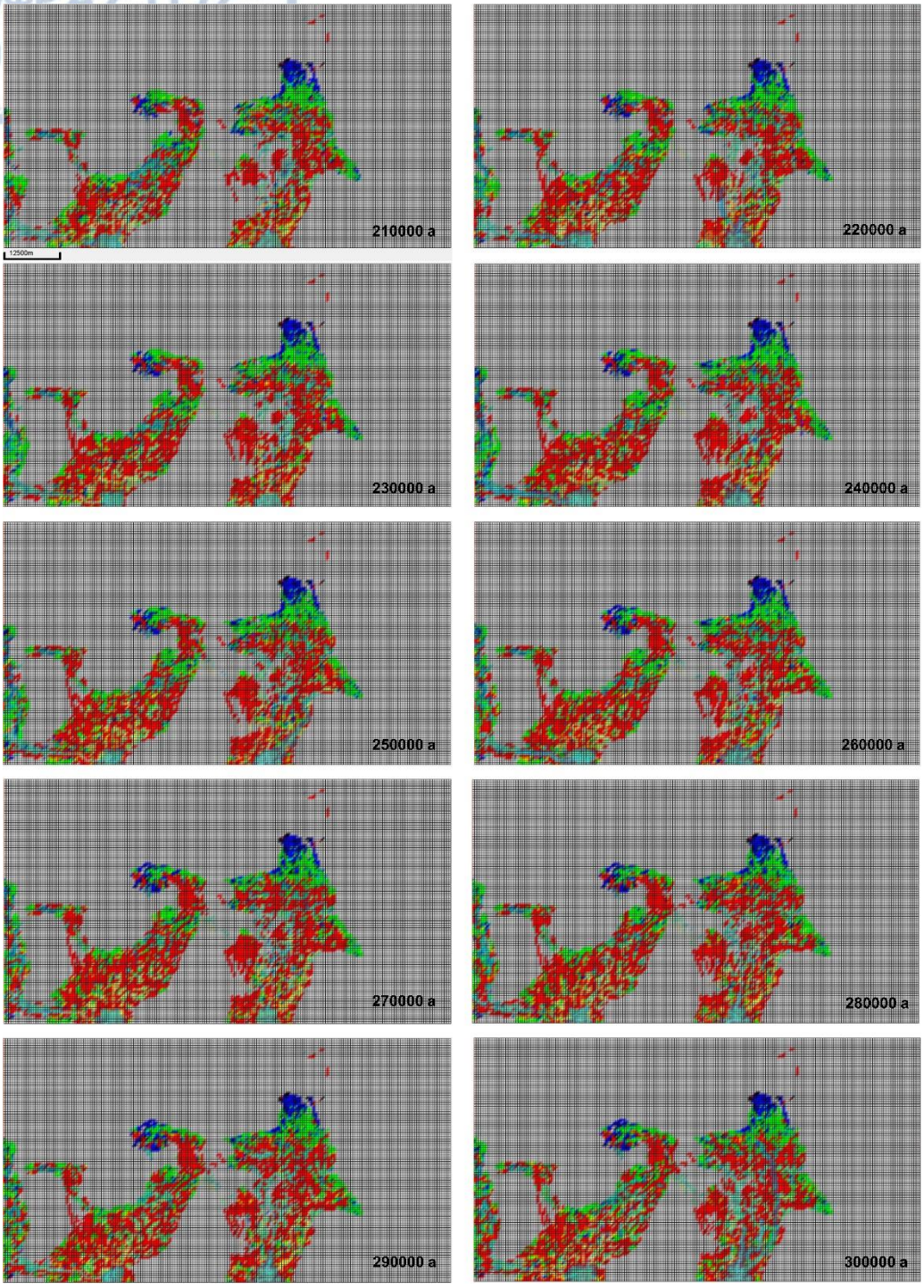

Figure 48 (continued): *Simulation results using as initial basin geomorphology the map introduced in Figure 44. Flow velocity of 5 m/s simulated including sediments movement from 200 to 300 thousand years. The results color is a single color if the lithology is not mixed, e.g., coarse sand (red), fine sand (green), silt (blue), and clay (black), and color mixtures if the sediments comprise mixed lithologies.*

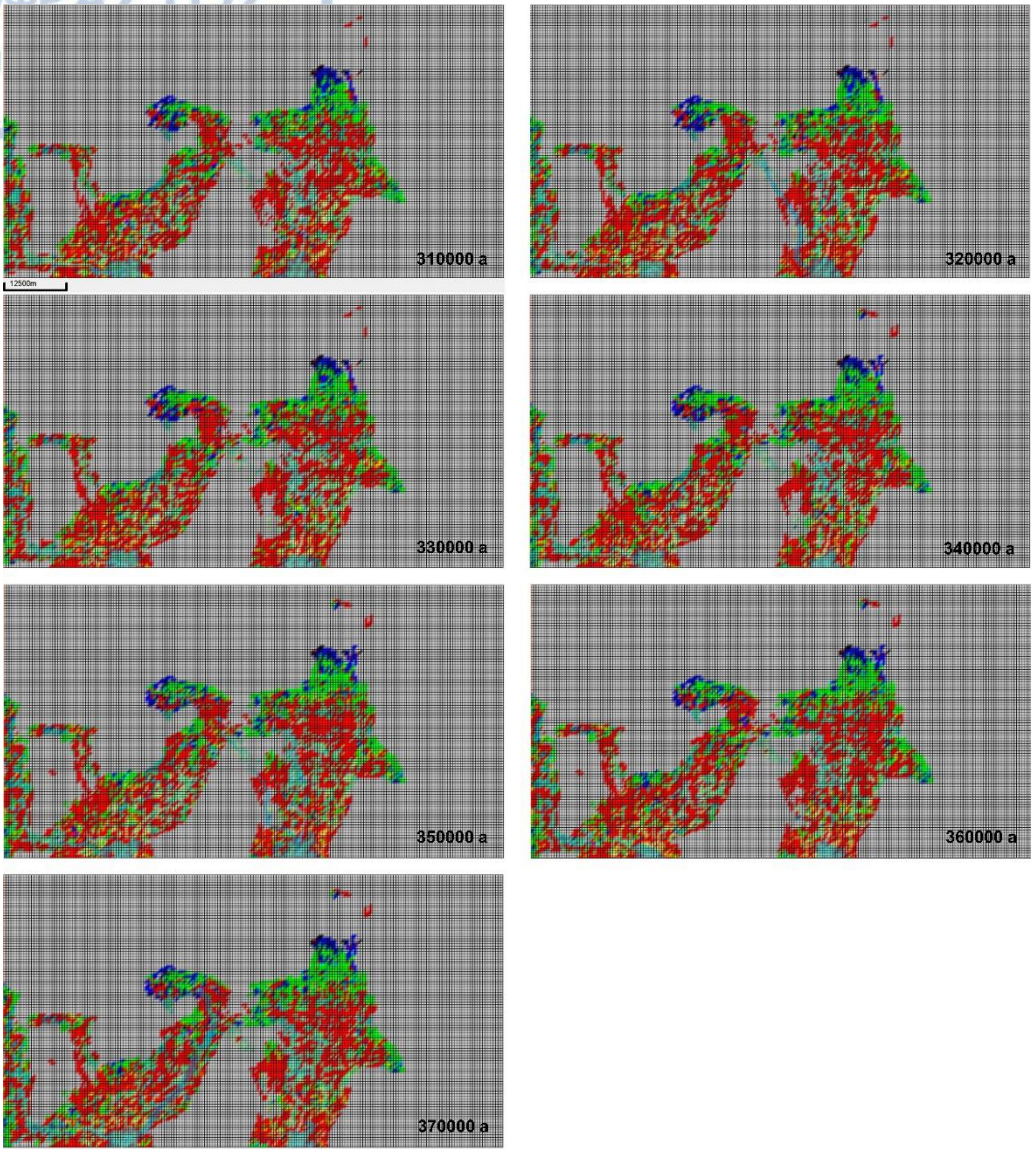

Figure 48 (continued): *Simulation results using as initial basin geomorphology the map introduced in Figure 44. Flow velocity of 5 m/s simulated velocity including sediments movement from 300 to 370 thousand years. The results color is a single color if the lithology is not mixed, e.g., coarse sand (red), fine sand (green), silt (blue), and clay (black), and color mixtures if the sediments comprise mixed lithologies.*

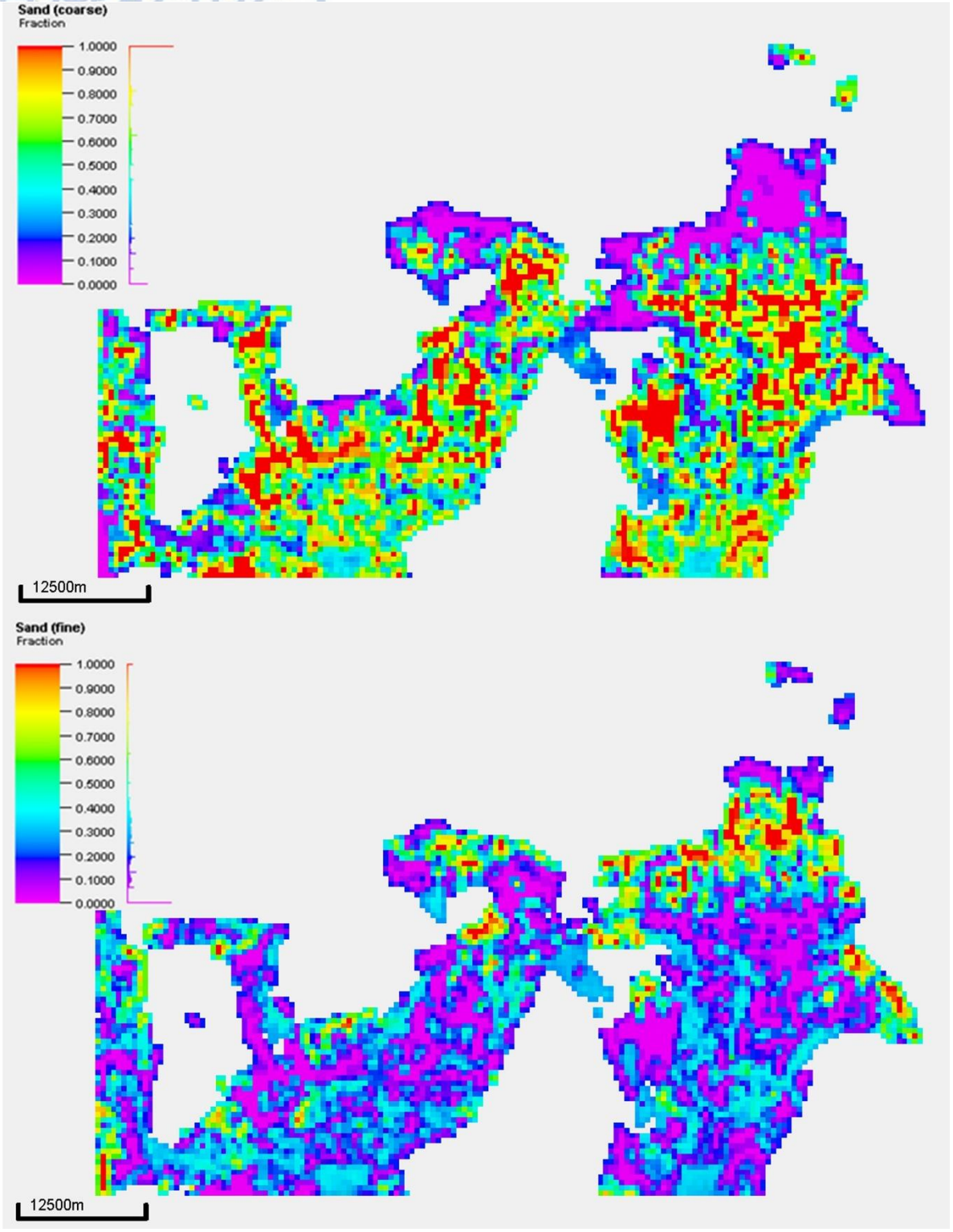

Figure 49: *Maps illustrating the coarse sand and fine sand fractions distribution as resulted from the simulations with velocities of 5 m/s.*

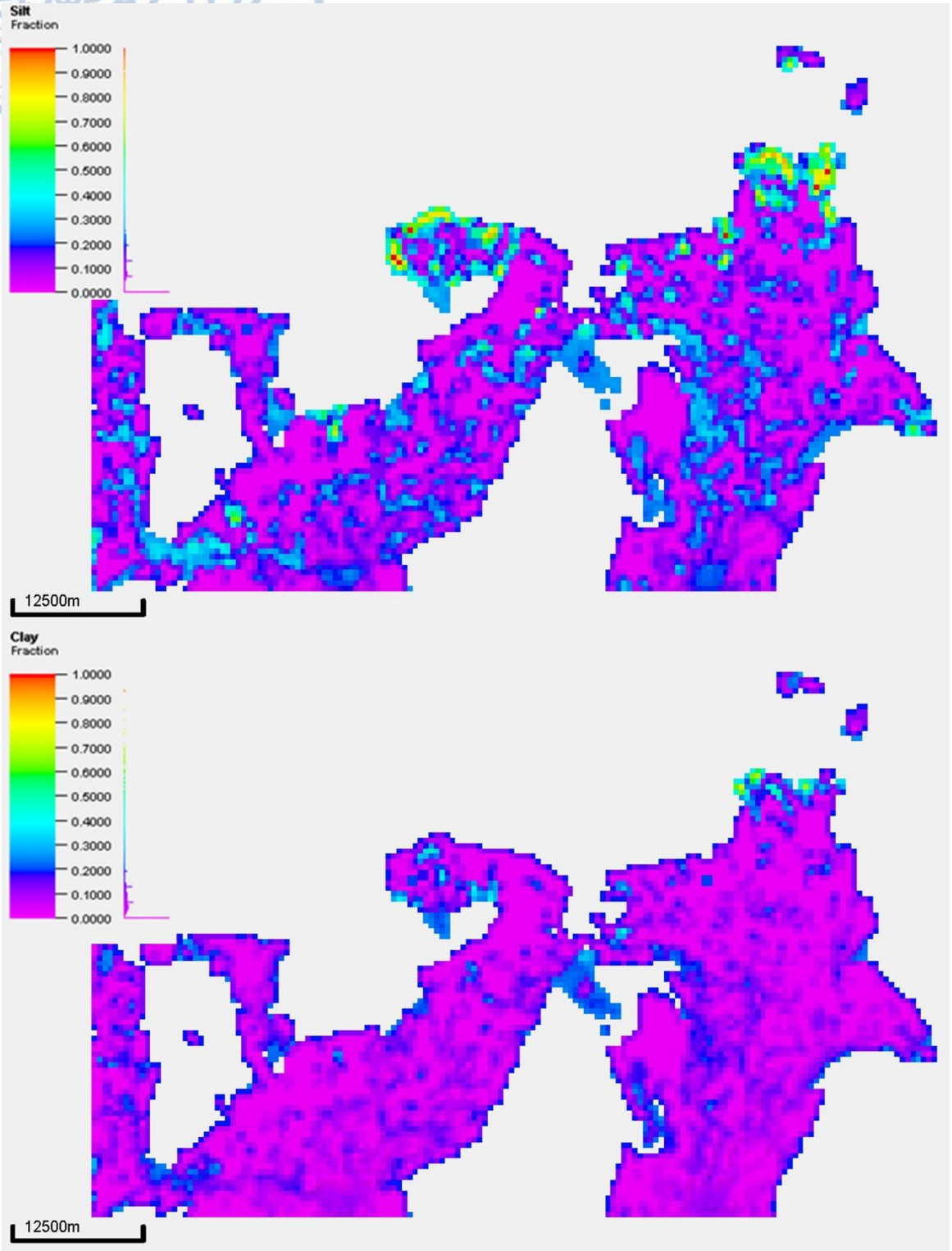

Figure 49 (continued): *Maps illustrating the silt and clay fractions distribution as resulted from the simulations with velocities of 5 m/s.*

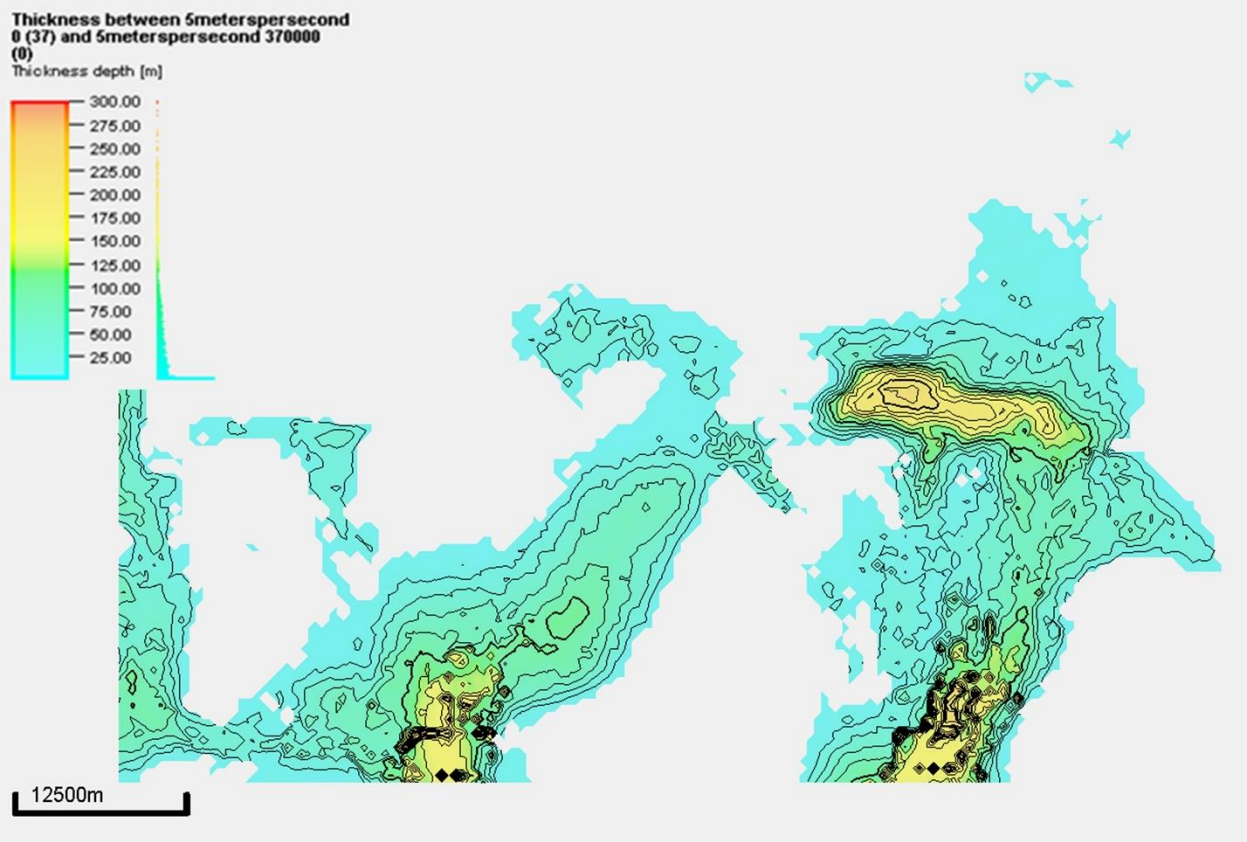

Figure 50: *Map illustrating the thickness of the clastic sediments simulated with 5 m/s.*

D.6.5.2 Experiments with 20 m/s

As previously mentioned, experiments without sediment movement were performed to test if the unsteady flow can reach the boundaries of the model (Fig. 51). Once the unsteady flow is checked, experiments are performed including the clastic sediments (Fig. 52). Again, the results are represented from a single color if the lithology is not mixed, e.g., coarse sand (red), fine sand (green), silt (blue), and clay (black), and color mixtures if the sediments comprise mixed lithologies (Fig. 52). Sediments fractions (sand coarse, sand fine, silt, and clay) are presented in Figure 53. Because of the higher velocity used in this experiment the coarse sand is mainly deposited immediately after the confined sections of the simulation surface while fine sand is deposited farther towards the most unconfined parts of the simulated area (Fig. 53). Silt and clay are mainly deposited at the most remote and

unconfined parts of the simulated surface (Fig. 53). Finally, an isopach map of the deposited sediments is presented in Figure 54.

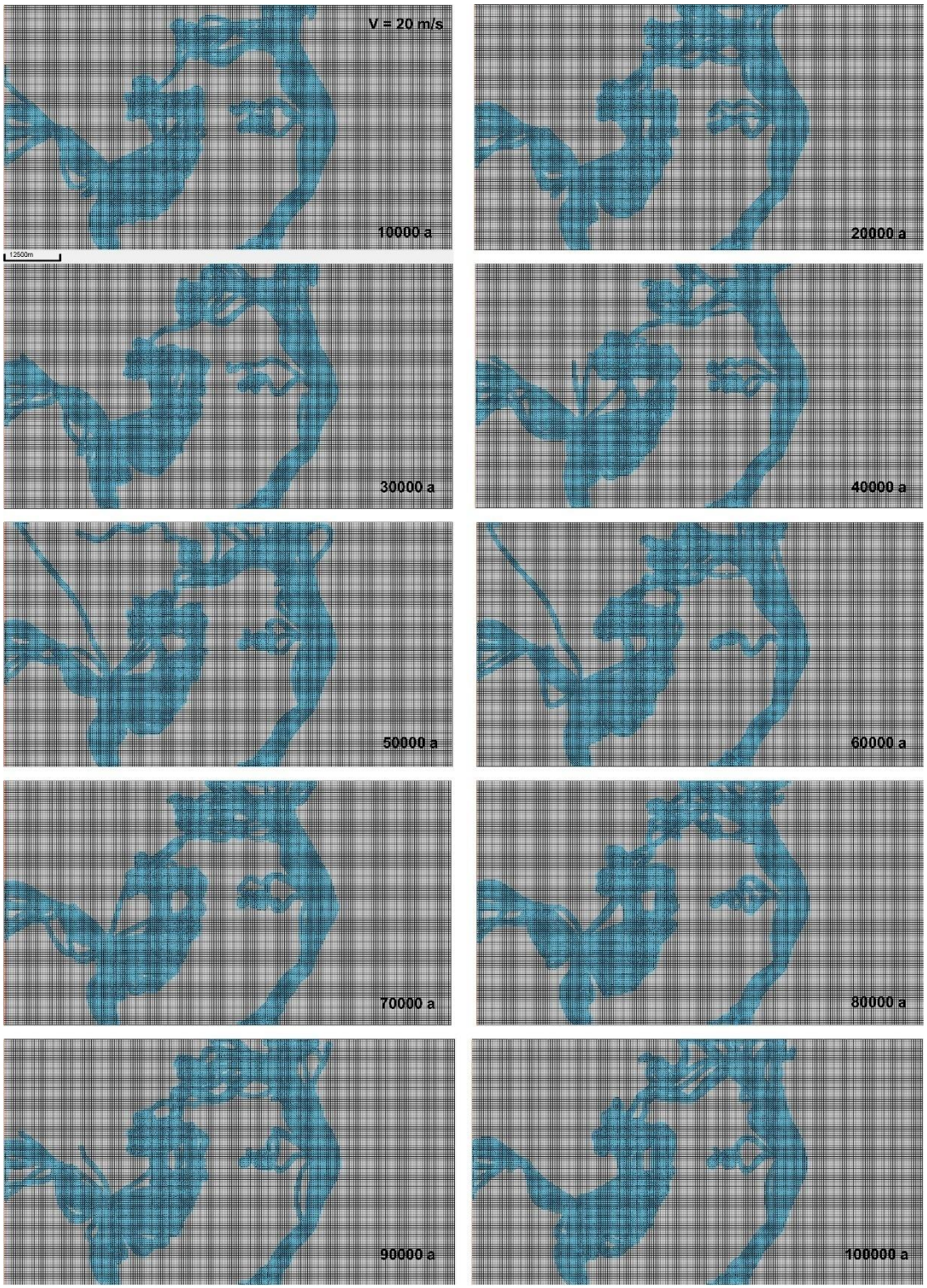

Figure 51: *Simulation results using as initial basin geomorphology the map introduced in Figure 44. Flow velocity of 20 m/s simulated without sediments movement from zero to 100 thousand years.*

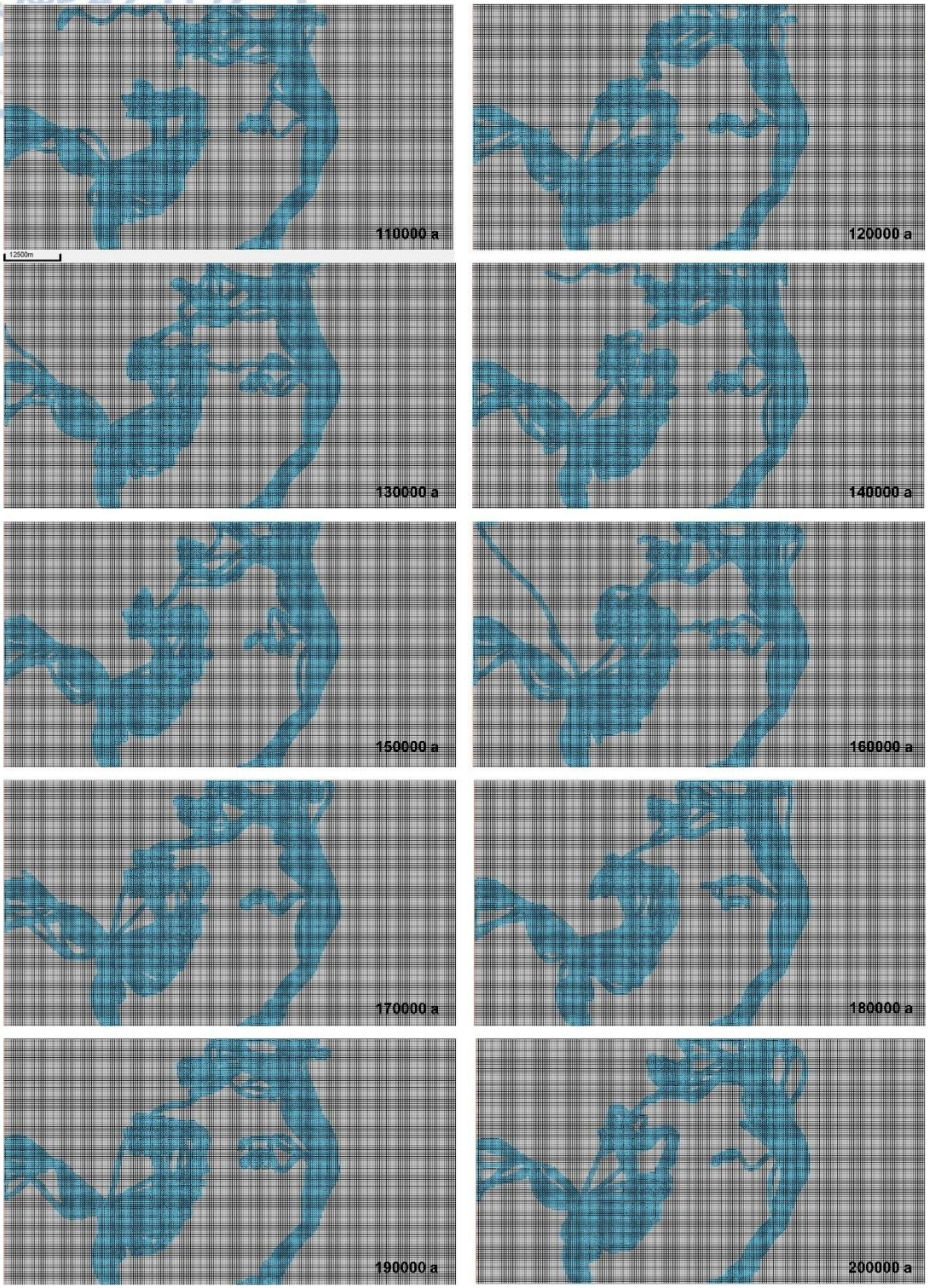

Figure 51 (continued): *Simulation results using as initial basin geomorphology the map introduced in Figure 44. Flow velocity of 20 m/s simulated without sediments movement from 100 to 200 thousand years.*

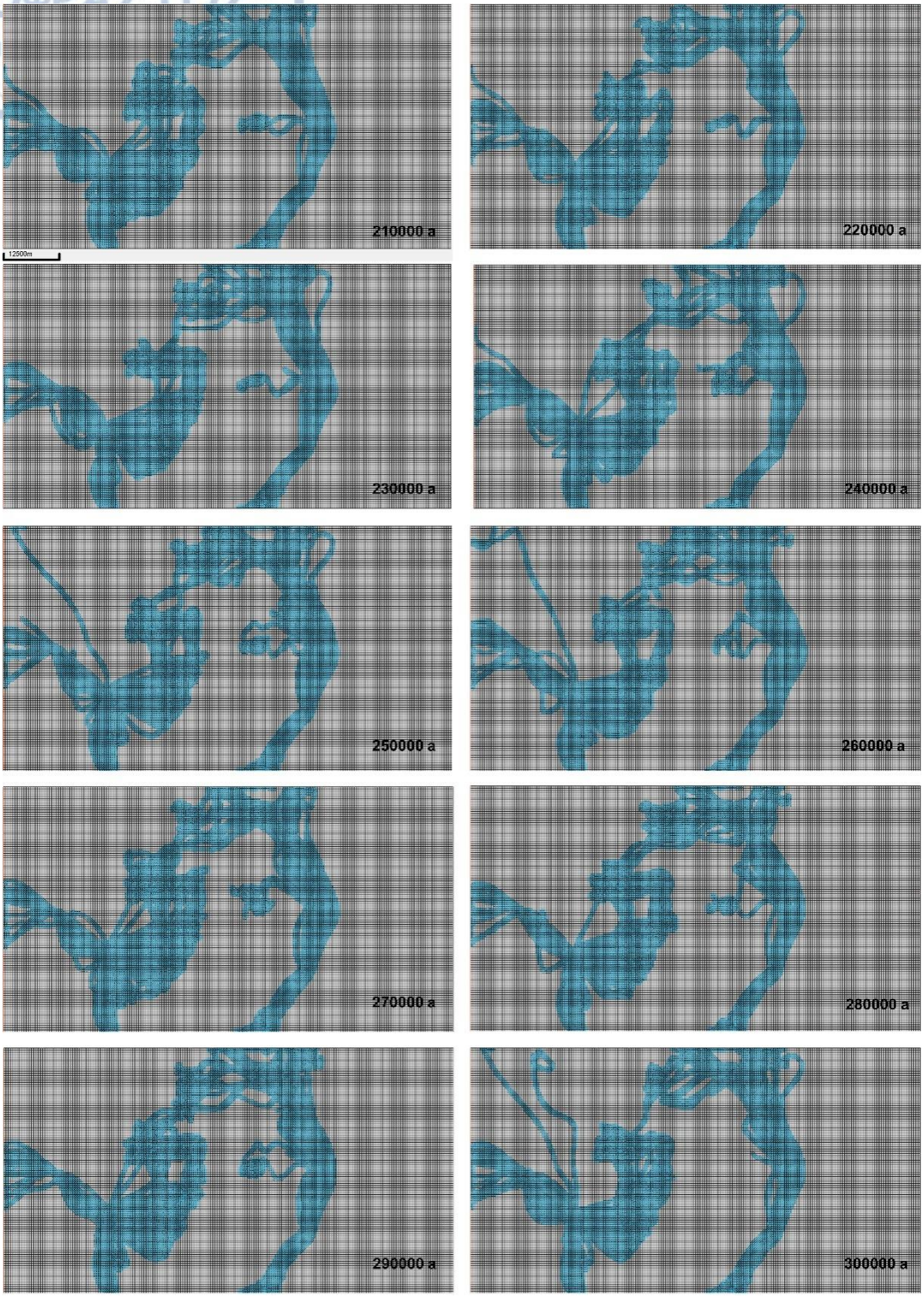

Figure 51 (continued): *Simulation results using as initial basin geomorphology the map introduced in Figure 44. Flow velocity of 20 m/s simulated without sediments movement from 200 to 300 thousand years.*

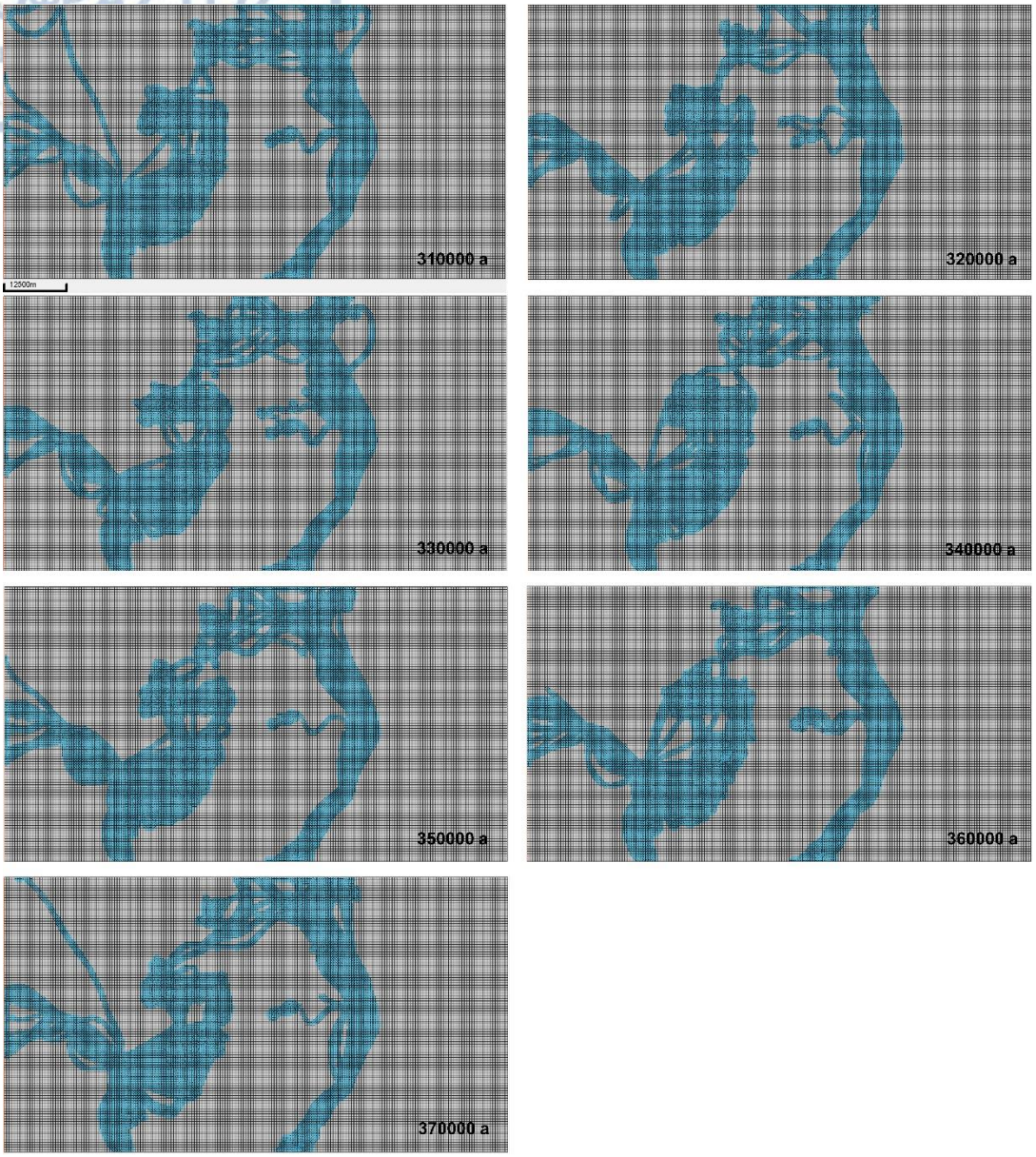

Figure 51 (continued): *Simulation results using as initial basin geomorphology the map introduced in Figure 44. Flow velocity of 20 m/s simulated without sediments movement from 300 to 370 thousand years.*

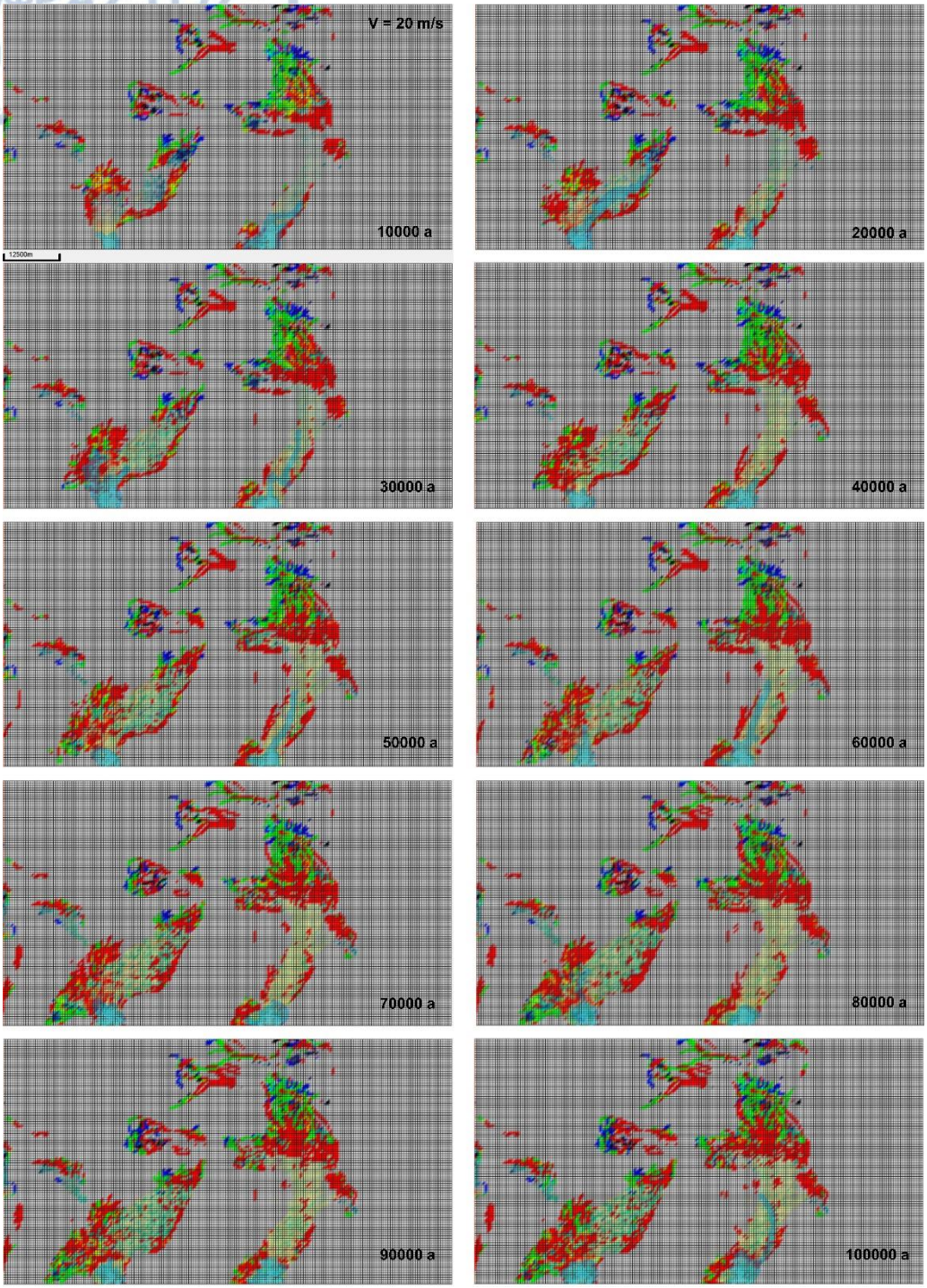

Figure 52: *Simulation results using as initial basin geomorphology the map introduced in Figure 44. Flow velocity of 20 m/s simulated including sediments movement from zero to 100 thousand years. The results color is a single color if the lithology is not mixed, e.g., coarse sand (red), fine sand (green), silt (blue), and clay (black), and color mixtures if the sediments comprise mixed lithologies.*

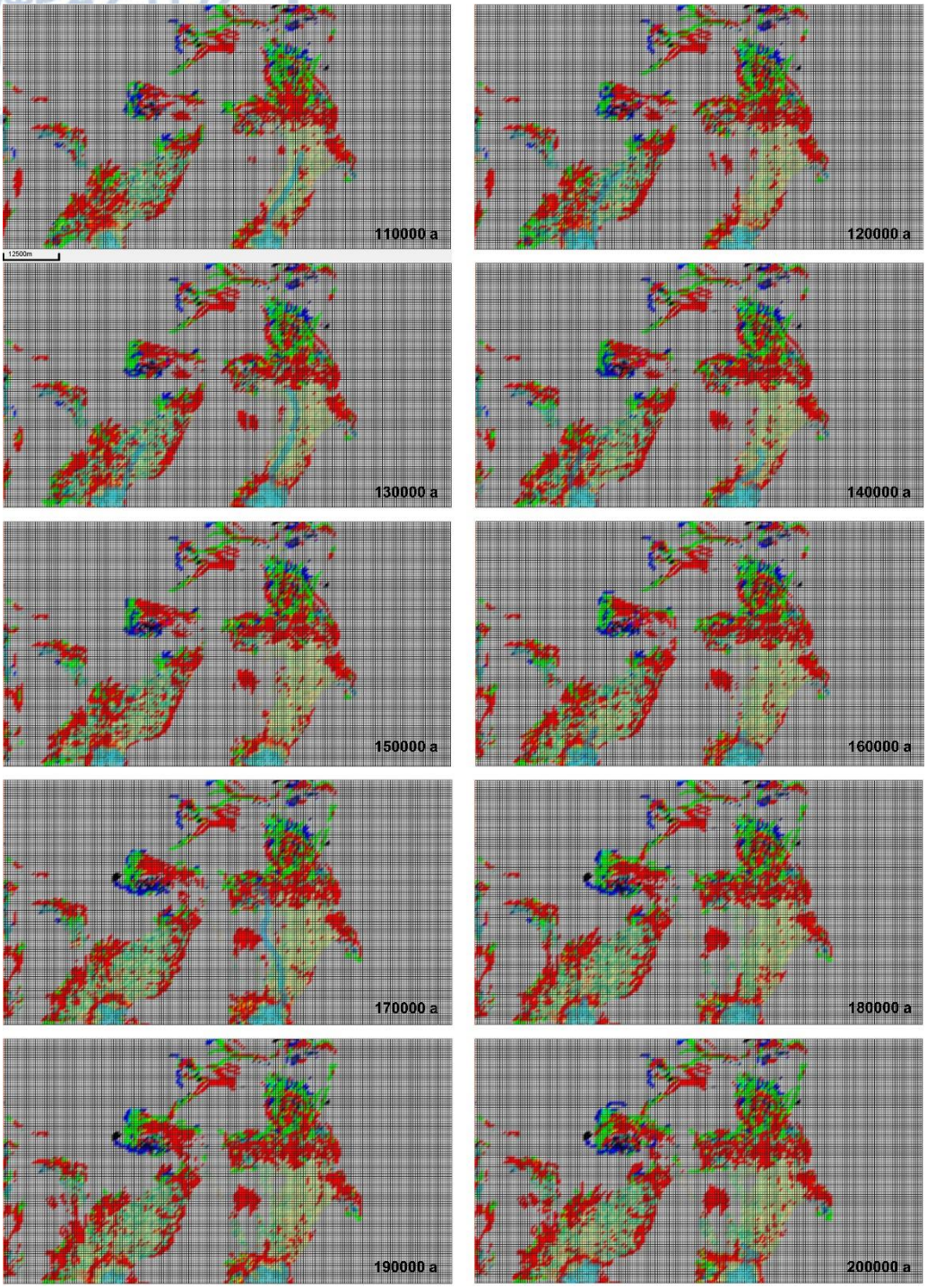

Figure 52 (continued): *Simulation results using as initial basin geomorphology the map introduced in Figure 44. Flow velocity of 20 m/s simulated including sediments movement from 100 to 200 thousand years. The results color is a single color if the lithology is not mixed, e.g., coarse sand (red), fine sand (green), silt (blue), and clay (black), and color mixtures if the sediments comprise mixed lithologies.*

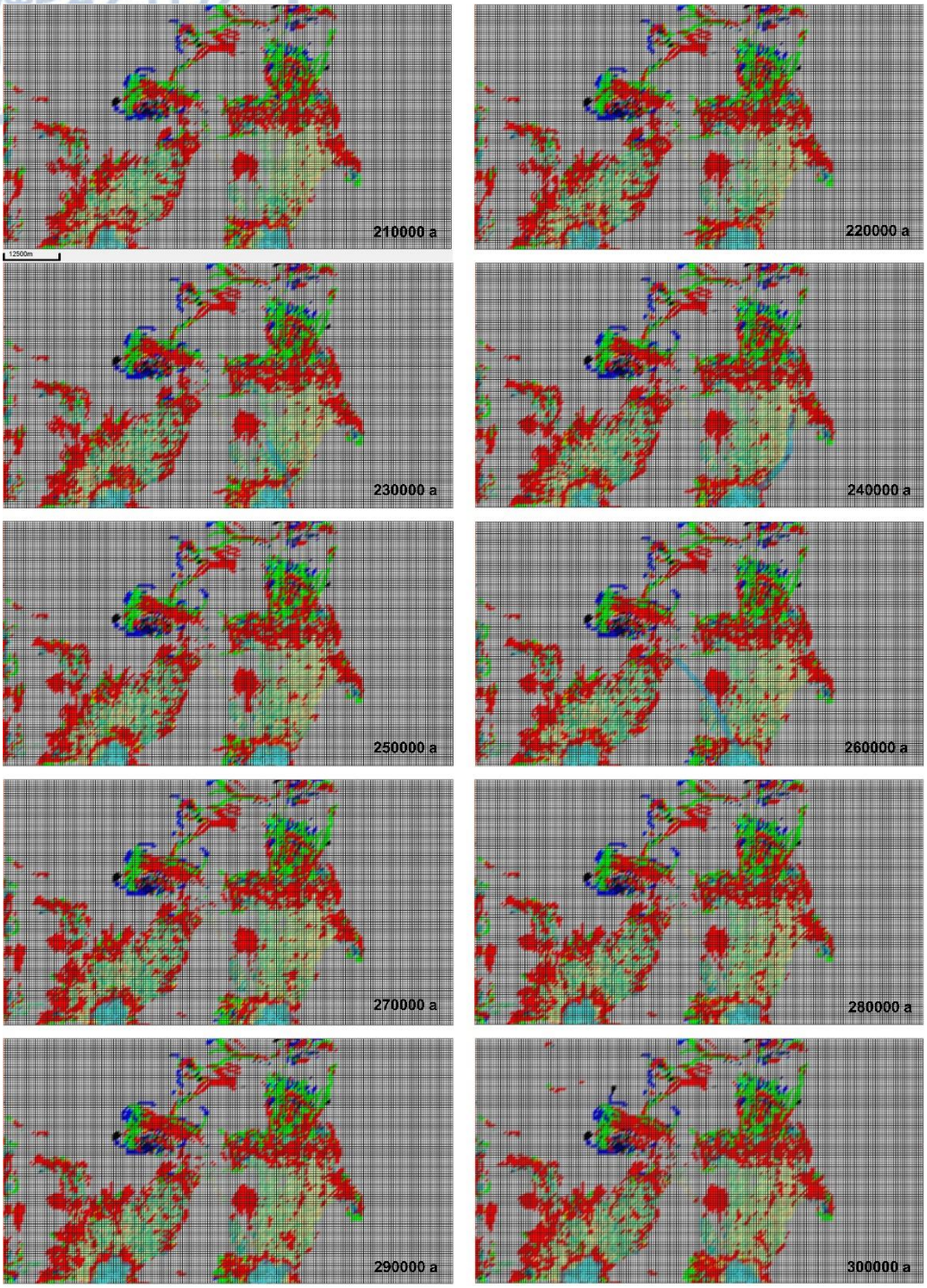

Figure 52 (continued): *Simulation results using as initial basin geomorphology the map introduced in Figure 44. Flow velocity of 20 m/s simulated including sediments movement from 200 to 300 thousand years. The results color is a single color if the lithology is not mixed, e.g., coarse sand (red), fine sand (green), silt (blue), and clay (black), and color mixtures if the sediments comprise mixed lithologies.*

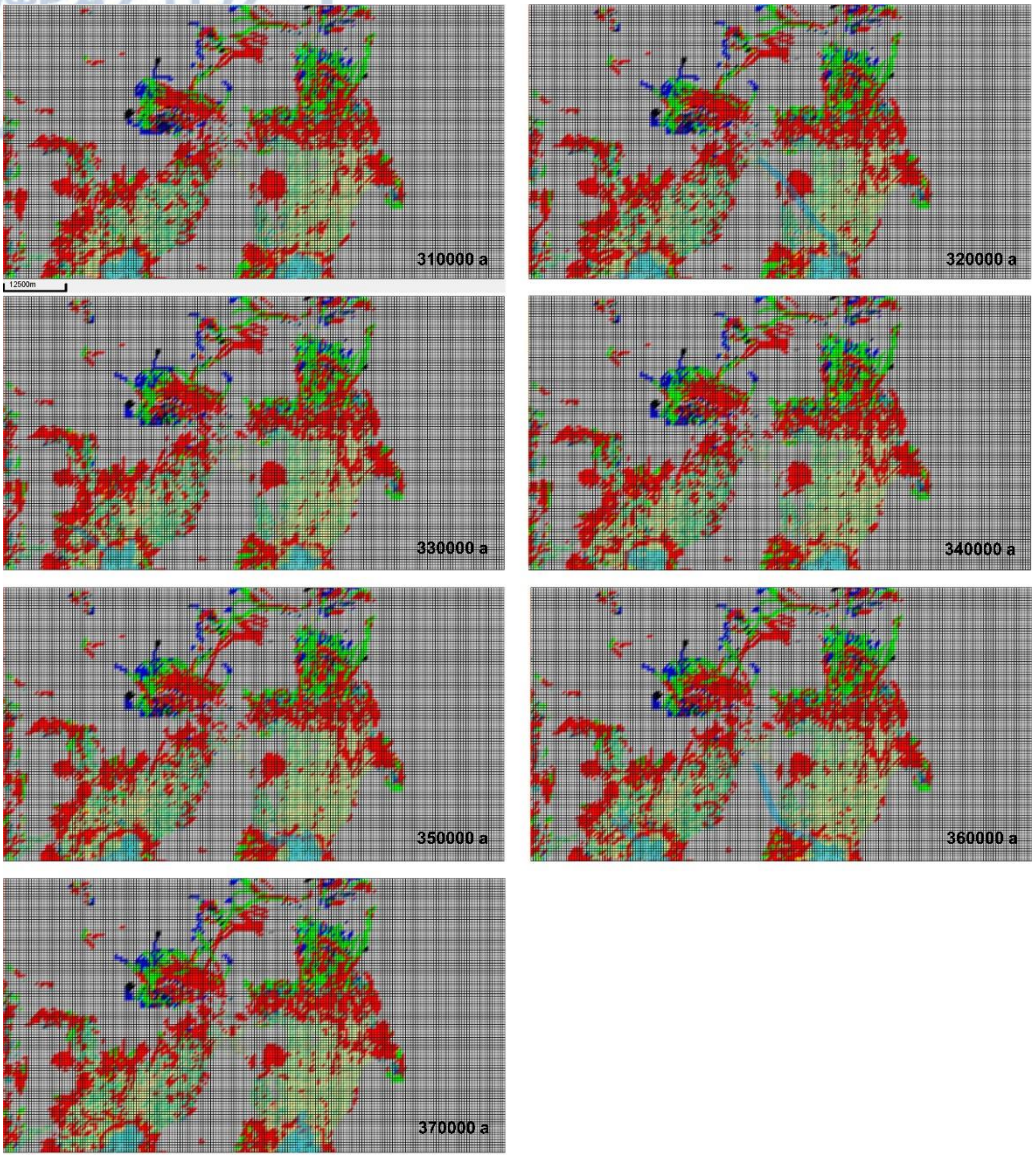

Figure 52 (continued): *Simulation results using as initial basin geomorphology the map introduced in Figure 44. Flow velocity of 20 m/s simulated including sediments movement from 300 to 370 thousand years. The results color is a single color if the lithology is not mixed, e.g., coarse sand (red), fine sand (green), silt (blue), and clay (black), and color mixtures if the sediments comprise mixed lithologies.*

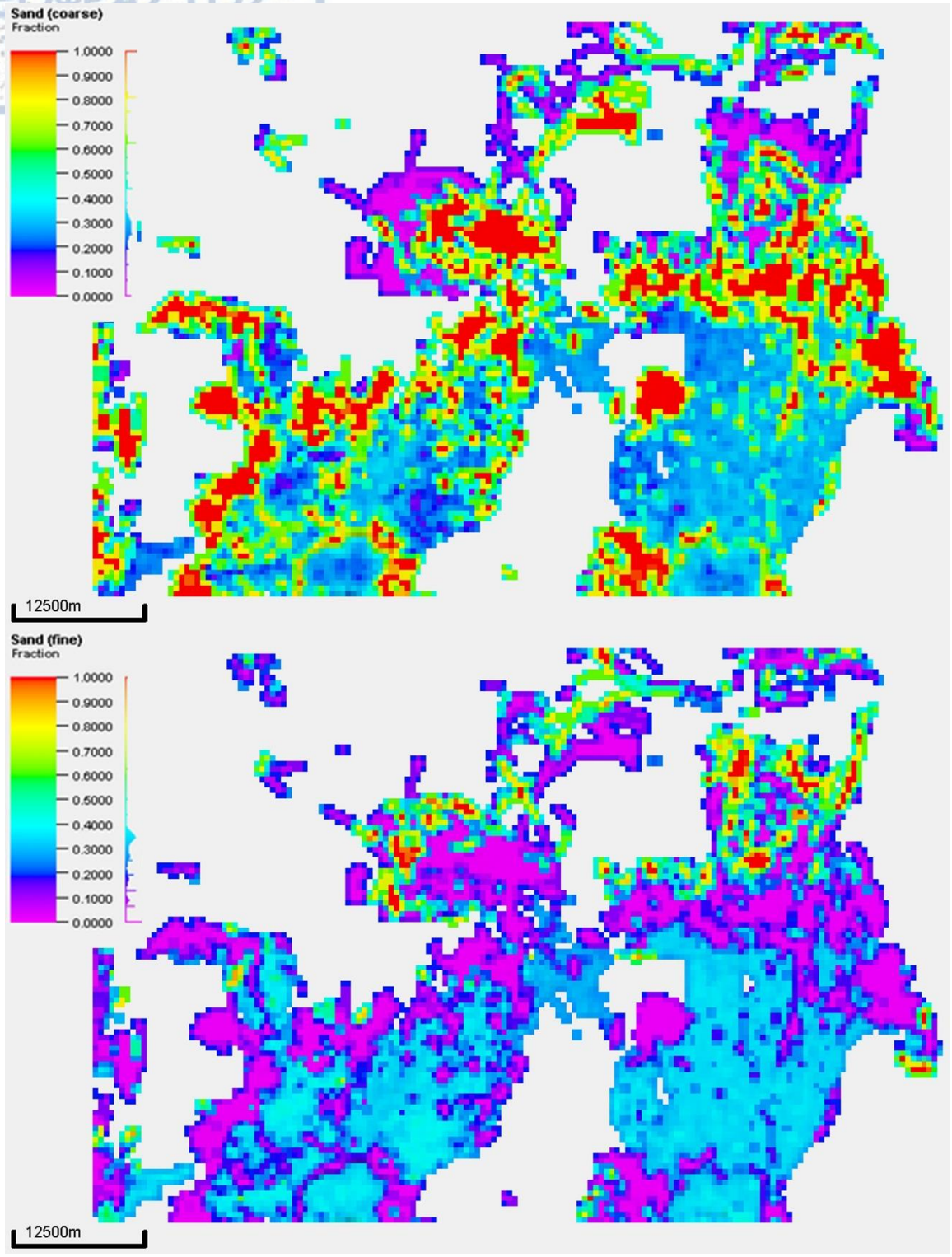

Figure 53: *Maps illustrating the coarse sand and fine sand fractions distribution as resulted from the simulations with velocities of 20 m/s.*

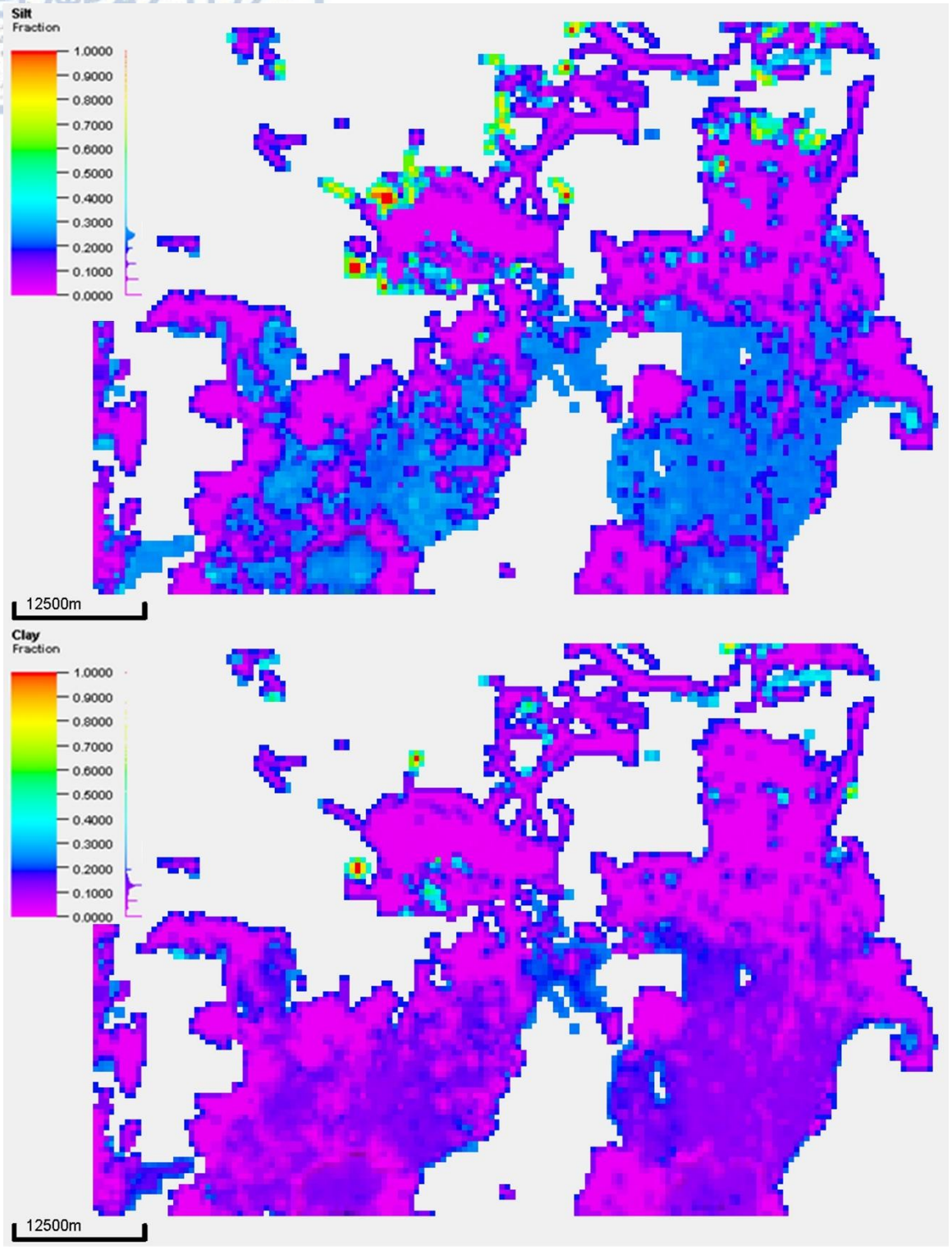

Figure 53 (continued): *Maps illustrating the silt and clay fractions distribution as resulted from the simulations with velocities of 20 m/s.*

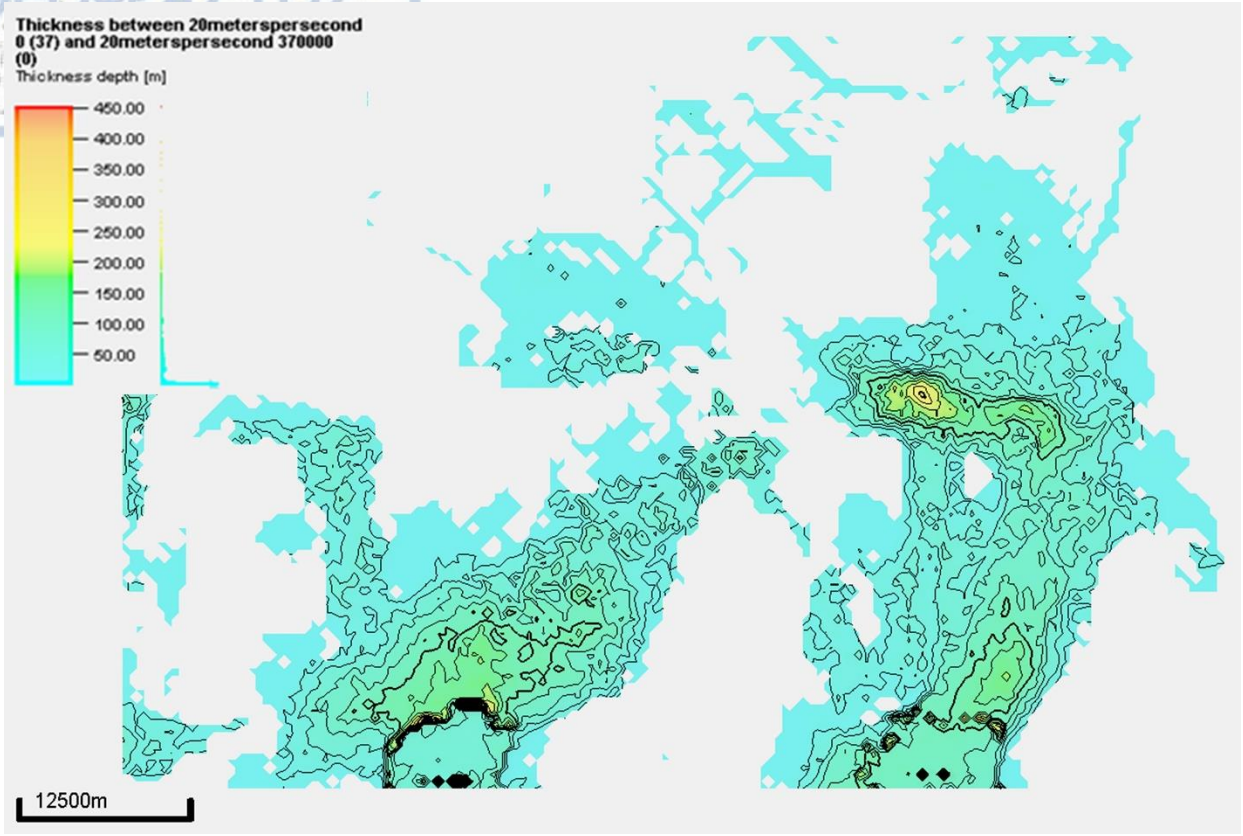

Figure 54: *Map illustrating the thickness of the clastic sediments simulated with 20 m/s.*

D.7 Comparison of seismic data with the simulation results

In this chapter, the final simulation results are compared with the high-quality 2D seismic data. This comparison mainly concerns the geometric characteristics of the pre-salt clastic sequences interpreted in the seismic data with the clastic sequences created by the Geological Process Model. The locations of the seismic lines presented in this chapter are annotated in Figure 55. The seismic lines presented in this chapter are in-depth (converted using the velocity model of PGS) with vertical exaggeration 1:1 to be comparable with the simulation results.

In the confined corridors 1A and 2A (see figure 31 and 36 A) the simulation results support a cut and fill concept. Discrete erosional surfaces that exhibit large lateral offset with limited aggradation, comprise corridors 1A and 2A in both experiments (Figs. 56 and 57). In corridor 1A a spill-over of the flow is discerned creating a proximal lobe complex as described in chapter 5.2 (Figs. 55 and 56). This spill-over of the flow occurs in both experiments with velocities of 5 m/s and 20 m/s (Fig. 56). In the unconfined corridor 1B immediately after the spread out of the flow the clastic deposits illustrate more lobate geometries with the erosion becoming weaker (Fig. 58) in the experiment with 5 m/s. However, in the experiment with t 20 m/s erosion is prevailing and the overall geometry of the clastic system refers to a cut and fill concept. In the northern area of the confined corridor 2A, the simulation experiments with velocities of 5 m/s suggest more lobate geometries while the 20 m/s experiments suggest a cut and fill concept (Fig. 59). Again, is observed that the higher the turbiditic velocity the higher is the erosion that is illustrated in the simulation experiments. In the unconfined corridor 1B the simulation results of both experiments suggest a lobe complex (Fig. 60). The lobe geometries in simulation result with 20 m/s are sharper indicating that erosion has still existed during the sedimentary processes.

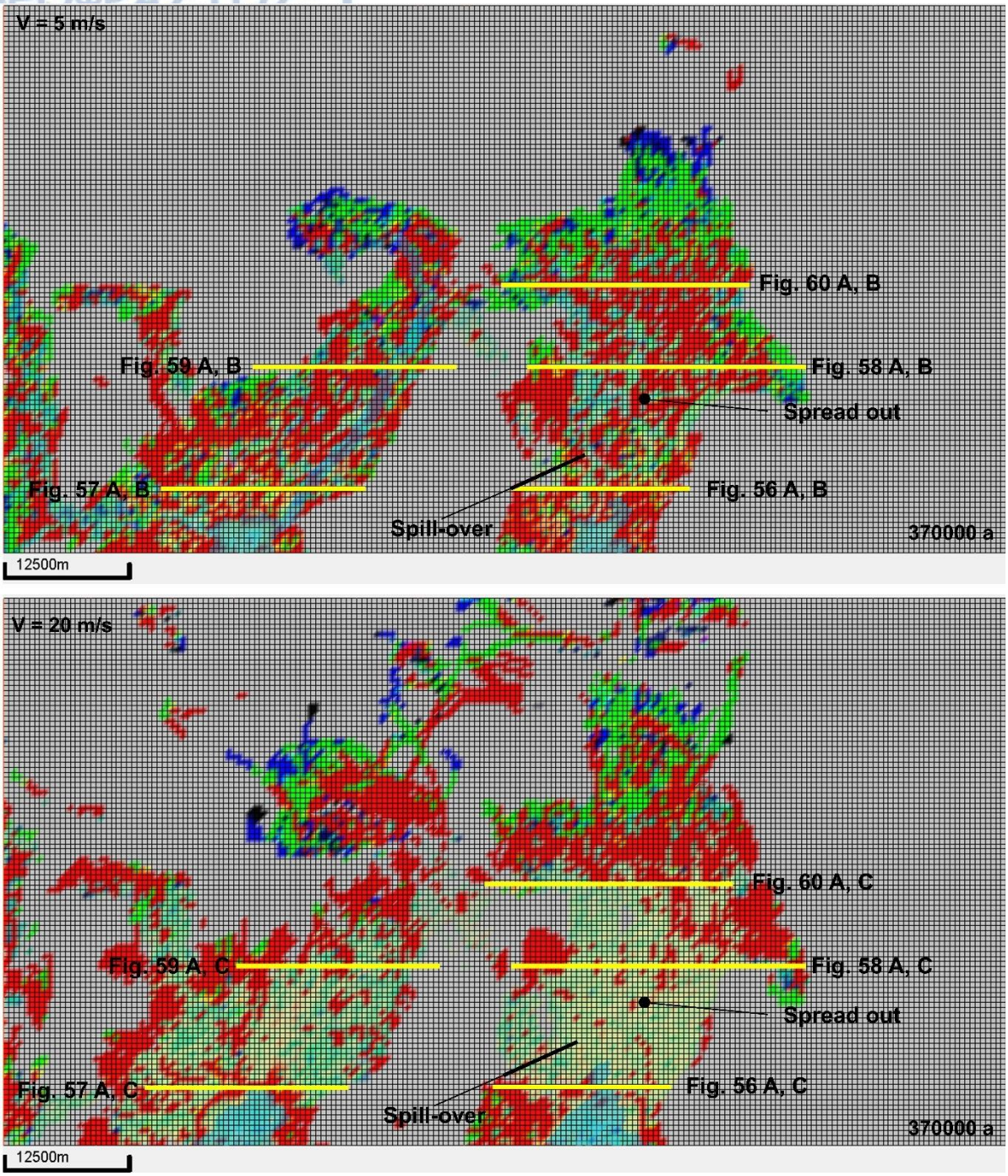

Figure 55: *Final simulation results (370 thousand years) using as initial basin geomorphology the map introduced in Figure 44. Flow velocity results of 5 m/s and 20 m/s are presented. The results are represented by a single color if the lithology is not mixed, e.g., coarse sand (red), fine sand (green), silt (blue), and clay (black), and color mixtures if the sediments comprise mixed lithologies. Yellow lines illustrate the positions of seismic sections and model slices presented in figures 56, 57, 58, 59, and 60. The spill-over area and the spread-out point are also annotated.*

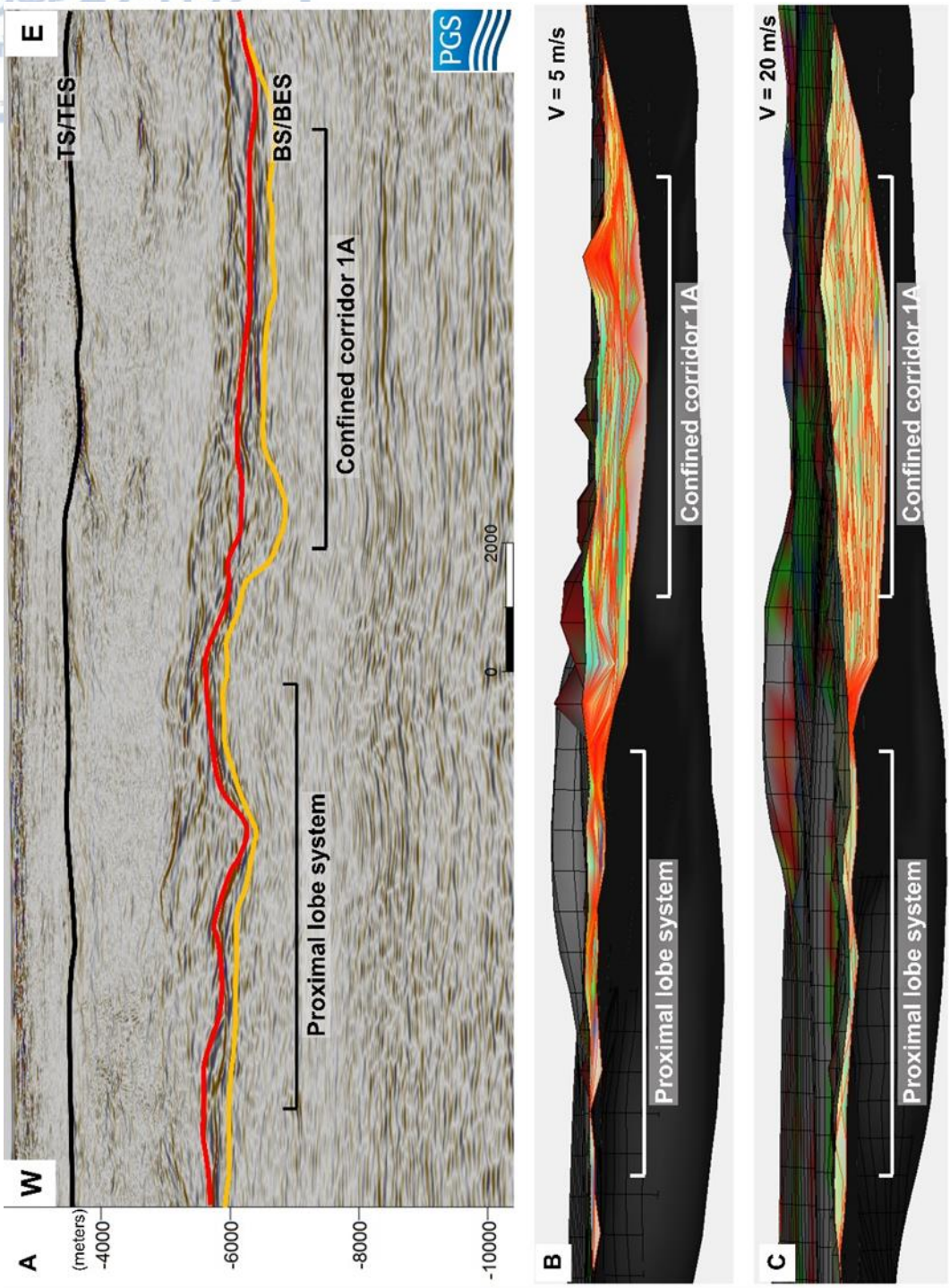

Figure 56: *(A) presents an interpreted west-east oriented depth seismic cross-section with vertical exaggeration 1:1. The pre-salt clastic system is delimited by the red line (top) and the orange line (base). The proximal lobe system created by the flow spill-over and the confined corridor 1A can be discerned. The Top Surface/Top Erosion Surface and Base Surface/ Base Erosion Surface are also presented. (B) illustrates a slice of the experiment result with a velocity of 5 m/s. (C) illustrates a slice of the experiment result with a velocity of 20 m/s. In both experiments, the proximal lobe complex and the confined corridor 1A can be discerned. For location see Figure 55.*

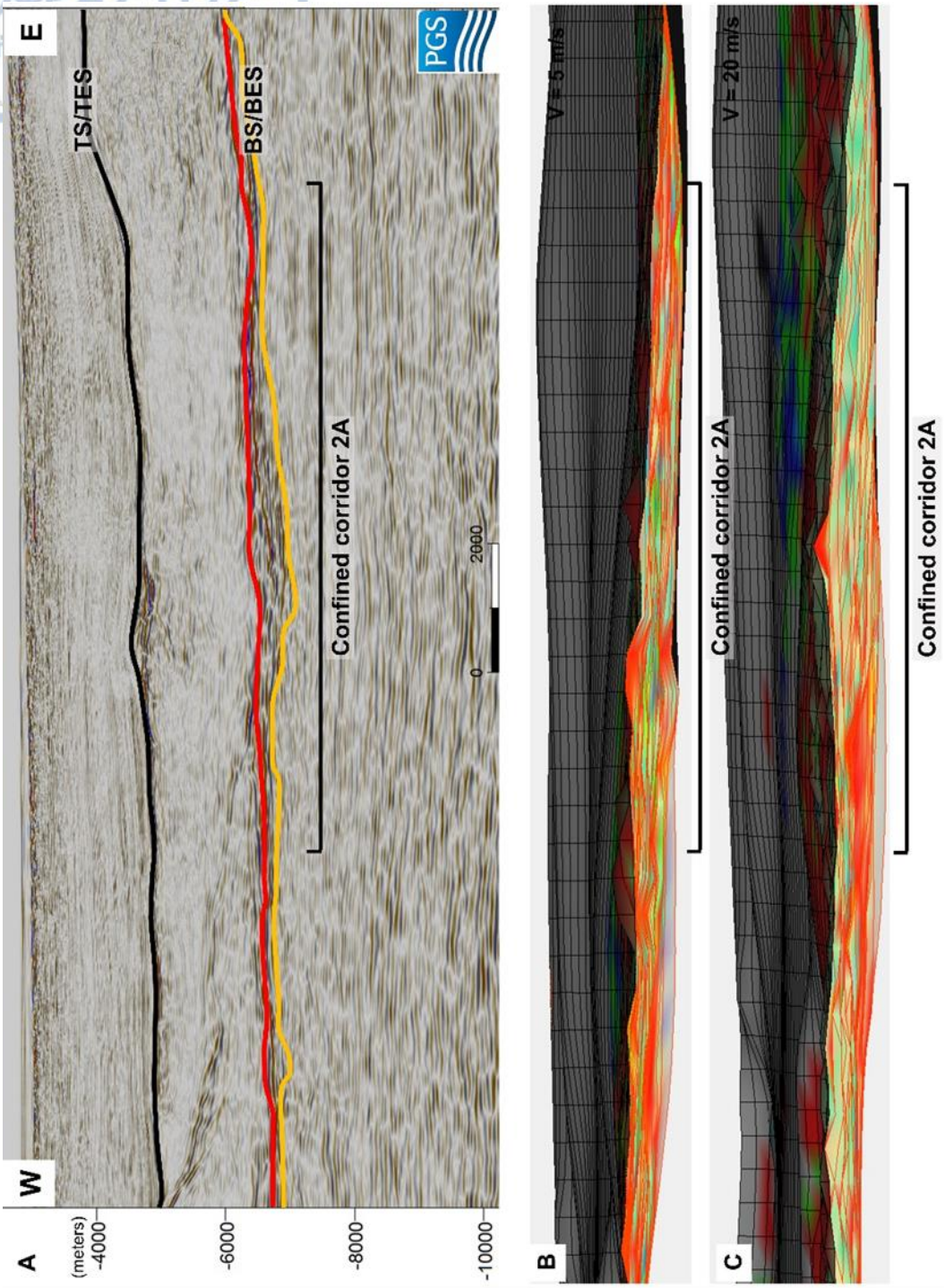

Figure 57: *(A) presents an interpreted west-east oriented depth seismic cross-section with vertical exaggeration 1:1. The pre-salt clastic system is delimited by the red line (top) and the orange line (base). Corridor 2A exhibits a large lateral offset with aggradation. The Top Surface/Top Erosion Surface and Base Surface/ Base Erosion Surface are also presented. (B) illustrates a slice of the experiment result with a velocity of 5 m/s. (C) illustrates a slice of the experiment result with a velocity of 20 m/s. In both experiments, the large lateral offset and the aggradation can be discerned. For location see Figure 55.*

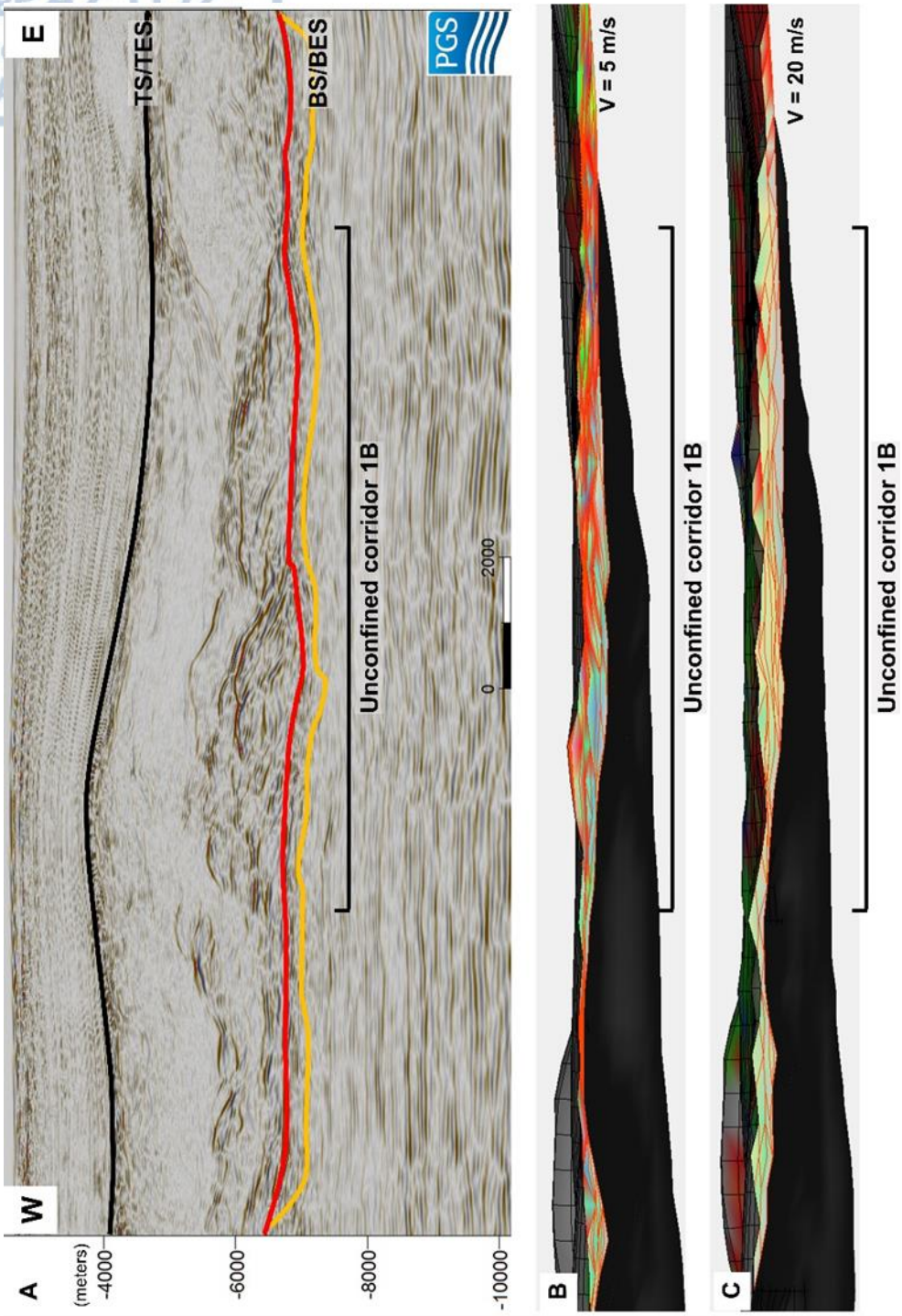

Figure 58: *(A) presents an interpreted west-east oriented depth seismic cross-section with vertical exaggeration 1:1. The pre-salt clastic system is delimited by the red line (top) and the orange line (base). Corridor 1B immediately after the spread out exhibits a large lateral offset with limited aggradation. More lobate geometries are observed. The Top Surface/Top Erosion Surface and Base Surface/ Base Erosion Surface are also presented. (B) illustrates a slice of the experiment result with a velocity of 5 m/s. Less erosion was observed in figure B with the overall geometry indicating a lobe complex. As the flow becomes unconfined and weaker more sand is deposited in the experiment with a velocity of 5 m/s. (C) illustrates a slice of the experiment result with a velocity of 20 m/s.In higher velocities, erosion is prevailing with the clastic system's overall geometry supporting a cut and feal concept. In both experiments, the large lateral offset and the limited aggradation can be discerned. For location see Figure 55.*

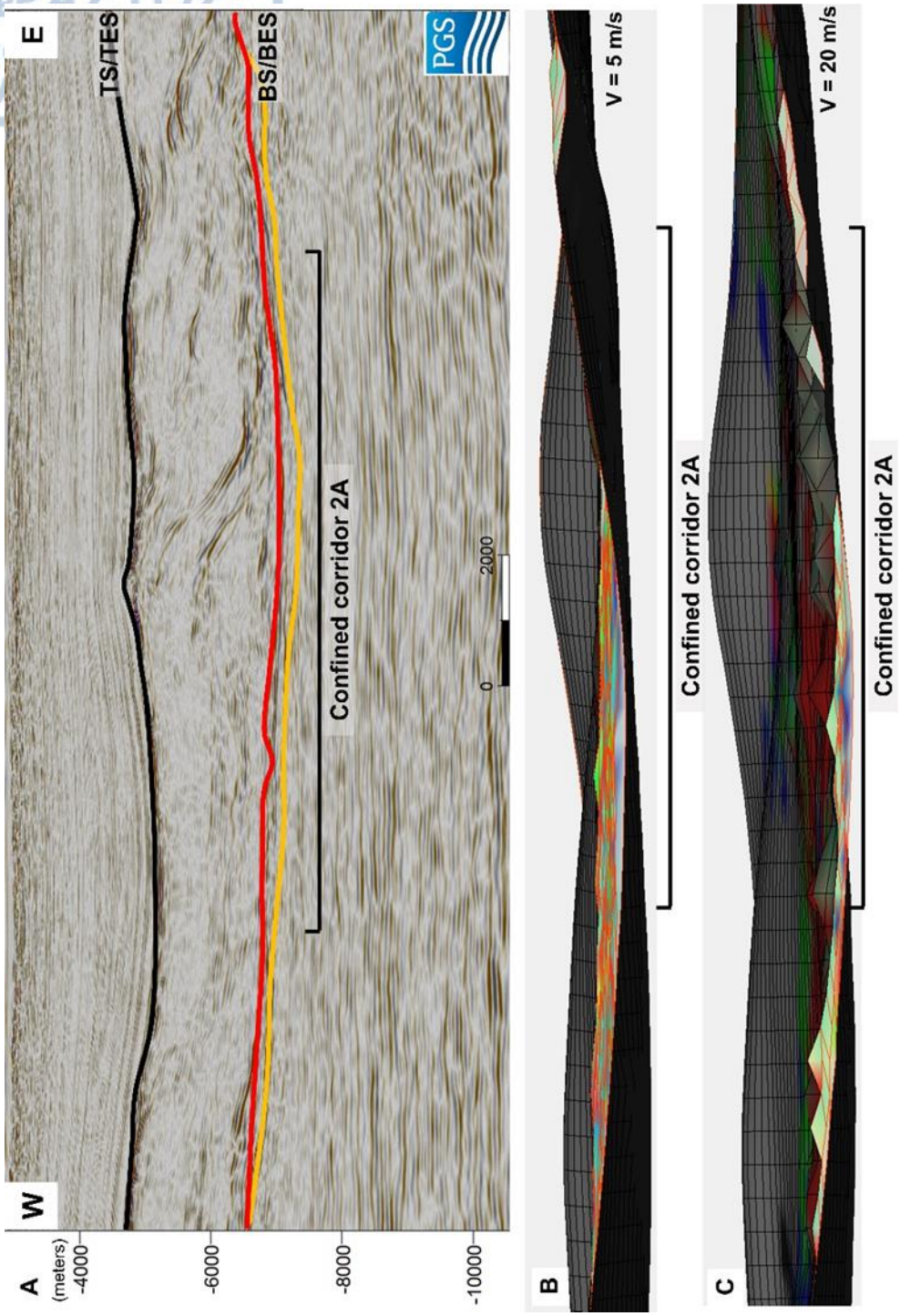

Figure 59: *(A) presents an interpreted west-east oriented depth seismic cross-section with vertical exaggeration 1:1. The pre-salt clastic system is delimited by the red line (top) and the orange line (base). The northern reaches of corridor 1A exhibit a large lateral offset with limited aggradation. The Top Surface/Top Erosion Surface and Base Surface/Base Erosion Surface are also presented. (B) illustrates a slice of the experiment result with a velocity of 5 m/s. Less erosion was observed in figure B with the overall geometry indicating more lobate geometries. Again, as the flow becomes unconfined and weaker more sand is deposited in the experiment with a velocity of 5 m/s. (C) illustrates a slice of the experiment result with a velocity of 20 m/s. In higher velocities, erosion is prevailing with the clastic system's overall geometry supporting a cut and feal concept. The clastic deposits are thinner in the results of the experiment with a velocity of 20 m/s. In both experiments, the large lateral offset and the limited aggradation can be discerned. For location see Figure 55.*

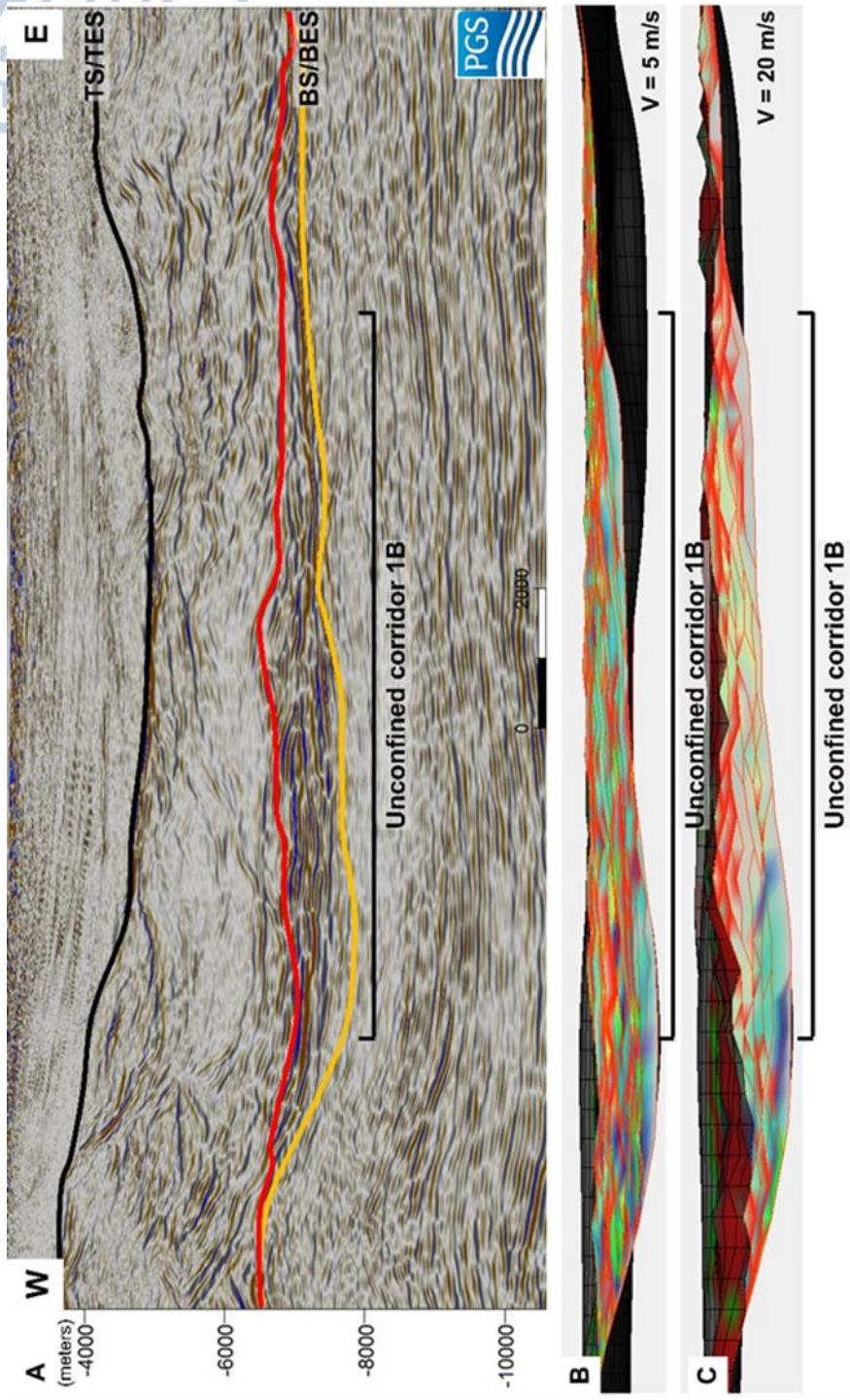

Figure 60: *(A) presents an interpreted west-east oriented depth seismic cross-section with vertical exaggeration 1:1. The pre-salt clastic system is delimited by the red line (top) and the orange line (base). Corridor 1B exhibits a large lateral offset with aggradation. The Top Surface/Top Erosion Surface and Base Surface/ Base Erosion Surface are also presented. (B) illustrates a slice of the experiment result with a velocity of 5 m/s. Erosion is not observed in figure B with the overall geometry indicating a lobe complex. Again, as the flow becomes unconfined and weaker more sediments are deposited in the experiment with a velocity of 5 m/s. (C) illustrates a slice of the experiment result with a velocity of 20 m/s. In higher velocities, erosion insists and the surfaces between the clastic sequences become sharper. In both experiments, the large lateral offset and aggradation can be discerned. For location see Figure 55.*

Finally, a comparison between the spatial distribution of the mapped pre-salt clastic systems and the distribution of the simulation results for velocities of 5 and 20 m/s is presented in Figure 61. The simulations with velocities of 5 m/s fail to create the extensive lobe complex mapped in the seismic data while the simulation results with velocities of 20 m/s have a better sediment spatial distribution which is closer to the mapped clastic deposits (Fig. 61). This difference is mainly attributed to the higher velocities of the experiments with 20 m/s resulted in an extensive spreading of the input sediments.

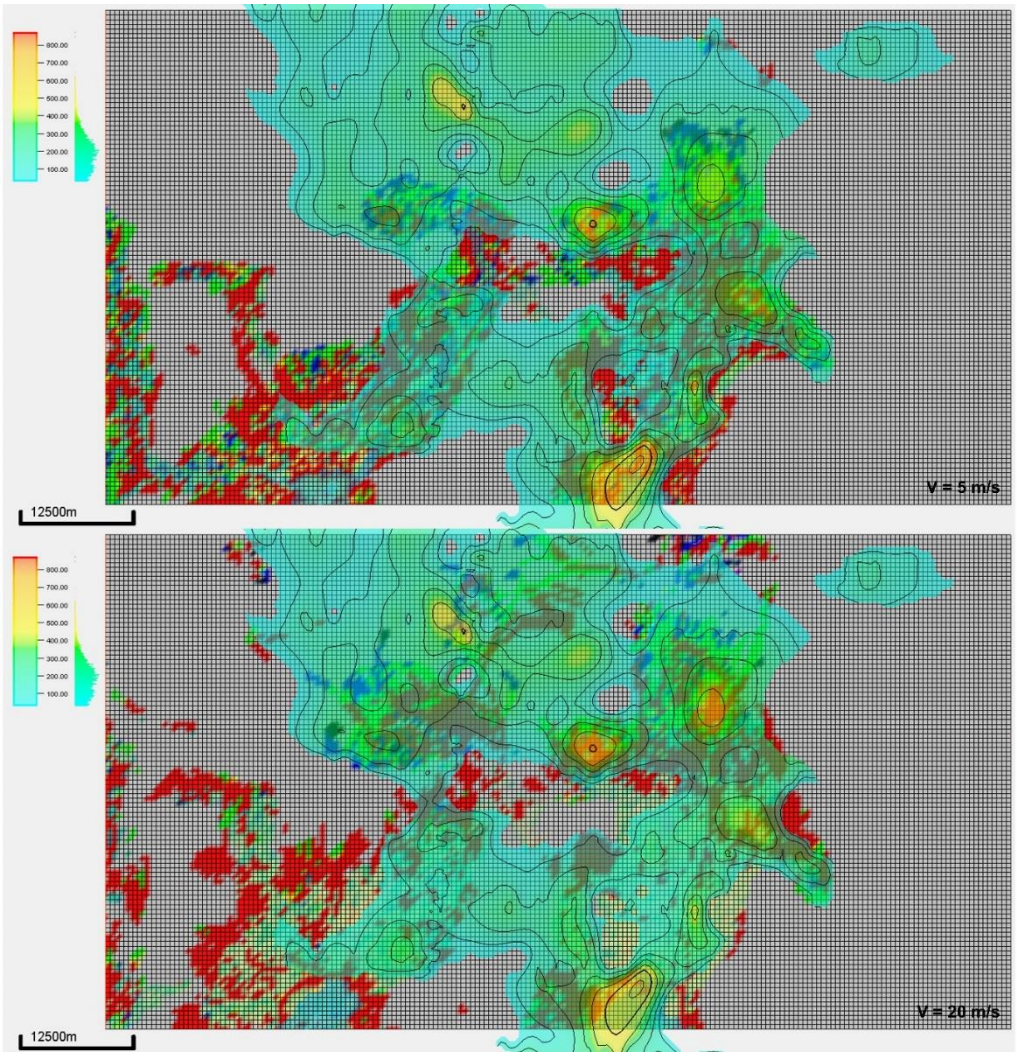

Figure 60: *Final simulation results (370 thousand years) using the initial basin geomorphology introduced in Figure 44. Flow velocity results for 5 m/s and 20 m/s are presented. In each simulation result, a similar distribution was obtained compared to the isopach map of the mapped pre-salt clastic systems shown in figure 36. A better sediment distribution similar to the mapped pre-salt clastic systems is obtained with the higher velocity of 20 m/s.*

D.7.1 Restrictions and implication for hydrocarbon potential

The results, therefore, need to be interpreted with caution because many restrictions are presented mainly related to the scarcity of the seismic data. 2310 km of 2D seismic data were used in the present study. More hardcore data are needed to derive more realistic results (e.g., 2D-3D seismic data, well data, well log data, etc.). The natural processes are continuous through time and the eleven-year interval was used only to save computation time. The available observations show that natural processes such as turbidity flows can occur very frequently in a single year (Heerema et al., 2020). The simulations are usually contacted to achieve an idea of reality but not reality and are subjective when the hardcore data are very limited.

The 1D backstripping applied in the present study was extended into 3 dimensions to achieve a reconstruction of the Messinian relief. The resulted surface is indicative of the geomorphology that was prevailing during Messinian. Again, to obtain a more realistic reconstruction (backstripping), more hardcore data are needed. Finally, tectonic backstripping is also an important issue to be considered but it presupposes the existence of well-mapped faults, something that can be achieved only with high-quality 3D seismic data.

The geometry of the pre-salt clastic systems interpreted from the 2D seismic lines is better described with the velocities of 5 m/s while their distribution is better described with higher velocities of 20 m/s. For this reason, future simulations must include more frequent turbiditic events with velocities lower than 20 m/s to obtain a similar spatial distribution. However, despite all the restrictions a very good match between the mapped pre-salt clastic systems and the simulation result was achieved indicating that these seismic facies can be produced from deep-sea processes such as turbidites. Such deposits may host important hydrocarbon reserves.

E.8. Conclusions

E.8.1 Conclusions about the MSC sequence deformation

2D seismic reflection data are used in this study to investigate salt tectonic deformation patterns of the Messinian Salinity Crisis (MSC) sequence at the eastern part of the Herodotus Basin in the Eastern Mediterranean. The seismic dataset reveals different mechanisms of salt and overburden deformation within five distinct salt-tectonic structural provinces (P1 - P5).

In the West Eratosthenes sub-Basin (WEsB; P1), the MSC sequence is well protected by regional salt tectonics due to the ECB carbonates morphology. Salt-related deformation is limited at the southern and eastern boundaries of the WEsB because of regional crust tectonics accompanied by gravity spreading. The seismic image of the MSC sequence is indicative of autochthonous salt precipitation comparable to the Levantine Basin.

Structureless salt segments characterize the salt-deformation in the area north-west of the Eratosthenes Continental Block (P2). These salt segments represent allochthonous salt, derived from the Cyprus-Eratosthenes collision zone due to compressional tectonics and comprise the westernmost boundary of a salt-shortening belt located north of the Eratosthenes Continental Block.

South and south-west of the Eratosthenes Continental Block (P3), salt deformation is driven by a combination of gravity spreading and gravity gliding shown by the formation of reverse faults with opposite offsets and the compressional thickened salt deposits. Salt flow is directed further west towards the Herodotus Basin.

In the easternmost part of the Herodotus Basin (P4) salt derived from the south and south-west of the Eratosthenes Continental Block is severely compressed. In the southern part of P4, salt compression due to regional tectonics and gravity gliding is accompanied by gravity spreading that predominates in the deep Herodotus Basin (P5). In the central and

northern parts of P4, salt-deformation is principally due to gravity spreading combined with gravity gliding.

The semi-circular bathymetric step observed at the northern, eastern, and southern flanks of the Eratosthenes Continental Block is attributed to different salt deformation mechanisms. In all three cases, the Plio-Quaternary clastic deposits act as a back stop to the Messinian salt and prevent its movement towards the Eratosthenes Continental Block. This process results in the uplift of the surrounding seafloor. At the western flank of the Eratosthenes Continental Block the bathymetric step is missing. The absence of the bathymetric step is attributed to the compressional thickening of the Messinian salt at the western flanks of the West Eratosthenes High that is driven by the combination of gravity gliding and spreading mechanisms. The irregular morphology of the underlying carbonates prevents the Messinian salt from overthrusting the western flanks of the Eratosthenes Continental Block and further force it to flow towards the north.

E.8.2 Conclusions about the pre-salt clastic systems

A 2D seismic dataset provides useful two-dimensional information and allowed a first description of the architecture, morphology, and quantification of the Messinian clastic systems. The clastic systems are made up of several channel - lobe complexes that originated ahead of major fluviatile canyons of the Messinian Nile low-stand delta. Questions remain about the three-dimensional character of the clastic systems, their temporal evolution, as well as their relation to the MSC sequence. At the initial stage of the MSC, late Messinian clastic sediments originated from the River Nile, had sufficient time to reach and be deposited in the deepest parts of the Herodotus basin before salt precipitation. According to seismic interpretation, a significant part of the clastic sediments was deposited before the massive

halite precipitation, while another important part was deposited simultaneously with the massive halite precipitation.

The late Messinian clastic systems deposited in a marine setting, due to their development directly underneath the MSC evaporitic sequence. Considering a sea-level drop down in the order of >1000 m (Barber, 1981; Gargani and Rigollet, 2007; Urgeles et al., 2011), it can be more specifically concluded that the late Messinian clastic systems developed in a deep-water depositional setting. This, in combination with the resemblance of the seismic facies to submarine channel and lobe complexes, indicates that the identified clastic systems represent a late Messinian deep-sea fan.

The Nile transported clastic sediments into the Herodotus Basin during the initial stage of the MSC. These deposits may have similar sedimentological properties and origin to the Messinian deposits found at the northern Nile Delta and could contain potential hydrocarbon reservoirs.

E.8.3 Conclusions about the forward modeling

2D seismic data were used in the present study to investigate through forwarding modeling if the mapped pre-salt clastic systems can be reproduced from turbidity flows. A similar geometry with the channel complexes that have been interpreted in the seismic data is achieved and the main processes that govern the evolution of sediment accumulation in deep-sea environments (e.g., velocity) are identified. Since the result of the forward model are very similar to the interpreted seismic lines, it is safer to conclude that the high to medium amplitude high-frequency reflectors may host important hydrocarbon reserves.

E.8.4 Synopsis

2310 km of high-quality 2D seismic lines covering the western part of the Cypriot Exclusive Economic Zone were used in the present dissertation.

- The general setting, the scope of the study, and the structure of the study were presented and analyzed.
- A detailed literature review concerning the evolution of the Eastern Mediterranean and the Messinian Salinity Crisis was presented.
- The study area was separated into seismic stratigraphic units (Gorini et al., 2015; Güneş et al., 2018; Gvirtzman et al., 2017; Feng et al., 2016). Each unit was described and analyzed. The dissertation mainly focuses on the internal seismic stratigraphy of the Messinian Salinity Crisis sequence separating the sequence into seismic stratigraphic subdivisions.
- Following the separation of the Messinian Salinity Crisis into seismic stratigraphic subdivisions (Gorini et al., 2015; Güneş et al., 2018; Gvirtzman et al., 2017; Feng et al., 2016), a detailed analysis of the observed salt-related deformation patterns is presented.
- Once the deformation patterns and the internal seismic stratigraphy of the Messinian Salinity Crisis sequence are described, the pre-salt clastic systems into the Herodotus Basin are spotted, analyzed, and correlated with the Messinian River Nile by using onshore and offshore published data from the Nile Delta area.
- The seismic interpretation of the pre-salt clastic systems is strengthened by using as a tool the stratigraphic forward modeling. Finally, a good correlation of the spatial distribution between the mapped clastic deposits and the model results is achieved.

References

Aal, A.A., El Barkooky, A., Gerrits, M., Meyer, H., Schwander, M. and Zaki, H., 2000. Tectonic evolution of the Eastern Mediterranean Basin and its significance for hydrocarbon prospectivity in the ultradeepwater of the Nile Delta. *The Leading Edge*, *19*(10), pp.1086-1102.

Abd El-Fattah, B.K., Moustafa, A.R. and Yousef, M., 2021. A new insight into the structural evolution of Rosetta Fault, eastern margin of Herodotus Basin, East Mediterranean. *Marine and Petroleum Geology*, p.105161.

Abd-Allah, A.M., Aal, M.H.A. and Ghandour, A., 2012. Structural characteristics and tectonic evolution of the northwestern margin of the Nile Delta, Egypt. *Journal of African Earth Sciences*, *68*, pp.82-95.

Abdel-Fattah, M.I. and Slatt, R.M., 2013. Sequence stratigraphic controls on reservoir characterization and architecture: case study of the Messinian Abu Madi incised-valley fill, Egypt. *Central European Journal of Geosciences*, *5*(4), pp.497-507.

Abdel-Fattah, M.I., 2014. Petrophysical characteristics of the messinianabumadi formation in the baltim east and north fields, offshore Nile delta, Egypt. *Journal of Petroleum Geology*, *37*(2), pp.183-195.

Abdelkareem, M., Ghoneim, E., El-Baz, F. and Askalany, M., 2012. New insight on paleoriver development in the Nile basin of the eastern Sahara. *Journal of African Earth Sciences*, *62*(1), pp.35-40.

Allen, H., Jackson, C.A.L. and Fraser, A.J., 2016. Gravity-driven deformation of a youthful saline giant: the interplay between gliding and spreading in the Messinian basins of the Eastern Mediterranean. *Petroleum Geoscience*, *22*(4), pp.340-356.

Allen, P.A. and Allen, J.R., 2013. *Basin analysis: Principles and application to petroleum play assessment*. John Wiley & Sons, pp. 335-339

Bache, F., Gargani, J., Suc, J.P., Gorini, C., Rabineau, M., Popescu, S.M., Leroux, E., Do Couto, D., Jouannic, G., Rubino, J.L. and Olivet, J.L., 2015. Messinian evaporite deposition during sea

level rise in the Gulf of Lions (Western Mediterranean). *Marine and Petroleum Geology*, *66*, pp.262-277.

Barber, P.M., 1981. Messinian subaerial erosion of the proto-Nile Delta. *Marine Geology*, *44*(3-4), pp.253-272.

Bayon, G., Loncke, L., Dupré, S., Caprais, J.C., Ducassou, E., Duperron, S., Etoubleau, J., Foucher, J.P., Fouquet, Y., Gontharet, S. and Henderson, G.M., 2009. Multi-disciplinary investigation of fluid seepage on an unstable margin: the case of the Central Nile deep sea fan. *Marine Geology*, *261*(1), pp.92-104.

Ben-Avraham, Z., Ginzburg, A., Makris, J. and Eppelbaum, L., 2002. Crustal structure of the Levant Basin, eastern Mediterranean. *Tectonophysics*, *346*(1-2), pp.23-43.

Bertoni, C. and Cartwright, J.A., 2006. Controls on the basinwide architecture of late Miocene (Messinian) evaporites on the Levant margin (Eastern Mediterranean). *Sedimentary Geology*, *188*, pp.93-114.

Bertoni, C. and Cartwright, J.A., 2007. Clastic depositional systems at the base of the late Miocene evaporites of the Levant region, Eastern Mediterranean. *Geological Society, London, Special Publications*, *285*(1), pp.37-52.

Bertoni, C., Kirkham, C., Cartwright, J., Hodgson, N. and Rodriguez, K., 2017. Seismic indicators of focused fluid flow and cross-evaporitic seepage in the Eastern Mediterranean. *Marine and Petroleum Geology*, *88*, pp.472-488.

Blanc, P.L., 2006. Improved modelling of the Messinian Salinity Crisis and conceptual implications. *Palaeogeography, Palaeoclimatology, Palaeoecology*, *238*(1), pp.349-372.

Brun, J.P. and Fort, X., 2011. Salt tectonics at passive margins: Geology versus models. *Marine and Petroleum Geology*, *28*(6), pp.1123-1145.

Brunstrom, R.G.W. and Walmsley, P.J., 1969. Permian evaporites in North Sea basin. *AAPG Bulletin*, *53*(4), pp.870-883.

Burke, K. and Wells, G.L., 1989. Trans-African drainage system of the Sahara: Was it the Nile?. *Geology*, *17*(8), pp.743-747.

Camerlenghi, A. and Cita, M.B., 1987. Setting and tectonic evolution of some Eastern Mediterranean deep-sea basins. *Marine geology*, *75*(1-4), pp.31-55.

Camerlenghi, A., 1990. Anoxic basins of the eastern Mediterranean: geological framework. *Marine chemistry*, *31*(1-3), pp.1-19.

Cameselle, A.L., Urgeles, R., De Mol, B., Camerlenghi, A. and Canning, J.C., 2014. Late Miocene sedimentary architecture of the Ebro Continental Margin (Western Mediterranean): implications to the Messinian Salinity Crisis. *International Journal of Earth Sciences*, *103*(2), pp.423-440.

Carmignani, L., Salvini, R. and Bonciani, F., 2009. Did the Nile River flow to the Gulf of Sirt during the late Miocene?. *BollettinodellaSocietaGeologicaItaliana*, *128*(2), pp.403-408.

Cartwright, J., Jackson, M., Dooley, T. and Higgins, S., 2012. Strain partitioning in gravity-driven shortening of a thick, multilayered evaporite sequence. *Geological Society, London, Special Publications*, *363*(1), pp.449-470.

Casten, U. and Snopek, K., 2006. Gravity modelling of the Hellenic subduction zone—a regional study. *Tectonophysics*, *417*(3-4), pp.183-200.

Catterall, V., Redfern, J., Gawthorpe, R., Hansen, D. and Thomas, M., 2010. Architectural style and quantification of a submarine channel–levee system located in a structurally complex area: offshore Nile Delta. *Journal of Sedimentary Research*, *80*(11), pp.991-1017.

Cita, M.B., 2006. Exhumation of Messinian evaporites in the deep-sea and creation of deep anoxic brine-filled collapsed basins. *Sedimentary Geology,188*, pp.357-378.

Cita, M.B., Beghi, C., Camerlenghi, A., Kastens, K.A., McCoy, F.W., Nosetto, A., Parisi, E., Scolari, F. and Tomadin, L., 1984. Turbidites and megaturbidites from the Herodotus abyssal plain (eastern Mediterranean) unrelated to seismic events. *MarineGeology*, *55*(1-2), pp.79-101.

Clauzon, G., Suc, J.P., Gautier, F., Berger, A. and Loutre, M.F., 1996. Alternate interpretation of the Messinian salinity crisis: Controversy resolved?.*Geology*, *24*(4), pp.363-366.

Coe, A.L., 2003. The sedimentary record of sea-level change. Cambridge University Press.

Colin, C., Siani, G., Liu, Z., Blamart, D., Skonieczny, C., Zhao, Y., Bory, A., Frank, N., Duchamp-Alphonse, S., Thil, F. and Richter, T., 2014. Late Miocene to early Pliocene climate variability

off NW Africa (ODP Site 659). *Palaeogeography, Palaeoclimatology, Palaeoecology*, *401*, pp.81-95.

Corney, R.K., Peakall, J., Parsons, D.R., Elliott, L., Amos, K.J., Best, J.L., Keevil, G.M. and Ingham, D.B., 2006. The orientation of helical flow in curved channels. *Sedimentology*, *53*(2), pp.249-257.

De Lange, G.J., Catalano, G., Klinkhammer, G.P. and Luther, G.W., 1990a. The interface between oxic seawater and the anoxic Bannock brine; its sharpness and the consequences for the redox-related cycling of Mn and Ba.*Marine chemistry*, *31*(1-3), pp.205-217.

De Lange, G.J., Middelburg, J.J., Van der Weijden, C.H., Catalano, G., Luther, G.W., Hydes, D.J., Woittiez, J.R.W. and Klinkhammer, G.P., 1990b. Composition of anoxic hypersaline brines in the Tyro and Bannock Basins, eastern Mediterranean. *Marine Chemistry*, *31*(1-3), pp.63-88.

De Voogd, B., Truffert, C., Chamot-Rooke, N., Huchon, P., Lallemant, S. and Le Pichon, X., 1992. Two-ship deep seismic soundings in the basins of the Eastern Mediterranean Sea (Pasiphae cruise). *Geophysical Journal International*, *109*(3), pp.536-552.

Denizot, G., 1952. Le Pliocène dans la vallée du Rhône. *Revue de géographie de Lyon*, *27*(4).

Deptuck, M.E., Steffens, G.S., Barton, M. and Pirmez, C., 2003. Architecture and evolution of upper fan channel-belts on the Niger Delta slope and in the Arabian Sea. *Marine and Petroleum Geology*, *20*(6-8), pp.649-676.

Deptuck, M.E., Sylvester, Z., Pirmez, C. and O'Byrne, C., 2007. Migration–aggradation history and 3-D seismic geomorphology of submarine channels in the Pleistocene Benin-major Canyon, western Niger Delta slope. *Marine and Petroleum Geology*, *24*(6-9), pp.406-433.

Di Celma, C.N., Brunt, R.L., Hodgson, D.M., Flint, S.S. and Kavanagh, J.P., 2011. Spatial and temporal evolution of a Permian submarine slope channel–levee system, Karoo Basin, South Africa. *Journal of Sedimentary Research*, *81*(8), pp.579-599.

Dolson, J.C., Boucher, P.J., Siok, J. and Heppard, P.D., 2005, January. Key challenges to realizing full potential in an emerging giant gas province: Nile Delta/Mediterranean offshore, deep water, Egypt. In *Geological Society, London, Petroleum Geology Conference series* (Vol. 6, No. 1, pp. 607-624). Geological Society of London.

Ducassou, E., Migeon, S., Mulder, T., Murat, A., Capotondi, L., Bernasconi, S.M. and Mascle, J., 2009. Evolution of the Nile deep-sea turbidite system during the Late Quaternary: influence of climate change on fan sedimentation. *Sedimentology*, *56*(7), pp.2061-2090.

Dupré, S., Buffet, G., Mascle, J., Foucher, J.P., Gauger, S., Boetius, A., Marfia, C., AsterX AUV Team and Quest ROV Team, 2008. High-resolution mapping of large gas emitting mud volcanoes on the Egyptian continental margin (Nile Deep Sea Fan) by AUV surveys. *Marine Geophysical Researches*, *29*(4), pp.275-290.

Dupré, S., Woodside, J., Foucher, J.P., De Lange, G., Mascle, J., Boetius, A., Mastalerz, V., Stadnitskaia, A., Ondréas, H., Huguen, C. and Harmégnies, F., 2007. Seafloor geological studies above active gas chimneys off Egypt (Central Nile Deep Sea Fan). *Deep Sea Research Part I: Oceanographic Research Papers*, *54*(7), pp.1146-1172.

Dupré, S., Woodside, J., Klaucke, I., Mascle, J. and Foucher, J.P., 2010. Widespread active seepage activity on the Nile Deep Sea Fan (offshore Egypt) revealed by high-definition geophysical imagery. *Marine Geology*,*275*(1), pp.1-19.

Eldrett, J., Tripsanas, E., Davis, C., McKie, T., Vieira, M., Osterloff, P. and Sandison, T., 2015. Sedimentological evolution of Sele Formation deep-marine depositional systems of the Central North Sea. *Geological Society, London, Special Publications*, *403*(1), pp.63-98.

Elfassi, Y., Gvirtzman, Z., Katz, O. and Aharonov, E., 2019. Chronology of post-Messinian faulting along the Levant continental margin and its implications for salt tectonics. *Marine and Petroleum Geology*, *109*, pp.574-588.

Farouk, S., Ziko, A., Eweda, S.A. and Said, A.E., 2014. Subsurface Miocene sequence stratigraphic framework in the Nile Delta, Egypt. *Journal of African Earth Sciences*, *91*, pp.89-109.

Feng, Y.E., Steinberg, J. and Reshef, M., 2017. Intra-salt deformation: Implications for the evolution of the Messinian evaporites in the Levant Basin, eastern Mediterranean. *Marine and Petroleum Geology*, *88*, pp.251-267.

Feng, Y.E., Yankelzon, A., Steinberg, J. and Reshef, M., 2016. Lithology and characteristics of the Messinian evaporite sequence of the deep Levant Basin, eastern Mediterranean. *Marine Geology*, *376*, pp.118-131.

Fort, X., Brun, J.P. and Chauvel, F., 2004. Salt tectonics on the Angolan margin, synsedimentary deformation processes. *Aapg Bulletin*, *88*(11), pp.1523-1544.

Frizon de Lamotte, D., Raulin, C., Mouchot, N., Wrobel-Daveau, J.C., Blanpied, C. and Ringenbach, J.C., 2011. The southernmost margin of the Tethys realm during the Mesozoic and Cenozoic: Initial geometry and timing of the inversion processes. *Tectonics*, *30*(3).

Galloway, W.E., 1998. Siliciclastic slope and base-of-slope depositional systems: component facies, stratigraphic architecture, and classification. *AAPG bulletin*, *82*(4), pp.569-595.

Gao, H., Wen, Z., Shi, B., Wang, Z. and Song, C., 2020. Tectonic characteristics of the Eratosthenes Seamount and its periphery: Implications for evolution of the eastern Mediterranean. *Marine Geology*, *428*, p.106266.

Garcia-Castellanos, D., Estrada, F., Jiménez-Munt, I., Gorini, C., Fernández, M., Vergés, J. and De Vicente, R., 2009. Catastrophic flood of the Mediterranean after the Messinian salinity crisis. *Nature*, *462*(7274), pp.778-782.

Gardosh, M.A., Garfunkel, Z., Druckman, Y. and Buchbinder, B., 2010. Tethyan rifting in the Levant Region and its role in Early Mesozoic crustal evolution. *Geological Society, London, Special Publications*, *341*(1), pp.9-36.

Garfunkel, Z., 1988. Relation between continental rifting and uplifting: evidence from the Suez rift and northern Red Sea. *Tectonophysics*, *150*(1-2), pp.33-49.

Garfunkel, Z., 1998. Constrains on the origin and history of the Eastern Mediterranean basin. *Tectonophysics*, *298*(1-3), pp.5-35.

Garfunkel, Z., 2004. Origin of the Eastern Mediterranean basin: a reevaluation. *Tectonophysics*, *391*(1), pp.11-34.

Gargani, J. and Rigollet, C., 2007. Mediterranean Sea level variations during the Messinian salinity crisis. *Geophysical Research Letters*, *34*(10), L10405

Gaullier, V. and Vendeville, B.C., 2005. Salt tectonics driven by sediment progradation: Part II—Radial spreading of sedimentary lobes prograding above salt. *AAPG bulletin*, *89*(8), pp.1081-1089.

Gaullier, V., Mart, Y., Bellaiche, G., Mascle, J., Vendeville, B.C., Zitter, T. and Party, S.L.P.I.S., 2000. Salt tectonics in and around the Nile deep-sea fan: insights from the PRISMED II cruise. *Geological Society, London, Special Publications*, *174*(1), pp.111-129.

Ge, H., Jackson, M.P. and Vendeville, B.C., 1997. Kinematics and dynamics of salt tectonics driven by progradation. *AAPG bulletin*, *81*(3), pp.398-423.

Gertman, I. and Hecht, A., 2002. The Dead Sea hydrography from 1992 to 2000. *Journal of marine systems*, *35*(3), pp.169-181.

Girdler, R.W. and Styles, P., 1974. Two stage Red Sea floor spreading. *Nature*, *247*(5435), p.7.

Gladstone, R., Flecker, R., Valdes, P., Lunt, D. and Markwick, P., 2007. The Mediterranean hydrologic budget from a Late Miocene global climate simulation. *Palaeogeography, Palaeoclimatology, Palaeoecology*, *251*(2), pp.254-267.

Gontharet, S., Pierre, C., Blanc-Valleron, M.M., Rouchy, J.M., Fouquet, Y., Bayon, G., Foucher, J.P., Woodside, J., Mascle, J. and Party, T.N.S., 2007. Nature and origin of diagenetic carbonate crusts and concretions from mud volcanoes and pockmarks of the Nile deep-sea fan (eastern Mediterranean Sea). *Deep Sea Research Part II: Topical Studies in Oceanography*, *54*(11), pp.1292-1311.

Gorini, C., Montadert, L. and Rabineau, M., 2015. New imaging of the salinity crisis: Dual Messinian lowstandmegasequences recorded in the deep basin of both the eastern and western Mediterranean. *Marine and Petroleum Geology*, *66*, pp.278-294.

Goudie, A.S., 2005. The drainage of Africa since the Cretaceous.*Geomorphology*, *67*(3), pp.437-456.

Govers, R., Meijer, P. and Krijgsman, W., 2009. Regional isostatic response to Messinian Salinity Crisis events. *Tectonophysics*, *463*(1), pp.109-129.

Granot, R., 2016. Palaeozoic oceanic crust preserved beneath the eastern Mediterranean: Nature Geoscience, v. 9. *Doi*, *10*(1038), pp.701-705.

Griffin, D.L., 2002. Aridity and humidity: two aspects of the late Miocene climate of North Africa and the Mediterranean. *Palaeogeography, Palaeoclimatology, Palaeoecology*, *182*(1), pp.65-91.

Güneş, P., Aksu, A.E. and Hall, J., 2018. Internal seismic stratigraphy of the Messinian evaporites across the northern sector of the eastern Mediterranean Sea. *Marine and Petroleum Geology*, *91*, pp.297-320.

Gvirtzman, Z., Manzi, V., Calvo, R., Gavrieli, I., Gennari, R., Lugli, S., Reghizzi, M. and Roveri, M., 2017. Intra-Messinian truncation surface in the Levant Basin explained by subaqueous dissolution. *Geology*, *45*(10), pp.915-918.

Gvirtzman, Z., Reshef, M., Buch-Leviatan, O. and Ben-Avraham, Z., 2013. Intense salt deformation in the Levant Basin in the middle of the Messinian Salinity Crisis. *Earth and Planetary Science Letters*, *379*, pp.108-119.

Gvirtzman, Z., Reshef, M., Buch-Leviatan, O., Groves-Gidney, G., Karcz, Z., Makovsky, Y. and Ben-Avraham, Z., 2015. Bathymetry of the Levant basin: interaction of salt-tectonics and surficial mass movements. *Marine Geology*, *360*, pp.25-39.

Hall, J., Calon, T.J., Aksu, A.E. and Meade, S.R., 2005. Structural evolution of the Latakia Ridge and Cyprus Basin at the front of the Cyprus Arc, eastern Mediterranean Sea. *Marine Geology*, *221*(1-4), pp.261-297.

Hall, J.K., Krasheninnikov, V.A., Hirsch, F., Benjamini, C. and Flexer, A., 2005. Geological Framework of the Levant, Volume II: The Levantine Basin and Israel. *Historical Productions, Jerusalem*.

Hawie, N., Gorini, C., Deschamps, R., Nader, F.H., Montadert, L., Granjeon, D. and Baudin, F., 2013. Tectono-stratigraphic evolution of the northern Levant Basin (offshore Lebanon). *Marine and Petroleum Geology*, *48*, pp.392-410.

Heerema, C.J., Talling, P.J., Cartigny, M.J., Paull, C.K., Bailey, L., Simmons, S.M., Parsons, D.R., Clare, M.A., Gwiazda, R., Lundsten, E. and Anderson, K., 2020. What determines the downstream evolution of turbidity currents?. *Earth and Planetary Science Letters*, *532*, pp.116023.

Hsü, K.J., Montadert, L., Bernoulli, D., Cita, M.B., Erickson, A., Garrison, R.E., Kidd, R.B., Mèlierés, F., Müller, C. and Wright, R., 1977. History of the Mediterranean salinity crisis. *Nature*, *267*(5610), pp.399-403.

Hsü, K.J., Ryan, W.B.F. and Cita, M.B., 1973. Late Miocene desiccation of the Mediterranean. *Nature*, *242*(5395), pp.240-244.

Hubbard, S.M., Covault, J.A., Fildani, A. and Romans, B.W., 2014. Sediment transfer and deposition in slope channels: Deciphering the record of enigmatic deep-sea processes from outcrop. *Geological Society of America Bulletin*, *126*(5-6), pp.857-871.

Hudec, M.R. and Jackson, M.P., 2007. Terra infirma: Understanding salt tectonics. *Earth-Science Reviews*, *82*(1-2), pp.1-28.

Hudec, M.R., Jackson, M.P. and Schultz-Ela, D.D., 2009. The paradox of minibasin subsidence into salt: Clues to the evolution of crustal basins. *Geological Society of America Bulletin*, *121*(1-2), pp.201-221.

Hussein, I.M. and Abd-Allah, A.M.A., 2001. Tectonic evolution of the northeastern part of the African continental margin, Egypt. *Journal of African Earth Sciences*, *33*(1), pp.49-68.

Imran, J., Islam, M.A. and Kassem, A., 2008. "The orientation of helical flow in curved channels" by Corney et al., Sedimentology, Vol. 53, pp. 249–257–discussion. *Sedimentology*, *55*(1), pp.235-239.

Issawi, B. and McCauley, J.F., 1992. The Cenozoic rivers of Egypt: the Nile problem. *The followers of Horus, Studies dedicated to Michael Allen Hoffman, Oxbow Monograph*, *20*, pp.121-138.

Issawi, B. and Osman, R., 2008. Egypt during the Cenozoic: geological history of the Nile River. *Bulletin of the Tethys Geological Society*, *3*, pp.43-62.

Jackson, J. and McKenzie, D., 1988. The relationship between plate motions and seismic moment tensors, and the rates of active deformation in the Mediterranean and Middle East. *Geophysical Journal International*, *93*(1), pp.45-73.

Jackson, M.P. and Hudec, M.R., 2017. *Salt tectonics: Principles and practice*. Cambridge University Press.

Jackson, M.P., Vendeville, B.C. and Schultz-Ela, D.D., 1994. Structural dynamics of salt systems. *Annual Review of Earth and Planetary Sciences*, *22*(1), pp.93-117.

Jagger, L.J., Bevan, T.G. and McClay, K.R., 2018. Tectono-stratigraphic evolution of the SE Mediterranean passive margin, offshore Egypt and Libya. *Geological Society, London, Special Publications*, *476*, pp. SP476-10.

Kolla, V., Posamentier, H.W. and Wood, L.J., 2007. Deep-water and fluvial sinuous channels—Characteristics, similarities and dissimilarities, and modes of formation. *Marine and Petroleum Geology*, *24*(6-9), pp.388-405.

Koltermann, C.E. and Gorelick, S.M., 1996. Heterogeneity in sedimentary deposits: A review of structure-imitating, process-imitating, and descriptive approaches. *Water Resources Research*, *32*(9), pp.2617-2658.

Krijgsman, W. and Meijer, P.T., 2008. Depositional environments of the Mediterranean "Lower Evaporites" of the Messinian salinity crisis: constraints from quantitative analyses. *Marine Geology*, *253*(3), pp.73-81.

Krijgsman, W., Capella, W., Simon, D., Hilgen, F.J., Kouwenhoven, T.J., Meijer, P.T., Sierro, F.J., Tulbure, M.A., van den Berg, B.C., van der Schee, M. and Flecker, R., 2018. The Gibraltar Corridor: Watergate of the Messinian Salinity Crisis. *Marine Geology*, *403*, pp.238-246.

Krijgsman, W., Hilgen, F.J., Raffi, I., Sierro, F.J. and Wilson, D.S., 1999. Chronology, causes and progression of the Messinian salinity crisis. *Nature*, *400* (6745), pp.652-655.

Leila, M. and Moscariello, A., 2019. Seismic stratigraphy and sedimentary facies analysis of the pre- and syn-Messinian salinity crisis sequences, onshore Nile Delta, Egypt: Implications for reservoir quality prediction. *Marine and Petroleum Geology*, *101*, pp.303-321.

Leila, M., Moscariello, A. and Šegvić, B., 2019. Depositional facies controls on the diagenesis and reservoir quality of the Messinian Qawasim and Abu Madi formations, onshore Nile Delta, Egypt. *Geological Journal*, *54*(3), pp.1797-1813.

Leroux, E., Aslanian, D., Rabineau, M., Moulin, M., Granjeon, D., Gorini, C. and Droz, L., 2015. Sedimentary markers in the Provençal Basin (western Mediterranean): a window into deep geodynamic processes. *Terra Nova*, *27*(2), pp.122-129.

Letouzey, J., Colletta, B., Vially, R. &Chermette, J.C. 1995. Evolution of salt-related structures in compressional settings. In: Jackson, M.P.A., Roberts, D.G. &Snelson, S. (eds) Salt Tectonics: a Global Perspective. *American Association of Petroleum Geologists, Memoirs*, 65, 29–40.

Lofi, J., 2018. Seismic Atlas of the Messinian Salinity Crisis markers in the Mediterranean Sea (Vol. 2). *CGMW and Mémoires de la Société Géologie de France*.

Lofi, J., Gorini, C., Berné, S., Clauzon, G., Dos Reis, A.T., Ryan, W.B. and Steckler, M.S., 2005. Erosional processes and paleo-environmental changes in the Western Gulf of Lions (SW France) during the Messinian Salinity Crisis. *Marine Geology*, *217*(1-2), pp.1-30.

Loget, N., Davy, P. and Van den Driessche, J., 2006. Mesoscale fluvial erosion parameters deduced from modeling the Mediterranean Sea level drop during the Messinian (late Miocene). *Journal of Geophysical Research: Earth Surface*, *111*(F3).

Loget, N., Driessche, J.V.D. and Davy, P., 2005. How did the Messinian salinity crisis end? *Terra Nova*, *17*(5), pp.414-419.

Loncke, L., Gaullier, V., Bellaiche, G. and Mascle, J., 2002. Recent depositional patterns of the Nile deep-sea fan from echo-character mapping.*AAPG bulletin*, *86*(7).

Loncke, L., Gaullier, V., Droz, L., Ducassou, E., Migeon, S. and Mascle, J., 2009. Multiscale slope instabilities along the Nile deep-sea fan, Egyptian margin: a general overview. *Marine and Petroleum Geology*, *26*(5), pp.633-646.

Loncke, L., Gaullier, V., Mascle, J., Vendeville, B. and Camera, L., 2006. The Nile deep-sea fan: an example of interacting sedimentation, salt tectonics, and inherited subsalt paleotopographic features. *Marine and Petroleum Geology*, *23*(3), pp.297-315.

Loncke, L., Mascle, J. and Parties, F.S., 2004. Mud volcanoes, gas chimneys, pockmarks and mounds in the Nile deep-sea fan (Eastern Mediterranean): geophysical evidences. *Marine and Petroleum Geology*, *21*(6), pp.669-689.

Lugli, S., Gennari, R., Gvirtzman, Z., Manzi, V., Roveri, M. and Schreiber, B.C., 2013. Evidence of clastic evaporites in the canyons of the Levant Basin (Israel): Implications for the Messinian salinity crisis. *Journal of sedimentary research*, *83*(11), pp.942-954.

Lugli, S., Manzi, V., Roveri, M. and Schreiber, B.C., 2015. The deep record of the Messinian salinity crisis: Evidence of a non-desiccated Mediterranean Sea. *Palaeogeography, Palaeoclimatology, Palaeoecology*, *433*, pp.201-218.

Macgregor, D., 2011. Rift shoulder source to prodelta sink: The Cenozoic development of the Nile drainage system. *Search and Discovery Article*,*50506*.

Macgregor, D.S., 2012. The development of the Nile drainage system: integration of onshore and offshore evidence. *Petroleum Geoscience*, *18*(4), pp.417-431.

Madof, A.S., Bertoni, C. and Lofi, J., 2019. Discovery of vast fluvial deposits provides evidence for drawdown during the late Miocene Messinian salinity crisis. *Geology*, *47*(2), pp.171-174.

Mahmoud, M., Ghorab, M., Shazly, T., Shibl, A. and Abuhagaza, A.A., 2017. Reservoir characterization utilizing the well logging analysis of Abu Madi Formation, Nile Delta, Egypt. *Egyptian Journal of Petroleum*, *26*(3), pp.649-659.

Makris, J., Abraham, Z.B., Behle, A., Ginzburg, A., Giese, P., Steinmetz, L., Whitmarsh, R.B. and Eleftheriou, S., 1983. Seismic refraction profiles between Cyprus and Israel and their interpretation. *Geophysical Journal International*, *75*(3), pp.575-591.

Makris, J., Papoulia, J. and Yegorova, T., 2013. A 3-D density model of Greece constrained by gravity and seismic data. *Geophysical Journal International*, *194*(1), pp.1-17.

Manzi, V., Gennari, R., Hilgen, F., Krijgsman, W., Lugli, S., Roveri, M. and Sierro, F.J., 2013. Age refinement of the Messinian salinity crisis onset in the Mediterranean. *Terra Nova*, *25*(4), pp.315-322.

Manzi, V., Gennari, R., Lugli, S., Persico, D., Reghizzi, M., Roveri, M., Schreiber, B.C., Calvo, R., Gavrieli, I. and Gvirtzman, Z., 2018. The onset of the Messinian salinity crisis in the deep Eastern Mediterranean basin. *Terra Nova*, *30*(3), pp.189-198.

Manzi, V., Lugli, S., Roveri, M., Dela Pierre, F., Gennari, R., Lozar, F., Natalicchio, M., Schreiber, B.C., Taviani, M. and Turco, E., 2016. The Messinian salinity crisis in Cyprus: a further step towards a new stratigraphic framework for Eastern Mediterranean. *Basin Research*, *28*(2), pp.207-236.

Marzocchi, A., Flecker, R., Van Baak, C.G., Lunt, D.J. and Krijgsman, W., 2016. Mediterranean outflow pump: An alternative mechanism for the Lago-mare and the end of the Messinian Salinity Crisis. *Geology*, *44*(7), pp.523-526.

Mascle, J., Benkhelil, J., Bellaiche, G., Zitter, T., Woodside, J. and Loncke, L., 2000. Marine geologic evidence for a Levantine-Sinai plate, a new piece of the Mediterranean puzzle. *Geology*, *28*(9), pp.779-782.

Mascle, J., Sardou, O., Loncke, L., Migeon, S., Caméra, L. and Gaullier, V., 2006. Morphostructure of the Egyptian continental margin: insights from swath bathymetry surveys. *Marine Geophysical Researches*, *27*(1), pp.49-59.

Mascle, J., Zitter, T., Bellaiche, G., Droz, L., Gaullier, V., Loncke, L. and Party, P.S., 2001. The Nile deep sea fan: preliminary results from a swath bathymetry survey. *Marine and Petroleum Geology*, *18*(4), pp.471-477.

Meijer, P.T. and Krijgsman, W., 2005. A quantitative analysis of the desiccation and re-filling of the Mediterranean during the Messinian Salinity Crisis. *Earth and Planetary Science Letters*, *240*(2), pp.510-520.

Meijer, P.T., 2006. A box model of the blocked-outflow scenario for the Messinian Salinity Crisis. *Earth and Planetary Science Letters*, *248*(1), pp.486-494.

Meilijson, A., Steinberg, J., Hilgen, F., Bialik, O.M., Waldmann, N.D. and Makovsky, Y., 2018. Deep-basin evidence resolves a 50-year-old debate and demonstrates synchronous onset of Messinian evaporite deposition in a non-desiccated Mediterranean. *Geology*, *46*(3), pp.243-246.

Micallef, A., Camerlenghi, A., Garcia-Castellanos, D., Otero, D.C., Gutscher, M.A., Barreca, G., Spatola, D., Facchin, L., Geletti, R., Krastel, S. and Gross, F., 2018. Evidence of the Zanclean megaflood in the eastern Mediterranean Basin. *Scientific Reports*, *8*(1), pp.1078.

Migeon, S., Ducassou, E., Le Gonidec, Y., Rouillard, P., Mascle, J. and Revel-Rolland, M., 2010. Lobe construction and sand/mud segregation by turbidity currents and debris flows on the western Nile deep-sea fan (Eastern Mediterranean). *Sedimentary Geology*, *229*(3), pp.124-143.

Montadert, L., Lie, Ø., Semb, P.H. and Kassinis, S., 2010. New seismic may put offshore Cyprus hydrocarbon prospects in the spotlight. *First Break*,*28*(4).

Montadert, L., Nicolaides, S., Semb, P.H. and Lie, Ø., 2014. Petroleum systems offshore Cyprus. AAPG Memoir 106: Petroleum Systems of the Tethyan Region, pp. 301-334

Morehead, M.D., Syvitski, J.P. and Hutton, E.W., 2001. The link between abrupt climate change and basin stratigraphy: a numerical approach. *Global and Planetary Change*, *28*(1-4), pp.107-127.

Moss, J.L., Cartwright, J. and Moore, R., 2012. Evidence for fluid migration following pockmark formation: Examples from the Nile Deep Sea Fan. *Marine Geology*, *303*, pp.1-13.

Mulder, T., Syvitski, J.P., Migeon, S., Faugeres, J.C. and Savoye, B., 2003. Marine hyperpycnal flows: initiation, behavior and related deposits. A review. *Marine and Petroleum Geology*, *20*(6-8), pp.861-882.

Murris, R.J., 1981. Middle East--Stratigraphic Evolution and Oil Habitat. *AAPG Bulletin*, *65*(7), pp.1358-1358.

Nesteroff, W.D., 1973. Mineralogy, petrography, distribution, and origin of the Messinian Mediterranean evaporites. *Initial reports of the deep sea drilling project*, *13*(part 2), pp.673-694.

Netzeband, G.L., Gohl, K., Hübscher, C.P., Ben-Avraham, Z., Dehghani, G.A., Gajewski, D. and Liersch, P., 2006. The Levantine Basin—crustal structure and origin. *Tectonophysics*, *418*(3-4), pp.167-188.

Netzeband, G.L., Hübscher, C.P. and Gajewski, D., 2006b. The structural evolution of the Messinian evaporites in the Levantine Basin. *Marine Geology*, *230*(3-4), pp.249-273.

Ottes, W., Lambregts, P. and El Barkooky, A., 2008. The Messinian Salinity Crisis in the Nile Delta: chasing shallow marine reservoirs in a deep-water basin. *CIESM*, pp.107-109.

Overeem, I., Syvitski, J.P. and Hutton, E.W., 2005. Three-dimensional numerical modeling of deltas.

Papadimitriou, N., Gorini, C., Nader, F.H., Deschamps, R., Symeou, V. and Lecomte, J.C., 2018. Tectono-stratigraphic evolution of the western margin of the Levant Basin (offshore Cyprus). *Marine and Petroleum Geology*, *91*, pp.683-705.

Peck, J., 2008. Giant oil prospects lie in distal portion of offshore East Mediterranean basin. *Oil and Gas Journal*, *106*(37).

Peck, J.M. and Horscroft, T.R., 2005. 'Bottom-up'analysis identifies eastern Mediterranean prospects. *Offshore*, *65*(6), pp.122-125.

Peel, F.J., 2014. How do salt withdrawal minibasins form? Insights from forward modelling, and implications for hydrocarbon migration. *Tectonophysics*, *630*, pp.222-235.

Pigott, J.D. and Abdel-Fattah, M.I., 2014. Seismic stratigraphy of the Messinian Nile Delta coastal plain: Recognition of the fluvial Regressive Systems Tract and its potential for hydrocarbon exploration. *Journal of African Earth Sciences*, *95*, pp.9-21.

Popescu, S.M., Dalibard, M., Suc, J.P., Barhoun, N., Melinte-Dobrinescu, M.C., Bassetti, M.A., Deaconu, F., Head, M.J., Gorini, C., Do Couto, D. and Rubino, J.L., 2015. Lago Mare episodes around the Messinian–Zanclean boundary in the deep southwestern Mediterranean. *Marine and Petroleum Geology*, *66*, pp.55-70.

Posamentier, H.W. and Kolla, V., 2003. Seismic geomorphology and stratigraphy of depositional elements in deep-water settings. *Journal of Sedimentary Research*, *73*(3), pp.367-388.

Posamentier, H.W., 2003. Depositional elements associated with a basin floor channel-levee system: case study from the Gulf of Mexico. *Marine and Petroleum Geology*, *20*(6-8), pp.677-690.

Posamentier, H.W., Davies, R.J., Cartwright, J.A. and Wood L., 2007. Seismic geomorphology: applications to hydrocarbon exploration and production. *Geological Society, London, Special Publications*, *277*, pp.1-14.

Rabineau, M., Cloetingh, S., Kuroda, J., Aslanian, D., Droxler, A., Gorini, C., García-Castellanos, D., Moscariello, A., Burov, E., Sierro, F. and Lirer, F., 2015. Probing connections between deep earth and surface processes in a land-locked ocean basin transformed into a giant saline basin: The Mediterranean GOLD project. *Marine and Petroleum Geology*, *66*, pp.6-17.

Rabineau, M., Leroux, E., Aslanian, D., Bache, F., Gorini, C., Moulin, M., Molliex, S., Droz, L., Dos Reis, A.T., Rubino, J.L. and Guillocheau, F., 2014. Quantifying subsidence and isostatic readjustment using sedimentary paleomarkers, example from the Gulf of Lion. *Earth and Planetary Science Letters*, *388*, pp.353-366.

Rabinowitz, P.D. and LaBrecque, J., 1979. The Mesozoic South Atlantic Ocean and evolution of its continental margins. *Journal of Geophysical Research: Solid Earth*, *84*(B11), pp.5973-6002.

Radeff, G., Schildgen, T.F., Cosentino, D., Strecker, M.R., Cipollari, P., Darbaş, G. and Gürbüz, K., 2017. Sedimentary evidence for late Messinian uplift of the SE margin of the Central Anatolian Plateau: Adana Basin, southern Turkey. *Basin Research*, *29*, pp.488-514.

Reading, H.G. ed., 2009. *Sedimentary environments: processes, facies and stratigraphy*. John Wiley & Sons, pp.424-434

Reeder, M.S., Rothwell, R.G. and Stow, D.A., 2000. Influence of sea level and basin physiography on emplacement of the late Pleistocene Herodotus Basin Megaturbidite, SE Mediterranean Sea. *Marine and Petroleum Geology*, *17*(2), pp.199-218.

Reiche, S., Hübscher, C. and Beitz, M., 2014. Fault-controlled evaporite deformation in the Levant Basin, Eastern Mediterranean. *Marine Geology*, *354*, pp.53-68.

Reiche, S., Hübscher, C. and Ehrhardt, A., 2016. The impact of salt on the late Messinian to recent tectonostratigraphic evolution of the Cyprus subduction zone. *Basin Research*, *28*(5), pp.569-597.

Robertson, A.H. and Mart, Y., 1998. Eratosthenes Seamount: an oceanographic yardstick recording the Late Mesozoic-Tertiary geological history of the Eastern Mediterranean. *Proceedings of the Ocean Drilling Program, Scientific Results, Vol. 160; Chapter 52*.

Robertson, A.H. and Mountrakis, D., 2006. Tectonic development of the Eastern Mediterranean region: an introduction. *Geological Society, London, Special Publications*, *260*(1), pp.1-9.

Robertson, A.H., 1998. Tectonic significance of the Eratosthenes Seamount: a continental fragment in the process of collision with a subduction zone in the eastern Mediterranean (Ocean Drilling Program Leg 160). *Tectonophysics*, *298*(1), pp.63-82.

Robertson, A.H.F. and Dixon, J.E., 1984. Introduction: aspects of the geological evolution of the Eastern Mediterranean. *Geological Society, London, Special Publications*, *17*(1), pp.1-74.

Robertson, A.H.F. and Kinnaird, T.C., 2016. Structural development of the central Kyrenia Range (north Cyprus) in its regional setting in the eastern Mediterranean region. *International Journal of Earth Sciences*, *105*(1), pp.417-437.

Rohling, E.J., Schiebel, R. and Siddall, M., 2008. Controls on Messinian lower evaporite cycles in the Mediterranean. *Earth and Planetary Science Letters*, *275*(1), pp.165-171.

Rouchy, J.M. and Caruso, A., 2006. The Messinian salinity crisis in the Mediterranean basin: a reassessment of the data and an integrated scenario.*Sedimentary Geology*, *188*, pp.35-67.

Roveri, M., Gennari, R., Lugli, S., Manzi, V., Minelli, N., Reghizzi, M., Riva, A., Rossi, M.E. and Schreiber, B.C., 2016. The Messinian salinity crisis: open problems and possible implications for Mediterranean petroleum systems. *Petroleum Geoscience*, *22*(4), pp.283-290.

Roveri, M., Lugli, S., Manzi, V., Gennari, R. and Schreiber, B.C., 2014a. High-resolution strontium isotope stratigraphy of the Messinian deep Mediterranean basins: Implications for marginal to central basins correlation. *Marine Geology*, *349*, pp.113-125.

Roveri, M., Manzi, V., Bergamasco, A., Falcieri, F.M., Gennari, R., Lugli, S. and Schreiber, B.C., 2014b. Dense shelf water cascading and Messinian canyons: a new scenario for the Mediterranean salinity crisis. *American Journal of Science*, *314*(3), pp.751-784.

Rowan, M.G., Peel, F.J. and Vendeville, B.C., 2004. Gravity-driven fold belts on passive margins.

Rowan, M.G., Peel, F.J. and Vendeville, B.C., 2004. Gravity-driven fold belts on passive margins. In K. R. McClay, Thrust tectonics and hydrocarbon systems: *AAPG Memoir*, 82, pp. 157-182.

Rowan, M.G., Peel, F.J., Vendeville, B.C. and Gaullier, V., 2012. Salt tectonics at passive margins: Geology versus models–Discussion. *Marine and Petroleum Geology*, *37*(1), pp.184-194.

Ryan, W.B. and Cita, M.B., 1978. The nature and distribution of Messinian erosional surfaces—Indicators of a several-kilometer-deep Mediterranean in the Miocene. *Marine Geology*, *27*(3-4), pp.193-230.

Ryan, W.B., 2008. Modeling the magnitude and timing of evaporative drawdown during the Messinian salinity crisis. *Stratigraphy*, *5*(1), pp.227-243.

Ryan, W.B., 2009. Decoding the Mediterranean salinity crisis.*Sedimentology*, *56*(1), pp.95-136.

Said, R., 1981. *The geological evolution of the River Nile*. Springer Science & Business Media, pp.13-17

Said, R., 1993. *The River Nile: geology, hydrology and utilization*. Elsevier.

Salvador, A., 1987. Late Triassic-Jurassic paleogeography and origin of Gulf of Mexico basin. *AAPG Bulletin*, *71*(4), pp.419-451.

Sarhan, M.A., 2015. High resolution sequence stratigraphic analysis of the Late Miocene Abu Madi Formation, Northern Nile Delta Basin. *NRIAG Journal of Astronomy and Geophysics*, *4*(2), pp.298-306.

Schattner, U. and Ben-Avraham, Z., 2007. Transform margin of the northern Levant, eastern Mediterranean: From formation to reactivation. *Tectonics*, *26*(5).

Schlumberger, 2019, GPM Geological Process Modeling Software. User Guide.

Schultz-Ela, D.D., 2001. Excursus on gravity gliding and gravity spreading. *Journal of structural geology*, *23*(5), pp.725-731.

Shanmugam, G., 2000. 50 years of the turbidite paradigm (1950s—1990s): deep-water processes and facies models—a critical perspective. *Marine and petroleum Geology*, *17*(2),pp.285-342.

Shanmugam, G., 2016. Submarine fans: a critical retrospective (1950–2015). *Journal of Palaeogeography*, *5*(2), pp.110-184.

Symeou, V., Homberg, C., Nader, F.H., Darnault, R., Lecomte, J.C. and Papadimitriou, N., 2018. Longitudinal and temporal evolution of the tectonic style along the Cyprus Arc system, assessed through 2-D reflection seismic interpretation. *Tectonics*, *37*(1), pp.30-47.

Syvitski, J.P. and Kettner, A., 2011. Sediment flux and the Anthropocene. *Philosophical Transactions of the Royal Society A: Mathematical, Physical and Engineering Sciences*, *369*(1938), pp.957-975.

Syvitski, J.P. and Milliman, J.D., 2007. Geology, geography, and humans battle for dominance over the delivery of fluvial sediment to the coastal ocean. *The Journal of Geology*, *115*(1), pp.1-19.

Tari, G.C., Ashton, P.R., Coterill, K.L. and Molnar, J.S., 2002. Are West Africa deepwater salt tectonics analogous to the Gulf of Mexico?. *Oil & Gas Journal*, *100*(9), pp.73-73.

Teama, M.A., Kassab, M.A., Cheadle, B.A., Mesbah, M.A., Mohamed, I.F. and El-Din, E.S., 2017. 3D seismic and formation micro-imager (FMI) integrated study to delineate depositional pattern of Abu Madi (Upper Miocene) clastic reservoir rocks in El-Wastani gas field, onshore Nile Delta, Egypt. *Egyptian Journal of Petroleum, 27(4)*, pp. 747-758

Tetzlaff, D., Tveiten, J., Salomonsen, P., Christ, A., Athmer, W., Borgos, H.G., Sonneland, L., Martinez, C. and Raggio, M.F., 2014. Geologic process modeling. In *IX Congreso de Exploración y Desarrollo de Hidrocarburos-IAPG, Mendoza, Argentina* (pp. 1-16).

Tetzlaff, D.M. and Schafmeister, M.T., 2007. Interaction among sedimentation, compaction, and groundwater flow in coastal settings. *Coastline Changes: Interrelation of Climate and Geological Processes*, *426*, p.65.

Tripsanas, E.K., Piper, D.J. and Campbell, D.C., 2008. Evolution and depositional structure of earthquake-induced mass movements and gravity flows: Southwest Orphan Basin, Labrador Sea. *Marine and Petroleum Geology*, *25*(7), pp.645-662.

Urgeles, R., Camerlenghi, A., Garcia Castellanos, D., De Mol, B., Garcés, M., Vergés, J., Haslam, I. and Hardman, M., 2011. New constraints on the Messinian Sea level drawdown from 3D seismic data of the Ebro Margin, western Mediterranean. *Basin Research*, *23*(2), pp.123-145.

Van Hinsbergen, D.J., Torsvik, T.H., Schmid, S.M., Maţenco, L.C., Maffione, M., Vissers, R.L., Gürer, D. and Spakman, W., 2019. Orogenic architecture of the Mediterranean region and kinematic reconstruction of its tectonic evolution since the Triassic. *Gondwana Research*, *81*, pp.79-229

Vandré, C., Cramer, B., Gerling, P. and Winsemann, J., 2007. Natural gas formation in the westernNile delta (Eastern Mediterranean): thermogenic versus microbial. *Organic Geochemistry*, 38(4), pp.523-539.

Vendeville, B.C., 2005. Salt tectonics driven by sediment progradation: Part I—Mechanics and kinematics. *AAPG bulletin*, *89*(8), pp.1071-1079.

Walley, C.D., 1998. Some outstanding issues in the geology of Lebanon and their importance in the tectonic evolution of the Levantine region. *Tectonophysics*, *298*(1-3), pp.37-62.

Zucker, E., Gvirtzman, Z., Steinberg, J. and Enzel, Y., 2020. Salt tectonics in the Eastern Mediterranean Sea: Where a giant delta meets a salt giant. *Geology*, *48*(2), pp.134-138.